SCHUOLA POLITECNICA DI INGEGNERIA , UNIVERSITÀ DEGLI STUDI DI GENOVA

DOCTORAL THESIS

Distributed Learning-Assisted Model Predictive Control (MPC) and Intelligent Energy Management for Interconnected Smart Greenhouses Integrated with Microgrids

Author:
Said Zahmoun

Supervisor:
Pr. Roberto Sacile
Pr. Ahmed Ouammi
Dr. Enrico Zero

Ph.D. Thesis in Computer Science and Systems Engineering Systems Engineering Curriculum
Dipartimento di Informatica, Bioingegneria, Robotica ed Ingegneria dei Sistemi,Via Opera Pia, 13 16145 Genova Italy

June 12, 2026

Declaration of Authorship

I, Said Zahmoun, hereby declare that this thesis, entitled " Distributed Learning-Assisted Model Predictive Control (MPC) and Intelligent Energy Management for Interconnected Smart Greenhouses Integrated with Microgrids", and the research work presented within it, are my own. I confirm the following:

- This thesis is submitted in partial fulfillment of the requirements for the degree of Doctor of Philosophy in Computer Science and Systems Engineering at the Polytechnic School of Engineering, University of Genoa. The work presented herein was conducted entirely, or primarily, during my candidature for this degree at this University.
- Where any part of this thesis has been submitted previously, either in whole or in part, for any other degree, diploma, or qualification at this or any other institution, this has been explicitly stated within the thesis.
- The contributions and published work of other researchers have been consulted throughout this research. All such material is explicitly acknowledged and appropriately cited.
- With the exception of such properly attributed references and quotations, this thesis represents my original work.
- All major sources of scholarly, technical, and collaborative assistance have been acknowledged in the relevant sections of this thesis.
- In instances where the research builds upon collaborative work, I have clearly identified my personal contribution and the contributions made by other parties.

Signature: ______________________________

Date: ______________________________

Acknowledgements

I wish to express my deepest gratitude to all who have supported me throughout this journey.

My first and most profound thanks go to my family. Your unwavering presence, steadfast support through every decision, and comfort during all difficulties have been my foundation. This achievement is as much yours as it is mine.

To my supervisors, I extend my sincere appreciation. Thank you for the invaluable time, patient guidance, and immense knowledge you have shared. You have not only shaped this work but have profoundly influenced my growth as a researcher.

I am also incredibly grateful to my colleagues. You have been friends first and foremost, sharing in both the challenges and small triumphs. Your camaraderie and helpful hands made the long hours meaningful and often enjoyable.

Finally, to all friends and mentors who have been part of these years thank you. Your encouragement has been a constant and essential gift.

Abstract

Energy management, optimization, and control are significant subjects that have garnered considerable attention across agricultural and industrial sectors. The relevance of productivity in agricultural output and effective energy management within greenhouse systems has become increasingly evident as global population growth intensifies the demand for food resources. In response to these challenges, this thesis develops and critically evaluates three distinct yet complementary control frameworks for smart greenhouse energy management situated within the broader contexts of smart farming and power grid integration.

The first proposed framework introduces a centralized energy management platform based on a dynamic nonlinear quantum particle swarm optimization algorithm embedded within a predictive control structure. This platform orchestrates renewable generators, HVAC systems, energy storage units, water reservoirs, CO_2 injectors, dehumidifiers, and smart metering infrastructure to regulate indoor microclimate variables while actively minimizing power exchange with the external grid during periods of low renewable generation. Comparative performance validation is conducted against classical particle swarm optimization and the Pyomo optimization environment solved with IPOPT.

In a subsequent contribution, a nonlinear model predictive control methodology is formulated for comparable greenhouse assets, with particular emphasis on adaptability across a comprehensive crop growth model that considers all plant organs. This model dynamically computes dry matter accumulation partitioned among leaves, stems, roots, fruits, and mature fruits. The control strategy prioritizes accurate regulation of temperature, relative humidity, and CO_2 concentration trajectories while reducing overall energy consumption.

The fourth section of this thesis expands the scope toward interconnected net zero-energy farm microgrids, wherein smart greenhouses operate alongside residential zones and animal housing facilities. A distributed optimization algorithm grounded in the alternating direction method of multipliers is developed to coordinate power exchanges among individual farms as well as between the farm cluster and the main utility grid. This architecture maximizes localized renewable energy utilization while preserving desirable microclimates across all building typologies. Collectively, these contributions provide a progressive trajectory from centralized optimization to distributed coordination and hybrid renewable scheduling, offering practical and theoretical insights for scalable, energy-efficient, climate-resilient greenhouse systems and power grid integration.

The final component of this thesis addresses hybrid renewable energy systems combining wind farms (WF) with pumped hydroelectric energy storage (PHES) for peak load reduction. A finite horizon scheduling optimization problem is formulated to control real-time WF-PHES operation using predictions of wind speed and power load. A three-layered ANN forecasts these variables from historical data, while a mathematical decision model accounts for seasonal (summer/winter) load-shaving requirements. The proposed framework is validated on a case study and compared against Pyomo with IPOPT and a Genetic Algorithm (GA), demonstrating its effectiveness through extensive numerical simulations.

Contents

Declaration of Authorship ii

Acknowledgements iii

Abstract iv

1 Introduction and Motivation 1
- 1.1 Main Contributions . . . 3
- 1.2 Thesis Organization . . . 4
- 1.3 List of Publications and editorial activity . . . 5
  - 1.3.1 Journal Papers - Published . . . 5
  - 1.3.2 Journal Papers - Under Review . . . 6
    - Conference Papers - Published . . . 6
    - Open Invite Track Organization . . . 6
    - Special Session Organization . . . 6
  - 1.3.3 Projects . . . 7

2 Optimizing Greenhouse Energy and Microclimate Control Under Harsh Climates Using a Quantum PSO Algorithm 8
- 2.1 Modeling Greenhouse System Components . . . 8
  - 2.1.1 PV Panels Model . . . 9
  - 2.1.2 Wind Turbine Generator Model . . . 10
  - 2.1.3 Battery Storage Model . . . 10
  - 2.1.4 Water Reservoir and Pumps Model . . . 10
- 2.2 Comprehensive Mathematical Model for Greenhouse Microclimate Dynamics 11
  - 2.2.1 Temperature Model . . . 11
  - 2.2.2 Air circulation model . . . 12
  - 2.2.3 Light Intensity Model . . . 12
  - 2.2.4 Relative Humidity Model . . . 13
  - 2.2.5 CO_2 Concentration Model . . . 14
  - 2.2.6 Power balance . . . 14
  - 2.2.7 Optimization Problem . . . 14
    - Objective Function . . . 14
    - System benefits . . . 15
    - Constraints governing the problem . . . 15
- 2.3 Computational Energy Management Strategy for a Greenhouse Connected to the Power Grid Using an Enhanced PSO Algorithm . . . 18
  - 2.3.1 Classical PSO Approach . . . 18
  - 2.3.2 PSO-Based Computational System Energy Management Strategy . . 19
  - 2.3.3 Quantum PSO Approach . . . 21
  - 2.3.4 QPSO-Based Computational System Energy Management Strategy . 22
- 2.4 Case Study and Numerical Results . . . 22
  - 2.4.1 Case Study Application . . . 22

2.4.2 Simulation Setup 24
2.4.3 Numerical Results and Discussion 25
2.5 Conclusion 31

3 Unified Model Predictive Control for Coordinated Microgrid Energy Management and Greenhouse Microclimate Control over Growth Cycles 33
3.1 Modeling of system component 34
3.1.1 PV Panels 34
3.1.2 Wind Turbine Generator 35
3.1.3 Water Reservoirs and Pumps 35
3.1.4 Energy Storage System 36
3.1.5 Greenhouse Microclimate Dynamics Model 37
Temperature Model 37
Air circulation model 38
Light Intensity Model 38
CO_2 Model 39
Model of Humidity 39
3.1.6 Dynamic Nutrient Supply During Growth Stages 40
3.1.7 Power Balance 40
3.2 Sweet Pepper Growth Model 41
3.2.1 Crop photosynthesis 42
Leaf area index 42
Leaf photosynthesis 42
3.2.2 Maintenance respiration 42
3.2.3 Crop dry weight 43
3.2.4 Organs dry weight 43
3.2.5 Mature fruit biomass 44
3.3 Optimization Problem 45
3.3.1 Objective Function and Constraints 46
3.3.2 System benefits 46
3.4 Case Study and Numerical Results 46
3.4.1 Case Study Application 46
3.4.2 Simulation Setup 47
3.4.3 Numerical Results and Discussion 47
3.5 Conclusion 56

4 Distributed Control ADMM Algorithm for Connected Net Zero-Energy Farms Integrated Microgrids 58
4.1 System architecture and modeling 58
4.1.1 Model of Renewable Energy Generators 59
Wind Model 60
PV Model 60
4.1.2 Model of Water Reservoirs and Pumps 60
4.1.3 Model of Thermal Comfort 60
4.1.4 Model of Air Circulation 61
4.1.5 Model of Humidity 61
4.1.6 Model of CO_2 Concentration 62
4.1.7 Model of Light Intensity 62
4.1.8 Energy Balance 63
4.2 Optimization Problem 63
4.2.1 Centralized Approach 63

Constraints governing the problem 63
4.2.2 Distributed Approach 65
ADMM Formulation 65
4.3 Case Study and Numerical Results 67
4.3.1 Case Study and Application 67
Optimal greenhouses reference signals 69
Residential and animal buildings reference signals 69
4.3.2 Numerical Results and Analysis 69
4.4 Conclusion 80

5 Optimal Operation Scheduling of a Combined Wind-Hydro System for Peak Load Shaving 81
5.1 Background and Rationale 81
5.1.1 Methodology 83
5.2 Model of Wind power plant production 84
5.2.1 Wind power 84
5.2.2 Wind speed extrapolation at various hub heights 85
5.2.3 Modelling a WPP's rotor 86
5.2.4 Modelling a WPP's gearbox 86
5.2.5 Modelling a WPP's generator 86
5.2.6 Modeling a WPP's energy production 87
5.3 Model of a pumped hydroelectric energy storage system 87
5.3.1 Power generation in hydroelectric power plants 88
5.3.2 Friction loss in transfer installations 88
5.3.3 Energy production in hydroelectric power plants 89
5.3.4 Modelling reservoir's 89
5.3.5 Power Consumption in Hydroelectric Power Plants 89
5.3.6 Energy Consumption in Hydroelectric Power Plants 90
5.3.7 Modelling of booster pump station 90
Energy of consumption of the booster pump station 90
5.4 Planning optimization for WF-PHES 90
5.4.1 Objective Function 90
5.4.2 State equations 90
Equations of the model 90
Benefits of the system 91
5.4.3 System operation (WF-PHES) in summer and winter seasons 91
Off-peak periods (Pumping - Mode) 91
Peaks periods (Turbining - Mode) 91
5.4.4 Constraints governing the problem 91
Power constraints 91
Storage constraints (volume stored) 91
Spillway constraints 91
5.5 Application to case studies and numerical results 92
5.5.1 WPP model accuracy 92
5.5.2 Hybrid model WF-PHES 93
5.5.3 Simulation setup 93
5.5.4 Price structure 94
5.5.5 Results and analysis 95
5.5.6 Comparison analysis 99
5.6 Conclusion 100

List of Figures

2.1 Greenhouse system components. 9
2.2 Flowchart of System Using different optimization methods. 19
2.3 Real and forecasted outdoor environmental variables fluctuate during various stages of growth. 24
2.4 Real and predicted power production from wind turbine and PV panel models 25
2.5 Water flows pumped into the water reservoir, optimal tracking to meet irrigation needs with their pump power consumption, and dynamics of water reservoir levels across growth phases. 26
2.6 Optimal greenhouse indoor temperature with their HVAC power consumption and coefficient of performance over the day across diffirent growth phases. . . 27
2.7 Optimal opening ventilation angle over different phase growth. 27
2.8 Optimal tracking of the illumination loads with their power consumption across growth phases. 28
2.9 Optimal relative humidity inside the greenhouse with optimal power consumed by fogger and dehumidifier equipment across different growth phases. 28
2.10 Optimal monitoring and control of CO2 concentration levels inside the greenhouse with optimal power consumed by the CO2 injector throughout different growth phases. 29
2.11 Optimal power exchange with the grid and dynamic of Batteery energy storage throughout the day for different growth phases. 29
2.12 Profits and consumption of the system operation throughout the day for different growth phases. 30
2.13 Total benefits of the system using proposed optimization methods. 30
2.14 The evolution of the objective function across iterations using different optimization methods. 30

3.1 System architecture. 34
3.2 Weather station (savona) 35
3.3 Diagram of the proposed sweet pepper growth model 41
3.4 Predected and measured outdoor environment data collected from weather station Fig.3.2. 47
3.5 MPC-based water flows are pumped into the water reservoir with optimal tracking to meet irrigation needs with their pump power consumption and dynamics of water reservoir levels across whole growth phases. 49
3.6 MPC-based optimal greenhouse indoor temperature with their HVAC power consumption and coefficient of performance over the typical days across different growth phases. 49
3.7 MPC-based optimal greenhouse indoor temperature with their HVAC power consumption and coefficient of performance over all growth phases. 50
3.8 Optimal opening ventilation angle over whole phases of growth. 50
3.9 MPC-based optimal tracking of the illumination loads with their power consumption across whole growth phases. 51

3.10 The MPC controls greenhouse CO_2 levels, managing the injector's power and operation across growth phases. 51
3.11 MPC-based optimal relative humidity inside the greenhouse with optimal power consumed by the fogger and dehumidifier across whole growth phases. 52
3.12 Renewable power production, optimal power exchange with the grid, and dynamics of battery energy storage for whole growth phases. 53
3.13 Accumulation of dry matter for each organ for sweet pepper at the whole phase of growth. 54
3.14 Percentage distribution of dry matter in each organ during different growth phase periods of sweet pepper. 55

4.1 System design (centralized approach) 59
4.2 System design inside each farm(m). 59
4.3 System Design Using (ADMM) 65
4.4 Renewable power production, outdoor temperature, CO_2 and humidity in each farm. 70
4.5 Optimal indoor temperature in each greenhouse. 70
4.6 Optimal indoor temperature in residential and animal buildings and their power consumption (kW) by HVAC's. 71
4.7 power consumed by HVAC's in each greenhouse (kW). 72
4.8 Optimal tracking of the water references in GH(1,n) with their power consumption. 72
4.9 Optimal tracking of the water references in animal buildings. 73
4.10 Optimal water is pumped into reservoirs with tier power consumption and level water reservoirs at each farm. 73
4.11 Optimal tracking of the artificial lighting loads in each GH(m,n) 74
4.12 Optimal tracking of CO_2, humidity inside greenhouses 75
4.13 Optimal powers are consumed by CO_2 injection, dehumidifiers, and fogging systems with an opening angle in each greenhouse. 75
4.14 The optimal Energy Storage Inventory (ESI) present on each farm and the optimal power exchanges between farms and with the main grid. 76
4.15 The optimal Energy Storage Inventory (ESI) is present on each farm, and the optimal power exchanges between farms without exchange with the main grid. 78
4.16 Optimal water is pumped into reservoirs with tier power consumption and level water reservoirs at each farm without exchange with the main grid. . . . 79
4.17 The ADMM time is spent for each iteration until max iterations to solve algorithm 1 in both scenarios (with exchange and penalized) compared to the centralized approach. 79

5.1 Methodology flow chart for model components. 84
5.2 Actual and forecasted load power for one week and the next week during the winter and summer seasons. 84
5.3 Actual and forecasted wind speed for the coming week and the following week during the winter and summer. 85
5.4 wind turbine simple schematization 85
5.5 The hybrid system of renewable energy. 88
5.6 power coefficient Cp of each technology as derived by equation (5.9), and a comparison between the manufacturer's power curve and the model's computed power curve. 93
5.7 The variation of the power produced and predicted by each wind farm over the course of a week during the summer season is determined by Eq (5.22). . 94

5.8 The variation of the power produced and predicted by each wind farm over the course of a week during the winter season is determined by Eq (5.22). . . 95
5.9 Reduction of the peak load by the system during the winter season in the deterministic and probabilistic cases. 96
5.10 Reduction of the peak load by the system during the winter season in the deterministic and probabilistic cases. 96
5.11 Optimal operation of the PHES technology proposed by the optimization model during a summer week. 96
5.12 The variation of the volumes of water stored in the reservoirs during the function of the PHES technology during a week. 97
5.13 The variation of the friction losses in transfer installation during the function of the PHES technology 97
5.14 Depicts the change in the amount of water evaporated by the two reservoirs over the course of a summer week. 98
5.15 The benefits of the system for the summer and winter seasons for one week in the probabilistic and deterministic cases. 98
5.16 Comparison of optimization methods for lowering the system's summertime peak load. 99
5.17 Percentages of wind and hydropower as well as their earnings for various optimization methods. 99
5.18 Total system incomes for different optimization methods. 100

List of Tables

2.1 System Components Parameters 17
2.2 Optimization Variables 18
2.3 PSO, QPSO indexes, and sets 22
2.4 Microclimate and water reference of pepper in different phases of growth . . 24
2.5 Performance Metrics Comparison 31

3.1 Total nutrient requirement (g) per greenhouse during each growth phase. . . . 40
3.2 Effect of Climatic Functions on Crop Growth 44
3.3 Parameters sweet pepper crop growth model 45
3.4 Microclimate and water references of pepper in different phases of growth . . 48
3.5 Biomass Values per Component 53
3.6 Economic Benefits from Grid Exchange per Growth Stage 54
3.7 Biomass Production per Growth Stage 54

4.1 System Components Parameters 68
4.2 Comparison of Optimization Methods 77

5.1 Optimization Variables 92
5.2 WPP parameters 92
5.3 PHES parameters 94

List of Abbreviations

NPSO	Non-linear Particle Swarm Optimization
NQPSO	Non-linear Quantum Particle Swarm Optimization
HVAC	Heating, Ventilation, and Air Conditioning
RFA	Random Forest Algorithm
IPOPT	Interior Point Optimizer
NMPC	Nonlinear Model Predictive Control
BES	Battery Energy Storage
E.G	Early Growth (Phase of Growth)
V	Vegetative (Phase of Growth)
F	Flowering (Phase of Growth)
F.F	Fruit Formation (Phase of Growth)
M.F	Mature Fruiting (Phase of Growth)
ADMM	Alternating Direction Method of Multipliers
REG	Renewable Energy Generators
ESI	Energy Storage Inventory
PV	Photovoltaic
$\mathbf{GH(m, n)}$	The n-th greenhouse existing at the m-th farm
WF	Wind Farms
PHES	Pumped Hydroelectric Energy Storage
ANN	Artificial Neural Network
MEHS	Multi-Energy Hybrid System
GA	Genetic Algorithm
WPP	Wind Power Plant
MPC	Model Predictive control

Physical Constants Sets and Parameters

ρ_a	air density	999.93	(kg/m^3)
g	gravity acceleration constant	9.81	$(m \cdot s^{-2})$
ρ	water density	1.225	(kg/m^3)

Parameters and variables of (Chap.2) are described in Tables (2.1) and (2.2)

Sets, indexes, parameters and variables of (Chap.3)

Symbol	**Description**	**Value**	**Unit**
Ω^*	Set of constraints		
Δk	Time-step length	15	(min)
n_p	Prediction horizon		
k	Index of time-step		
P_r	Wind turbine rated power	15	(kW)
v_c	Wind turbine cut-in wind speed	2.5	(m/s)
v_r	Wind turbine rated wind speed	9	(m/s)
v_f	Wind turbine cut-out wind speed	45	(m/s)
V_{mp}^{ref}	Module maximum power voltage	47.71	(V)
V_{oc}^{ref}	Module open-circuit voltage	52.63	(V)
I_{sc}^{ref}	Module short-circuit current	14.13	(A)
I_{mp}^{ref}	Module maximum power current	13.50	(A)
G_{st}	Standard light intensity	1000	(W/m^2)
T^{amb}	Ambient temperature	25	(°C)
μ	Module voltage temperature coefficient	-0.13	(V/°C)
η	Module current temperature coefficient	0.0063	(A/°C)
ξ^{loss}	Connection loss	0.9	
$\epsilon^{pv,s}$	Serial connection number of PV modules	8	
$\epsilon^{pv,p}$	Parallel connection number of PV modules	1	
ρ	Water density	999.93	(kg/m^3)
g	Gravity acceleration constant	9.81	(m·s^{-2})
h_m	Height between water source and reservoir	10	(m)
h_l	Height between reservoir and greenhouse plants	2	(m)
η_m	Master pump efficiency	0.8	
η_l	Local pumps efficiency	0.75	
β_c	Battery charging coefficient	0.9	
β_d	Battery discharging coefficient	0.9	
ρ_a	Air density	1.225	(kg/m^3)
V_g	Volume of greenhouse	192.5	(m^3)
S_g	Greenhouse cover surface area	182.7	(m^2)
τ	Greenhouse material transmission	0.15	

e	Greenhouse glazing material thickness	0.025	(m)
k_c	Material thermal conductivity	0.04	(W/m·K)
J^{inf}	Infiltration rate	0.000208	(1/s)
h^{conv}	Convective heat transfer coefficient	2.27	(W/m^2 K)
A^v	Window area of natural ventilation	1	(m)
k_{sol}	Factor of solar radiation contributing to PAR	0.5	
η_l	LED efficiency	2.8	(μmol/J)
N_x	Number of artificial lighting products	35	
$\delta I^l_{\min}$	Minimum light intensity	36	(W/m^2)
$C^{inj}_{\max}$	Maximum CO_2 injection capacity	0.2e-3	(kg/m^2)
λ_s	Percentage of wind entering greenhouse	0.0075	
C^{phot}	Photosynthesis coefficient of crops	2.0e-5	(W/m^2)
C_{res}	Respiration coefficient of crops	0.3e-6	(kg/(m^2 Δk K))
P_r^{CO2}	CO_2 generator rated power	2	(kW)
a_1	Empirical constant	-0.15	
a_2	Respiration coefficient rate of crop	0.03	(1/K)
a_3	Constant	0.05	
C_r^{ev}	Crop evaporation rate	0.1258	(kg/(m^2 h))
c_1	Constant	100	(nodim.)
c_2	Constant	1.7001	(Pa)
c_3	Constant	7.7835	(Pa)
c_4	Constant	1/17.0789	(K^{-1})
c_5	Constant	0.6228	(kg_w/kg_a)
L^{fog}_{max}	Maximum water flow rate of fogger	0.0096	(kg/(m^2 Δk))
L^{deh}_{max}	Maximum rate of dehumidifier	1	(kg/(m^2 Δk))
P_r^{fog}	Fogger rated power	1	(kW)
P_r^{deh}	Dehumidifier rated power	1	(kW)
α_f	Maximum partitioning coefficient	0.65	
θ	Transition coefficient	0.15	
ψ^T_{part}	Optimal temperature for partitioning	25	(°C)
ψ^T_h	High temperature threshold	32	(°C)
ψ^T_{dev}	Optimal temperature for fruit development	22	(°C)
ψ^{Tmin}_{dev}	Minimum temperature for fruit development	12	(°C)
ψ^{Tmax}_{dev}	Maximum temperature for fruit development	35	(°C)

Sets and indexes of (Chap.4) parameters are detailed in Table (4.1)

M	Set of farms	4	
N	Set of greenhouses	3	
L	Set of power links	5	
Δt	Step time	15	(min)
T	Set of total time steps over 24 hours	96	
m	Index of farms	–	–
n	Index of greenhouses	–	–
l	Index of power links	–	–
t	Index of time step	–	–

Variable	Description	Unit
P_{pv}	PV system power production	(kW)
P_{wind}	Wind turbine power production	(kW)
Q_m	Water flow pumped into the reservoir	($m^3/\Delta k$)
Q_l	Water flow pumped into greenhouse	($m^3/\Delta k$)
P^m_{water}	Power consumed by master pump	(kW)
P^l_{water}	Power consumed by local pumps	(kW)
P^{hvac}	HVAC power consumption	(kW)
C_{op}	HVAC performance coefficient	(kW)
P^{art}	Artificial lighting power consumption	(kW)
P^{CO_2}	CO_2 injector power consumption	(kW)
L^{in}	Greenhouse inside air water quantity	(g/m^2 h)
P^{fog}	Power consumed by fogger	(kW)
P^{deh}	Power consumed by dehumidifier	(kW)
P^{sold}_{grid}	Power sold to the grid	(kW)
P^{buy}_{grid}	Power purchased from the grid	(kW)
χ^{nut}	Amount of nutrient supplied	(g)
m	Water reservoir level	(m^3)
BES	Battery energy storage	(kWh)
ψ^{Tin}	Greenhouse indoor temperature	(°C)
ψ^{Lin}	Greenhouse indoor light intensity	(W/m^2)
$\psi^{CO_2^{in}}$	Greenhouse indoor CO_2 concentration	(ppm)
$\psi^{H^{in}}$	Greenhouse indoor relative humidity	(%)
α	Greenhouse angle opening	(deg)
W_L	Leaf dry matter	(g/m^2)
W_S	Stem dry matter	(g/m^2)
W_R	Root dry matter	(g/m^2)
W_F	Fruit dry matter	(g/m^2)
W_M	Matter fruit development	(g/m^2)
W_T^{bio}	Total biomass plant dry weight	(g/m^2)
β_{hvac}	HVAC operation status $\in [0, 1]$	
β_l	Artificial lighting operation status $\in [0, 1]$	
β_{CO_2}	Operation status of CO_2 enrichment $\in [0, 1]$	
β_{fog}	Fogger operation status $\in [0, 1]$	
β_{deh}	Dehumidifier operation status $\in [0, 1]$	
δ^{v_s}	Outdoor Wind speed	(m/s)
δ^{I_l}	Solar irradiation	(W/m^2)
$\delta^{T^{\mathrm{out}}}$	Outdoor temperature	(°C)
$\delta^{H^{out}}$	Outdoor relative humidity	(%)
$\delta^{CO_2^{out}}$	Outdoor CO_2 concentration	(ppm)

Parameters and variables of (Chap.5) are described in Tables (5.2), (5.3) and Table (5.1)

Chapter 1

Introduction and Motivation

The need to feed the world's anticipated 10 billion people by 2050 faces the harsh reality of growing resource limitations, such as dwindling freshwater supplies and arable land, which are made worse by the effects of climate change, environmental degradation, and biodiversity loss [1, 2]. Conventional agricultural paradigms are increasingly perceived as unable to address the twin issues of growing demand and increased sustainability requirements [3, 4]. This realization has sparked a fundamental change toward precision smart farming, a paradigm that makes use of cutting-edge technologies to maximize productivity while optimizing resource use, especially water and energy. However, this shift adds a great deal of complexity, requiring complicated decision-making frameworks that function at the intersection of smart agriculture and the updated smart grid [5, 6, 7, 8, 9, 10].

Greenhouses have become a crucial technological answer in this crucial context, transforming horticulture and floriculture by establishing a regulated environment for crop production. They provide significant advantages, such as longer growing seasons, defense against pests and severe weather, and more effective use of land, water, and energy [11, 12]. In order to maximize plant growth, quality, and yield, the primary goal is to precisely control the indoor microclimate, namely the interdependent variables of temperature, humidity, CO_2 concentration, and light intensity [13, 14]. This process is further enhanced by intelligent irrigation systems that reduce water waste [15]. However, because of the non-linear interactions between these variables and their coupling with unexpected external weather conditions, intelligent management of this environment is a highly complicated, multivariate control issue [14].

As a result, several different control mechanisms have been studied. These include more sophisticated approaches like Model Predictive Control (MPC), fuzzy logic, and adaptive systems [16, 17, 18, 19], as well as more conventional ones like Proportional-Integral-Derivative (PID) control and Linear-Quadratic Regulators (LQR). Additionally, model parameters and control setpoints have been adjusted using optimization algorithms such as Particle Swarm Optimization (PSO) [20]. However, a recurring flaw in a lot of this research is that it mostly ignores the related energy issues in favor of internal climate regulation. One of the main obstacles to the sustainable development and scalability of sophisticated greenhouse systems is the high energy consumption needed for heating, cooling, dehumidification, and additional lighting [21].

It is critical to resolve this energy constraint. A practical route to sustainability is the incorporation of Renewable Energy Sources (RES) into specialized agricultural microgrids. A microgrid is a localized energy system that combines programmable loads, energy storage, and distributed generation (such as solar PV and wind turbines). It can function independently in islanded mode or in tandem with the main grid [22, 23, 24, 25, 26, 27]. Microgrids help the modernization and sustainability of farming operations, improve the autonomy of renewable energy in rural regions, and provide a dependable and secure energy supply for the agricultural sector [28, 29, 12]. A greenhouse can serve as the core of such a microgrid due to its varied energy profile and possibility for on-site generation (e.g., via agrivoltaics), enabling bidirectional energy exchange and advancing toward net-zero energy operations [30, 31, 32].

The control challenge is completely changed when a greenhouse is integrated with a microgrid. Optimizing the environment alone is no longer adequate; real-time co-optimization of the microclimate and the energy flows inside the microgrid is required. This results in a non-convex, constrained, high-dimensional optimization problem. The availability, pricing, and storage status of energy from photovoltaics, wind turbines, batteries, and the grid must be dynamically balanced with decisions about lighting, heating, cooling, and irrigation. Many current techniques lack a comprehensive framework that concurrently addresses all crop growth parameters and the dynamic integration of RES [33, 34], despite the potential of predictive strategies like MPC for renewable energy management [29, 35, 36]. Moreover, prior methods often implement partial control, neglecting the global optimization of the entire coupled system where parameter interactions are critical [37, 38].

A thorough examination of the existing literature reveals several critical gaps that the present study addresses. First, the vast majority of greenhouse control studies focus on very short simulation horizons, typically 24 hours or a few days [39, 40, 41, 42, 43], and therefore fail to capture the evolving crop requirements across a full growing cycle. In contrast, the present work in the second section simulates and optimizes the entire 161-day growth period, adapting control actions to each stage, from early growth to harvest. Second, conventional greenhouse control strategies are limited to regulating only temperature and humidity [44, 45], often neglecting lighting, CO_2 concentration, irrigation scheduling, and the precise nutrient delivery that plants require for optimal development. Also, most existing research does not integrate energy dynamics, including renewable generation, storage, and grid interaction, into the same control framework as the microclimate variables, treating energy as an afterthought rather than a core constraint. In addition, the interaction between the greenhouse and the external microgrid is frequently overlooked, missing opportunities for demand response, energy arbitrage, and islanded operation.

Critically, the majority of greenhouse control studies do not include a mechanistic crop growth model. Those that do typically use only a single aggregated biomass variable, ignoring how environmental conditions differentially affect individual plant organs. By contrast, the present work develops and embeds a full sweet pepper crop growth model that dynamically calculates the dry matter accumulation of leaves, stems, roots, fruits, and mature fruits separately. This allows the control system to optimize not just overall yield but also the timing and quality of harvestable produce.

At a higher systemic level, these findings point to two important and related research gaps. First, a cohesive, intelligent control system is required that can simultaneously optimize the performance of a heterogeneous renewable microgrid and manage the intricate, cooperative interactions within a greenhouse microclimate. Second, and perhaps most importantly, current research focuses on optimizing individual, independent greenhouse units. Despite being crucial for attaining scalability, resilience, and overall grid stability, the possibility of cooperative, distributed management among a network of linked farms or greenhouses inside a common microgrid environment is yet mainly unexplored [46, 47, 48, 49].

This thesis presents a novel two-tiered intelligent control architecture to close these gaps. We create and apply a Nonlinear Quantum-inspired Particle Swarm Optimization (NQPSO) algorithm in conjunction with a Nonlinear Model Predictive Control (NMPC) framework at the level of a single integrated greenhouse-microgrid system. This sophisticated metaheuristic makes use of quantum computing concepts to improve global search and parallel processing. Its purpose is to dynamically balance microgrid energy flows with greenhouse microclimate factors through real-time predictive co-optimization. This method is designed to overcome the shortcomings of conventional optimization techniques in navigating the system's high-dimensional and non-linear solution space [20, 50, 51]. It is enhanced with a machine learning-based predictor for precise environmental predictions. To the best of our knowledge, this is the first study to employ NMPC for dynamically controlling the inside microclimate of a smart greenhouse integrated into a microgrid over a full 161-day growing cycle, adapting control actions to the specific requirements of each growth phase while simultaneously tracking organ-level crop development to promote more efficient and sustainable greenhouse operations.

At the broader, systemic level, we formulate a distributed optimization and control strategy for a network of interconnected net-zero energy farms. Utilizing the Alternating Direction Method of Multipliers (ADMM), this framework enables scalable, privacy-preserving, real-time coordination among multiple autonomous entities such as greenhouses, residential buildings, and animal facilities to efficiently manage collective energy exchanges and individual microclimate setpoints. Together, these contributions aim to transform the advanced, closed greenhouse from an energy-intensive concept into a practical, efficient, and sustainable cornerstone of future resilient food production systems.

1.1 Main Contributions

The principal contributions of this thesis, which address the identified research gaps, are as follows:

- **Development of an Integrated Optimization Framework and Mathematical Model**
  We formulate a comprehensive, non-linear mathematical model that unifies the dynamics of a closed greenhouse microclimate encompassing temperature, humidity, CO_2, lighting, irrigation, and ventilation with the operational constraints of a hybrid renewable microgrid comprising photovoltaic panels, wind turbines, energy storage systems, and a connection to the main electrical grid. This integrated model establishes the foundation for a novel control paradigm that simultaneously optimizes for crop physiological requirements and overall energy efficiency.

- **Design, Implementation, and Validation of a Novel NQPSO-Based Control Algorithm**
  We pioneer the application of a Nonlinear Quantum-inspired Particle Swarm Optimization (NQPSO) algorithm for the real-time, predictive management of a smart greenhouse integrated with a microgrid. Enhanced with a machine learning model (e.g., Random Forest) for reliable prediction of key environmental variables, this algorithm is rigorously tested and shown to outperform classical optimization methods (including standard PSO and Pyomo-based models) in solving the complex, high-dimensional optimization problem. It ensures robust, energy-efficient greenhouse operation across an entire crop growth cycle, as validated through extensive simulations and a detailed real-world case study.

- **We developed and embedded a full organ-level crop growth model that separately tracks dry matter in leaf, stem, root, fruit, and mature fruits over phase of growths**
  A central contribution of this work is the development and embedding of a comprehensive crop growth model that separately tracks dry matter accumulation in leaves, stems, roots, fruits, and mature fruits. This model serves as the core of a broader mathematical framework for controlling a smart greenhouse farming setup, where the control scheme simultaneously adjusts all key variables influencing crop development, namely indoor air temperature, relative humidity, CO_2 concentration, lighting, natural ventilation, and nutrient delivery while also optimizing energy and water use under unpredictable outdoor conditions and fluctuating renewable energy output. The primary

challenge addressed by this framework is the design of a centralized predictive control structure capable of handling complex crop-environment interactions, balancing competing objectives, coping with random and unpredictable inputs, and optimizing energy exchanges at the microgrid level. Achieving this required properly modeling all system components and simulating their operation under dynamic conditions. Although the proposed control framework is relatively standard from a purely theoretical standpoint, it offers practical value for this specific agricultural application and lays the groundwork for more advanced nonlinear model predictive control methods in future work. Overall, the model provides an efficient and sustainable response to key challenges in precision agriculture.

- **Formulation and Demonstration of a Scalable ADMM-Based Distributed Control Strategy**
  To address the challenge of scaling sustainable agriculture, we propose a pioneering distributed optimization strategy for a network of interconnected net-zero energy farms. By developing an ADMM-based supervisory controller, we enable efficient, parallel computation for the real-time coordination of energy exchanges (purchasing, selling, sharing) and climate control setpoints among multiple autonomous operational units (e.g., greenhouses, residential buildings). This framework enhances overall system resilience, respects data privacy, and offers superior computational scalability and efficiency compared to centralized optimization approaches, as demonstrated through comparative numerical simulations.

- **Holistic System Validation and a Pathway to Sustainable Implementation**
  The performance and practical efficacy of both the NQPSO, NMPC (single-system) and ADMM (multi-system) frameworks are comprehensively validated through integrated simulation case studies that account for harsh climatic conditions and full growth periods. This work not only proves the technical and economic feasibility of achieving net-zero energy operations for advanced greenhouses but also provides a scalable, algorithmic blueprint for the design and management of next-generation, intelligent, and sustainable agricultural systems.

1.2 Thesis Organization

This thesis is organized into five chapters, each systematically addressing the critical aspects of controlling and optimizing closed greenhouse systems for sustainable agriculture, with a particular focus on renewable energy integration and smart grid interaction. The research progresses from establishing the foundational problem to developing and validating novel algorithmic solutions for microclimate control and energy management. The final chapter 5 addresses the external energy system challenge of peak power loads, proposing and evaluating a novel hybrid renewable energy storage system as a practical solution . The chapters are structured as follows:

- **Chapter 1: Introduction and Motivation**
  This chapter.1 provides the context, motivation, and objectives of the research. by outlining the dual challenge of global food security and smart farming . It introduces closed greenhouses as a high-potential solution while identifying their critical drawback: substantial energy consumption. To contextualize this problem, the chapter surveys existing literature on greenhouse modeling, climate control strategies, and renewable energy integration within agricultural microgrids.

- **Chapter 2: Optimizing Greenhouse Energy and Microclimate Control Under Harsh Climates Using a Quantum PSO Algorithm**
  This chapter.2 presents a high-level optimization framework using a novel Nonlinear Quantum-inspired PSO (NQPSO) algorithm . The method optimizes greenhouse climate and energy consumption throughout the growing season by managing real-time interactions between environmental and power variables. A real-world case study validates the approach, showing it outperforms traditional optimization methods in simulations. The results demonstrate the framework's effectiveness in addressing nonlinear, multi-variable control, offering a practical path toward sustainable greenhouse management.

- **Chapter 3: Unified Model Predictive Control for Coordinated Microgrid Energy Management and Greenhouse Microclimate Control over Growth Cycles**
  The following chapter.3 outlines a centralized predictive control framework that handles complex crop-environment interactions, balances competing objectives, copes with random and unpredictable inputs, and optimizes energy exchanges at the microgrid level. This requires properly modeling all components and simulating their operation under dynamic conditions. While our control framework is relatively standard from a theoretical perspective, we believe it offers real value for this specific application and could open the door to more advanced NMPC methods later. The proposed model is an efficient, sustainable answer to key challenges in precision agriculture.

- **Chapter 4: Distributed Control ADMM Algorithm for Connected Net Zero-Energy Farms Integrated Microgrids**
  This chapter.4 investigates advanced control strategies to manage the operational challenges of the distributed optimization problem for interconnected farms, and develops an ADMM-based control framework for scalable, cooperative energy management across multiple agricultural units .

- **Chapter 5: Optimal Operation Scheduling of a Combined Wind-Hydro System for Peak Load Shaving**
  This chapter.5 proposes a wind farm and pumped hydro storage (WF-PHES) hybrid system to reduce peak power loads. It develops and validates an optimization model to control the system operation, demonstrating its effectiveness through seasonal case studies and performance comparisons.

1.3 List of Publications and editorial activity

This section summarizes the research contributions made during the course of this PhD, including published journal papers, conference presentations, and organizational activities.

1.3.1 Journal Papers - Published

- **"Optimal Operation Scheduling of a Combined Wind-Hydro System for Peak Load Shaving"** *IEEE Transactions on Automation Science and Engineering*[1].

- **"Integrating Digital Twins and MPC for Sustainable Greenhouse Management in Smart Agriculture"** *IEEE Transactions on Agrifood Electronics*.[2]

[1] https://ieeexplore.ieee.org/document/10348533
[2] https://ieeexplore.ieee.org/document/11033172

- **"Smart greenhouse farming: a review towards near zero energy consumption"** *Springer Discover Cities.* [3]

1.3.2 Journal Papers - Under Review

- **"Optimizing Greenhouse Energy and Microclimate Control Under Harsh Climates Using a Quantum PSO Algorithm"** *IEEE Transactions on Sustainable Computing*.
- **"Distributed Control ADMM Algorithm for Connected Net Zero-Energy Farms Integrated Microgrids"** *IEEE Transactions on Sustainable Computing*.
- **"Unified Model Predictive Control for Coordinated Microgrid Energy Management and Greenhouse Microclimate Control over Growth Cycles"** *EEE Transactions on Automation Science and Engineering*.

Conference Papers - Published

- **"Optimal Operation of a Smart Greenhouse-Integrated Microgrid for Strawberry Growth in Atlantic Climate"** *IEEE International Conference on System of Systems Engineering (SoSE)*[4].
- **"Integrating Digital Twin Technology for Sustainable Smart Greenhouse Management: A Case Study for Liguria Region in Italy"** presented at the *IEEE International Conference on System of Systems Engineering (SoSE)*[5].
- **"A Performance Comparison of Path Planning Strategies for Autonomous Drone Swarms in Greenhouses"** presented at the *IEEE International Congress on Smart Agriculture and Sustainable Systems(SoSE)*[6].
- **"Grid Integration of Renewable Energy Through Wind-Pumped Hydro Storage for Load Limiting"** presented at the *IEEE International Conference on System of Systems Engineering (SoSE)*[7].
- **"Design of an IoT-Driven Smart Irrigation and Energy Management System for Enhanced Energy Efficiency in Sustainable Autonomous Agriculture"** presented at the *IEEE International Conference on System of Systems Engineering (SoSE)*[8].

Open Invite Track Organization

- Co-organized the Open Invited Track "Optimal Control, Management, and Scheduling in Energy Hubs" at IEEE International Conference on System of Systems Engineering (SoSE), Tirana, Albania, Jun 08–12, 2025.

Special Session Organization

- Co-chaired the Special Session "IEEE International Congress on Smart Agriculture and Sustainable Systems Engineering" held in Marrakech, Morocco, December 5–9, 2025

[3] https://link.springer.com/article/10.1007/s44327-025-00096-w
[4] https://ieeexplore.ieee.org/document/11083815
[5] https://ieeexplore.ieee.org/document/11083791
[6] https://ieeexplore.ieee.org/document/11466709
[7] https://ieeexplore.ieee.org/document/11466716
[8] https://ieeexplore.ieee.org/document/11467101

1.3.3 Projects

- During the course of this PhD, I actively participated in a major research project, which focused on “bio-inspired micro aerial vehicles for sustainable pest control in horticulture Flappy." Collaboration between the University of Genoa, Inholland University of Applied Sciences, and TU Delft, Netherlands, on the project This project aims at developing monitoring systems based on the use of flapping-wing drones for pest and disease detection in greenhouse crops.

Chapter 2

Optimizing Greenhouse Energy and Microclimate Control Under Harsh Climates Using a Quantum PSO Algorithm

This chapter examines the challenges in greenhouse optimization, which include managing energy use, preserving ideal growing conditions, and incorporating renewable energy. Sections 2.1 and 2.2 describe the proposed system, featuring a comprehensive mathematical model of a grid-connected greenhouse. The section 2.3 is dedicated to explaining the methodology, which integrates a Nonlinear Classical Particle Swarm Optimization algorithm with a Nonlinear Quantum Particle Swarm Optimization (NQPSO) algorithm and a prediction module based on Random Forests to address these interconnected complexities. Section 2.4 details the experimental design and case study used to evaluate the framework over a complete crop cycle. The results show gains in energy and water efficiency relative to traditional optimization approaches, highlighting implications for sustainable greenhouse management and microgrid integration. The chapter concludes with a summary in Section 2.5.

2.1 Modeling Greenhouse System Components

A grid-connected greenhouse integrated into a microgrid system with renewable energy sources (solar panels and wind turbines), water storage, and climate control elements (HVAC, CO2 injection, fogger, dehumidifier, and artificial lighting) is shown in Figure 2.1. The 160–165 day life cycle is divided into five phases: early growth (E.G., 22 days), vegetative (V, 58 days), flowering (F, 20 days), fruit formation (F.F., 30 days), and mature fruiting (M.F., 32 days). Several sensors track environmental parameters to maintain ideal growing conditions.

The study simulates 24-hour periods for each growth phase, applying optimization and control strategies based on two data sources: (1) real-world measurements from Qatar's harsh climate (deterministic case) and (2) forecasted environmental parameters generated by a random forest (RF) model (probabilistic case). The RF algorithm, implemented in Python using scikit-learn, predicts external conditions at 15-minute intervals over 24-hour horizons. Time-series data is encoded via sine/cosine transformations to capture cyclical patterns. Hyperparameters such as tree depth and ensemble size are systematically tuned, yielding specialized models for each environmental factor. Performance is assessed using mean absolute error (MAE), root mean square error (RMSE), and the coefficient of determination (R^2), demonstrating robust predictive accuracy for operational use.

It is important to note that this study employs a discrete-time system model, using a 15-minute sampling period for simulation.

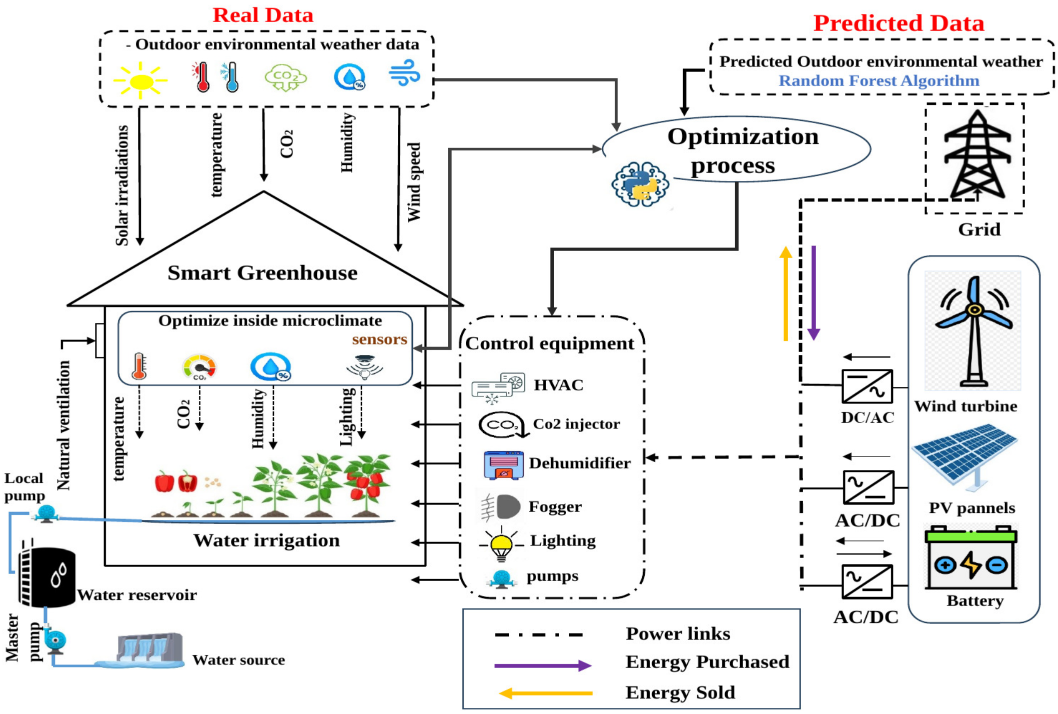

Figure 2.1: Greenhouse system components.

2.1.1 PV Panels Model

The expected power output of the JKM590N-72HL4 PV panels used in this study[52], assuming operation at maximum power point (MPP), can be described as follows[53]:

$$I_{\text{pv}} = I_{\text{sc}}^{\text{ref}} \left[1 - A \left(\exp\left(\frac{V_{\text{mp}}^{\text{ref}}}{B \cdot V_{\text{oc}}^{\text{ref}}} \right) - 1 \right) \right] + \Delta I^{l}, \tag{2.1}$$

$$V_{\text{pv}} = V_{\text{mp}} \left(1 + 0.0539 \cdot \log\left(\frac{I^{l}}{I_{\text{st}}} \right) \right) + u \cdot \Delta T, \tag{2.2}$$

$$\text{where} : A = \left(1 - \frac{I_{\text{mp}}^{\text{ref}}}{I_{\text{sc}}^{\text{ref}}} \right) \exp\left(- \frac{V_{\text{mp}}^{\text{ref}}}{B \cdot V_{\text{oc}}^{\text{ref}}} \right), \tag{2.3}$$

$$B = \frac{V_{\text{mp}}^{\text{ref}}}{V_{\text{oc}}^{\text{ref}} - 1} \cdot \frac{1}{\log\left(1 - \frac{I_{\text{mp}}^{\text{ref}}}{I_{\text{sc}}^{\text{ref}}} \right)}, \tag{2.4}$$

$$\Delta I^{l} = \eta \left(\frac{I^{l}}{G^{\text{st}}} \right) T + \left(\frac{I^{l}}{G^{\text{st}}} - 1 \right) I_{\text{sc}}^{\text{ref}}, \tag{2.5}$$

$$\Delta T = T^{\text{amb}} + 0.02 \cdot I^{l}. \tag{2.6}$$

The PV array's output voltage and power are as follows:

$$V^{\text{pv,out}} = \epsilon^{\text{pv,s}} V_{\text{pv}} \tag{2.7}$$

$$P^{\text{pv}} = \epsilon^{\text{pv,s}} \epsilon^{\text{pv,p}} V_{\text{pv}} I_{\text{pv}} \eta_{\text{pv}} \xi^{\text{loss}}. \tag{2.8}$$

where V_{mp}^{ref} is the module's maximum power voltage (V), I_{sc}^{ref} is the module's short-circuit current (A), and I_{mp}^{ref} is the module's maximum power current (A). I^{l} is solar irradiance (W/m^2), and V_{oc}^{ref} is the module open-circuit voltage (V), G^{st} represents standard light intensity (W/m^2), μ is module voltage temperature coefficient (V/°C), and η is module current temperature coefficient (A/°C) and T^{amb} is the ambient temperature (°C), η_{pv} is the efficiency of the solar panel , ξ^{loss} stands for both connection loss and additional loss brought on by other variables. $\epsilon^{\mathrm{pv,s}}$ is the serial connection number of PV modules, $\epsilon^{\mathrm{pv,p}}$ is the parallel connection number of PV module strings, and P^{pv} is the PV output power (kW).

2.1.2 Wind Turbine Generator Model

the power generated by a wind turbine that considers the three main parts: the generator, gearbox, and rotor. possibly calculated in this way:

$$P^{wind} = 0.5 \cdot \rho_a \cdot A_r \cdot \sum_{w_c}^{w_f} Cp_{tot} \cdot (w_s^{hub})^3 \tag{2.9}$$

where P^{wind} is power generated by the wind turbine (kW), ρ_a is the air density (kg/m^3), A_r is the rotor swept surface (m^2), w^s_{hub} is wind speed extrapolated at hub height (m/s), w_c, w_f are cut-in and cut-out wind speeds (m/s), and C_p^{tot} represents total efficiency of a wind turbine as a function of the power coefficient of the rotor and gearbox and generator efficiencies. The full model description is not provided here due to space constraints. It should be mentioned that the Aeolos-H-30kW wind turbine was employed in this investigation[54]. It's also crucial to note that the model has been thoroughly detailed and validated in this earlier study [55].

2.1.3 Battery Storage Model

The battery storage system allows the greenhouse to either use stored energy or sell it to the grid. By storing excess power when generation exceeds demand, the battery supports demand response and ensures reliable operation during low wind or solar output. The dynamic of a battery's energy can be expressed as follows:

$$\frac{dSoc}{dt} = \frac{\alpha_{ch}}{E_{\mathrm{n}}} P^{ch} - \frac{1}{\alpha_{dch} E_{\mathrm{n}}} P^{dch} \tag{2.10}$$

$$\begin{cases} 0 \le P_{\mathrm{ch}} \le P_{\mathrm{max}}^{\mathrm{ch}} \\ 0 \le P_{\mathrm{dch}} \le P_{\mathrm{max}}^{\mathrm{dch}} \\ \mathrm{Soc}_{\mathrm{min}} \le \mathrm{Soc} \le \mathrm{Soc}_{\mathrm{max}} \end{cases} \tag{2.11}$$

Where P^{ch} and P^{dch} are charging and discharging powers, respectively (kW); α^{ch} and α^{dch} are the charging and discharging efficiencies, respectively; and E_n is the nominal battery capacity (kWh). Charge and discharge are not assumed to occur simultaneously according to the equation.

$$P^{ch}.\ P^{dch} = 0 \tag{2.12}$$

2.1.4 Water Reservoir and Pumps Model

Climate change makes water management essential; thus, water-efficient greenhouse farming is crucial. Because it delivers water directly to roots, minimizes waste, and maintains optimal soil moisture, drip irrigation performs better than conventional techniques like flood irrigation or border furrow irrigation [56]. It is essential for greenhouse sustainable agriculture since it reduces water usage by 30–50% and stops erosion and nutrient loss. To support drip irrigation, an underground water reservoir is installed near the greenhouse, with its dynamics modeled as follows:

$$\frac{dM^{res}}{dt} = w^m - w^{gh} \tag{2.13}$$

where the reservoir water volume is $M^{res}(m^3)$. The water flows entering the reservoir are defined by w^m (m^3/s), while the water flows entering the greenhouse are defined by w^{gh}

(m^3/s). The powers used for pumping are correlated with the water flows in the following way:

$$w^{gh} = \frac{P^{lp}.\beta_{lp}}{1000.\rho.g.h^{gh}}.\eta_{gh} \tag{2.14}$$

$$w^{m} = \frac{P^{m}.\beta_{m}}{1000.\rho.g.h^{m}}.\eta^{m} \tag{2.15}$$

where ρ is the water density (kg/m^3) and g is the gravity acceleration constant (m/s^2), η^{mp}, η^{gh}, are the pump efficiencies, β_{lp}, β_m are control variables of pumps; h^{mp} is the difference in level height between the reservoir and source of water (m). h^{gh} is the difference in height between the reservoir and plants of the greenhouse (m), and P^{mp} and P^{lp} are the powers consumed by the master pump and locale pump (kW).

2.2 Comprehensive Mathematical Model for Greenhouse Microclimate Dynamics

A complete physical system-level formulation model has been employed to depict the greenhouse's interior microclimate for different phases of growth.

2.2.1 Temperature Model

Temperature plays a crucial role in photosynthesis, increasing activity at low to moderate levels as per the Arrhenius equation. To ensure optimal conditions and prevent reduced growth, the greenhouse regulates interior temperature using HVAC. The dynamic temperature model is as follows:

$$x\frac{dT^{in}}{dt} = \overbrace{Q^{\text{sol}} + Q^{\text{hvac}} + Q^{\text{art}}}^{\text{gain}} - \overbrace{Q^{\text{cond}} - Q^{\text{conv}} - Q^{\text{trs}} - Q^{\text{vent}} - Q^{\text{inf}}}^{\text{loss}} \tag{2.16}$$

$$x = C_a \rho_a V_g \tag{2.17}$$

Where C_a is the air specific heat capacity (J/kgK), ρ_a is air density (kg/m^3), and V_g is the volume of the greenhouse (m^3), T^{in} represents desired indoor air temperature (°C). The total thermal flux gain in the greenhouse consists of the sum of heat gain by solar radiation (Q^{sol}) (W), HVAC system (Q^{hvac}) (W) and artificial lighting (Q^{art}) (W). The total thermal flux loss in the greenhouse consists of heat loss by conduction (Q^{cond}) (W), convection through the cover (Q^{conv}) (W), latent heat effect due to crop transpiration (Q^{trs}) (W), natural ventilation (Q^{vent}) (W), and infiltration (Q^{inf}) (W). In this model, the latent heat effect due to crop transpiration (Q^{trs}) is assumed to be neglected. By substituting each heat flux with its respective definition, the differential equation governing the greenhouse temperature dynamic expression becomes:

$$\begin{aligned}\frac{dT^{\text{in}}}{dt} = \frac{1}{C_a \rho_a V_g}\Bigg[& \overbrace{S_g \tau I^l}^{Q^{\text{sol}}} + \overbrace{Q^{\text{hvac}}}^{Q^{\text{hvac}}} + \overbrace{(1-\eta_l) P_r^{art} \beta_l}^{Q^{\text{art}}} \\ & - \overbrace{\frac{S_g \cdot e}{k_c}(T^{\text{out}} - T^{\text{in}})}^{Q^{\text{cond}}} - \overbrace{J^{\text{inf}} \rho_a V_g c_a \left[(T^{\text{out}} - T^{\text{in}}) + J^{lh}(H^{\text{in}} - H^{\text{out}})\right]}^{Q^{\text{inf}}} \\ & - \overbrace{h^{\text{conv}} S_g (T^{\text{out}} - T^{\text{in}})}^{Q^{\text{conv}}} - \overbrace{Q^{\text{vent}}}^{Q^{\text{vent}}} \Bigg]\end{aligned} \tag{2.18}$$

The heat and cooling air fluxes Q^{hvac} supplied from the HVAC system can be expressed by the following equation, while heat loss through natural ventilation Q^{vent} will be detailed in the next subsection.

$$Q^{hvac} = C_{op} \beta_{\text{hvac}} P^{\text{hvac}} \tag{2.19}$$

where S_g is the total external surface area (cover) of the greenhouse (m^2), τ is the material transmissivity of polycarbonate used for the greenhouse cover, I^l is solar radiation intensity (W/m^2), and η_l and P_r^{art} are the efficiency of artificial lighting ($\mu mol/J$) and their rated power (W), respectively. e and k_c are the glazing material thickness (m) and material thermal conductivity (W/mK), and T^{in} and T^{out} are the indoor and outdoor greenhouse temperatures (°C). η_h represents the performance coefficient of the HVAC unit, and P^{hvac} is HVAC power consumption (kW). e and k_c are the glazing material thickness (m) and material thermal conductivity (W/mK), J^{inf} and J^{lh} are the infiltration rate ($1/s$) and latent heat of vaporization of water at T^{in}, H^{in} and H^{out} are the indoor and outdoor greenhouse humanities. h^{conv} is the convective heat transfer coefficient (W/m^2K), while C_{op} and P^{hvac} are the coefficient of performance (positive for cooling and negative for heating) and power consumed by the HVAC (kW), and β_{hvac} represents the control variable.

and J^{ven} is the air exchange rate depending on external wind speed and the type of ventilator window. It can be determined using air circulation model.

2.2.2 Air circulation model

In this model, when the greenhouse gets too hot, a window for natural ventilation is used. It is possible to determine the overall heat loss brought on by the ventilation window's operation as follows[57]:

$$Q^{\text{vent}} = J^{\text{ven}} \rho_a V_g c_a (T^{\text{out}} - T^{\text{in}}) + J^{lh} (H^{\text{in}} - H^{\text{out}}) \tag{2.20}$$

J^{vent} which stands for air exchange rate, may be computed based on ventilator window type and outdoor wind speed as described below:

$$J^{\text{vent}} = \frac{A^v}{S_g} w_s \left(1 - e^{\left(\frac{-\alpha}{21.1}\right)}\right) \cdot 82,44 \tag{2.21}$$

$$\alpha = \begin{cases} \alpha_{\min} \leq \alpha \leq \alpha_{\max} \;\; ; & if \;\; T^{in} - T^{in}_{ref} \geq 1 \\ 0 \;\; otherwise & \end{cases} \tag{2.22}$$

where α denotes the window's angle opening (deg), A^v denotes the window area of natural ventilation (m^2) and w_s denotes the wind speed (m/s).

2.2.3 Light Intensity Model

LED lighting serves as an energy-efficient supplemental lighting solution in greenhouses, with studies showing they convert up to 49% of electrical energy into plant-usable light [58]. A major advantage is their compatibility with pulse-width modulation (PWM), which precisely adjusts light intensity to optimize energy use without compromising plant health [59]. Dynamic Lighting Control (DLC) enhances this efficiency further. Systems like Fluence's SPYDR 2p47 [60] integrate photosynthetically active radiation (PAR) sensors and microcontrollers to dynamically shift spectra such as red (660 nm) for flowering and blue (450 nm) for vegetative growth based on real-time canopy conditions [61]. Compared to fixed-spectrum lighting, this approach reduces energy consumption by 20% while improving crop yields. The dynamic light intensity in the greenhouse is a combination of artificial lighting and natural sunlight and can be described as follows:

$$\frac{dI^{light}}{dt} = I^{nat} + I^{art} \tag{2.23}$$

$$I^{nat} = \tau \cdot k_{sol} \cdot I^l \tag{2.24}$$

where I^{nat} represents the natural light intensity that comes from solar radiation ($\mu mol/m^2/s$), τ is the material transmissivity, I^l solar radiation (W/m^2) and k_{sol} is factor of solar radiation contributing to PAR. The power consumed by artificial lighting P^{art} as a function of I^{art} artificial light intensity can be expressed as follows:

$$P^{art} = \beta_l . \frac{I^{art} \cdot S_c}{\eta_l} N_x \tag{2.25}$$

$$\beta_l = \begin{Bmatrix} 1 & if \quad I^{nat} \leq I^l_{\min} \\ 0 & otherwise \end{Bmatrix} \tag{2.26}$$

where S_c denotes cultivated area (m^2), ηl is the LED efficiency ($\mu mol/J$), $I^l min$ represents the minimal light intensity ($\mu mol/m^2/s$) and N_x number of fixtures of artificial lighting products used for covering the cultivated area.

2.2.4 Relative Humidity Model

To offer a favorable climate for plant growth and to avoid fungal diseases, the humidity within a greenhouse must be managed and controlled. High humidity, which typically occurs at night, causes plants to stop transpiring, and condensation from the roof and plant leaves can lead to fungal illnesses. Low-flow humidity causes plants to stop absorbing CO_2 and the process of photosynthesis, which slows plant growth. Consequently, the mathematical model should accurately represent adjusting the relative humidity in greenhouses[62]. Inside relative humidity of a greenhouse is defined as follows:

$$H^{in} = \frac{P^{pvp}}{P^{sat}} \times 100\% \tag{2.27}$$

Where P^{pvp} the partial vapor pressure and P^{sat} saturated water vapor pressure can be calculated using:

$$P^{\text{sat}} = a_1 \left(-a_2 + a_3 e^{a_4 T^{in}} \right) \; ; \; P^{\text{pvp}} = \frac{W^{\text{in}} P_{atm}}{a_5} \tag{2.28}$$

Where P_{atm} is the atmospheric air pressure and $a_1 ... a_5$ are constants and W^{in} represent water content of the indoor air is calculated using the mass balance theory, taking into account the moisture expelled by natural ventilation and the amount of water added or removed by the dehumidifier or fogging system, as follows:

$$\begin{aligned} \frac{dW^{in}}{dt} = \frac{1}{\rho_a V_g} \big[& W^{\text{evp}} S_g + \rho_a \lambda_s J^{ven} (W^{out} - W^{in}) \\ & + \beta_{\text{fog}} W^{fog}_{max} S_g - \beta_{\text{deh}} W^{deh}_{max} S_g \big] \end{aligned} \tag{2.29}$$

W^{evp} denotes the crop's rate of evaporation ($kg/m^2 h$), while λ_s is the wind ratio entering the greenhouse. The power consumed by the fogging equipment P^{fog} (kW) and its operational status β_{fog}= ($Pfog/P^{fog}_{\max}$). Similarly, the amount of water content absorbed by the dehumidifier is a function of the power consumed by the dehumidifier equipment P^{deh} and its operational status. $\beta_{deh} = (P^{deh}/P^{deh}_{\max})$ The outdoor water content of air can be calculated as a function of outdoor humidity and outdoor temperature as follows:

$$W^{out} = \frac{a_5 H^{out}}{P_{atm}} a_1 \cdot (a_3 e^{a_4 T^{out}} - a_2) \tag{2.30}$$

The Relative humidity dynamics can be derived as the below equation.

$$\frac{dH_{in}}{dt} = \frac{P_{atm}}{a_5 P^{\text{sat}}} \frac{dW^{in}}{dt} - \frac{\text{H}_{in}}{P^{\text{sat}}} \frac{dP^{\text{sat}}}{dt} \tag{2.31}$$

Where :

$$\frac{dP_{\text{sat}}}{dt} = a_1 a_3 a_4 e^{a_4 T^{in}} \frac{dT^{in}}{dt} \tag{2.32}$$

The relative humidity can be limited between the following minimum and maximum values:

$$H^{in}_{min} \left(\frac{P^{\text{sat}} a_5}{P_{\text{atm}}} \right) \leq W^{in} \leq H^{in}_{max} \left(\frac{P^{\text{sat}} a_5}{P_{\text{atm}}} \right) \tag{42}$$

2.2.5 CO_2 Concentration Model

CO_2 concentration and lighting are necessary for photosynthesis in plants. Supplying CO_2 into the greenhouse and maintaining CO_2 concentration within a specific range is crucial to maintaining a high degree of photosynthesis and plant growth because plants in the greenhouse use CO_2 when there is sunlight, which lowers CO_2 concentration[62]. The dynamic model of the greenhouse's CO_2 concentration is based on the mass balance concept:

$$\begin{aligned}\frac{dCO_2^{in}}{dt} =& \frac{1}{V_g \rho_a} \Bigg[\frac{\beta_{CO_2} P^{CO_2}}{P_r^{CO_2}} C_{\max}^{inj} S_g + a_6 w_s A^v \lambda_s J^{ven} \left(CO_2^{out} - \right. \\ & \left. CO_2^{in} \right) + C^{res} \left(a_7 + a_8 T^{in} \right) S_g - a_6 C^{phot} I^{light} S_g \Bigg]\end{aligned} \tag{2.33}$$

Where ρ_a (kg/m^3) and V_g (m^3) are air density and volume of greenhouse, CO_2^{in}, CO_2^{out} (kg/m^2) are the greenhouse internal and external $CO2$ concentrations, $C\max^{inj}$ (kg/m^2) is the maximum carbon that a CO2 generator may introduce. w_s (m/s), A^v (m^2), λ_s $(1/s)$, J^{ven} are wind speed, ventilation window area, percentage of wind speed that enters into the greenhouse, and air exchange rate through natural ventilation respectively. $a6...a8$ are coefficients associated with the respiration rate of the crop, C^{res} $(kg/(m^2hK))$ is the respiration coefficient of crops, C^{phot} (kg/Wh) is the photosynthesis coefficient of crops, I^{light} $(\mu mol/m^2/s)$ is the indoor light intensity, S_g (m^2) is the area of the greenhouse, βCO_2 represent the operational status of the CO_2 injector and P^{CO2} and Pr^{CO_2} (kW) are consumed and rated powers of the CO_2 injector.

2.2.6 Power balance

The proposed greenhouse system includes renewable generators and battery storage, and it is connected to the main electric grid, allowing power exchanges in both cases of excess or shortage in local energy production. By defining P_{grid}^{buy} and P_{grid}^{sold} as purchased and sold power from/to the grid (kW), the power balance of the system can be written as follows:

$$\begin{aligned}& P^{pv} + P^{wind} + P_{grid}^{buy} = P_{grid}^{sold} + P^{mp} + P^{lp} + P^{hvac} + P^{CO2} + \\ & P^{light} + P^{fog} + P^{deh} + (P^{ch} - P^{dch})\end{aligned} \tag{2.34}$$

$$P_{\text{grid}}^{\text{buy}} \cdot P_{\text{grid}}^{\text{sell}} = 0 \tag{2.35}$$

The parameters of the system modeling components used in the simulation case study are outlined in Table (2.1), detailing their respective roles. Additionally, the optimization variables, along with their corresponding bounds, are comprehensively described in Table (2.2) , providing a clear framework for the simulation process.

2.2.7 Optimization Problem

Objective Function

The primary objective is to establish an optimal microclimate within the greenhouse to support sustainable crop growth. This involves minimizing deviations between key indoor microclimate variables such as water irrigation, temperature, lighting, humidity, and CO_2 concentration and usage and their respective reference values. Additionally, the strategy aims to reduce the reliance on power exchanged with the main grid, promoting energy efficiency and sustainability. This is achieved by minimizing the following objective function:

$$\begin{aligned}J =& \alpha_1 \sum_{d \in D} \lambda_{w,d}^{gh} + \alpha_2 \sum_{d \in D} \lambda_{T,d}^{Tin} + \alpha_3 \sum_{d \in D} \lambda_{L,d}^{L} + \alpha_4 \sum_{d \in D} \lambda_{H,d}^{Hin} + \ldots \\ & \alpha_5 \sum_{d \in D} \lambda_{C,d}^{CO_2} + \alpha_6 \sum_{d \in D} (P_{grid,d}^{buy} - P_{grid,d}^{sold})\end{aligned} \tag{2.36}$$

Where:
$\lambda^{gh}_{w,d} = (w^{gh}_{d} - w^{gh}_{ref,d})^2$, $\lambda^{Tin}_{T,d} = (T^{in}_{d} - T^{in}_{ref,d})^2$, $\lambda^{L}_{L,d} = (I^{art}_{d} - I^{art}_{ref,d})^2$, $\lambda^{Hin}_{H,d} = (H^{in}_{d} - H^{in}_{ref,d})^2$, $\lambda^{CO_2}_{C,d} = (CO_2{}^{in}_{,d} - CO_{2ref,d})^2$, D represent data length and α_1,..., α_6 are weighting parameters that are used to trade off the objective function's different components.

System benefits

In this study, we assume an interaction with the energy grid, representing the external electricity supplier. The energy purchase price from the grid is set at $C_{buy} = 0.33$ (€/kWh), while surplus energy is sold back at $C_{sold} = 0.25$ (€/kWh). This pricing model emphasizes the need for effective energy management to minimize costs and maximize profits from excess energy sales. The benefits of the system $S_{benefit}$ (€/kW) are calculated using the following equation:

$$S_{benefit} = \left[C_{sold} \cdot P^{sold}_{grid} \; - \; C_{buy} \cdot P^{buy}_{grid}\right] \tag{2.37}$$

Constraints governing the problem

- Water flows and reservoir

$$M^{res}_{\min} \leq M^{res} \leq M^{res}_{\max} \tag{2.38}$$

$$w^{gh}_{\min} \leq w^{gh} \leq w^{gh}_{\max} \tag{2.39}$$

$$w^{m}_{\min} \leq w^{m} \leq w^{m}_{\max} \tag{2.40}$$

$$P^{m}_{\min} \leq P^{m} \leq P^{m}_{\max} \tag{2.41}$$

$$P^{lp}_{\min} \leq P^{lp} \leq P^{lp}_{\max} \tag{2.42}$$

- Temperature

$$T^{in}_{\min} \leq T^{in} \leq T^{in}_{\max} \tag{2.43}$$

$$P^{hvac}_{\min} \leq P^{hvac} \leq P^{hvac}_{\max} \tag{2.44}$$

$$C_{op,\min} \leq C_{op} \leq C_{op,\max} \tag{2.45}$$

- Air circulation

$$\alpha_{\min} \leq \alpha \leq \alpha_{\max} \tag{2.46}$$

$$J^{vent}_{\min} \leq J^{vent} \leq J^{vent}_{\max} \tag{2.47}$$

- Artificial lighting

$$I^{art}_{\min} \leq I^{art} \leq I^{art}_{\max} \tag{2.48}$$

$$P^{art}_{\min} \leq P^{art} \leq P^{art}_{\max} \tag{2.49}$$

- Humidity, fogger and dehumidifier

$$H^{in}_{\min} \leq H^{in} \leq H^{in}_{\max} \tag{2.50}$$

$$P^{deh}_{\min} \leq P^{deh} \leq P^{deh}_{\max} \tag{2.51}$$

$$P^{fog}_{\min} \leq P^{fog} \leq P^{fog}_{\max} \tag{2.52}$$

- CO_2 concentration

$$CO_{2min}^{in} \leq {CO_2}^{in} \leq CO_{2max}^{in} \tag{2.53}$$

$$P_{min}^{CO_2} \leq P^{CO_2} \leq P_{max}^{CO_2} \tag{2.54}$$

- Grid power exchanged

$$P_{grid,min}^{sold} \leq P_{grid}^{sold} \leq P_{grid,max}^{sold} \tag{2.55}$$

$$P_{grid,min}^{buy} \leq P_{grid}^{buy} \leq P_{grid,max}^{buy} \tag{2.56}$$

Table 2.1: System Components Parameters

$Parameters$	$Value$	$Unit$
V_{mp}^{ref} , V_{oc}^{ref}	47.71 , 52.63	$[V]$
I_{mp}^{ref} , I_{sc}^{ref}	13.50 , 14.13	$[A]$
G_{st} , T^{amb}	1000 , 25	$[W/m^2]$, [°C]
μ, η, ξ^{loss}	-0.13, 0.0063 , 0.9	[V/°C], [A/°C], [—]
$\epsilon^{pv,s}$, $\epsilon^{pv,p}$	4 , 2	[—] , [—]
ρ_a, A_r	1.225 , 191	$[kg/m^3]$, $[m^2]$
w_c , w_f	3 , 52	$[m/s]$
ρ , g	999.93 , 9.81	$[kg.m^{-3}]$, $[m.s^{-2}]$
h^{gh}, h^m	5 , 21	[m]
η^{mp}, η^{gh}	0.8 , 0.75	[—] , [—]
α_{ch} , α^{dch} , E_n	0.95 , 0.9 ,50	[—-]
C_a, V_g, S_g	1005, 192.5 , 182.7	[W/kg·K], $[m^3]$, $[m^2]$
τ , η_l , P_r^{art}	0.65 , 2.46 , 650	[—] , $[\mu mol/J]$, $[W]$
e , k_c , J^{inf}	0.025, 0.04, 0.75	$[m]$, [W/m·K] $[1/s]$
h^{conv}	2.27	$[W/m^2K]$
R_{hvac} , C_{hvac}	1.3 , 3.2	[J/K] , $[K/W]$
A^v , α	1 , (0 - 90)	$[m^2]$, [deg]
k_{sol} , S_c , N_x	0.5 , 70 , 35	$[--]$, $[m^2]$,$[--]$
I_{min}^l , η_l	36 , 2.46	$[\mu mol/m^2/s]$,$[\mu mol/J]$
P_{atm}, W^{ev}, λ_s	101325, 0.12,0.075	$[Pa]$, $[kg/m^2h]$,$[1/s]$
W_{max}^{fog}, W_{max}^{deh}, a_1	0.0096, 1.4, 100	$[kgw/m^2h]$,$[kg/(m^2h)]$,–
a_2, a_3, a_4	1.7, 7.78,0.058	[Pa] , [Pa],$[K^{-1}]$
a_5,P_{max}^{fog}, P_{max}^{deh}	0.622, 2, 5	(kgw/kga),$[kW]$,$[kW]$
a_6, a_7, a_8	-0.15 , 0.03, 0.05	$[C]$,$[--]$, $[W/mK]$
C_{max}^{inj}, C^{res}	$0.2.e^{-3}$, $0.3e^{-6}$	$[kg/m^2]$, $[kg/(m^2hK)]$
C^{phot}, $P_r^{CO_2}$	$2.e^{-5}$, 2	$[kg/Wh]$, $[kW]$
D	480	[—]
C_{buy}, C_{sold}	0.33 , 0.25	[€/kWh]

Table 2.2: Optimization Variables

$Variable$	$Definition$	$Bounds\ [lb - ub]$	$Unit$
P^{ch}	battery charging power	[0 - 50]	[kW]
P^{dch}	battery discharging power	[0 - 50]	[kW]
S_{oc}	battery energy stored	[2 - 50]	[kWh]
w^{gh}	water flows entering the GH.	[0 - 0.9]	$[m^3/s]$
w^{m}	reservoir inflow.	[0 - 2]	$[m^3/s]$
P^{lp}	local pump power consumed.	[0 - 2]	[kW]
P^{m}	master pump power consumed.	[0 - 2]	[kW]
M^{res}	water reservoir level.	[0 - 10]	$[m^3]$
T^{in}	GH indoor temperature.	[20 - 32]	[°C]
P^{hvac}	HVAC power consumed.	[0 - 15]	[kW]
C_{op}	HVAC performance coefficient	[-4 - 4]	[—]
α	window opening angle	[0 - 3]	[deg]
J^{ven}	air exchange rate	[0 - 2.25]	[1/s]
I^{art}	artificial light intensity	[0 - 1500]	$[\mu mol/s]$
P^{art}	lighting power consumed.	[0 - 2]	[kW]
H^{in}	Indoor relative humidity	[55 - 80]	[%]
P^{fog}	fogger power consumed	[0 - 2]	[kW]
P^{deh}	dehumidifier power consumed	[0 - 1]	[kW]
${CO_2}^{in}$	indoor GH CO_2 concentration.	[550 - 880]	[ppm]
P^{CO_2}	CO_2 injector power consumed.	[0 - 2]	[kW]
P^{sold}_{grid}	power sold to the grid.	[0 - 15]	[kW]
P^{buy}_{grid}	power purchased.	[0 - 15]	[kW]
β_{lp}	operation status of local pump	[0 - 1]	[—]
β_{hvac}	operation status of HVAC	[0 - 1]	[—]
β_{l}	operation status of lighting	[0 - 1]	[—]
β^{fog}	operation status of fogger	[0 - 1]	[—]
β^{deh}	operation status of dehumidifier	[0 - 1]	[—]
β^{CO2}	operation status of CO_2 injector	[0 - 1]	[—]

2.3 Computational Energy Management Strategy for a Greenhouse Connected to the Power Grid Using an Enhanced PSO Algorithm

To solve the optimization problem formulated above, which is dedicated to greenhouse energy management, we employ NPSO- and NQPSO-based approaches following the flowchart depicted in Fig. 2.2. Additionally, we include Pyomo as a Python-based open-source software package to provide a basis for comparison and to validate the effectiveness of the results obtained from PSO and QPSO. The following sections present the methods in detail.

2.3.1 Classical PSO Approach

The Particle Swarm Optimization (PSO) algorithm emulates the collective behavior observed in bird flocks and fish schools. In this algorithm, potential solutions are represented as particles that move within the search space. Each particle updates its position based on its own best-known position and the best-known position of the group, effectively balancing exploration and exploitation. PSO is widely used for solving both constrained and unconstrained optimization problems.

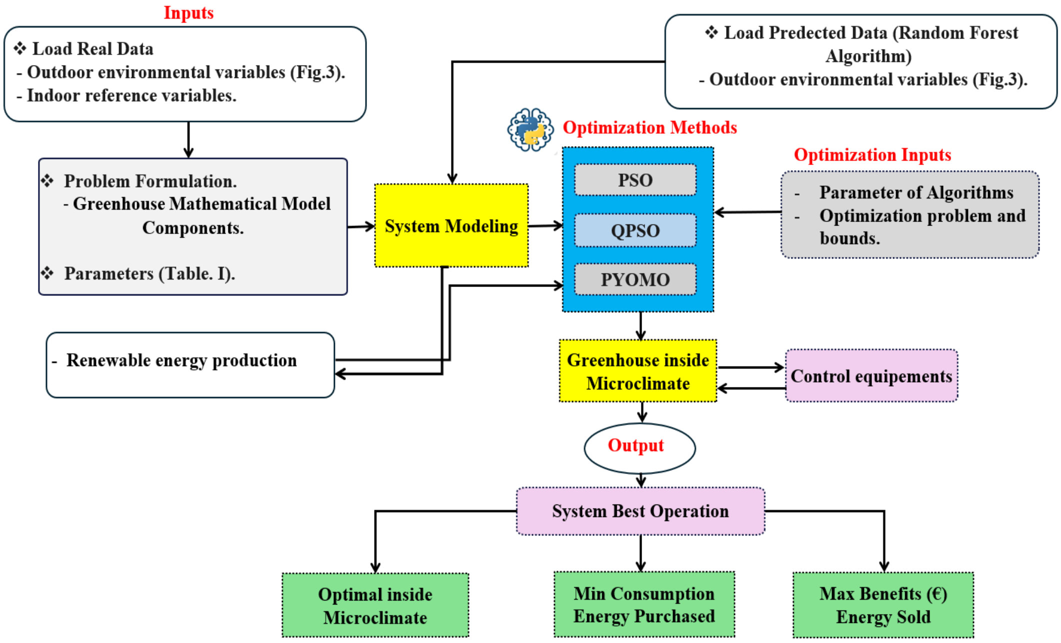

Figure 2.2: Flowchart of System Using different optimization methods.

Consider a K-dimensional optimization problem, swarm of particles N can be represented as $x_j = \{x_j^1, x_j^2, \ldots, x_j^K\}$. At the j-th iteration, the position of the i-th particle is $x_{i,j} = [x_{i,j}^1, x_{i,j}^2, \ldots, x_{i,j}^K], \quad i = 1, 2, \ldots, N$.

The best position achieved by each particle, known as the personal best, is

$$P_{i,j}^{\text{best}} = \begin{cases} x_{i,j}, & \text{if } f[x_{i,j}] < f[P_{i,j-1}^{\text{best}}], \\ P_{i,j-1}^{\text{best}}, & \text{if } f[x_{i,j}] \geq f[P_{i,j-1}^{\text{best}}]. \end{cases} \tag{2.57}$$

Where, $f[x_{i,j}]$ represents the fitness value of the particle i at j iteration, while $f[P_{i,j}^{best}]$ denotes the fitness value of the best position achieved by the i-th particle at the previous j-iteration. The global best position is determined by :

$$g = \arg\min(f[P_{i,j}^{\text{best}}]), \quad i = 1, 2, \ldots, N. \tag{2.58}$$

$$G_j^{\text{best}} = P_{g,j}^{\text{best}} \tag{2.59}$$

After identifying the personal best and global best positions, the particles adjust their movement toward these best positions. This adjustment is achieved by updating their velocity and position in the k-dimensional search space as follows:

$$v_{i,j+1}^k = \omega \cdot v_{i,j}^k + c_1 r_{1}{}_{i,j}^k \left(P_{i,j}^{best,k} - x_{i,j}^k\right) + c_2 r_{2}{}_{i,j}^k \left(G_j^{best,k} - x_{i,j}^k\right) \tag{2.60}$$

$$x_{i,j+1}^k = x_{i,j}^k + v_{i,j}^k \quad i = 1, \ldots, N, \quad k = 1, \ldots, K \tag{2.61}$$

where $v_{i,j}^k$ and $x_{i,j}^k$ are the velocity and position of particle i in the kth dimensional space at the jth iteration, respectively. The algorithm includes an inertia weight, ω, which balances the global and local search capabilities of PSO. Additionally, $r_{1}{}_{i,j}^k$ and $r_{2}{}_{i,j}^k$ are random values uniformly distributed in the range $[0, 1]$, while c_1 and c_2 are the personal and global learning parameters, respectively, which influence the particle's cognitive and social behavior.

2.3.2 PSO-Based Computational System Energy Management Strategy

The NPSO algorithm is applied to optimize and control the indoor greenhouse microclimate in addition to ensuring energy management by minimizing power exchanged with the grid while meeting the greenhouse's equipment load requirements. This ensures efficient energy use and cost-effective operation, maintaining optimal growing conditions. The procedure for implementing the global version of PSO for greenhouse energy management is given by the following algorithm (1).

Algorithm 1: (NPSO)-based Optimization Energy Management System

Input: Outdoor environmental variables
Indoor reference variables needed
System Parameters
Renewable energy production
Problem Formulation (decisional variables, objective function, constraints)
$N \rightarrow$ population size
$(\mathrm{lb}, \mathrm{ub}) \rightarrow$ (lower bound, upper bound)
$K \rightarrow$ dimension
$c_1, c_2 \rightarrow$ QPSO parameters
$J_{tr}^{\max} \rightarrow$ max iterations
$C_c \rightarrow$ Convergence condition

Initialize each particle's random position x_i and velocity v_i;
Determine personal best p_i^{best} and global best g^{best};
Set $j = 0$;
while $j \leq J_{tr}^{max}$ **do**
    for $i = 1$ *to* N **do**
        Set $r_1, r_2 \in [0, 1]$;
        for $k = 1$ *to* K **do**
            $v_{i,j+1}^k = \omega \cdot v_{i,j}^k + c_1 r_1 (p_i^{\text{best},k} - x_{i,j}^k) + c_2 r_2 (g^{\text{best},k} - x_{i,j}^k)$;
            $x_{i,j+1}^k = x_{i,j}^k + v_{i,j+1}^k$;
            if $x_{i,j+1}^k > ub^k$ **then**
                $x_{i,j+1}^k = \mathrm{ub}^k$;
            if $x_{i,j+1}^k < lb^k$ **then**
                $x_{i,j+1}^k = \mathrm{lb}^k$;
        if $f(x_i) < f(p_i^{best})$ **then**
            Update personal best: $p_i^{\text{best}} = x_i$;
    Update global best: $\arg\min(p^{\text{best}}) \rightarrow g^{\text{best}}$;
    Set $j = j + 1$;

Output: Minimal fitness value with solutions:
- Optimal inside microclimate variables
- Optimal operation of equipment
- Optimal power purchased from grid
- Optimal power sold to grid

2.3.3 Quantum PSO Approach

The speed limitations of the standard PSO method during convergence limit the search space and frequently make it difficult to find the global optimal solution. In contrast, QPSO leverages quantum mechanics to improve search capabilities while utilizing fewer control parameters [63]. Through their collective activity, particles in a quantum bound state explore the possible solution space. The probability density function $|\psi(x_j)|^2$ indicates the probability that a particle will emerge at a specific point, whereas the wave function $\psi(x_j)$ describes the state of each particle. The Schrödinger equation for particles in a δ potential well is followed here.

$$i\hbar\frac{\partial}{\partial j}\psi(x_j) = -\frac{\hbar^2}{2m}\frac{\partial^2}{\partial x_j^2}\psi(x_j) + V(x_j)\psi(x_j) \tag{2.62}$$

Where $V(x_j)$ is the potential energy function, m is mass of the particle, j is the number of iterations, and $\hbar$ is Planck's constant. The center of particle motion, p_j, is where the one-dimensional δ potential well is established, and the potential energy function is able to be written as:

$$V(x_{j+1}) = -\gamma\delta(x_{j+1} - p_j) \tag{2.63}$$

There is a bound state in the δ potential well where γ is a number in [0,1]. When y_{j+1} is added, the potential energy function can be transformed into the following form since y_{j+1} is the coordinate transform of x, or $y_{j+1} = x_{j+1}$ - p_j.

$$V(y_{j+1}) = -\gamma\delta(y_{j+1}) \tag{2.64}$$

It is possible to express the normalized wave function and the associated probability density function as [63]:

$$\psi(y_{j+1}) = \sqrt{\frac{1}{L_j}}e^{(-\frac{|y_{j+1}|}{L_j})} \tag{2.65}$$

which satisfies the bound requirement that $\psi(y_j) \to 0$ as $y_j \to \infty$. L_j is the wave function's characteristic length of a one-dimensional δ potential well. The probability density function is provided by the wave function definition, which is:

$$P_r(y_j) = |\psi(y_j)|^2 = \frac{1}{L_j}e^{(-\frac{2|y_j|}{L_j})} \tag{2.66}$$

Consequently, the function of the probability distribution is

$$F(y_{j+1}) = 1 - \exp\left(-\frac{2(y_{j+1})}{L_j}\right) \tag{2.67}$$

The exact location of the particle can be determined using Monte Carlo simulation if a quantum state collapses into a classical state. The particle traveling around point p has a position update at j-iteration according to the following equation:

$$x_{j+1} = p_j \pm \frac{L_j}{2}\ln(\frac{1}{u_{j+1}}) \tag{2.68}$$

where p_j is the local attractor of the particle motion, u_{j+1} is a uniformly distributed series of random numbers on [0,1], and L_j is the typical length of a one-dimensional δ potential well. The motion of N particles within a K-dimensional search space at j-iterations is determined by update equations. These equations facilitate the convergence of each particle toward its local attractor. The local attractor for a particle is described as $p_{i,j} = [p^1_{i,j}, p^2_{i,j}, \ldots, p^K_{i,j}]$, which specifies its position in the search space.

$$p^k_{i,j} = \phi^k_{i,j}P^{best,k}_{i,j} + (1 - \phi^k_{i,j})G^{best,k} \tag{2.69}$$

Where $P^{best,k}_{i,j}$ and $G^{best,k}$ are the personal and global best positions of particle i, $\phi^k_{i,j}$ It is composed of a sequence of uniformly distributed random numbers $(\overset{1}{r})^k_{i,j}$ and $(\overset{2}{r})^k_{i,j}$ in $[0, 1]$, and acceleration coefficients c_1 and c_2, as follows:

$$\phi^k_{i,j} = \frac{c_1(\overset{1}{r})^k_{i,j}}{c_1(\overset{1}{r})^k_{i,j} + c_2(\overset{2}{r})^k_{i,j}} \tag{2.70}$$

The value of L_j in Equation (39) for a particle i in the k-dimension can be calculated using the following method, as described by Sun, Feng, et al. [63]:

$$L_{i,j}^k = 2\alpha |C_j^k - x_{i,j}^k| \tag{2.71}$$

where The expansion-contraction factor, denoted by α, is commonly expressed as a fixed value or as a linear decline from 1 to 0.5, and C_j^k is the particle swarm's average best position, which can be written as:

$$C_j^k = \frac{1}{N} \sum_{i=1}^{N} p_{i,j}^k \tag{2.72}$$

In conclusion, the quantum particle swarm's position update equation is [64]:

$$x_{i,j+1}^k = p_{i,j}^k \pm \alpha |C_j^k - x_{i,j}^k| \times \ln\left(\frac{1}{u_{i,j+1}^k}\right) \tag{2.73}$$

The indexes, sets, and parameters of the proposed algorithms considered in the simulation case study are described in Table (2.3).

2.3.4 QPSO-Based Computational System Energy Management Strategy

Quantum Particle Swarm Optimization (QPSO) optimizes greenhouse energy management by minimizing grid power use while meeting microclimate needs. The global version of NQPSO is outlined in the pseudocode algorithm (2).

Table 2.3: PSO, QPSO indexes, and sets

Symbol	*Description*	*PSO*	*QPSO*
i	Index of particles	-	-
j	Index of iterations	-	-
k	Index of dimension	-	-
N	Population size	2700	2700
J_{max}^{tr}	Max iterations	3000	3000
c_1, c_2	Acceleration coefficients	1.85	1.87
C_c	Convergence condition	150000	150000

2.4 Case Study and Numerical Results

2.4.1 Case Study Application

The proposed optimization problem is formulated based on the system modeling described in Sections 2.1 and 2.3 is simulated and compared with classical NPSO and Pyomo with Ipopt as a solver during different phases of growth, which are early growth (E.G.), vegetative (V), flowering (F), fruit formation (F.F.), and mature fruiting (M.F.), and by applying the deterministic case based on real data from Qatar's hard climate and the probabilistic case based on outputs obtained by a forecast using the random forest algorithm. The proposed control strategy is applied to a smart greenhouse connected with the grid and contains a master pump that pumps water from the water source to the water reservoir, energy storage inventory, and renewable generators (wind turbine and PV modules). It is assumed in this study that the smart greenhouse is specifically designed to grow peppers, a crop that is extremely vulnerable to wind, cold, and frost during its vegetative and flowering stages.

The optimal inside microclimate and water reference variables for different phase growth are presented in Table(2.4). They are provided by Vertify, a company specializing in applied research across outdoor vegetables, greenhouse horticulture, arable farming, flower bulbs, and fruit production in the Netherlands [65]. Their expertise ensures reliable and practical insights for agricultural practices.

Algorithm 2: (NQPSO)-based Optimization Energy Management System.

Input:
- Outdoor environmental variables;
- Indoor reference variables needed;
- System Parameters
- Renewable energy production;
- Problem Formulation (decisional variables,...., objective function, constraints);
- $N \longrightarrow$ population size;
- (lb, ub) $\longrightarrow$ (lower bound, upper bound);
- $K \longrightarrow$ dimension;
- $c_1, c_2 \longrightarrow$ QPSO parameters;
- $J_{tr}^{\max} \longrightarrow$ max iterations;
- $C_c \longrightarrow$ Convergence condition;

begin

Initialize current positions $x_{i,0}^{k}$, personal best positions $P_{i,0}^{best,k}$, evaluate their fitness values, and find the global best position $G_0{}^{best}$;

Set $j = 0$;

while $j \leq J_{tr}^{max}$ *or Convergence condition not met* **do**

 Compute C_j^k, the mean best position (Eq.2.72);

 α drops linearly from 1 to 0.5;

 for $i = 1$ *to* N **do**

  for $k = 1$ *to* K **do**

   Set $(\overset{1}{r})_{i,j}^{k} = (\overset{2}{r})_{i,j}^{k} = rand[0, 1]$;

   Compute : $\phi_{i,j}^{k}$ (Eq.2.70);

   $p_{i,j}^{k} = \phi_{i,j}^{k} P_{i,j}^{best,k} + (1 - \phi_{i,j}^{k}) G^{best,k}$;

   if *rand[0,1] > 0.5* **then**

    $x_{i,j+1}^{k} = p_{i,j}^{k} + \alpha |C_j^k - x_{i,j}^{k}| \ln\left(\frac{1}{u_{i,j+1}^{k}}\right)$;

   else

    $x_{i,j+1}^{k} = p_{i,j}^{k} - \alpha |C_j^k - x_{i,j}^{k}| \ln\left(\frac{1}{u_{i,j+1}^{k}}\right)$;

   if $x_{i,j+1}^{k} > ub^k$ **then**

    $x_{i,j+1}^{k} = \mathrm{ub}^k$;

   if $x_{i,j+1}^{k} < lb^k$ **then**

    $x_{i,j+1}^{k} = \mathrm{lb}^k$;

  Evaluate fitness (objective function value)

  if $f(x_{i,j}) \leq f(P_{i,j}^{best})$ **then**

   update personal best: $P_{i,j}^{best} = x_{i,j}$

 update global best: $\arg\min(P_j^{best}) = G_j^{\text{best}}$

 Set $j = j + 1$;

end

Output: Minimal fitness value with solutions:
- Optimal inside microclimate variables.
- Optimal Best operation of equipments.
- Optimal Power purshed from grid.
- Optimal Power sold to grid.

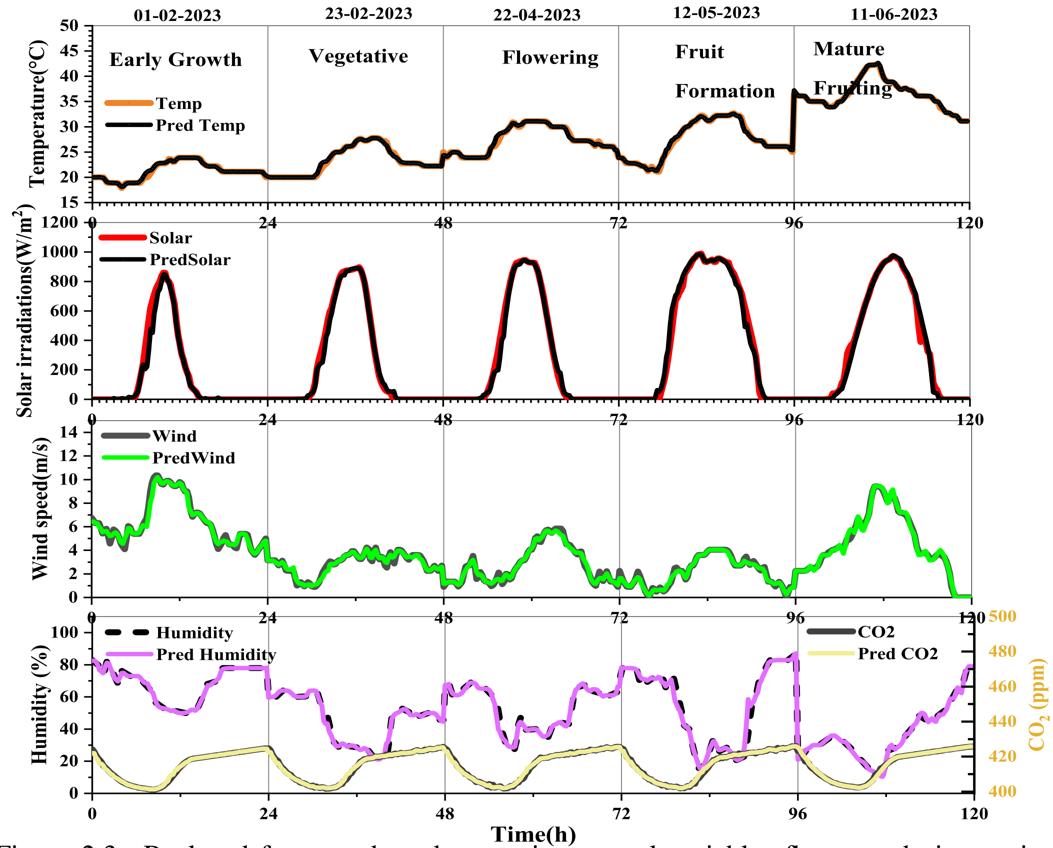

Figure 2.3: Real and forecasted outdoor environmental variables fluctuate during various stages of growth.

Table 2.4: Microclimate and water reference of pepper in different phases of growth

Phase	T^{in}_{ref} (°C)	I^{art}_{ref} (μmol m^{-2} s^{-1})	H^{in}_{ref} (%)	CO_{2ref} (ppm)	w^{gh}_{ref} (L m^{-2} d^{-1})
E.G	[22–22]	200	75	600	2
V	[22–28]	400	65	800	4
F	[24–30]	600	60	850	6
F.F	[24–30]	650	67	850	6
M.F	[24–28]	650	60	850	4

2.4.2 Simulation Setup

In this study the real and forecasted environmental variables, including wind speed, solar irradiation, outside temperature, humidity and outdoor CO_2 are depicted in Figure 2.3. However, the reference vector of internal temperature expressing the optimal growth temperature in different phases of growth of crops available in greenhouse is detailed in Table (2.4), with left values that represent nighttime and right values that represent daytime. It is anticipated that the irrigation water requirement per day is changing in each phase of growth. The total water needed per day was divided into irrigation for 15 minutes of each hour in order to help the plant for an efficient absorption process. This is achieved through local pumps with an efficiency of 0.75, which are activated exclusively during the first time interval of each hour and remain switched off for the rest. The master pump efficiency is set at 0.8. However, h^{gh} is configured to be equal to 5(m). Furthermore, the desired internal illumination, humidity, and CO_2 level are also assumed to be controlled. Although the GH is equipped with renewable energy production in the form of a PV system of 5 (kW), a wind turbine of 30 (kW), an energy storage inventory with a maximum capacity of 50 (kWh), and a water reservoir of 7 (m^3), it

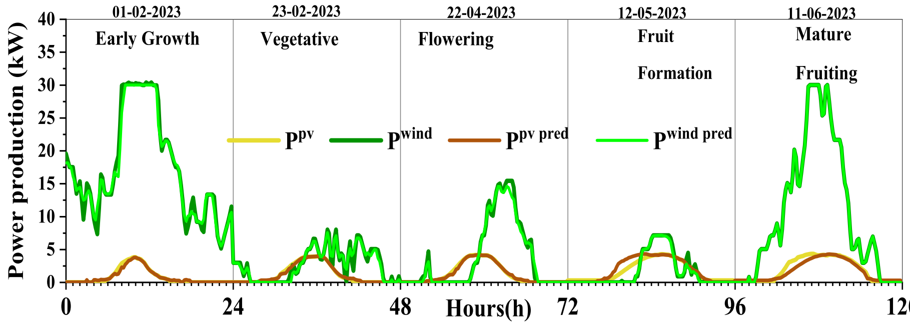

Figure 2.4: Real and predicted power production from wind turbine and PV panel models

is also connected to the grid. This connection allows the greenhouse to buy energy when needed and sell excess energy when available. The real and forecasted powers generated by the wind and solar (PV) models are presented in Fig.2.4.

2.4.3 Numerical Results and Discussion

The optimization problem focuses on effectively managing and controlling the indoor microclimate by minimizing deviations from the set reference signals. It also aims to reduce energy purchases from the grid by implementing optimized operational methods. These methods are designed to account for the real and predicted outdoor environmental conditions, ensuring efficient and sustainable system performance. It should be noted that the starting states of the water reservoir and the S_{oc} are set to $M^{res}(0) = 2(\mathrm{m}^3)$ and $S_{oc}(0) = 20(\mathrm{kWh})$, respectively. Furthermore, the initial states of the greenhouses' indoor variables are supposed to be the same as their initial references. In this study we assume that all weighting parameters α_1,..., α_6 have the same value = 1, which means all objectives have the same priority. The performance of water flow pumped into the reservoir and water load dedicated to irrigation and the dynamics of the water reservoir using different optimization methods are presented in Fig.2.5, respectively. Fig.(2.5-b-c) describes the dynamics of water irrigation with their related power consumption. It can be seen that the local pump shows a successful performance by fulfilling the water load with optimal power consumption during different phases of growth by achieving a minimal deviation from their reference. The dynamics of the water storage reservoir have been illustrated in Fig.(2.5-d). Starting at an initial level of 2 (m^3), the reservoir undergoes cyclical charging and discharging phases corresponding to the activations of both the local and master pumps. This pattern ensures the reservoir maintains a steady water supply for greenhouse operations, with the same behavior occurring for the forecast case. In general, all optimization methods are showing a perfect performance, successfully satisfying the water requirements. especially NQPSO and Pyomo stand out with their superior accuracy and stability, closely following the reference water load with minimal deviations. While NPSO demonstrates good performance, with small occasional mismatches during some periods. Optimal control decisions regarding indoor temperature, generated by various optimization methods and strategies for cooling and heating along with their respective HVAC power consumption and coefficients of performance, are illustrated in Fig.2.6. It can be observed that the HVAC system operates within predefined power ranges to regulate the greenhouse's internal temperature. The control algorithms are designed to track the reference temperature signal throughout different growth phases. As shown in Fig.(2.6-a) the HVAC first raises the temperature from an initial 20 (°C) to 22(°C) the optimal value for the early growth stage. Subsequently, the system adjusts to meet cooling demands caused by high outdoor temperatures and solar radiation during later phases, where distinct day and night temperature setpoints are required. During nighttime, the HVAC operates at optimal power for heating, while daytime requires cooling, as illustrated in Fig.(2.6-c). The system maintains close alignment with the reference signal, except for brief deviations caused by harsh external conditions such as microclimate fluctuations and wind speed, affecting both real and forecasted scenarios. Fig.(2.6-b) displays the HVAC's coefficient of performance (C_{op}), which adopts positive values during heating and negative values during cooling, reflecting its efficient separation of heating and cooling modes. In terms of optimization and temperature control, the NQPSO and PYOMO methods demonstrate superior reference tracking with minimal deviations compared to

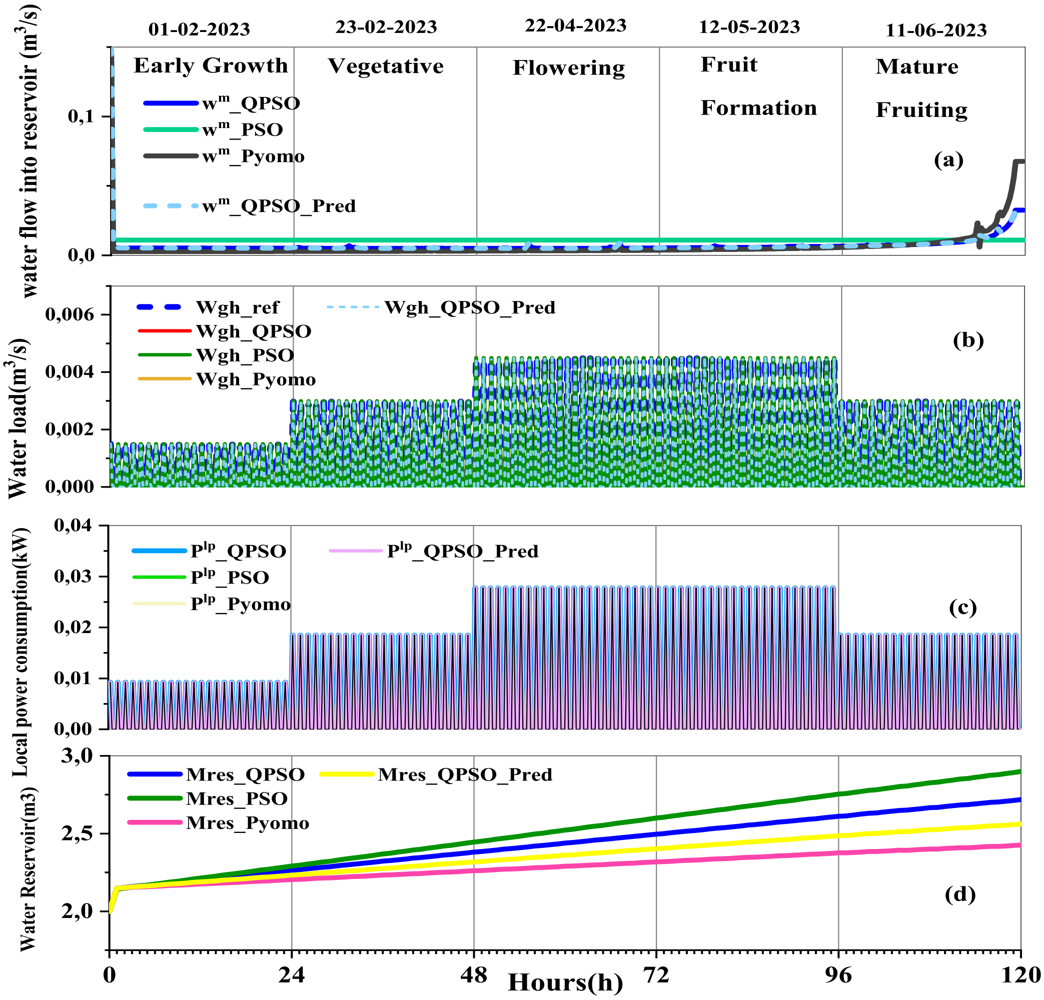

Figure 2.5: Water flows pumped into the water reservoir, optimal tracking to meet irrigation needs with their pump power consumption, and dynamics of water reservoir levels across growth phases.

NPSO. The latter exhibits slower convergence due to inherent speed limitations. In greenhouse natural ventilation, small opening angles are typically maintained across all optimization methods throughout most growth phases. However, a deviation occurs near the end of the early growth phase, where the internal temperature dynamics begin to diverge from the reference. The ventilation system adjusts its opening angle optimally to cool the interior and realign with the target temperature, as dictated by the constraints in (2.22). This behavior is particularly evident in the NQPSO and Pyomo results Fig.2.7, whereas NPSO exhibits larger openings due to less stable temperature regulation. The restrained ventilation strategy intentionally minimizes heat and CO_2 losses, thereby reducing the energy needed to compensate for air exchange disruptions. A similar trend appears in the forecasted scenario, though minor variations arise from outdoor environmental predictions.

Efficient lighting is crucial for enhancing plant growth and boosting greenhouse productivity. Fig.2.8 illustrates how blue light tracking optimizes illumination load while managing power consumption effectively. During daylight hours, artificial lighting remains off since natural sunlight provides adequate illumination, reducing energy usage. At night, artificial lights activate, primarily powered by renewable energy sources. The grid supplies occasional backup support during short intervals across all growth phases. All tested methods perform well in consistently meeting illumination demands, ensuring ideal growing conditions in both real-time and forecasted scenarios.

Fig.2.9 illustrates the optimal control of relative humidity and the corresponding power consumption of the fogger and dehumidifier across different growth phases for real and forecasted scenarios. Generally, relative humidity remains within 65(%) to 75(%) during growth phases, closely aligning

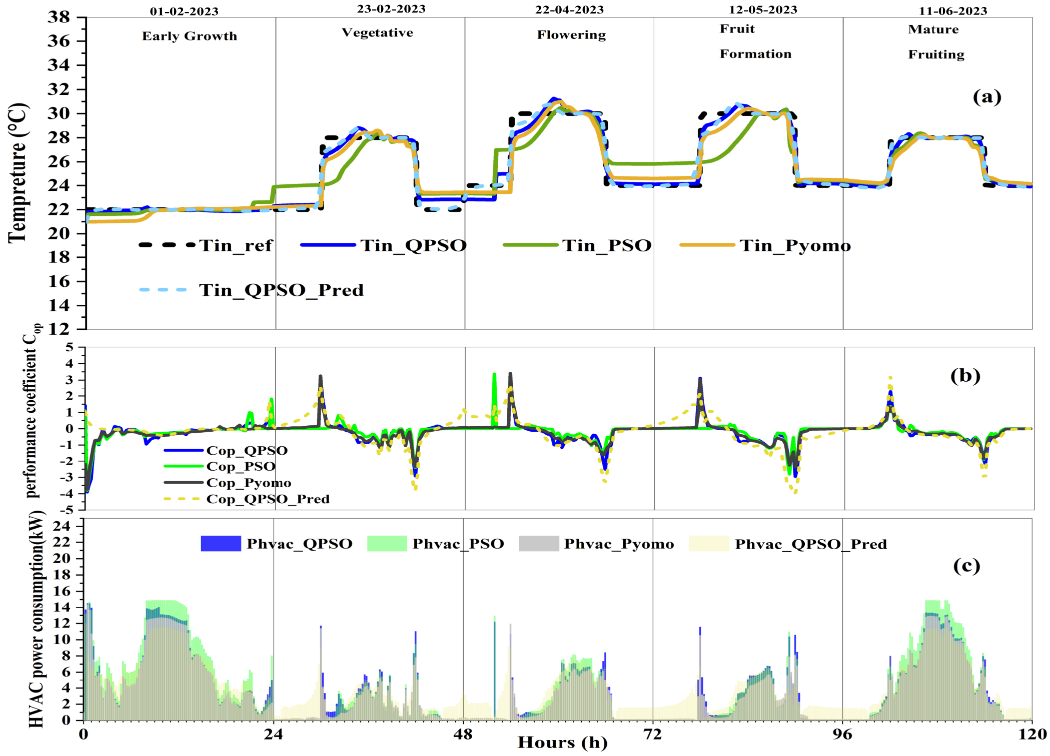

Figure 2.6: Optimal greenhouse indoor temperature with their HVAC power consumption and coefficient of performance over the day across diffirent growth phases.

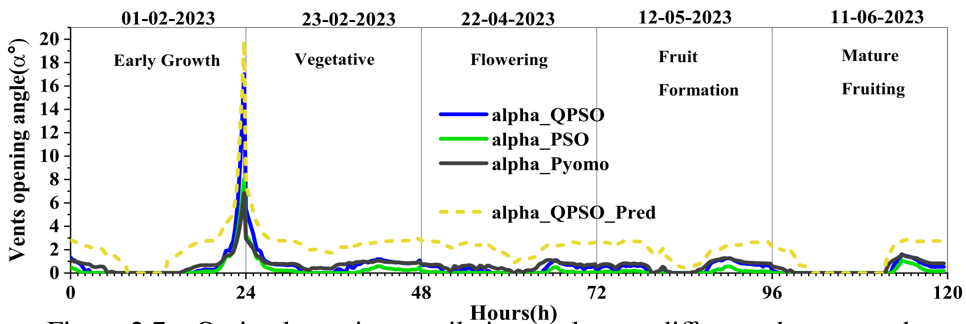

Figure 2.7: Optimal opening ventilation angle over different phase growth.

with reference values at night. However, a slight daytime drop occurs, primarily due to dynamic high-temperature fluctuations inside the greenhouse, a physically expected trend given the inverse relationship between humidity and temperature compared to nighttime conditions (Fig.2.9-a). This regulation is achieved through a combination of the greenhouse's natural air moisture content and the optimized operation of the fogger and dehumidifier (Fig.2.9-b-c). The fogger is primarily active during daylight hours to cool the greenhouse across all growth phases, with minimal nighttime power usage. Meanwhile, the dehumidifier operates efficiently at lower power levels, thanks to reduced natural airflow and minor deviations from the target humidity setpoints. In real-case evaluations, the NQPSO and PYOMO methods demonstrate superior tracking performance with negligible deviations, outperforming the NPSO approach.

The optimal control of indoor CO_2 levels and the associated power consumption of the CO_2 injector across different growth phases for real and forecasted scenarios are shown in (Fig 2.9-a-b). The CO_2 injector consumes significantly more power during transitions, particularly from early growth to vegetative and from vegetative to flowering, due to the higher CO_2 demand. However, its operation is most critical during daylight hours when plants actively absorb CO_2 for photosynthesis. Power usage drops in the final growth phases as CO_2 requirements stabilize. Among the tested methods,

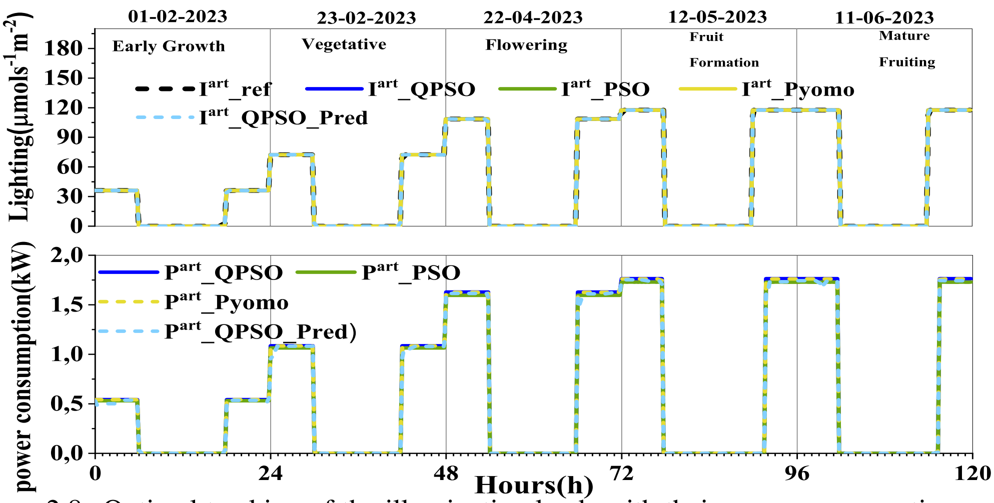

Figure 2.8: Optimal tracking of the illumination loads with their power consumption across growth phases.

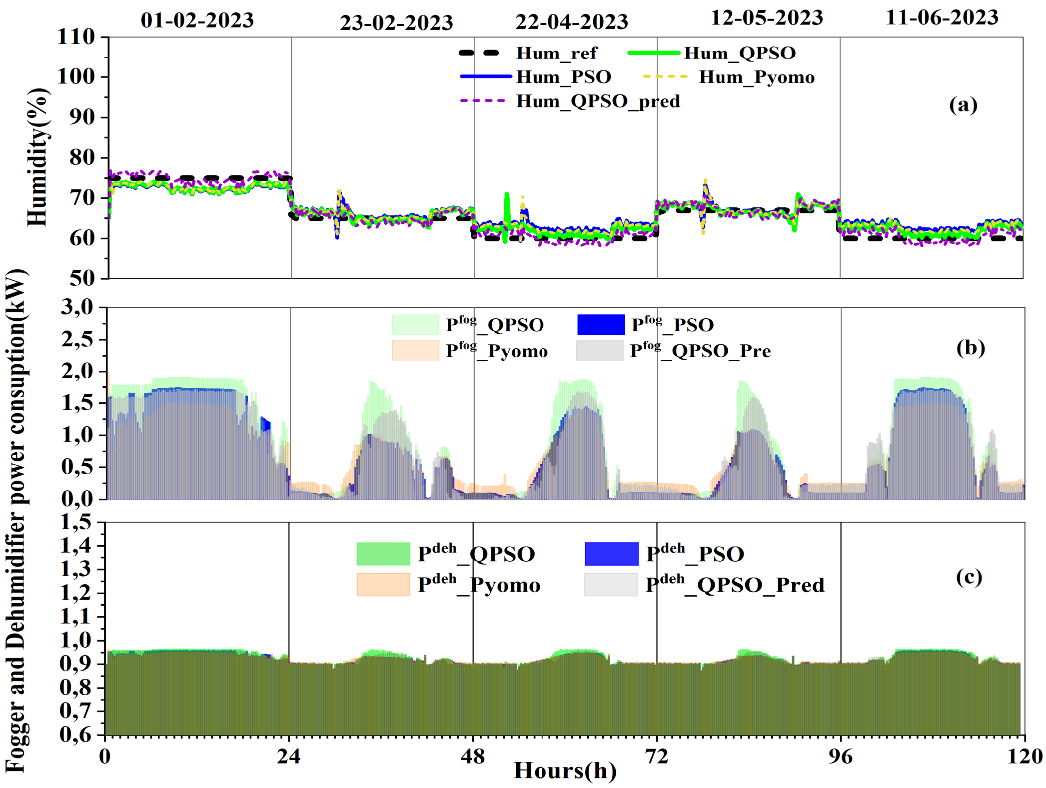

Figure 2.9: Optimal relative humidity inside the greenhouse with optimal power consumed by fogger and dehumidifier equipment across different growth phases.

NQPSO and Pyomo outperform others, showing remarkable stability, minimal fluctuations, and near-perfect tracking of the reference signal. These approaches ensure precise CO_2 regulation, maintaining the closest alignment with the target curve and significantly reducing deviations compared to NPSO.

Fig.(2.11-a-b-c) illustrates the results for the optimal energy state of the battery and the power exchanged with the grid. The battery energy state (S_{oc}) could theoretically compensate for renewable intermittency; the implemented strategy prioritized energy sales maximization over battery charging, limiting its effectiveness in this role. As shown in Fig.(2.11-a-b), the system primarily sold energy to the grid, especially in the early growth period, even with the presence of all equipment loads caused by the availability of renewable energy production. On the other hand, minimal energy is purchased by the system, occurring only during periods of low battery reserves. This pattern stems from consistent

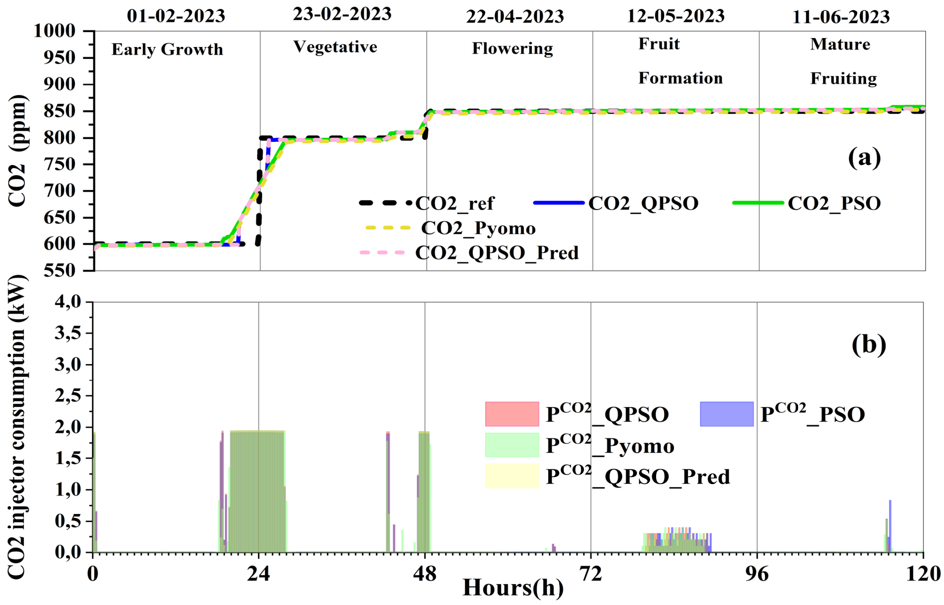

Figure 2.10: Optimal monitoring and control of CO2 concentration levels inside the greenhouse with optimal power consumed by the CO2 injector throughout different growth phases.

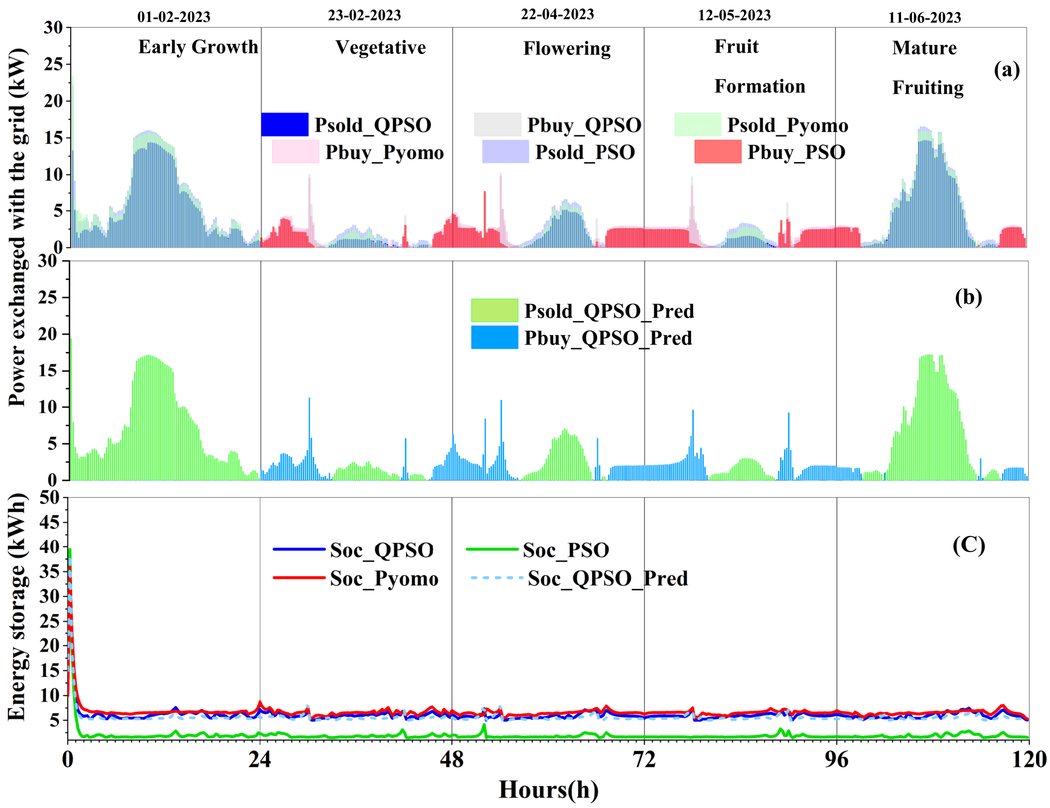

Figure 2.11: Optimal power exchange with the grid and dynamic of Batteery energy storage throughout the day for different growth phases.

wind availability throughout the day combined with daytime photovoltaic (PV) production. Fig.(2.11-c) reveals the battery's operational strategy: starting from 20 (kWh), it charges to approximately 36 (kWh) to fulfill the minimal power load during the first hours after. The energy storage unit demonstrates adaptive discharging and charging behavior to maintain power balance with the grid, responding to both energy availability and demand fluctuations. This intelligent cycling enables maximized energy exports while limiting imports to essential periods of renewable shortfall. These results demonstrate QPSO and Pyomo's superior performance in enforcing optimal control strategies for both battery management and grid power exchange, as mathematically defined in Equation (2.2.6) in real and forecasted cases. The methods ensure precise coordination between storage dynamics and renewable generation patterns. The profits and consumption of the system operation throughout the

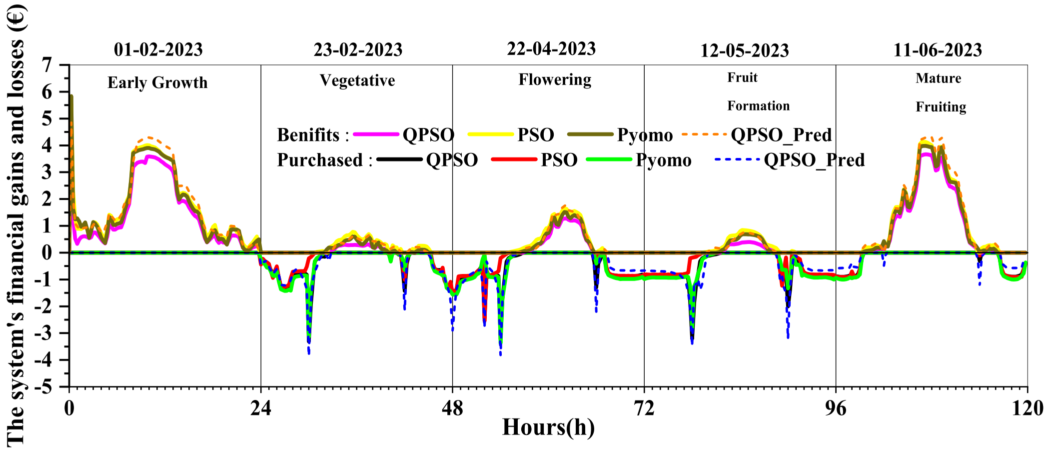

Figure 2.12: Profits and consumption of the system operation throughout the day for different growth phases.

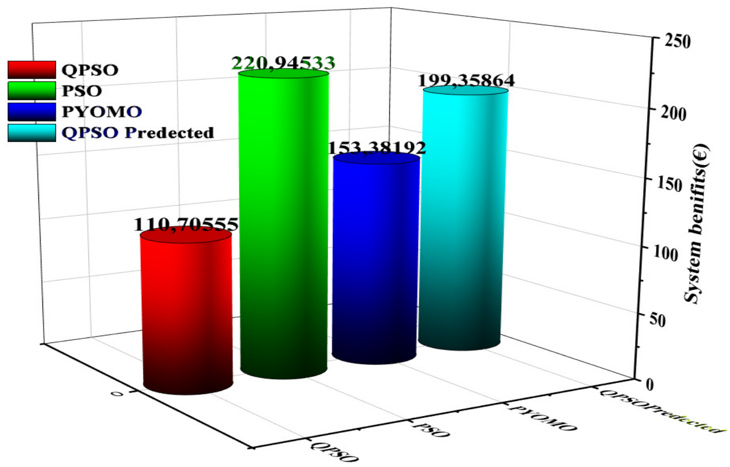

Figure 2.13: Total benefits of the system using proposed optimization methods.

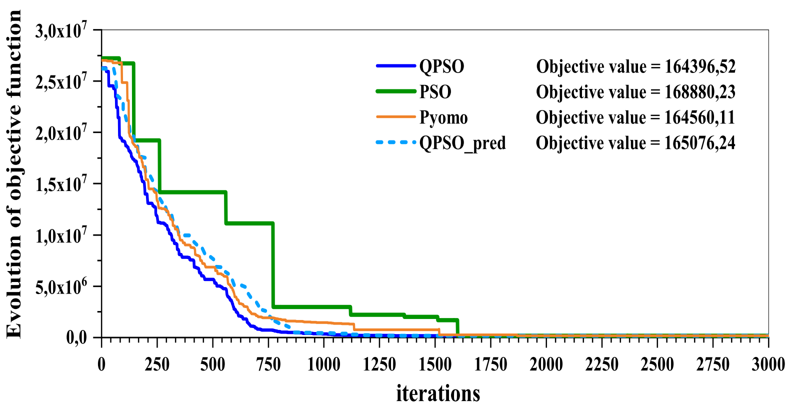

Figure 2.14: The evolution of the objective function across iterations using different optimization methods.

day, across different growth phases for real and forecasted cases, along with the total system benefits, are shown in Figs 2.12 and 2.13. Compared to other methods, the NQPSO algorithm demonstrates higher consumption but lower system benefits. Additionally, as illustrated in Figure 2.14, the NQPSO yields minimal benefits and the lowest objective function value, which aligns with expectations. This is due to the high energy consumption required by the equipment to maintain an optimal microclimate for the peppers, which is our primary objective, as defined in equation (2.36). Figure 2.14 compares the performance of three algorithms, NQPSO, NPSO, and Pyomo, for optimizing energy management in a greenhouse, revealing distinct convergence patterns. NQPSO reached the lowest objective value of 164,396.52 by iteration 2226, while Pyomo achieved 165,076.24 by iteration 2143. NPSO converged later, at iteration 2875, with a value of 168,880.23. Although none of the algorithms met the original convergence target of 150,000 within 3000 iterations, they stabilized at their respective minima. Initial runs started near 197,000, prompting adjustments to the convergence threshold to 180,000, which all methods eventually satisfied. Further tuning of parameters and population sizes, along with a stricter target of 150,000, led to improved, though not fully converged, solutions.

Table 2.5: Performance Metrics Comparison

Varaiable	*Method*	*MAE*	*RMSE*
Water	*NQPSO*	0.0025	0.0033
	NPSO	0.0037	0.0049
	Pyomo	0.0036	0.0091
Temperatue	*NQPSO*	0.3778	0.5959
	NPSO	1.0070	1.4557
	Pyomo	0.6117	0.8525
Lighting	*NQPSO*	0.0358	0.0368
	NPSO	0.1012	0.1293
	Pyomo	0.0301	0.0343
Humidity	*NQPSO*	1.7274	2.1026
	NPSO	2.2426	2.6171
	Pyomo	2.0605	2.4533
CO_2	*NQPSO*	0.3778	0.5959
	NPSO	1.0070	1.4557
	Pyomo	0.6117	0.8525

Complementing this convergence analysis, Table (2.5) presents performance metrics across microclimate variables, demonstrating that NQPSO consistently outperforms both NPSO and Pyomo in tracking reference signals. For water, temperature, CO_2, and humidity control, NQPSO achieves the lowest Mean Absolute Error (MAE) and Root Mean Square Error (RMSE) values, indicating superior tracking accuracy and stability. While Pyomo shows competitive performance in lighting control, NQPSO maintains the most robust overall performance across all environmental variables, establishing it as the most effective optimization method for microclimate reference tracking applications.

2.5 Conclusion

In this work, an optimization framework was developed to provide an optimal indoor microclimate for greenhouse operations by tracking reference signals for variables such as temperature, CO_2 concentration, artificial lighting, and irrigation water while minimizing energy exchanged with the grid during periods of limited renewable energy generation for real and forecasted case studies during different phases of growth. To achieve this, three optimization methods, NQPSO, NPSO, and Pyomo, were implemented and compared. The results demonstrated that NQPSO and Pyomo outperformed NPSO, achieving minimal objective function with favorable outcomes by delivering an optimal microclimate for crops, minimizing energy purchased, and selling important energy to the grid, making it the most efficient method for greenhouse energy management. Additionally, this optimization framework offers automation and control capabilities for the greenhouse system, enabling real-time decision-making and efficient resource utilization. This study underscores the potential of NQPSO as a highly effective tool for greenhouse energy management, particularly under challenging harsh climate conditions, as it optimizes the microclimate, enhances energy efficiency, and supports automated, sustainable greenhouse operations.

Chapter 3

Unified Model Predictive Control for Coordinated Microgrid Energy Management and Greenhouse Microclimate Control over Growth Cycles

This chapter tackles the main challenges in greenhouse energy management optimization: balancing energy and water use, maintaining optimal growing conditions, and integrating renewable sources by proposing a novel Nonlinear Model Predictive Control (NMPC) framework for a grid-connected smart greenhouse. Section 3.1 and Section 3.3 are dedicated to the system description and mathematical modeling breakdown of the complete sweet pepper organ-level crop growth dynamics alongside the microclimate control equations and introduce the NMPC formulation approach, which is specifically designed to handle complex crop-environment interactions, manage competing objectives, and optimize energy exchanges at the microgrid level. A real case study conducted over a full 161-day growing cycle evaluates the proposed framework against a nonlinear optimization method developed in Python Gekko. Section 3.4 describes The results demonstrate that the NMPC approach effectively tackles complex nonlinear (non-convex) problems while delivering robust, automated, and scalable performance for greenhouse energy management and microclimate control. The findings also highlight meaningful gains in both energy and water efficiency compared to traditional methods, indicating the potential for this framework to support more sustainable greenhouse operations and smarter microgrid integration. The chapter concludes in Section 3.5.

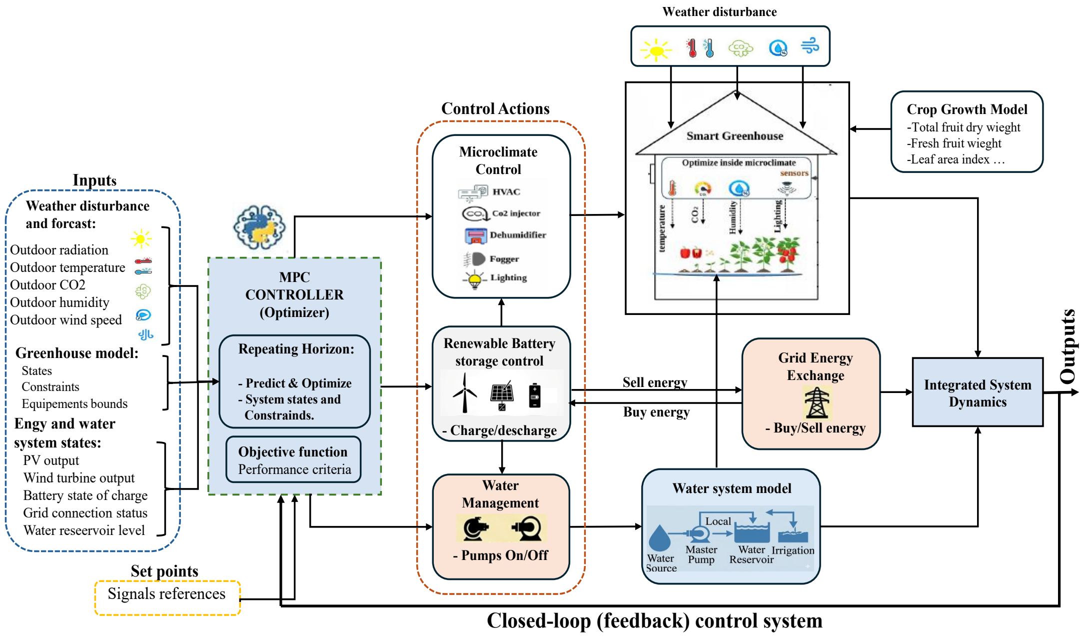

Figure 3.1: System architecture.

3.1 Modeling of system component

3.1.1 PV Panels

The expected power output of the JKM590N-72HL4 PV panels used in this study, assuming operation at maximum power point (MPP), can be described as follows[53]:

$$I_{\text{pv}}[k] = I_{\text{sc}}^{\text{ref}} \left[1 - A \left(\exp\left(\frac{V_{\text{mp}}^{\text{ref}}}{B \cdot V_{\text{oc}}^{\text{ref}}} \right) - 1 \right) \right] + \Delta\delta^{I_l}[k], \tag{3.1}$$

$$V_{\text{pv}}[k] = V_{\text{mp}} \left(1 + 0.0539 \cdot \log\left(\frac{\delta^{I_l}[k]}{I_{\text{st}}} \right) \right) + u \cdot \Delta T[k], \tag{3.2}$$

$$\text{where} : A = \left(1 - \frac{I_{\text{mp}}^{\text{ref}}}{I_{\text{sc}}^{\text{ref}}} \right) \exp\left(- \frac{V_{\text{mp}}^{\text{ref}}}{B \cdot V_{\text{oc}}^{\text{ref}}} \right), \tag{3.3}$$

$$B = \frac{V_{\text{mp}}^{\text{ref}}}{V_{\text{oc}}^{\text{ref}} - 1} \cdot \frac{1}{\log\left(1 - \frac{I_{\text{mp}}^{\text{ref}}}{I_{\text{sc}}^{\text{ref}}} \right)}, \tag{3.4}$$

$$\Delta\delta^{I_l}[k] = \eta \left(\frac{\delta^{I_l}[k]}{G^{\text{st}}} \right) \Delta T[k] + \left(\frac{\delta^{I_l}[k]}{G^{\text{st}}} - 1 \right) I_{\text{sc}}^{\text{ref}}, \tag{3.5}$$

$$\Delta T[k] = T^{\text{amb}} + 0.02 \cdot \delta^{I_l}[k]. \tag{3.6}$$

The PV array's output voltage and power are as follows:

$$V_{\text{pv,out}}[k] = \epsilon^{\text{pv,s}} V_{\text{pv}}[k] \tag{3.7}$$

$$P_{pv}[k] = \epsilon^{\text{pv,s}} \epsilon^{\text{pv,p}} \frac{V_{\text{pv}}[k] I_{\text{pv}}[k]}{1000} \eta_{\text{pv}} \xi^{\text{loss}}. \tag{3.8}$$

where V_{mp}^{ref} is the module's maximum power voltage, I_{sc}^{ref} is the module's short-circuit current, and I_{mp}^{ref} is the module's maximum power current. $\delta^{I_l}[k]$ is solar irradiance, and V_{oc}^{ref} is the module open-circuit voltage, G^{st} represents standard light intensity, μ is the module voltage temperature coefficient, η is the module current temperature coefficient, T^{amb} is the ambient temperature, η_{pv} is the efficiency of the solar panel, and ξ^{loss} stands for both connection loss and additional loss brought on by other variables. $\epsilon^{\text{pv,s}}$ is the serial connection number of PV modules, $\epsilon^{\text{pv,p}}$ is the parallel connection number of PV

Figure 3.2: Weather station (savona)

module strings, $I_{\mathrm{pv}}[k], V_{\mathrm{pv}}[k]$ are the output current and voltage of the PV modules, and P^{pv} is the PV output power.

The above equation can be rewritten considering the MPC format and the prediction horizon n_p as follows:

$$\mathbf{P}_{pv}[k, n_p] = \begin{bmatrix} P_{pv}[k+1] \\ P_{pv}[k+2] \\ \vdots \\ P_{pv}[k+n_p] \end{bmatrix} \tag{3.9}$$

3.1.2 Wind Turbine Generator

The expected power output of the wind turbine is determined as [66]:

$$P_{wind}[k] = \begin{cases} 0 & \delta^{v_s}[k] < v_c \\ P_r\left(\frac{v_c}{v_c - v_r} + \frac{1}{v_r - v_c}\delta^{v_s}[k]\right) & v_c \le \delta^{v_s}[k] \le v_r \\ P_r & v_r \le \delta^{v_s}[k] \le v_f \\ 0 & \delta^{v_s}[k] > v_f \end{cases} \tag{3.10}$$

where, δ^{v_s}[k] and P_{wind}[k] are respectively the wind speed and power generated by the wind turbine. P_r is turbine rated power, v_c, v_r and v_f are cut-in, rated and cut-out wind speeds respectively. The equation can be formulated considering the MPC format as follow:

$$\mathbf{P}_{wind}[k, n_p] = \begin{bmatrix} P_{wind}[k+1] \\ P_{wind}[k+2] \\ \vdots \\ P_{wind}[k+n_p] \end{bmatrix} \tag{3.11}$$

3.1.3 Water Reservoirs and Pumps

The irrigation system include a water reservoir in charge of ensuring water loads for irrigation purposes. The time-varying dynamics of the water reservoir is described as follow:

$$m[k+1] = m[k] + \left[Q_m[k] - Q_l[k]\right] \tag{3.12}$$

where, $m[k]$, is water reservoir, $Q_m[k]$ and $Q_l[k]$ are respectively the water flow entering the reservoir from water sourced and water flow pumped to irrigate the greenhouse. Considering the MPC format, it can be re-written as:

$$\underbrace{\begin{bmatrix} m[k+1] \\ m[k+2] \\ \vdots \\ m[k+n_p] \end{bmatrix}}_{\mathbf{m}[k+1,n_p]} = \underbrace{\begin{bmatrix} m[k] \\ m[k+1] \\ \vdots \\ m[k+n_p-1] \end{bmatrix}}_{\mathbf{m}[k,n_p]} + \underbrace{\begin{bmatrix} Q_m[k] \\ Q_m[k+1] \\ \vdots \\ Q_m[k+n_p-1] \end{bmatrix}}_{\mathbf{Q}_m[k,n_p]} - \underbrace{\begin{bmatrix} Q_l[k] \\ Q_l[k+1] \\ \vdots \\ Q_l[k+n_p-1] \end{bmatrix}}_{\mathbf{Q}_l[k,n_p]}$$

The water flow pumped through the local pump into greenhouse can be expressed as follow[67]:

$$Q_l[k] = \underbrace{\left[\eta_l \frac{\Delta k}{\rho g h_l}\right]}_{\gamma_l} P^l_{water}[k] = \gamma_l P^l_{water}[k] \tag{3.13}$$

where ρ is the water density and g is the gravity acceleration constant, $P^l_{water}[k], h_l$ and η_l are the needed power of local pump, distance of greenhouse from the reservoir and efficiency of local pump and Δk is time step length. The MPC formulation for the water flow supplied by the local pump to the greenhouse is given by:

$$Q_l[k,n_p] = \begin{bmatrix} Q_l[k] \\ Q_l[k+1] \\ \vdots \\ Q_l[k+n_p-1] \end{bmatrix} = \gamma_l \begin{bmatrix} P^l_{water}[k] \\ P^l_{water}[k+1] \\ \vdots \\ P^l_{water}[k+n_p-1] \end{bmatrix} \tag{3.14}$$

The water flow entering the reservoir is determined according to the power consumed by the main pump. It can be defined in MPC format as follows:

$$Q_m[k] = \underbrace{\left[\eta_m \frac{\Delta k}{\rho g h_m}\right]}_{\gamma_\mathbf{m}} P^m_{water}[k] = \gamma_m P^m_{water}[k] \tag{3.15}$$

where $P^m_{water}[k], h_m$ and η_l are the needed power of main pump, distance of greenhouse from the reservoir and efficiency of main pump.

$$Q_m[k,n_p] = \begin{bmatrix} Q_m[k] \\ Q_m[k+1] \\ \vdots \\ Q_m[k+n_p-1] \end{bmatrix} = \gamma_m \begin{bmatrix} P^m_{water}[k] \\ P^m_{water}[k+1] \\ \vdots \\ P^m_{water}[k+n_p-1] \end{bmatrix} \tag{3.16}$$

By combining equations (3.15), and (3.13) the final form of water reservoir can be obtained:

$$m[k+1,n_p] = m[k,n_p] + \gamma_m P^m_{water}[k,n_p] - \gamma_l P^l_{water}[k,n_p] \tag{3.17}$$

Constraints of reservoir and pumps can be described as follows:

$$\forall[k,n_p] \begin{cases} m^{\min} \cdot \mathbf{1}_{n_p\times 1} \le \mathbf{m}[k+1,n_p] \le m^{\max} \cdot \mathbf{1}_{n_p\times 1} \\ \mathbf{0}_{n_p\times 1} \le P^l_{\text{water}}[k,n_p] \le P^{l,\max}_{\text{water}} \cdot \mathbf{1}_{n_p\times 1} \\ \mathbf{0}_{n_p\times 1} \le P^m_{\text{water}}[k,n_p] \le P^{m,\max}_{\text{water}} \cdot \mathbf{1}_{n_p\times 1} \end{cases} \tag{3.18}$$

where $\mathbf{1}_{n\times 1}$ and $\mathbf{0}_{n\times 1}$ are defined as $\mathbf{1}_{n\times 1} = \underbrace{\begin{bmatrix} 1 & \dots & 1 \end{bmatrix}}_{\text{n times}}^{n_p}$ and $\mathbf{0}_{n\times 1} = \underbrace{\begin{bmatrix} 0 & \dots & 0 \end{bmatrix}}_{\text{n times}}^{n_p}$.

3.1.4 Energy Storage System

The system is assumed to include a battery energy storage (BES) that is in charge of supporting the microgrid in fulfilling the total electrical load and supporting the local power quality and stability [68].

The time-varying dynamics of the BES is given by:

$$\underbrace{\begin{bmatrix} BES[k+1] \\ BES[k+2] \\ \vdots \\ BES[k+n_p] \end{bmatrix}}_{\mathbf{BES}[k+1,n_p]} = \underbrace{\begin{bmatrix} BES[k] \\ BES[k+1] \\ \vdots \\ BES[k+n_p-1] \end{bmatrix}}_{\mathbf{BES}[k,n_p]} + \beta_c \underbrace{\begin{bmatrix} P_{ch}[k] \\ P_{ch}[k+1] \\ \vdots \\ P_{ch}[k+n_p-1] \end{bmatrix}}_{\mathbf{P}_{ch}[k,n_p]} - \beta_d \underbrace{\begin{bmatrix} P_{dch}[k] \\ P_{dch}[k+1] \\ \vdots \\ P_{dch}[k+n_p-1] \end{bmatrix}}_{\mathbf{P}_{dch}[k,n_p]} \tag{3.19}$$

where BES[k] is the state of charge of BES. $\beta_c, \beta_d, P_{ch}[k]$ and $P_{dch}[k]$ are charging coefficient, discharging coefficient, charging power and discharging power respectively. Constraints of BES can also be described as follow:

$$\forall [k, n_p] \begin{cases} BES^{\min} \leq BES[k+1, n_p] \leq BES^{\max} \\ 0 \leq P_{\text{ch}}[k, n_p] \leq P_{\text{ch}}^{\max}[k, n_p] \\ 0 \leq P_{\text{dch}}[k, n_p] \leq P_{\text{dch}}^{\max}[k, n_p] \\ P_{\text{ch}}[k, n_p] \cdot P_{\text{dch}}[k, n_p] = \mathbf{0} \end{cases} \tag{3.20}$$

3.1.5 Greenhouse Microclimate Dynamics Model

The inside microclimate of the greenhouse has been represented for various growth stages using a full physical system-level formulation model. The model replicates the variations over time in the greenhouse's air temperature, lighting, air humidity, and CO_2 concentration using the following state-equation model:

$$\psi^i[k+1] = f(k, \psi^i[k], \beta_j[k], W_u[k], \delta^n[k], C_s) \tag{3.21}$$

With discrete time $k \in \mathbb{Z}^+$, ψ^i stands for the greenhouse state microclimate variables, where the index $i \in \{\text{Tin}, \text{Lin}, \text{CO}_2^{\text{in}}, \text{H}^{\text{in}}\}$, β_j is the input vector for actuator control signals where $j \in \{\text{l}, \text{hvac}, \text{CO}_2, \text{fog}, \text{deh}\}$, $W_u[k]$ represents the state of organs' crop growth and fruit matter, where $u \in \{\text{L(leaf)}, \text{S(stem)}, \text{R(root)}, \text{F(fruit)}, \text{M(matter fruit)}\}$, and δ_n is a quantifiable disturbance (mostly outdoor environmental variables), where $n \in \{\text{v}_\text{s}(\text{wind speed}), I^{\text{l}}(\text{solar irradiation}), T^{\text{out}}, H^{\text{out}}, \text{CO}_2^{\text{out}}\}$. The system's parameter and constant vectors are denoted by C_s, whereas f stands for the nonlinear functions that describe the greenhouse dynamics.

Temperature Model

temperature plays a crucial role in photosynthesis, increasing activity at low to moderate levels as per the Arrhenius equation. To ensure optimal conditions and prevent reduced growth, the greenhouse regulates interior temperature using HVAC. The dynamic temperature model is as follows [69]:

$$\begin{aligned} \psi^{Tin}[k+1, n_p] = \psi^{\text{Tin}}[k, n_p] + \frac{\Delta k}{x} \Bigg[& \underbrace{S_g \tau \delta^{I_l}[k, n_p]}_{Q^{\text{sol}}} + (1-\eta_l) \underbrace{P_r^{art}[k, n_p] \beta_l[k, n_p]}_{Q^{\text{art}}} \\ + \underbrace{C_{\text{op}}[k, n_p] \beta_{\text{hvac}}[k, n_p] P^{\text{hvac}}[k, n_p]}_{Q^{\text{hvac}}} & - \underbrace{\frac{S_g \cdot e}{k_c} (\chi^T[k, n_p]}_{Q^{\text{cond}}} - \underbrace{J^{\text{inf}} x (\chi^T[k, n_p]}_{Q^{\text{inf}}} - \underbrace{h^{\text{conv}} S_g \cdot \chi^T[k, n_p]}_{Q^{\text{conv}}} \\ - \underbrace{Q^{\text{vent}}[k, n_p]}_{Q^{\text{vent}}} \Bigg] & \end{aligned} \tag{3.22}$$

$$\chi^T[k, n_p] = (\delta^{T^{\text{out}}}[k, n_p] - \psi^{T^{\text{in}}}[k, n_p]) \tag{3.23}$$

$$x = C_a \rho_a V_g \tag{3.24}$$

C_a is the air specific heat capacity, ρ_a is air density, V_g is the volume of the greenhouse, S_g is the total external surface area (cover) of the greenhouse, τ is the material transmissivity of polycarbonate used for the greenhouse cover, $\delta^{I_l}[k]$ is solar radiation intensity, η_l and P_r^{art} are the efficiency of artificial lighting and their rated power, respectively, $C_{op}[k]$ and $P^{hvac}[k]$ are the coefficient of performance (positive for cooling and negative for heating) and power consumed by the HVAC, $\beta_{hvac}[k]$ represents the operation status, e and k_c are the glazing material thickness and material thermal conductivity, $\psi^{\mathrm{Tin}}[k]$ and $\delta^{T^{\mathrm{out}}}[k]$ are the indoor and outdoor greenhouse temperatures, J^{inf} is the infiltration rate, and h^{conv} is the convective heat transfer coefficient. The total thermal flux gain in the greenhouse consists of the sum of heat gain by solar radiation (Q^{sol}), HVAC system (Q^{hvac}), and artificial lighting (Q^{art}). The total thermal flux loss in the greenhouse consists of heat loss by conduction (Q^{cond}), convection through the cover (Q^{conv}), latent heat effect due to crop transpiration (Q^{trs}), natural ventilation (Q^{vent}), and infiltration (Q^{inf}). In this model, the latent heat effect due to crop transpiration (Q^{trs}) is assumed to be neglected. The indoor temperature, coefficient of performance, and HVAC power consumption must each remain within limits that change over time.

$$\forall[k,n_p]\begin{cases}\psi^{Tin}_{min}[k,n_p] \le \psi^{Tin}[k,n_p] \le \psi^{Tin}_{max}[k,n_p]\\ C^{min}_{op}[k,n_p] \le C_{op}[k,n_p] \le C^{max}_{op}[k,n_p]\\ P^{hvac}_{min}[k,n_p] \le P^{hvac}[k,n_p] \le P^{hvac}_{max}[k,n_p]\\ \beta_{hvac}[k,n_p] \in [0,1]\end{cases} \tag{3.25}$$

The heat loss through natural ventilation Q^{vent} will be detailed in the next subsection.

Air circulation model

In this model, when the greenhouse gets too hot, a window for natural ventilation is used. It is possible to determine the air exchanged with outdoor environment brought on by the ventilation window's operation as follows[70]:

$$Q^{\mathrm{vent}}[k,n_p] = \underbrace{\frac{A^v}{S_g}\delta^{v_s}[k,n_p]\left(1-e^{\left(\frac{-\alpha[k,n_p]}{21.1}\right)}\right)\cdot 82.44}_{J^{\mathrm{ven}}} \tag{3.26}$$

The airflow rate term, represented as J^{vent}, can be calculated based on the ventilator window area type, outdoor wind speed, and the angle of the window opening. This opening angle α must be kept within a specific range, which also varies over time.

$$\forall[k,n_p]\begin{cases}0 \le \alpha[k,n_p] \le \alpha_{\max}, & \text{if } \psi^{Tin}[k,n_p] - \psi^{Tin}_{ref}[k,n_p] \ge 2\\ 0 & \text{otherwise}\end{cases} \tag{3.27}$$

where α denotes the window's angle opening (deg), A^v denotes the window area of natural ventilation and δ^{v_s} denotes the wind speed.

Light Intensity Model

According to research, LEDs can convert up to 49% of electricity into light that plants can really consume, making them a wise and economical choice for greenhouses[58]. Their compatibility with pulse-width modulation (PWM), which enables exact light modifications that conserve energy without stressing plants, is a major benefit[71]. DLC, or dynamic lighting control, increases this efficiency. Smart sensors are used by systems like Fluence's SPYDR 2p47 to modify light spectra in real time, changing to blue (450 nm) for vegetative development or red (660 nm) for blooming depending on canopy circumstances[61]. This method increases agricultural yields while using 20% less energy than fixed-spectrum illumination. The dynamic light intensity in the greenhouse is a combination of artificial lighting and natural sunlight and can be described as follows:

$$\psi^{Lin}[k] = \psi^{Lin}_{nat}[k] + \psi^{Lin}_{art}[k] \tag{3.28}$$

$$\psi^{Lin}[k,np] = \underbrace{\tau \cdot k_{sol} \cdot \delta^{I_l}[k,np]}_{\psi^{Lin}_{nat}} + \underbrace{\frac{P^{art}[k,np]\,\eta_l}{S_c\, N_x\, \beta_l[k,np]}}_{\psi^{Lin}_{art}} \tag{3.29}$$

$$\beta_l[k,np] = \begin{Bmatrix} 1 & if \;\; \psi^{Lin}_{nat}[k,np] \le \delta^{I_l}_{\min} \\ 0 & otherwise \end{Bmatrix} \tag{3.30}$$

where ψ^{Lin}_{nat} represents the natural light intensity that comes from solar radiation, τ is the material transmissivity, δ^{I_l} solar radiation and k_{sol} is factor of solar radiation contributing to PAR. The power consumed by artificial lighting P^{art} as a function of ψ^{Lin}_{art} artificial light intensity, S_c denotes cultivated area, η_l is the LED efficiency, $\delta^{I_l}_{min}$ represents the minimal light intensity and N_x number of fixtures of artificial lighting products used for covering the cultivated area.

CO_2 Model

In different phases of growing a plant, CO_2 is another essential parameter which must be regulated and controlled. The dynamic model for CO_2 concentration within the MPC structure is given by [72]:

$$\psi^{CO_2^{in}}[k+1,n_p] = \psi^{CO_2^{in}}[k,n_p] + \frac{S_g \Delta k}{V_g \rho_a}\Bigg[\beta_{CO_2}[k,n_p]C^{inj}_{\max} + \ldots$$

$$\underbrace{\frac{a_1}{S_g}\delta^{v_s}[k,n_p]A^v\lambda_s J^{ven}[k,n_p]\cdot\chi^{CO_2}[k,n_p]}_{\text{Ventilation exchange}} + \underbrace{\frac{C^{res}}{S_g}\left(a_2 + a_3\psi^{Tin}[k,n_p]\right)}_{\text{Plant respiration}} - \underbrace{a_1 C^{phot}\psi^{Lin}[k,n_p]}_{\text{Photosynthesis}}\Bigg] \tag{3.31}$$

$$\chi^{CO_2}[k,n_p] = \left(\delta^{CO_2^{out}}[k,n_p] - \psi^{CO_2^{in}}[k,n_p]\right)$$
$$P^{CO_2}[k,n_p] = \beta_{CO_2}[k,n_p]\cdot P^{CO_2}_r \tag{3.32}$$

Where $\psi^{CO_2^{in}}[k]$, $\delta^{CO_2^{out}}[k]$ are the greenhouse internal and external CO_2 concentrations, $C^{inj}_{\max}$ is the maximum carbon that a CO_2 generator may introduce. $w_s, A^v, \lambda_s, J^{ven}$ are wind speed, ventilation window area, percentage of wind speed that enters into the greenhouse, and air exchange rate through natural ventilation respectively. $a_6 ... a_8$ are coefficients associated with the respiration rate of the crop, C^{res} is the respiration coefficient of crops, C^{phot} is the photosynthesis coefficient of crops, $\psi^{Lin}[k]$ is the indoor light intensity, β_{CO_2} represent the operational status of the CO_2 injector and $P^{CO_2}[k]$ and $P^{CO_2}_r$ are consumed and rated powers of the CO_2 injector. This amount of CO_2 must be maintained in a certain range, which depends on time too:

$$\forall[k,n_p]\begin{cases}\psi^{CO_2^{in},\min}[k,n_p] \le \psi^{CO_2^{in}}[k,n_p] \le \psi^{CO_2^{in},\max}[k,n_p] \\ P^{CO_2,\min}[k,n_p] \le P^{CO_2}[k,n_p] \le P^{CO_2,\max}[k,n_p] \\ \beta_{CO_2}[k,n_p] \in [0,1]\end{cases} \tag{3.33}$$

Model of Humidity

Optimal humidity is vital for crops development. High humidity leads to issues like tissue damage and disease spread, while low humidity stresses plants and hampers photosynthesis. Monitoring and controlling humidity are essential for creating an ideal climate for crops development. This aspect is commonly referred to as[73]:

$$\psi^{H^{in}}[k+1,n_p] = \psi^{H^{in}}[k,n_p] + \frac{L^{in}[k+1,n_p]\cdot P_{atm}\cdot 100\%}{c_1 - (c_3 e^{c_4\psi^{\text{Tin}}[k,n_p]} - c_2)\cdot c_5} \tag{3.34}$$

$$L^{in}[k+1,n_p] = L^{in}[k,n_p] + \frac{\Delta t.S_g}{V^{gh}\rho^a}\Bigg[\underbrace{C^{ev}_r}_{evap} + \underbrace{J^{ven}[k,n_p]\ldots}_{ventilation}\underbrace{(L^{out}[k,n_p] - L^{in}[k,n_p])}_{ventilation}$$
$$+\underbrace{\beta_{fog}[k,n_p]L^{fog}_{\max}}_{fogging} - \underbrace{\beta_{deh}[k,n_p]L^{deh}_{\max}}_{dehumidific}\Bigg] \tag{3.35}$$

$$L^{out}[k,n_p] = \frac{c_5 \delta^{H^{out}}[k,n_p]}{P_{atm}} c_1 \cdot (c_3 e^{c_4 \delta^{T^{out}}[k,n_p]} - c_2) \tag{3.36}$$

$$P^{fog}[k,n_p] = \beta^{fog}[k,n_p] \cdot P_r^{fog} \tag{3.37}$$

$$P^{deh}[k,n_p] = \beta^{deh}[k,n_p] \cdot P_r^{deh} \tag{3.38}$$

where $\psi^{H^{in}}[k]$ represents the indoor humidity level of the greenhouse, P_{atm} is the atmospheric air pressure, and c_1 through c_5 are constants. S_g and V^{gh} are the surface area and volume of each greenhouse, and C_r^{ev} is the crop evaporation rate. ρ^a is the air density, $\alpha^{fog}[k]$ is the operational status of the fogging system, and $L_{\max}^{deh}$ and $L_{\max}^{fog}$ are the maximum water flow rates of the dehumidifier and fogger, respectively. $\alpha^{deh}[k]$ is the operational status of the dehumidifier, while $L^{out}[k]$ and $\delta^{H^{out}}[k]$ represent the outdoor humidity level of the greenhouse. $P^{fog}[k]$ and P_r^{fog} are the power consumed and the rated power of the fogging system, respectively, and $P^{deh}[k]$ and P_r^{deh} are the power consumed and the rated power of the dehumidifier, respectively. The indoor humidity must be maintained in a certain range as follows:

$$\forall [k,n_p] \begin{cases} \psi^{H^{in},\min}[k,n_p] \le \psi^{H^{in}}[k,n_p] \le \psi^{H^{in},\max}[k,n_p] \\ P^{fog,\min}[k,n_p] \le P^{fog}[k,n_p] \le P^{fog,\max}[k,n_p] \\ P^{deh,\min}[k,n_p] \le P^{deh}[k,n_p] \le P^{deh,\max}[k,n_p] \\ \beta_{fog}[k,n_p] \in [0,1] \\ \beta_{deh}[k,n_p] \in [0,1] \end{cases} \tag{3.39}$$

3.1.6 Dynamic Nutrient Supply During Growth Stages

To get the best possible growth from the plants, we mixed up a complete fertilizer solution and sent it out through the irrigation system from the main water tank. The goal was to supply all the key macronutrients the plants needed: nitrogen (N), phosphorus (P), potassium (K), calcium (Ca), and magnesium (Mg). We used water-soluble fertilizers to get the concentrations just right. Throughout the trial, we didn't keep the nutrient levels the same the whole time. We adjusted the nutrients on the fly, giving the plants what they needed when they needed it for every phase of growth. For example, during vegetative growth and fruit formation, the nutrient demands were different. Table.3.1 shows the amount of each nutrient supplied during the different growth phases in our greenhouse. These quantities are based on Marcussi et al[74].

Table 3.1: Total nutrient requirement (g) per greenhouse during each growth phase.

Phase	Days	N (g)	K (g)	Ca (g)	Mg (g)	P (g)
E.G	50	128.0	80.0	64.0	24.0	9.6
V	32	352.0	192.0	96.0	40.0	22.4
F	15	160.0	144.0	112.0	40.0	32.0
F.F	49	320.0	448.0	112.0	80.0	35.2
M.F	15	96.0	160.0	32.0	24.0	12.8

3.1.7 Power Balance

The proposed system includes renewable generators, and it is connected to the main electric grid, allowing the energy exchanges in both cases of excess or shortage in local energy production. By defining $P_{grid}^{buy}[k]$ and $P_{grid}^{sold}[k]$ are purchased and sold power from/to the grid, The dynamic of power

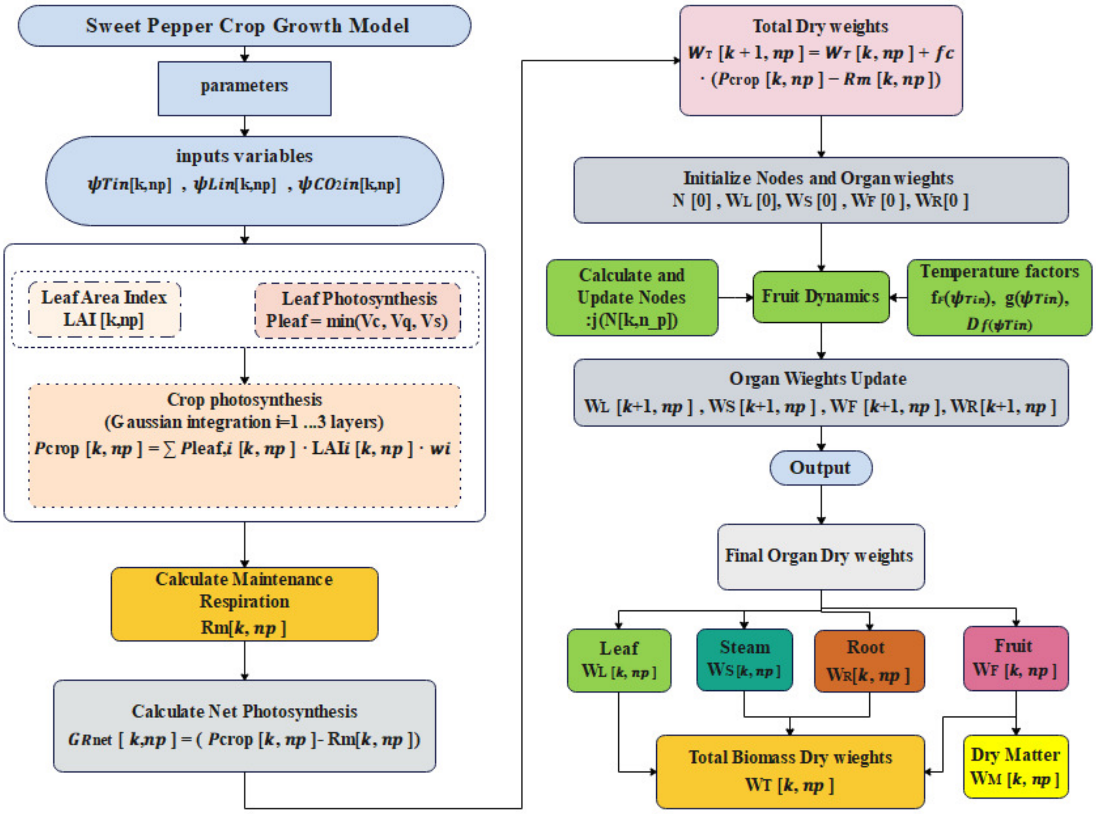

Figure 3.3: Diagram of the proposed sweet pepper growth model

balance can be expressed in MPC format as:

$$\underbrace{P_{pv}[k,np] + P_{wind}[k,np]}_{Renewable\ \ Power} + \underbrace{P_{grid}^{buy}[k,np] - P_{grid}^{sold}[k,np]}_{Grid} = \underbrace{P^{ch}[k,np] - P^{dch}[k,np]}_{Battery}$$
$$\underbrace{P_{water}^{m}[k,np] + P_{water}^{l}[k,np] + P^{hvac}[k,np] + P^{CO2}[k,np] + P^{art}[k,np] + (P^{fog} + P^{deh})[k,np]}_{Greenhouse\ \ Load} \tag{3.40}$$

The power exchanged with the grid must adhere to this constraint and be maintained within a certain range, which also depends on time.

$$\forall[k,n_p] \begin{cases} P_{grid}^{\text{sold}}[k,n_p] \cdot P_{grid}^{\text{buy}}[k,n_p] = 0 \\ P_{grid}^{\text{sold,min}}[k,n_p] \leq P_{grid}^{\text{sold}}[k,n_p] \leq P_{grid}^{\text{sold,max}}[k,n_p] \\ P_{grid}^{\text{buy,min}}[k,n_p] \leq P_{grid}^{\text{buy}}[k,n_p] \leq P_{grid}^{\text{buy,max}}[k,n_p] \end{cases} \tag{3.41}$$

3.2 Sweet Pepper Growth Model

In this study, sweet pepper growth was simulated using the general model originally presented in [75] and [70]. The model was adapted for Mediterranean conditions based on calibrations from [75]. It describes the crop using five state variables: fruit dry matter (W_F), mature fruit (W_M), node count (N), leaf area index (X_{LAI}), and total plant dry weight (W_T). This last variable depends on other components: leaf dry weight (W_L), stem dry weight (W_S), root dry weight (W_R), and fruit dry matter as described in equation (3.58). The architecture of the proposed sweet pepper growth model has been described in Fig.3.3.

3.2.1 Crop photosynthesis

Using the Gaussian method, crop photosynthesis P_{crop} is calculated as the sum of the leaf photosynthesis P_{leaf} rate per canopy leaf area index LAI:

$$P_{crop}[k, n_p] = \sum_{i=1}^{3} P_{\text{leaf},i}[k, n_p] \cdot \text{LAI}_i[k, n_p] \cdot w_i \tag{3.42}$$

where w is canopy layers wieghts $w = [0.5556, 0.8889, 0.5556]$

Leaf area index

The one-sided green leaf area per unit ground area in broadleaf canopies is called the leaf area index LAI, and it usually ranges from 0 to 6. LAI is a standard for crop growth and forecasts photosynthetic primary output. It may be computed in this way:

$$LAI_i[k, n_p] = 0.5 \cdot \left[LAI_{\max} \cdot \left(\frac{LAI_{\min}}{LAI_{\max}} \right)^{\exp\left(-C_{lai} \cdot \psi^{Tin}[k, n_p]\right)} \right] \cdot (1 - x_i) \tag{3.43}$$

where $LAI_{\max}, LAI_{\min}$ and C_{lai} are the maximum, minimum, and growth coefficient leaf area index, respectively.

Leaf photosynthesis

Leaf photosynthesis is calculated using LAI and climatic variables. The CO_2 assimilation by the Rubisco enzyme is determined as follows:

$$P_{\text{leaf},i}[k, n_p] = \min(V_c[k, n_p], V_q[k, n_p], V_s)$$

$$V_c[k, n_p] = V_{\text{cmax}} \cdot \frac{c_{in} \cdot \psi^{\text{CO}_2^{\text{in}}}[k, n_p] - \Gamma}{c_{in} \cdot \psi^{\text{CO}_2^{\text{in}}}[k, n_p] + K_c \cdot \left(1 + \frac{O}{K_o}\right)} \tag{3.44}$$

$$V_q[k, n_p] = e_q \cdot \alpha_l \cdot I_{\text{par,i}}[k, n_p] \cdot \frac{c_{in} \cdot \psi^{\text{CO}_2^{\text{in}}}[k, n_p] - \Gamma}{c_{in} \cdot \psi^{\text{CO}_2^{\text{in}}}[k, n_p] + 2 \cdot \Gamma} \tag{3.45}$$

$$I_{\text{par},i}[k, np] = \psi^{Lin}[k, np] \cdot \exp(-k_{\text{light}} \cdot LAI_i[k, n_p]) \tag{3.46}$$

$$V_s = \frac{V_{\text{cmax}}}{2} \tag{3.47}$$

where V_{cmax} is the maximum carboxylation velocity of the enzyme, c_{in} is the intercellular CO_2 concentration, O is the partial pressure of O_2, and Γ is the CO_2 compensation point without dark respiration. The parameters K_c and K_o are the Michaelis-Menten constants for CO_2 and O_2, respectively. e_q is quantum efficiency for CO_2 fixation, α_l is the leaf absorption for PAR, and I_{par} is the PAR flux incident on a unit leaf area. The intercellular CO_2 concentration c_{in} is calculated from the CO_2 concentration in the greenhouse and k_{light} light extinction coefficient.

3.2.2 Maintenance respiration

Plant maintenance respiration $R_{m,r}$ uses some of the carbohydrates from photosynthesis to supply energy for the maintenance of existing biostructures.

$$R_m[k, np] = R_{m,r}[k, np] \cdot 2^{\left[\frac{\psi^{\text{Tin}}[k, n_p] - \psi_r^{\text{T}}}{10}\right]} \tag{3.48}$$

$$R_{m,r}[k, n_p] = 0.03 \cdot W_L[k, n_p] + 0.015 \cdot W_S[k, n_p] + 0.015 \cdot W_R[k, n_p] + 0.01 \cdot W_F[k, n_p] \tag{3.49}$$

where $R_{m,r}$ is the maintenance respiration rate at a reference temperature ψ_r^T of 25 (°C), and W is the dry weight of the organ , whose subscripts refer to leaves (W_L), stems (W_S), roots (W_R), and storage organs such as fruits (W_F), respectively.

3.2.3 Crop dry weight

The total dry weight is determined by adding the data after crop photosynthesis and maintenance respiration have been determined. Growth is thought to take a backseat to maintenance breathing. The assimilates generated by photosynthesis are deducted from the assimilates required for maintenance respiration. The remaining assimilates might be increased in dry weight. There is a CH_2O to dry weight conversion factor. The dry weight's temporal fluctuation is described as follows:

$$W_T[k+1,n_p] = W_T[k,n_p] + f_c \cdot \underbrace{\left(P_{\text{crop}}[k,n_p] - R_m[k,n_p]\right)}_{GR_{\text{net}}[k,n_p]} \tag{3.50}$$

where GR_{net} represent the Net Growth The weight of each plant organ is calculated by multiplying the daily total dry weight by the daily proportion of assimilates allotted to that organ after the total dry weight has been computed. The four fractions always add up to one.

3.2.4 Organs dry weight

$$W_L[k+1,n_p] = W_L[k,n_p] + f_L \cdot \Delta W_T[k,n_p] \tag{3.51}$$

$$W_S[k+1,n_p] = W_S[k,n_p] + f_S \cdot \Delta W_T[k,n_p] \tag{3.52}$$

$$W_R[k+1,n_p] = W_R[k,n_p] + f_R \cdot \Delta W_T[k,n_p] \tag{3.53}$$

The fractions of total dry leaves f_L and stems f_S are determined in the same manner as those of roots f_R , approximated by a sinusoidal function. The dry weight fraction allocated to fruits and roots is multiplied by the daily total dry weight to determine the dry weight of roots, respectively according to Sánchez-Molina [75].
The basic ripe fruit biomass model was used in this work to replicate the growth model. The original presentation in [70] and [69] was modified to account for the growing of sweet peppers. The evolution of fruit dry matter accumulation which depends of node development $j(N)$, functions that influence the partitioning of biomass to fruit $f_F(\psi^{Tin})$ and temperature stress function $g(\psi^{Tin})$ can be calculated as follows:

$$\begin{aligned} W_F[k+1,n_p] &= W_F[k,n_p] + \Delta k \left[G_{Rnet}[k,n_p]\alpha_{F,actual}[k,n_p]\right] \\ \alpha_{F,actual}[k,n_p] &= \alpha_F f_F(\psi^{Tin}[k,n_p]) \cdot \underbrace{\left[1 - e^{-\theta(N[k,n_p]-N_{PP})}\right]}_{j(N[k])} \cdot g(\psi^{Tin}[k] \end{aligned} \tag{3.54}$$

$$j(N[k,n_p]) = \begin{cases} 0, & if \quad N \leq N_{pp} \\ 1 - e^{-\theta(N[k,n_p]-N_{pp})}, & if \quad N > N_{pp} \end{cases} \tag{3.55}$$

where $G_{Rnet}[k]$ is the maximum value of the difference between crop photosynthesis and maintenance respiration, which is determined by Sánchez-Molina[75] and depends on solar radiation and atmospheric CO2 levels, α_F is the maximum partitioning coefficient of new growth to fruit, and the term $j(N)$ represents the node development factor dependent on the θ transition coefficient between vegetative and full fruit growth and N as the number of nodes at time step and of N_{pp} node number at first fruit appearance. The functions that influence the partitioning of biomass to fruit are $f_F(\psi^{Tin})$ and the function $g(\psi^{Tin})$, which inhibits growth when high temperatures ψ^{Tin} occur are explained in the following way:

$$f_F(\psi^{Tin}[k,n_p]) = \begin{cases} 0, \quad if \quad \psi^{Tin} < 10 \text{ or } \psi^{Tin} > 35 \\ \left[\dfrac{\psi^{T}_{part} - \psi^{Tin}[k]}{2 \times 14}\right]^2 if \;\; 10 \leq \psi^{Tin} \leq \psi^{Tin}_{part} \\ \max\left[0,\ 1 - \left(\dfrac{\psi^{Tin}[k] - \psi^{T}_{part}}{11}\right)^2\right], \\ if \;\; \psi^{T}_{part} < \psi^{Tin} \leq 35 \end{cases} \tag{3.56}$$

$$g(\psi^{Tin}[k,n_p]) = \begin{cases} 1, & if \quad \psi^{Tin} \leq \psi_h^T \\ \max\left[0.3,\ 0.9(\psi^{Tin}[k] - \psi_h^T)\right], & if\ \psi^{Tin} > \psi_h^T \end{cases} \tag{3.57}$$

where ψ_{part}^T is optimal temperature for partitioning and ψ_h^T represents a high temperature threshold. The many functionalities of the model are summarized in Table(3.2).

The total plant dry weight is the sum of all organs described as follows:

$$W_T[k+1,n_p] = W_T[k,n_p] + \left(W_L[k,n_p] + W_S[k,n_p]\ + W_R[k,n_p] + W_F[k,n_p]\right) \tag{3.58}$$

where W_T is the total biomass plant dry weight, W_L is the dry weight of leaves, W_S is the dry weight of stems, W_R is the dry weight of roots, and W_F is the total dry weight of fruits, including mature fruits.

Table 3.2: Effect of Climatic Functions on Crop Growth

Function	Description	Affects
$j(N)$	reduces the growth of vegetation	N
$f_F(\psi^{Tin})$	changes the partitioning to fruit	W_F
$g(\psi^{Tin})$	decreases fruit growth when $\psi^{Tin} > 31°C$.	W_F
$D_f(\psi^{Tin})$	modifies the rate at which fruit develops.	W_M

3.2.5 Mature fruit biomass

The accumulation of mature fruit biomass is the most significant state variable in the model for the optimization issue as it reflects the development of mature sweet pepper. It uses the following equation to be computed in discrete time:

$$W_M[k+1,n_p] = W_M[k,n_p] + \Delta k\left[D_f(\psi^{Tin}[k,n_p])\left(W_F[k,n_p] - \ W_M[k,n_p]\right)\delta[k,n_p]\right]$$
$$\delta[k,n_p] = \begin{cases} 0, & \text{if } N[k,n_p] \leq N_{pp} + h_n \\ 1, & \text{if } N[k,n_p] > N_{pp} + h_n \end{cases} \tag{3.59}$$

where ψ^{Tin} is the indoor temperature, N_{pp} is the number of nodes on a plant when the first fruit shows up, h_n is the time (in nodes) it takes for that fruit to mature from appearance, and $D_f(\psi^{Tin})$ represents how greenhouse temperatures affect fruit development of sweet pepper as follows:

$$D_f(\psi^{Tin}[k,n_p]) = \begin{cases} 0, & if\ \ \psi^{Tin} < \psi_{dev}^{Tmin} \text{ or } \psi^{Tin} > \psi_{dev}^{Tmax} \\ \left[\dfrac{\psi^{Tin}[k] - \psi_{dev}^{Tmin}}{\psi_{dev}^{T} - \psi_{dev}^{Tmin}}\right]^{0.8}, & \psi_{dev}^{Tmin} \leq \psi^{Tin} \leq \psi_{dev}^{T} \\ \left[\dfrac{\psi_{dev}^{Tmax} - \psi^{Tin}[k]}{\psi_{dev}^{Tmax} - \psi_{dev}^{T}}\right]^{0.8}, & \psi_{dev}^{T} < \psi^{Tin} \leq \psi_{dev}^{Tmax} \end{cases} \tag{3.60}$$

where ψ_{dev}^T is optimal temperature for fruit development, and ψ_{dev}^{Tmin} and ψ_{dev}^{Tmax} are minimum and maximum for fruit development.

Table 3.3: Parameters sweet pepper crop growth model

Symbol	Description	Value	Units
LAI_{max}	Maximum Leaf Area Index	6.7	$(\mathrm{m^2\,m^{-2}})$
LAI_{min}	Minimum Leaf Area Index	0.3	$(\mathrm{m^2\,m^{-2}})$
C_{lai}	LAI growth rate coefficient	0.0017	(–)
c_{in}	Intercellular CO_2 concentration	0.7	$(\mathrm{\mu mol\,mol^{-1}})$ (ppm)
V_{cmax}	Maximum carboxylation velocity	200	$(\mathrm{\mu mol\,mol^{-1}\,s^{-1}})$
K_c	Michaelis-Menten constant for CO_2	300	$(\mathrm{\mu mol\,mol^{-1}})$ (ppm)
K_o	Michaelis-Menten constant for O_2	300	$(\mathrm{mmol\,mol^{-1}})$
O	Oxygen partial pressure	210000	$(\mathrm{\mu mol\,mol^{-1}})$ (ppm)
Γ	CO_2 compensation point	38	$(\mathrm{\mu mol\,mol^{-1}})$ (ppm)
e_q	quantum efficiency for CO_2 fixation	0.063	(−)
α_l	Leaf absorptance for PAR	0.78	(–)
k_{light}	Light extinction coefficient	0.55	(–)
ψ_r^T	Reference temperature for maintenance respiration	25	(°C)
f_c	CH_2O to dry weight conversion factor	0.29	(–)
α_F	Maximum partitioning coefficient to fruit	0.65	(–)
θ	Transition coefficient between vegetative and full fruit growth	0.15	(–)
N_{pp}	Node number at first fruit appearance	18	(–)
ψ_{part}^T	Optimal temperature for partitioning	25	(°C)
ψ_h^T	High temperature threshold for growth inhibition	31	(°C)
ψ_{dev}^T	Optimal temperature for fruit development	22	(°C)
ψ_{dev}^{Tmin}	Minimum temperature for fruit development	12	(°C)
ψ_{dev}^{Tmax}	Maximum temperature for fruit development	35	(°C)

3.3 Optimization Problem

The goal of the multiobjective optimization problem, which has a quadratic cost function, is to regulate the microclimate in the greenhouse while enhancing overall system functionality. The first part of the objective function minimizes deviations from reference signals and desired indoor microclimate variables. It also accounts for equipment load consumption and aims to reduce power exchanges with the main grid, particularly by limiting purchases and encouraging sales, as reflected in the third term. The final term focuses on minimizing deviations from reference nutrient demands.

3.3.1 Objective Function and Constraints

The complete objective function is defined as follows:

$$J^* = \min\Bigg(\sum_{k=1}^{n_p}\left[\alpha_1\phi^Q[k] + \alpha_2\psi^T[k] + \alpha_3\psi^L[k] + \alpha_4\psi^C[k] \ + \alpha_5\psi^H[k] + \alpha_6(m[k] - m_{ref}[k])^2\right] + \sum_{k=1}^{n_p}\alpha_7\left[P_{\text{grid}}^{\text{buy}}[k] - P_{\text{grid}}^{\text{sold}}[k]\right] + \sum_{k=1}^{n_p}\alpha_8 P_{Gh}^{\text{load}}[k] + \sum_{k=1}^{n_p}\sum_{z\in\{\text{Nut}\}}\alpha_9\left(\chi_z^{\text{nut}}[k] - \chi_{z,\text{ref}}^{\text{nut}}[k]\right)^2\Bigg) \tag{3.61}$$

$\{\text{Nut}\} = \{N, P, K, Ca, Mg\}_{(3.1)}$

$$\text{subject to: } \Omega^* = \left\{\begin{array}{l}\text{Constraints: (3.18),(3.20), (3.25), (3.27),}\\ \text{(3.30),(3.33),(3.39), (3.41),(3.60),(3.56),(3.57).}\\ \forall[k, n_p]\end{array}\right\} \tag{3.62}$$

where : $\phi^Q[k] = (Q^l[k] - Q^l_{\text{ref}}[k])^2$,
$\psi^T[k] = (\psi^{Tin}[k] - \psi^{Tin}_{ref}[k])^2$,
$\psi^L[k] = (\psi^{Lin}[k] - \psi^{Lin}_{ref}[k])^2$,
$\psi^H[k] = (\psi^{Hin}[k] - \psi^{Hin}_{ref}[k])^2$,
$\psi^C[k] = (\psi^{CO_2^{in}}[k] - \psi^{CO_2^{in}}_{ref}[k])^2$ and $\alpha^1, ..., \alpha_9 = 1$ are weighting parameters used to trade off the various components of the objective function. The same value = 1 indicates that all objectives have the same priority. $P^{load}_{Gh}[k] = \left(P^m_{\text{water}}[k] + P^{\text{hvac}}[k] + P^{\text{art}}[k] + P^{\text{CO}_2}[k] + P^{\text{fog}}[k] + P^{\text{deh}}[k]\right)$ and The amount of nutrients required and their reference are $\chi^{nut}_z[k]$, $\chi^{nut}_{z,\text{ref}}[k]$, as stated in Table(3.1).

3.3.2 System benefits

In this study, the external electricity supply is represented by an interaction with the energy grid. The grid's energy purchase price is set at $C^{buy} = 0.33$ (€/kWh), while excess energy is sold back at $C^{sold} = 0.25$ (€/kWh). In order to reduce expenses and increase revenue from excess energy sales, this pricing model highlights the necessity of efficient energy management. The following formula is used to determine the system's advantages $S_{benefit}$ (€):

$$S_{benefit}[k, n_p] = \left[C^{sold} \cdot P^{sold}_{grid}[k, n_p] \ - \ C^{buy} \cdot P^{buy}_{grid}[k, n_p]\right]\Delta k \tag{3.63}$$

3.4 Case Study and Numerical Results

3.4.1 Case Study Application

The MPC-based optimization problem is formulated based on the system modeling described in Sections 3.1 and 3.3. It is implemented and simulated in Python over a period of 161 days, covering the different phases of growth: early growth (E.G.), vegetative (V), flowering (F), fruit formation (F.F.), and mature fruiting (M.F.). The simulation applies a case study based on real data from the Savona weather station, which reflects the Ligurian Mediterranean climate Fig.3.2. The proposed MPC control strategy is applied to a smart greenhouse that is connected to the grid. The system includes a master pump that supplies water from the source to a water reservoir, a battery energy storage, and renewable generators such as wind turbines and photovoltaic modules. In this study, the smart greenhouse is assumed to be specifically designed for growing peppers, a crop that is particularly vulnerable to wind, cold, and frost during its vegetative and flowering stages. Table 3.4 presents the duration of each growth phase, along with the optimal indoor microclimate and water reference variables for each stage. These values were provided by Vertify, a company specialized in applied research in outdoor vegetables, greenhouse horticulture, arable farming in the Netherlands. Their expertise ensures reliable and practical insights for agricultural applications.

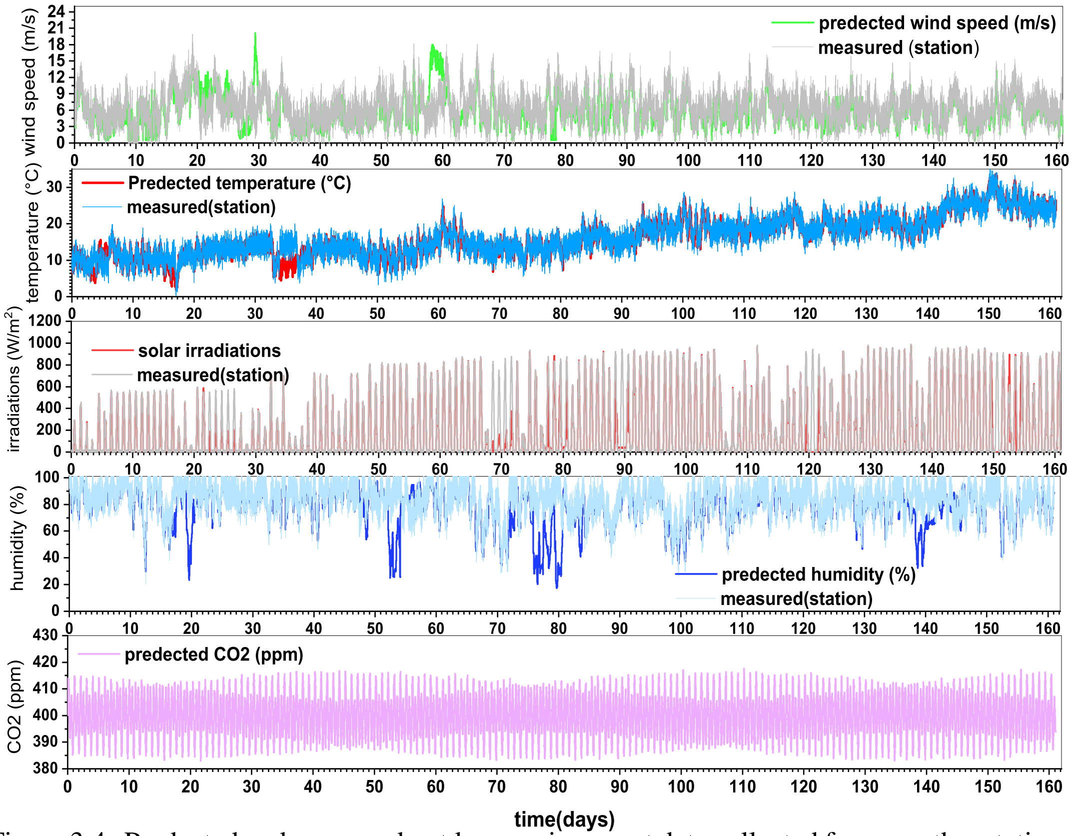

Figure 3.4: Predected and measured outdoor environment data collected from weather station Fig.3.2.

3.4.2 Simulation Setup

In this study, we trained a Random Forest algorithm using actual meteorological data from 2023 and 2024 (80% training, 20% testing, and 10% validation) to produce accurate forecasts utilized during the growth cycle (February 1, 2025, to July 10, 2025). At a 15-min time step, the model produced daily forecasts of outside environment variables. These predictions were then used as inputs to our NMPC framework and are depicted in Fig.3.4. However, the reference vector of internal microclimate expressing the optimal growth in different phases of growth of crops available in the greenhouse and nutrients needed are detailed in Table.3.4 and Table.3.1 with left values that represent nighttime and right values that represent daytime for temperature. It is anticipated that the irrigation water requirement per day is changing in each phase of growth. The total water needed per day was divided into irrigation for 15 minutes out of each hour in order to help the plant for an efficient absorption process. This is achieved through local pumps with an efficiency of 0.75, which are activated exclusively during the first time interval of each hour and remain switched off for the rest. The master pump efficiency is set at 0.8. However, h_m is configured to be equal to $12(m)$. Furthermore, the desired internal illumination, humidity, and CO_2 level are also assumed to be controlled. Although the GH is equipped with renewable energy production in the form of a PV system of 5 (kWh), a wind turbine of 15 (kWh), an battery energy storage with a maximum capacity of 50 (kWh), and a water reservoir of 5 (m^3), it is also connected to the grid. This connection allows the greenhouse to buy energy when needed and sell excess energy when available.

3.4.3 Numerical Results and Discussion

The performance of the system covering the water flow into the reservoir, the irrigation load, and the associated power use is shown in Fig.3.5. The master pump runs at its most efficient point to match the irrigation demand, especially during the critical flowering and fruit-setting stages. These are the periods when crops need a steady, reliable water supply to support things like cell growth, nutrient movement, and fruit development, all of which directly affect yield and quality. By keeping

Table 3.4: Microclimate and water references of pepper in different phases of growth

$Phase$	ψ^{Tin}_{ref} (°C)	$\psi^{Lin}_{art,ref}$ (W/m^2)	$\psi^{H^{in}}_{ref}$ (%)	$\psi^{CO_2^{in}}_{ref}$ [ppm]	$Q_{l,ref}$ (L/day)	$Q_{l,ref}$ (m^3/Δk)
$E.G$	[22-22]	36,2	70	600	140	0.0058
V	[22-28]	72,4	65	800	280	0,0116
F	[24-30]	108,6	62	850	420	0,017
$F.F$	[24-30]	117,65	67	850	420	0,017
$M.F$	[24-28]	117,65	62	850	280	0,0116
$Phase$		$E.G$	V	F	$F.F$	$M.F$
$Period(days)$		49	32	15	50	15

the water supply stable during these phases, the system not only meets the plants' physiological needs but also helps with overall water management efficiency, which you can see in Fig.3.5-a-c. Keeping the reservoir level close to the target setpoint supports this further; it ensures water is available when demand is highest, without wasting energy. Fig.3.5-b shows how the irrigation system behaves over time, along with the corresponding power consumption. The local pump performs well, accurately matching the irrigation demand while keeping power use in check across all growth stages. There's a very small deviation from the reference, which points to tight control, less energy wasted, and water delivery that actually matches what the crops need. As for the water storage reservoir, its dynamics are presented in Fig. 3.5-c. The reservoir undergoes repeated cycles of charging and discharging that correspond with the operation of the local and master pumps, starting with an initial volume of 2 (m^3). This cycle demonstrates how well coordinated the control approach is; the reservoir serves as a buffer, mitigating supply and demand fluctuations. As a consequence, the greenhouse has a consistent and reliable water supply, which enhances operational stability and resource efficiency. Optimal control decisions regarding indoor temperature, generated by MPC for cooling and heating along with their respective HVAC power consumption and coefficients of performance, are illustrated in Fig.3.6. It can be observed that the HVAC system operates within predefined power ranges to regulate the greenhouse's internal temperature, effectively responding to heat flux gains and heat flux losses due to ambient conditions, showing near-perfect tracking of reference temperature signals compared to the Gekko method throughout typical days across different important growth phases where the temperatures fluctuate between day and night temperatures, especially for vegetative (V), flowering (F), fruit formation (F.F), and mature formation (M.F). As shown in Fig.3.6-a, the indoor temperature closely follows the setpoint with only minor deviations. During the daytime, the HVAC operates in heating mode to compensate for heat losses and to achieve the needed high temperature, while nighttime requires cooling due to the dropping of reference temperatures and additional compensation for the absence of solar gains, as reflected in the coefficient of performance (C_{op}) shown in Figs.3.6-c. Positive C_{op} values correspond to cooling, and negative values to heating, with the MPC smoothly transitioning between modes without abrupt cycling. The system maintains close alignment with the reference signal across all phases, though brief deviations occur during periods of harsh external conditions, such as sudden wind speed and high outdoor temperature changes during the last days of mature fruit and microclimate fluctuations, which challenge real-time responses as described in Fig. 3.7. indicating that the MPC successfully balances disturbances while maintaining phase-specific requirements compared to the Gekko method, where temperature shows more deviation. The controller prioritizes precision during crucial reproductive phases like (F) and (F.F.) while preserving energy-efficient operation throughout, as demonstrated by the slight tracking faults found. When it comes to natural ventilation in the greenhouse, the opening angle typically ranges from 0 to 90 degrees. However, in our control strategy, we observed a minimal opening angle, as shown in Fig.3.8. This means the ventilation is deliberately kept closed to reduce heat and CO_2 losses, avoiding the extra energy that would otherwise be needed to compensate for excessive air exchange. Effective artificial illumination is essential for promoting healthy plant growth and increasing greenhouse yields. The MPC-based illumination tracking controls the lighting load while limiting power consumption, with operations illustrated in Figs.3.9-a-b-c. To optimize energy, the system switch off lighting during the day and relies on natural lighting of solar irradiations. At night, artificial lights are mostly powered by

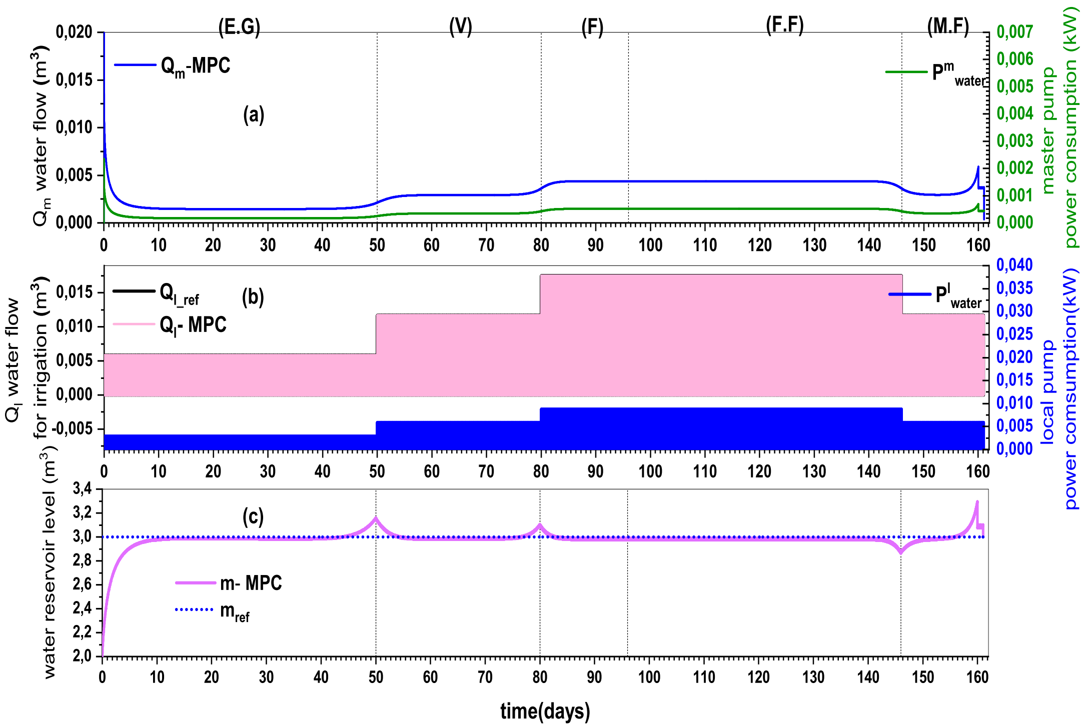

Figure 3.5: MPC-based water flows are pumped into the water reservoir with optimal tracking to meet irrigation needs with their pump power consumption and dynamics of water reservoir levels across whole growth phases.

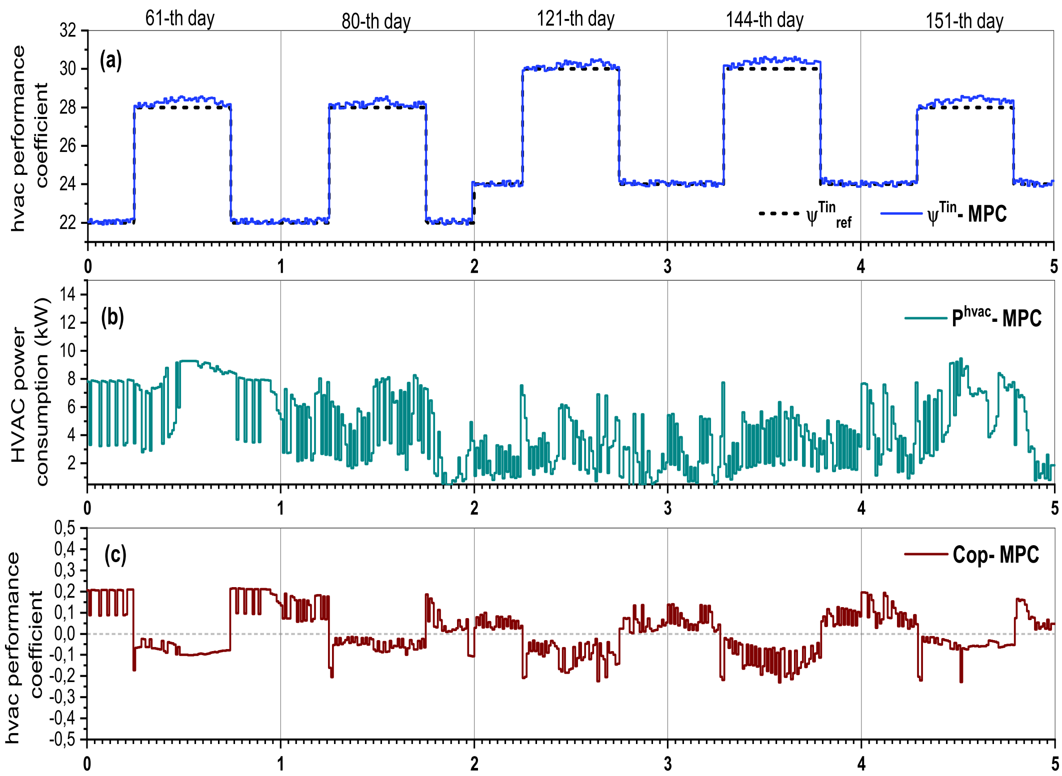

Figure 3.6: MPC-based optimal greenhouse indoor temperature with their HVAC power consumption and coefficient of performance over the typical days across different growth phases.

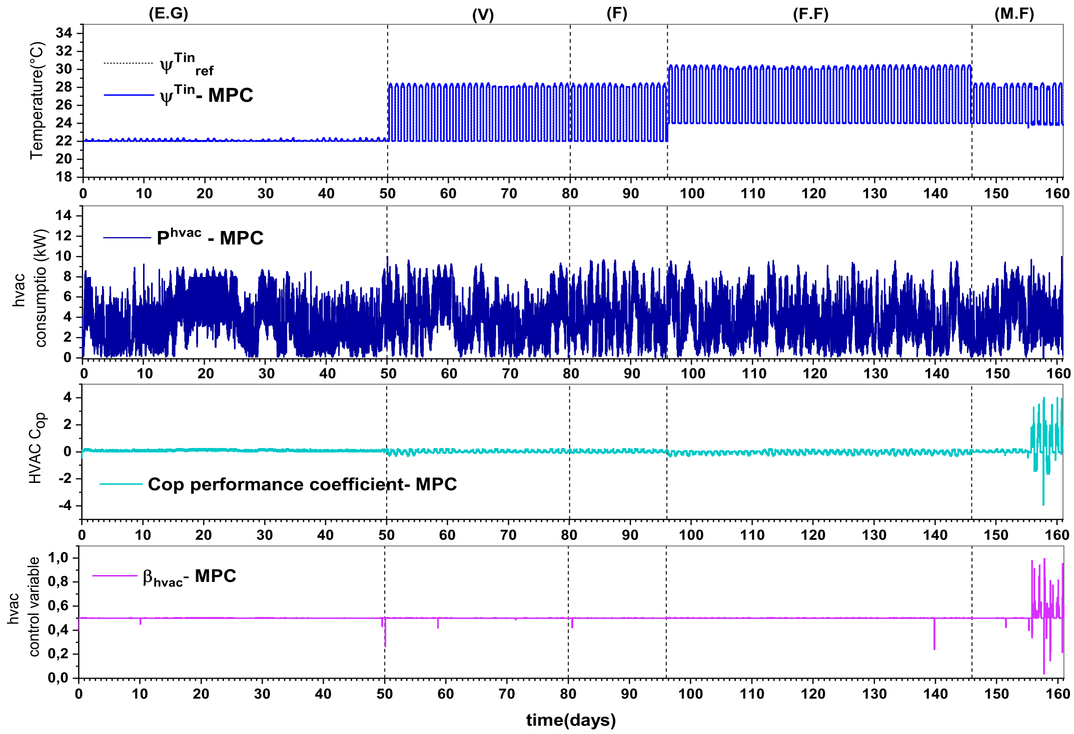

Figure 3.7: MPC-based optimal greenhouse indoor temperature with their HVAC power consumption and coefficient of performance over all growth phases.

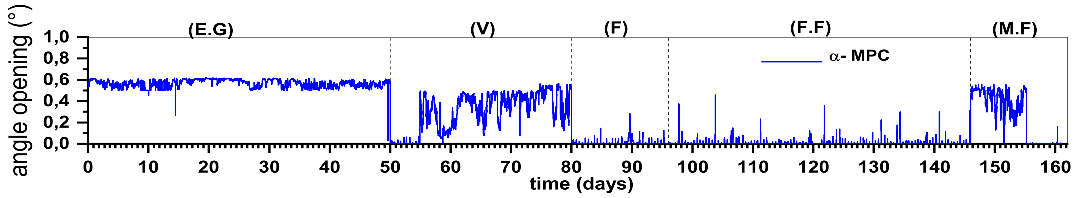

Figure 3.8: Optimal opening ventilation angle over whole phases of growth.

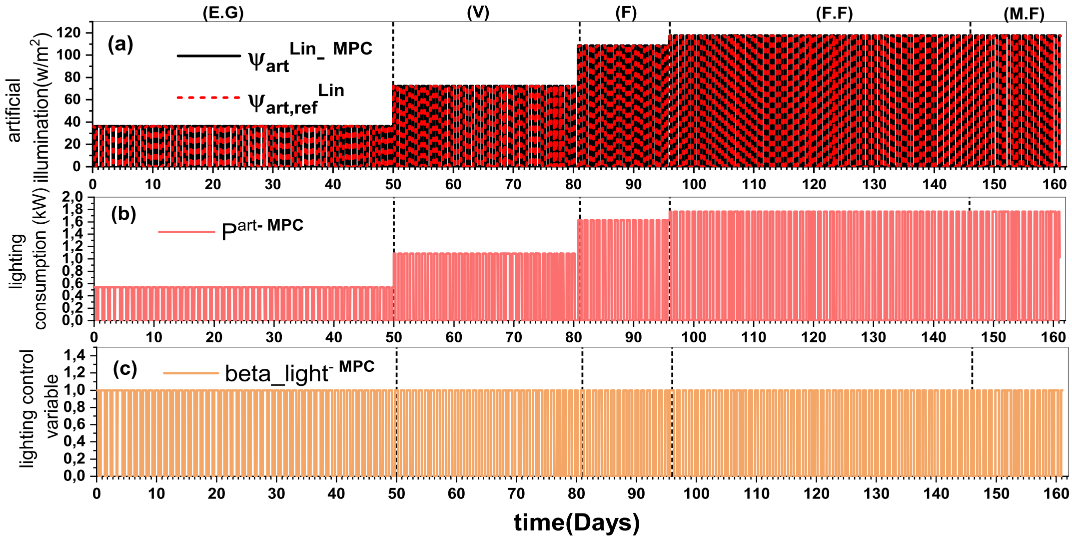

Figure 3.9: MPC-based optimal tracking of the illumination loads with their power consumption across whole growth phases.

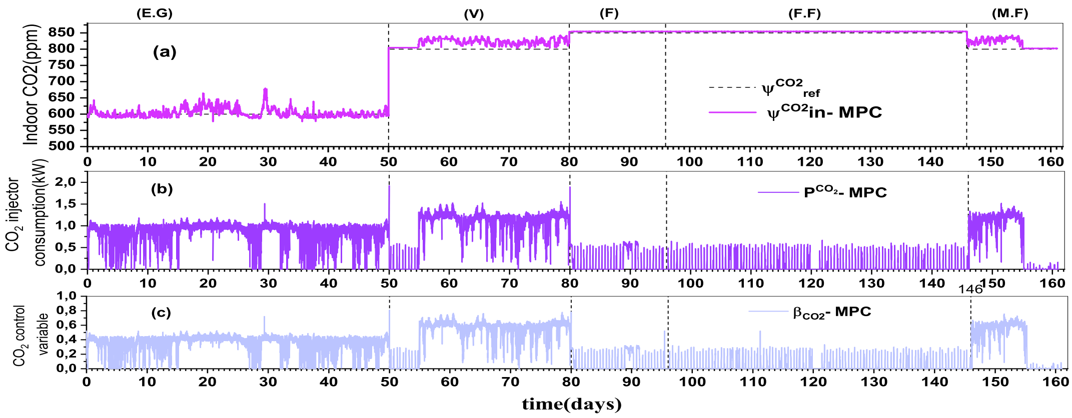

Figure 3.10: The MPC controls greenhouse CO_2 levels, managing the injector's power and operation across growth phases.

renewable energy sources, with the grid offering temporary backup power as necessary. Throughout the growth cycle, lighting levels also fluctuate. During the early growing period, the system uses low illumination to help seedlings establish without stress. It can be seen higher illumination during fruit formation and maturity to support flowering and fruit development. Running artificial lighting at night also offers benefits it allows photosynthesis during cooler hours and helps maintain consistent day night cycles. Figure.3.10-a-b illustrates the MPC-based optimal control of indoor CO_2 concentrations and injector power consumption at various stages of growth. The CO_2 setpoint is incrementally adjusted, commencing at 600 (ppm)) during the initial growth phase, subsequently increasing to 800 (ppm) during the vegetative stage, and ultimately reaching 850 (ppm) from flowering through fruit development. These higher levels help the plants photosynthesize more and produce better fruit yields. At the outset, the injector activates periodically to maintain a CO_2 level of roughly 600 (ppm). As the plants develop larger leaves, their demand for CO_2 increases, leading to more frequent injector operation throughout the day, coinciding with photosynthesis. The busiest period is during flowering and fruit formation, when the 850 (ppm) target gives the plants the boost they need to set flowers and grow fruits. Since plants only take in CO_2 during daylight, the injector stays off at night. One thing worth noting is CO_2 levels sometimes go above the target during fruit formation. That's probably because the ventilation is reduced and the plants are respiring at night, causing a bit of a buildup. By the time the plants reach maturity, the system settles down and keeps things steady without wasting energy. The results of the MPC-based optimal state of relative humidity, along with the corresponding power consumption of the fogger and dehumidifier and their operational status across the whole growth

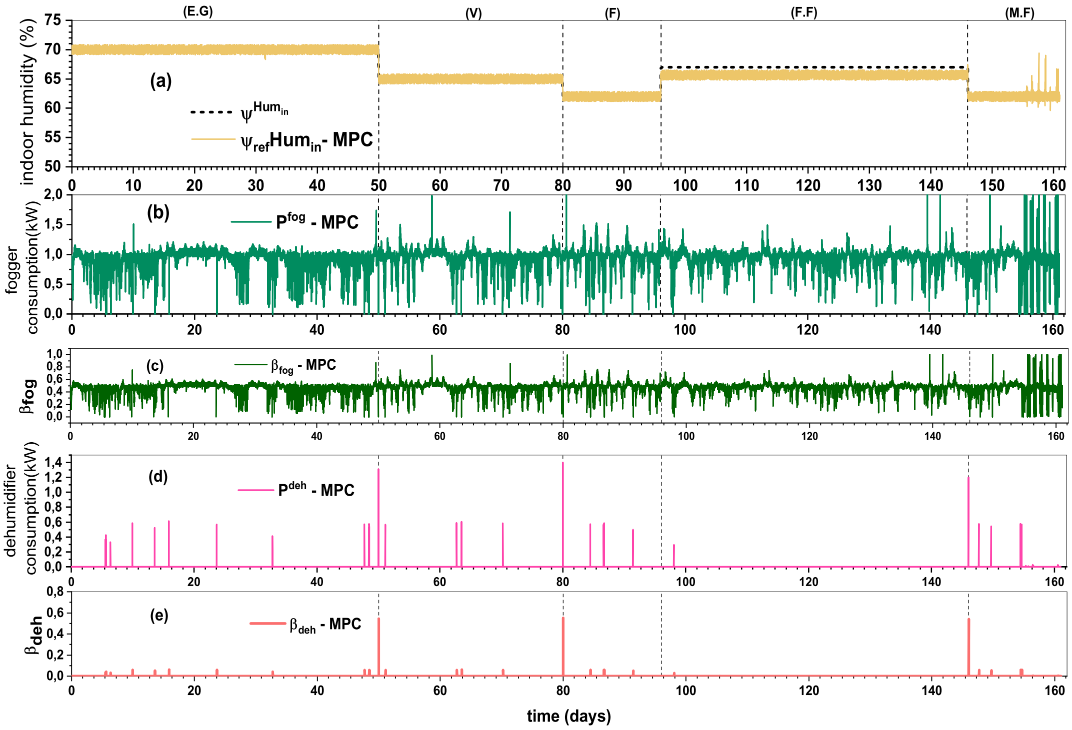

Figure 3.11: MPC-based optimal relative humidity inside the greenhouse with optimal power consumed by the fogger and dehumidifier across whole growth phases.

phases, are shown in Fig.3.10. The controlled indoor humidity consistently tracks the reference value, which is fixed at 70(%) during the early growth phase to help young plants with limited root systems stay hydrated, keep their stomata open for photosynthesis, and protect delicate leaves from water stress. Minimal deviations occur due to small fluctuations in indoor temperature. During the other growth phases, relative humidity stays between 61(%) and 68(%), closely aligning with the reference values at night. However, a slight drop happens during the fruit formation phase, mainly because of dynamic high temperature fluctuations inside the greenhouse, as shown in Fig.3.11-a. This is a physically expected trend given the inverse relationship between humidity and temperature compared to nighttime conditions. This regulation is achieved through the optimized operation of the fogger and dehumidifier (Fig.3.11-b-c, d-e). The dehumidifier runs at full power toward the end of the early growth phase to remove humidity, as well as during the end of the vegetative and fruit formation stages, mainly because the humidity setpoint drops during these periods. Meanwhile, the fogger operates to cool the greenhouse and boost humidity when needed. This is especially noticeable during fruit formation, where the dehumidifier stays off most of the time. The power production and results of the MPC-based optimal control of the battery energy storage (BES) within the microgrid, including its charging and discharging behavior and the power exchanged with the grid using rolling optimization, are shown in Figs.3.12-a-b-c and 3.12-d, respectively. In theory, the BES could help compensate for the intermittency of renewable energy sources. However, the implemented strategy prioritized selling energy over charging the battery, which limited how effectively it could play that role. As shown in Fig.3.12-b, the energy storage system exhibits various charging and discharging patterns depending on the power balance and the power exchanges with the grid. Looking at Fig.3.12-c, there are moments, especially on days like the $16th$, $61st$, and $100th$, which fall across different growth phases where the BES reaches its maximum stored energy level of 48 (kWh), then gradually decreases until it hits the minimum allowed value of 1 (kWh). This pattern can be explained by the greenhouse need for artificial lighting at those times combined with a lack of photovoltaic generation. Fig.3.12-d shows the power exchanged between the system and the grid. Throughout all growth periods, the system actually sold energy to the grid, even with all the greenhouse equipment running, thanks to the availability of renewable energy production, particularly between the $17th$ and $26th$ days. On the other hand, there were only brief periods when the system had to buy energy from the grid, and those happened when battery reserves were low due to limited renewable generation, for instance, between the $27th$

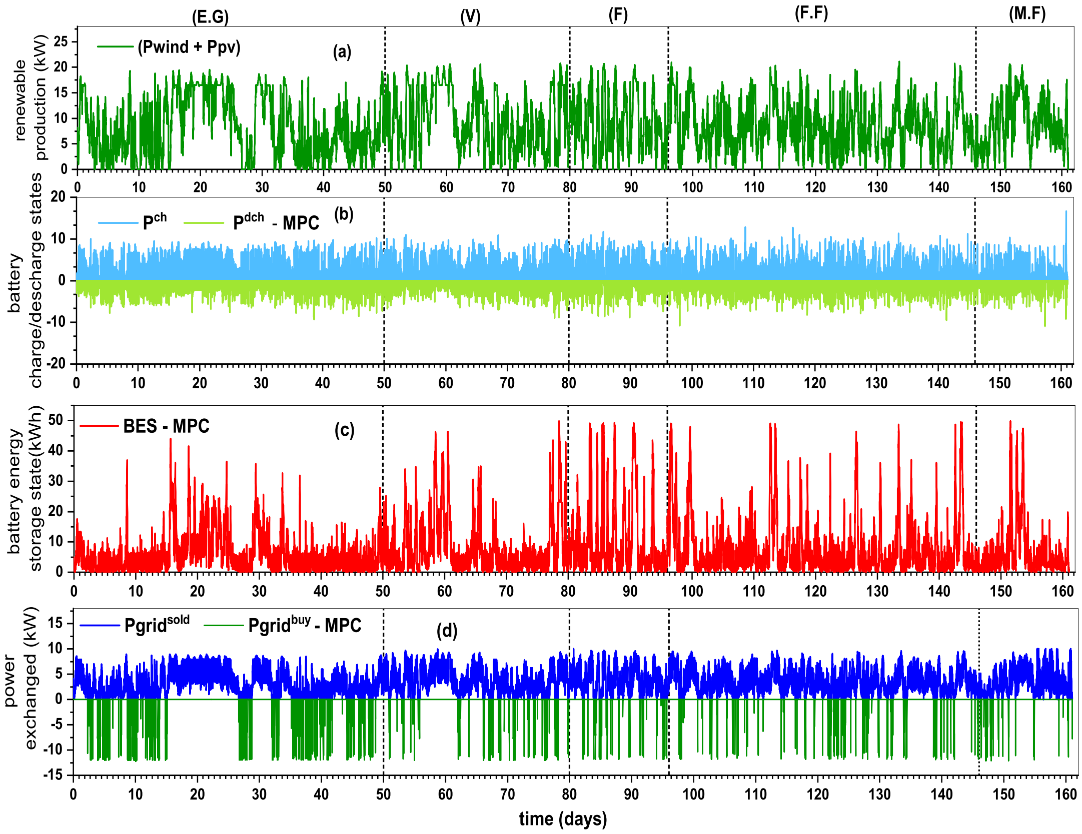

Figure 3.12: Renewable power production, optimal power exchange with the grid, and dynamics of battery energy storage for whole growth phases.

and 29th days as an example. This overall pattern comes from having consistent wind available throughout the day along with daytime solar production. The energy storage unit responds adaptively, charging and discharging as needed to keep the power balance with the grid while reacting to changes in both energy supply and demand. This kind of intelligent cycling allows the system to maximize how much energy it exports while limiting imports to only those times when renewables fall short.

3.13 illustrates dry matter partitioning among leaves, stems, roots, fruits, and mature fruits over a

Table 3.5: Biomass Values per Component

Component	Value (g/m^2)	Value (kg/80 m^2)	Value (g/plant)
Leaf	3456.572	276.525	1152.190
Stem	1991.306	159.304	663.768
Root	1066.938	85.355	355.646
Fruit	6954.036	556.322	2318.012
Mature_Fruit	6389.261	511.140	2129.753
Total_Biomass	13 468.854	1077.508	4489.618

161-day growth cycle. The growth patterns match what I'd expect to see like in a real sweet pepper crop. During the initial (E.G.) and (V) phases (days [1–80]), biomass accumulation is exclusively vegetative. Leaves act as the dominant sink, increasing from 7.4 to 1462.3 [g/m^2], while stems and roots follow a similar exponential trajectory, which shows that the plant is focused on building its vegetative structure before it even thinks about fruit, which is logical; plants need a solid canopy and root system first. The transition to reproduction occurs during the Flowering (F) and Fruit Formation (F.F.) phases [days 82–146], marked by the emergence of fruit biomass around day 88. As fruits begin to accumulate, the leaf growth curve visibly plateaus, indicating a shift in carbon allocation from

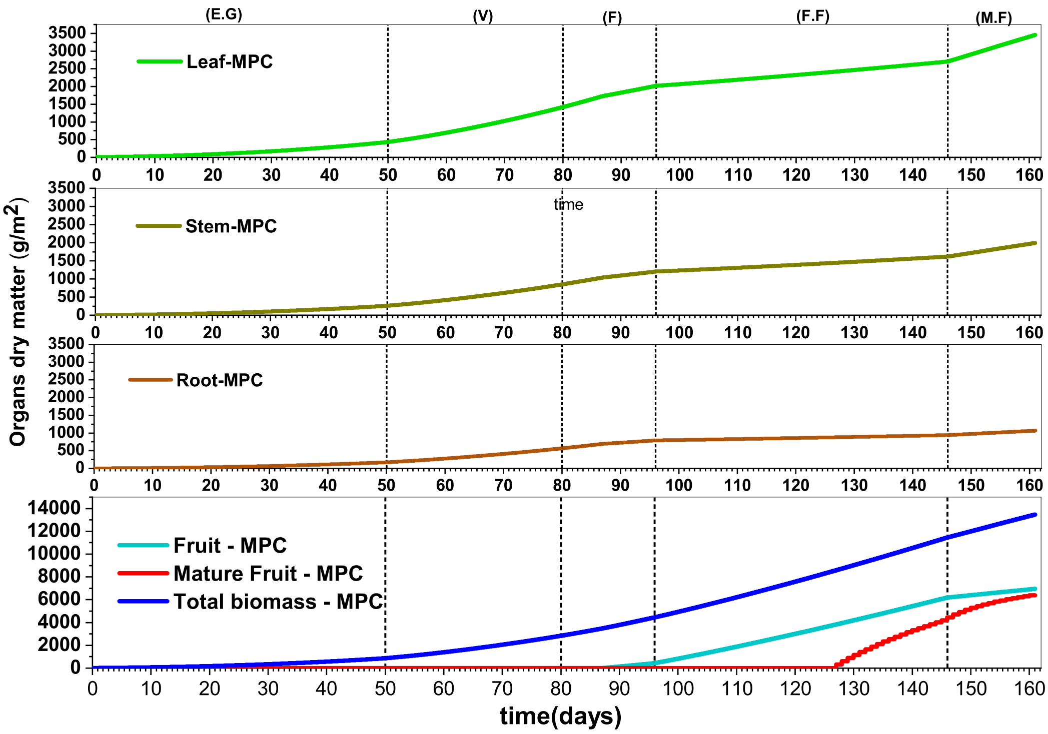

Figure 3.13: Accumulation of dry matter for each organ for sweet pepper at the whole phase of growth.

Table 3.6: Economic Benefits from Grid Exchange per Growth Stage

Phase growth (days)		**Energy** sold (€)	**Energy** buy (€)	**Benefits** (€)
E.G	[1 – 50]	3853.67	1581.23	2272.44
V	[50 – 81]	2818.69	1360.00	1458.69
F	[81 – 96]	1503.49	235.00	1268.49
F.F	[96 – 146]	4294.78	520.00	3774.78
M.F	[146 – 161]	1259.90	154.54	1136.36

Table 3.7: Biomass Production per Growth Stage

Phase growth (days)		**Leaf** [kg/Sc(m^2)]	**Stem** [kg/Sc(m^2)]	**Root** [kg/Sc(m^2)]	**Fruit** [kg/Sc(m^2)]	**Mature Fruit** [kg/Sc(m^2)]
E.G	[1 – 50]	34.76	20.77	13.86	0	0
V	[50 – 81]	113.41	67.96	45.32	0	0
F	[81 – 96]	161.59	96.35	63.37	34.55	0
F.F	[96 – 146]	216.46	129.27	75.34	495.11	335.26
M.F	[146 – 161]	276.52	159.30	85.35	556.32	511.14

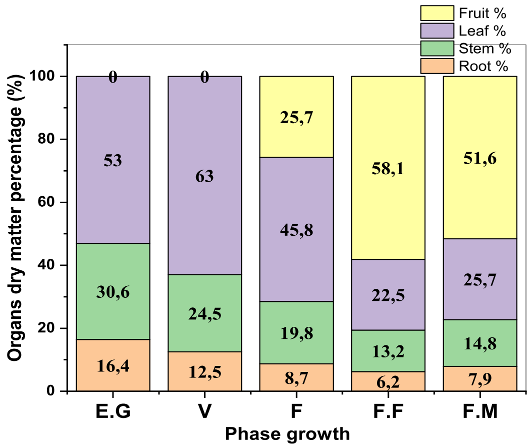

Figure 3.14: Percentage distribution of dry matter in each organ during different growth phase periods of sweet pepper.

leaf expansion to reproductive structures. By day 127, fruit biomass reaches 3824.9 (g/m^2), while leaves increase only modestly from 1462 to 2424 (g/m^2) over the same period. This competition for assimilates reflects the principle of sink strength, where developing fruits outcompete vegetative organs for photoassimilates. The microclimate during these phases, with increased light intensity 107 (W/m^2), which is around 600 (μmol, m^{-2}, s^{-1}), and elevated temperatures [24–30] (°C), is optimally configured to support flowering, pollination, and early fruit expansion. What also stands out is that mature fruit only starts appearing around day 128, about 40 days after the first fruit mass is recorded. That lag makes sense biologically because fruits take time to expand and ripen after fruit set. You can see total fruit accumulating well before any mature fruit shows up, which reflects that real green fruit stage. Overall, the model seems to be capturing the natural sequence of how peppers allocate dry matter over time, and the climate control strategy appears to be supporting that process as it should. The percentage distribution of dry matter at each organ during different growth phase periods of sweet pepper is presented in Fig.3.14. It can be seen that the plants are going through a very natural life cycle. In the early stages, the young plant is putting most of its energy into building leaves over half of its biomass, which makes perfect sense because it needs to establish a strong canopy to capture light. The roots and stems are developing too, but leaves are clearly the priority. The percentage of leaves actually increases to 63(%) when we enter the vegetative phase, indicating that the plant is really strengthening its photosynthetic apparatus before any fruit develops. Around day 88, the plant enters the blooming stage, which is when things start to get interesting. Fruit begins to form and consumes roughly 25(%) of the plant's energy, while leaves decrease to 45(%). The plant is starting to shift gears from just growing leaves to preparing for production. During fruit formation from day 97 to 146, the change is dramatic; fruit now dominates at 58(%), while leaves drop to just 22(%), which means that the plants are throwing everything they have into filling those peppers. What is special is during the final maturation phase, leaf percentage actually bounces back a bit to 25(%). That's a good sign the plants are maintaining enough leaf area to support the ripening process rather than letting them run out of steam. Overall, this distribution shows a plant that builds a solid foundation first, transitions smoothly into reproduction, and finishes strong without completely neglecting its leaves. That's exactly how a healthy, well-managed sweet pepper crop should behave. Table's.3.7 and 3.6 show the biomass distribution across the greenhouse area, telling an even clearer story. With 80 (m^2) of the cultivated area, the plants produced 276.5 (kg) of leaves, 159.3 (kg) of stems, 85.4 (kg) of roots, and most importantly, 556.3 (kg) of total fruit, of which 511.1 (kg) reached full maturity. This indicates that more than half a ton of marketable peppers were produced for every 80 (m^2). The plants effectively converted their robust vegetative basis into a sizable harvest while maintaining a healthy balance between leaves and fruit during the final ripening period. Table 3.6 shows the benefits of integrating a microgrid into a greenhouse system at all growth stages. Through energy trading, the system continued to provide positive advantages even in the early stages (days 1–81) when there was no fruit production, roughly 2272 (€) during early growth and 1458 (€) vegetatively. Fruit ($34.55kg/Sc$) arrives when flowering begins, and energy benefits remain at 1268 (€). Everything peaks during the fruit development period (days 96–146), with 495 (kg/Sc) of fruit output and 3774 (€) in energy benefits. In addition to an additional 1136 (€) via grid exchange, the crop reaches 556 (kg/Sc) total fruit, with 511 (kg/Sc) marketable by maturity. Unlike traditional greenhouses, which only make money at harvest, this microgrid system generates cash continually while still producing more than half a ton.

3.5 Conclusion

This study addressed the urgent need to improve water management and optimize energy consumption in greenhouses while maintaining crop growth and yield. We proposed a novel control framework based on model predictive control with a receding horizon to optimally manage greenhouse indoor microclimate while coordinating energy and water flows for irrigation, artificial lighting, CO_2 enrichment, dehumidification, ventilation, and heating. The optimization model incorporates uncertainties from renewable generation and loads, weather forecasts, electricity prices, and a discrete reward-based demand response scheme, enabling flexible operation throughout the entire growth cycle. The microgrid-powered greenhouse offers two clear benefits: important crop yields from optimal microclimate growing conditions, plus extra revenue from selling excess renewable energy to the grid. This dual advantage makes the approach both productive and economically viable.

4

Chapter 4

Distributed Control ADMM Algorithm for Connected Net Zero-Energy Farms Integrated Microgrids

This chapter addresses the limitations of conventional greenhouse management by developing a distributed optimization framework for networked agricultural systems (farms) integrated with microgrids. It identifies the research gap in existing approaches that treat microclimate parameters in isolation and proposes a coordinated strategy that accounts for system-wide interdependencies. Section 4.1 introduces the architectural design of interconnected net-zero energy farms that comprise greenhouses, residential buildings, and animal facilities. Section 4.2.2 presents the comprehensive mathematical model governing the coupled dynamics of water, temperature, humidity, CO_2 concentration, lighting, and ventilation within each greenhouse, along with power exchange constraints across the network. The methodological approach is detailed in Section 1, which explains the distributed optimization framework based on the Alternating Direction Method of Multipliers (ADMM) for real-time coordination among farms. Section 4.3 the experimental setup and case study used to validate the framework across multiple crop cycles under varying climatic conditions. Results demonstrate significant improvements in energy efficiency, resource utilization, and operational scalability compared to centralized and isolated optimization strategies, underscoring the benefits of cooperative management in sustainable agriculture. The chapter concludes with a summary of findings and future research directions in Section 4.4.

4.1 System architecture and modeling

The architectural framework is based on a network of collaborating farms that supply energy to an integrated system of smart greenhouses, animal buildings, and residential buildings. The network of interconnected farms is represented as a directed connected graph $G = \{M; L\}$, where $M = \{m_1, \dots, M\}$ is the vertex set defining farms, and $L = \{l_1, \dots, L\}$ are the links. Each farm integrated microgrid is connected to others, and at least one farm is linked to the main grid as shown in Fig.4.1. The greenhouses within the farm are denoted as $GH(m, n)$. Within this framework, each farm-integrated microgrid is composed of a set of intelligent greenhouses, residential and animal buildings, renewable energy generators (REG), advanced communication systems, a water reservoir, energy storage inventory (ESI), and a connection to the main grid. The interconnection among farms streamlines power exchanges, optimizing the utilization of local renewable resources. A power link establishes a connection between the clustered farms and the main grid, enabling power exchange in instances of excess or shortage, as described in Fig.4.2. Cooperative coordination is achieved through an advanced bidirectional communication infrastructure, employing a centralized and distributed ADMM-based algorithm approach to manage control signals. Each greenhouse operates as a microclimate unit, fostering optimal crop development through features such as artificial lighting, a CO_2 generator, heating and cooling systems, pumps, and natural ventilation. The main objective of these farms is to collaboratively balance power production and loads at the local network level.

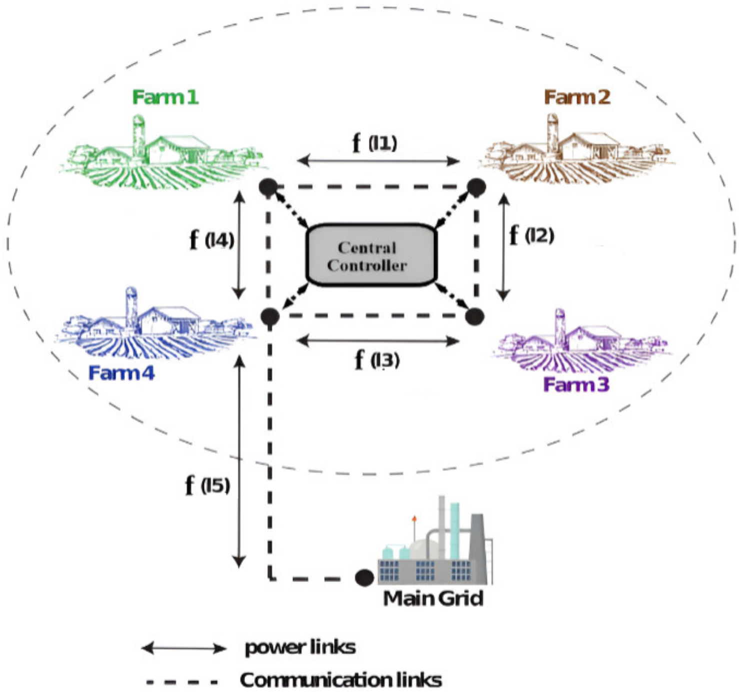

Figure 4.1: System design (centralized approach)

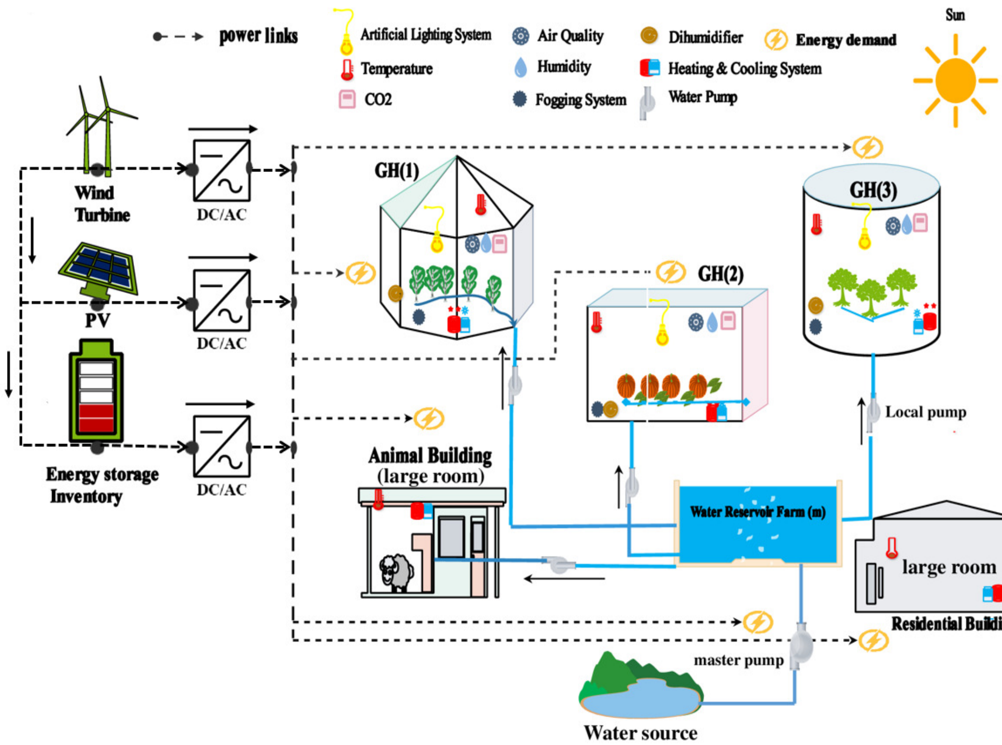

Figure 4.2: System design inside each farm(m).

4.1.1 Model of Renewable Energy Generators

In this study, photovoltaic (PV) panels and a wind turbine are employed as REG for energy production in each farm (m).

Wind Model

The wind turbine anticipated power production in each farm is calculated as follows[66]:

$$p_m^{wind}(t) = \begin{cases} 0 & w_m(t) < w_a \\ P_m^r\left(\frac{w_a}{w_a - w_r} + \frac{1}{w_r - w_a} w_m(t)\right) & w_a \le w_m(t) \le w_r \\ P_m^r & w_r \le w_m(t) \le w_b \\ 0 & w_m(t) > w_b \end{cases} \tag{4.1}$$

where the wind turbine power generated and wind speed are denoted by $p^{wind}m(t)$ (kW) and $wm(t)$ (m/s), respectively. The turbine rated power is P_m^r (kW). For cut-in, rated, and cut-out wind speeds, respectively, use w_a, w_r, and w_c (m/s).

PV Model

The PV system's power output for every farm can be calculated using the formula below[76]:

$$P_m^{\mathrm{pv}}(t) = A_{\mathrm{pv}}\, \eta_{\mathrm{pv}}\, P_f\, \eta_{\mathrm{pc}}\, G_m(t) \tag{4.2}$$

where η_{pv} and η_{pc} are module reference efficiency and power conditioning efficiency, respectively. A_{pv} represents the solar cell array area (m^2), $G_m(t)$ is the solar irradiance, and P_f is the packing factor.

4.1.2 Model of Water Reservoirs and Pumps

The dynamics of the water reservoir available in m-th farm is defined as follows:

$$L_m^{vr}(t + \Delta t) = L_m^{vr}(t) + [Q_m(t) - Q_m^{gh}(t) - Q_m^{ab}(t)]\Delta t \tag{4.3}$$

where $L_m^{vr}(t)$ is the volume of water in the reservoir(m^3). $Q_m(t)$ defines the water flows entering each reservoir in m-th farm (m^3/s), and $Q_m^{gh}(t)$ defines the sum of the water flows entering each greenhouse in m-th farm.

$$Q_m^{gh}(t) = \sum_{n=1}^{N} Q_{m,n}^{gh}(t) \tag{4.4}$$

$Q_m^{ab}(t)$ is the water flow entering the animal building.
The water flows are determined as a function of the power consumed by the pumps [77]:

$$Q_m(t) = \frac{u_m^{mp}(t)}{\rho_w g h_m^{mp}} \eta_m^{mp} \quad , \quad Q_{m,n}^{gh}(t) = \frac{u_{m,n}^{lp}(t)}{\rho_w g h_{m,n}^{gh}} \eta_n^{lp} \quad , \quad Q_m^{ab}(t) = \frac{u_m^{ab}(t)}{\rho_w g h_m^{ab}} \eta_m^{a} \tag{4.5}$$

where ρ_w is the water density (kg/m^3) and g is the gravity acceleration constant (m/s^2), $\eta^{mp}m$, $\eta^{lp}n$, and $\eta^{a}m$ are the pump efficiencies of master and local pumps at each farm, greenhouse, and animal building; $h^{mp}m$ is the difference in level height between the reservoirs of each farm and source of water (m). $h^{gh}m, n$ is the difference in height between the reservoir and plants of each greenhouse at the same farm (m), and $h^{ab}m$ is the difference in height between the reservoir and small tank existing at the animal building of each farm (m). $u^{mp}m(t)$ is the power consumed by the master pump that pumps water from water source to reservoir at the m-th farm (kW). $u^{lp}m, n(t)$ and $u_m^{ab}(t)$ are the powers consumed by the local pumps in order to pump water from reservoirs to greenhouses and animal buildings of each farm (kW).

4.1.3 Model of Thermal Comfort

Each greenhouse contains an HVAC system that is in charge of regulating the thermal comfort. It is important to note that the thermal comfort for residential and animal buildings is modeled for a single zone considered as a large room, rather than accounting for all individual zones within the buildings. The dynamics of the internal temperatures are defined as follows[78]:

$$T_{m,n}^{in,gh}(t+\Delta t) = T_{m,n}^{in,gh}(t) - \frac{\Delta t}{R_n^{gh} C_n^{gh}}((T_{m,n}^{in,gh}(t) - T_m^{out}(t)) + \eta_n^{gh} R_n^{gh} u_{m,n}^{h,gh}(t)) \tag{4.6}$$

$$T_m^{in,rb}(t+\Delta t) = T_m^{in,rb}(t) - \frac{\Delta t}{R_m^{rb} C_m^{rb}}((T_m^{in,rb}(t) - T_m^{out}(t)) + \eta_m^{rb} R_m^{rb} u_m^{h,rb}(t)) \tag{4.7}$$

$$T_m^{in,ab}(t+\Delta t) = T_m^{in,ab}(t) - \frac{\Delta t}{R_m^{ab} C_m^{ab}}(T_m^{in,ab}(t) - T_m^{out}(t)) + \eta_m^{ab} R_m^{ab} u_m^{h,ab}(t)) \tag{4.8}$$

where $T_m^{out}(t)$ is the outdoor temperature of the farms $(°C)$, $T_{m,n}^{in,gh}(t)$, $T_m^{in,rb}(t)$, and $T_m^{in,ab}(t)$ are the indoor temperatures in greenhouses, residential buildings, and animal buildings, respectively $(°C)$. $R^{gh}n$ $(°C/kW)$, $R^{rb}m$ $(°C/kW)$, and $R^{ab}m$ $(°C/kW)$ are the thermal resistances of HVAC systems used, $C^{gh}n$ $(kW\Delta t/°C)$, $C^{rb}m$ $(kW\Delta t/°C)$, and $C^{ab}m$ $(kW\Delta t/°C)$ are the thermal capacities of the HVAC systems, $\eta^{gh}n$, $\eta^{rb}m$, and $\eta^{ab}m$ are the coefficients of performance of the m,n-th HVAC unit (positive for cooling and negative for heating), and $u^h m, n(t)$ (kW), $u^{h,rb}m(t)$ (kW), and $u^{h,ab}m(t)$ (kW) are the power consumed by HVAC systems in greenhouses, residential buildings, and animal buildings, respectively.

It is important to note that the greenhouse design, material conductivity, and thickness determine the thermal resistance of the greenhouse covering material. The same is true for residential and animal structures.

$$R_n^{gh} = \frac{e_n^{gh}}{S_n^{gh} \cdot k_n^{gh}} \quad , \quad R_m^{rb} = \frac{e_m^{rb}}{S_m^{rb} \cdot k_m^{rb}} \quad , \quad R_m^{ab} = \frac{e_m^{ab}}{S_m^{ab} \cdot k_m^{ab}} \tag{4.9}$$

where e_n^{gh} is glazing material thickness used for greenhouses (m), $e^{rb}m$, $e^{ab}m$ are the material thickness of walls in residential and animal buildings (m). $S^{gh}m, n$ (m^2), S_m^{rb} (m^2), S_m^{ab} (m^2) are the areas of greenhouses and areas of controllable zones in residential, animal buildings, and $k^{gh}n$ $(kW/m \cdot^{\circ} C)$, $k^{rb}m$ $(kW/m \cdot^{\circ} C)$, $k^{ab}m$ $(kW/m \cdot^{\circ} C)$ are the materials conductivity used in greenhouses, residential, and animal buildings.

4.1.4 Model of Air Circulation

air circulation significantly influences the greenhouse environment, necessitating the maintenance of a consistent climate throughout the structure [79, 80]. The described ventilation air flow rate is as follows:

$$o_{m,n}^{vent}(t) = \frac{A_{m,n}^{vo}}{S_{m,n}^{gh}} w_m(t) D(\alpha_{m,n}(t)) \cdot 3600 \tag{4.10}$$

where $A_{m,n}^{vo}$ is the Vent opening of the n-th greenhouse (m^2), w_m is the wind speed in the m-th farm (m/s) and $D(\alpha_{m,n}(t))$ represents the angle of the window which is defined as:

$$D(\alpha_{m,n}(t)) = 0.0229 \cdot (1 - e^{(\frac{-\alpha_{m,n}(t)}{21,1})}) \tag{4.11}$$

4.1.5 Model of Humidity

Optimal humidity is vital for crops development. High humidity leads to issues like tissue damage and disease spread, while low humidity stresses plants and hampers photosynthesis. Monitoring and controlling humidity are essential for creating an ideal climate for crops development. This aspect is commonly referred to as[81]:

$$H_{m,n}^{in}(t+\Delta t) = \frac{L_{m,n}^{in,gh}(t+\Delta t) \cdot P_{atm}}{c_1 - (c_3 e^{c_4 T_{m,n}^{\text{in},gh}(t+\Delta t)} - c_2) \cdot c_5} \cdot 100\% \tag{4.12}$$

where $H_{m,n}^{int}(t)$ represent the level of humidity indoors in the greenhouse, P_{atm} is the atmospheric air pressure and $c_1 ... c_5$ are constants. Applying the mass balance theory involves simulating indoor air and water content. This simulation accounts for factors like moisture released through natural air ventilation and water introduced or extracted by the dehumidifier or fogger. The process is outlined as follows:

$$\begin{aligned} L_{m,n}^{in,gh}(t+\Delta t) &= L_{m,n}^{in,gh}(t) + \frac{\Delta t.S_{m,n}^{gh}}{V_{m,n}^{gh}\rho^a}[C_r^{ev} + o_{m,n}^{vent}(t)(L_m^{out}(t) \\ &- L_{m,n}^{in,gh}(t))] + \alpha_{m,n}^{fog}(t)L_{\max(m,n)}^{fog}S_{m,n}^{gh} - \alpha_{m,n}^{deh}(t)L_{\max(m,n)}^{deh}S_{m,n}^{gh} \end{aligned} \tag{4.13}$$

where $S_{m,n}^{gh}$, $V_{m,n}^{gh}$ are the area and volumes of each greenhouse in m-th farm, C_r^{ev} is the amount of crop evaporation. ρ^a is air density, $\alpha_{m,n}^{fog}(t)$ is the operation status of fogger, $L_{\max(m,n)}^{deh}$ and $L_{\max(m,n)}^{fog}$ are the maximum system water flow rates of the dehumidifier and fogger. $\alpha_{m,n}^{deh}(t)$ is the operation status of the dehumidifier and $L_m^{out}(t)$ is the water content outside can be calculated by:

$$L_m^{out}(t) = \frac{c_5 H_m^{out}(t)}{P_{atm}} c_1 \cdot (c_3 e^{c_4 T_{m,n}^{out,gh}(t)} - c_2) \tag{4.14}$$

where $H_m^{out}(t)$ represents the level of humidity outdoors of the greenhouse. The powers consumed by fogging and dehumidification $u_{m,n}^{fog}(t)$, $u_{m,n}^{deh}(t)$ are described as follows:

$$u_{m,n}^{fog}(t) = \alpha_{m,n}^{fog}(t) \cdot P_{m,n}^{fog} \tag{4.15}$$

$$u_{m,n}^{deh}(t) = \alpha_{m,n}^{deh}(t) \cdot P_{m,n}^{deh} \tag{4.16}$$

where $P_{m,n}^{fog}$,$P_{m,n}^{deh}$ are the rated powers of the fogger system and dehumidifier.

4.1.6 Model of CO_2 Concentration

The amount of CO_2 in the atmosphere has a significant impact on crop development. CO_2 concentration can impact photosynthesis in plants. Increasing CO_2 levels can increase crop productivity[82]. The model for CO_2 concentration is modeled as.

$$\begin{aligned} Z_{m,n}^{CO_2,\text{int}}(t+\Delta t) &= Z_{m,n}^{CO_2,\text{int}}(t) + \frac{\Delta t}{V_{m,n}^{gh}\rho^a}[S_{m,n}^{gh}.\alpha_{m,n}^{CO_2}(t)C_{\max}^{inj} + \rho^a S_{m,n}^{gh} o_{m,n}^{vent}(t)(Z_m^{CO_2,out}(t) \\ &- Z_{m,n}^{CO_2,\text{int}}(t+\Delta t) + S_{m,n}^{gh}C_{res}(c_6 + c_7 T_{m,n}^{in,gh}(t)) - \frac{C^{phot} I_m^l(t) S_{m,n}^{gh}}{R_{m,n}^{gh}}] \end{aligned} \tag{4.17}$$

where $Z_{m,n}^{CO2,int}(t)$, $Zm^{CO2,out}(t)$ are the greenhouse's internal and external $CO2$ concentrations (ppm), $C_{\max}^{inj}$ is the maximum carbon that a $CO2$ generator may introduce (kg/m^2), $Cres$ Respiration coefficient of crops $(kg/(m^2hK))$, C^{phot} Photosynthesis coefficient of crops (kg/Wh), $I^l m(t)$ is outdoor sunlight intensity (W/m^2), $\alpha^{CO2} m,n(t)$ is the $CO2$ enrichment's state of operation, and C_6 $(---)$, C_7 (W/mK) are constants. The power consumed by the $CO2$ injector $u_{m,n}^{CO2}(t)$ in the n-th greenhouse at the m-th farm is modeled as follows: (kW)

$$u_{m,n}^{CO_2}(t) = \alpha_{m,n}^{CO_2}(t) \cdot P_{m,n}^{CO2} \tag{4.18}$$

where $P_{m,n}^{CO2}$ is the CO_2 generator rated power.

4.1.7 Model of Light Intensity

Greenhouses use artificial lighting, particularly when natural light is insufficient. Light-emitting diodes (LEDs) are favored for their technical advantages, but their design requires careful consideration of unique specifications with a paramount focus on ensuring the necessary flux, which involves[83]:

$$u_{m,n}^l(t) = \frac{E_{m,n}^{light}(t)}{\eta_l} \tag{4.19}$$

$$E_{m,n}^{light}(t) = l_{m,n}^{\text{int}}(t) \cdot S_{m,n}^{gh} \tag{4.20}$$

where ηl is the LED efficiency (lm/W) and $lm,n^{\text{int}}(t)$ is the light intensity (Lux) and $u_{m,n}^l(t)$ represents the power consumed by artificial lighting in each greenhouse of the m farm (kW).

4.1.8 Energy Balance

By enabling power exchange with the main grid via a dedicated link, energy surpluse or deficit inside the microgrids are balanced, preserving production and consumption equilibrium amongst the networked farms. The dynamic of energy balance for m-th smart farm is defined as follows:

$$x_m(t+\Delta t) = a_m x_m(t) + \sum_{l=1}^{L} b_{(m,l)} f_l(t)\Delta t + P_m^B(t)\Delta t \tag{4.21}$$

$$\begin{aligned} P_m^B(t) = {} & p_m^{REG}(t) - u_m^{mp}(t) - \sum_{n=1}^{N} u_{m,n}^{lp}(t) - u_m^{ab}(t) - \sum_{n=1}^{N} u_{m,n}^{h}(t) \\ & - u_m^{h,rb}(t) - u_m^{h,ab}(t) - \sum_{n=1}^{N} u_{m,n}^{l}(t) - \sum_{n=1}^{N} u_{m,n}^{CO2}(t) - \sum_{n=1}^{N} u_{m,n}^{fog}(t) - \sum_{n=1}^{N} u_{m,n}^{deh}(t) \end{aligned} \tag{4.22}$$

Where $x_m(t)$ represents the energy storage inventory of the m-th farm at time (t) (kWh), a_m is a scalar that represents the efficiency of the energy storage technology at the m-th farm, where $0 < a_m < 1$ and $f_l(t)$ is power flow exchanged between farms and the grid through the l-th link (kW), $b_{(m,l)}$ is a matrix that describes the m-farm's network link topology, $P_m^B(t)$ is the vector stating the power balance in the m farm (kW), $p^{REG}m(t)$ is the sum of renewable power production by photovoltaic panels $p^{pv}m(t)$ (kW) and wind turbine $p_m^{wind}(t)$ (kW) in the m-th farm.

4.2 Optimization Problem

4.2.1 Centralized Approach

The aim is to create an optimal microclimate for sustainable crop growth in greenhouses and ensure thermal comfort for residential and animal buildings across the farm network. This is achieved by minimizing deviations from reference standards and reducing fluctuations in power exchange between farms. The objective function is defined as follows:

$$\begin{aligned} F = {} & \sum_{t=0}^{T-1}\sum_{l=1}^{L} Z_{(l,l)}(f_l(t)) + \sum_{t=0}^{T-1}\sum_{m=1}^{M} \xi_1(T_m^{in,rb}(t) - \bar{T}_m^{in,rb}(t))^2 \\ & + \xi_2(Q_m^{an}(t) - \bar{Q}_m^{an,in}(t))^2 + \xi_3(T_m^{in,ab}(t) - \bar{T}_m^{in,ab}(t))^2 + \\ & \sum_{t=0}^{T-1}\sum_{m=1}^{M}\sum_{n=1}^{N} \xi_4(Q_{m,n}^{gh}(t) - \bar{Q}_{m,n}^{gh}(t))^2 + \xi_5(T_{m,n}^{in,gh}(t) - \bar{T}_{m,n}^{in,gh}(t))^2 \\ & + \xi_6(H_{m,n}^{in}(t) - \bar{H}_{m,n}^{in}(t))^2 + \xi_7(u_{m,n}^{l}(t) - \bar{u}_{m,n}^{l}(t))^2 \\ & + \xi_8(Z_{m,n}^{CO2}(t) - \bar{Z}_{m,n}^{CO2}(t))^2 \end{aligned} \tag{4.23}$$

in which $Z_{(l,l)}$ is the cost of the power in each link represented by a diagonal matrix with identical elements equal to 0.001. $\bar{T}_m^{in,rb}$ is the desired temperature inside residential buildings, $\bar{T}_m^{in,ab}$. $\bar{Q}_m^{in,ab}$ are the desired temperatures and water inside animal buildings. $\bar{Q}_{m,n}^{gh}$, $\bar{T}_{m,n}^{in,gh}$, $\bar{H}_{m,n}^{in}$, $\bar{u}_{m,n}^{l}$, $\bar{Z}_{m,n}^{CO2}$ are the desired water, temperature, humidity, lighting, and CO_2 concentration inside each greenhouse at m-th farms, respectively, and ξ_1,...,ξ_8 are weighting parameters that are used to trade off the various components of the objective function. All objectives in this study are assumed to have the same priority since all weighting parameters have the same value, which is 1.

Constraints governing the problem

- Water flows and reservoir
  The reservoir's top and lower limitations should be met by the water flow and the water stored there:

$$L_{m,\min}^{vr} \le L_m^{vr}(t) \le L_{m,\max}^{vr} \qquad \forall m, t. \tag{4.24}$$

$$Q_{m,n}^{gh,\min} \leq Q_{m,n}^{gh}(t) \leq Q_{m,n}^{gh,\max} \qquad \forall\, m, n, t. \tag{4.25}$$

$$Q_{m}^{ab,\min} \leq Q_{m}^{ab}(t) \leq Q_{m}^{ab,\max} \qquad \forall\, m, t. \tag{4.26}$$

$$u_{m}^{mp,\min} \leq u_{m}^{mp}(t) \leq u_{m}^{mp,\max} \qquad \forall\, m, t. \tag{4.27}$$

$$u_{m,n}^{lp,\min} \leq u_{m,n}^{lp}(t) \leq u_{m,n}^{lp,\max} \qquad \forall\, m, n, t. \tag{4.28}$$

$$u_{m}^{ab,\min} \leq u_{m}^{ab}(t) \leq u_{m}^{ab,\max} \qquad \forall\, m, t. \tag{4.29}$$

- Temperature
  The greenhouse's interior temperature is constrained by lower and upper bounds:

$$T_{m,n,\min}^{in,gh} \leq T_{m,n}^{in,gh}(t) \leq T_{m,n,\max}^{in,gh} \qquad \forall\, m, n, t. \tag{4.30}$$

$$u_{m,n}^{h,\min} \leq u_{m,n}^{h}(t) \leq u_{m,n}^{h,\max} \qquad \forall\, m, n, t. \tag{4.31}$$

$$T_{m,\min}^{in,rb} \leq T_{m}^{in,rb}(t) \leq T_{m,\max}^{in,rb} \qquad \forall\, m, t. \tag{4.32}$$

$$u_{m}^{h,rb\,\min} \leq u_{m}^{h,rb}(t) \leq u_{m}^{h,rb,\max} \qquad \forall\, m, t. \tag{4.33}$$

$$T_{m,\min}^{in,an} \leq T_{m}^{in,an}(t) \leq T_{m,\max}^{in,an} \qquad \forall\, m, t. \tag{4.34}$$

$$u_{m}^{h,ab\,\min} \leq u_{m}^{h,ab}(t) \leq u_{m}^{h,ab,\max} \qquad \forall\, m, t. \tag{4.35}$$

- Humidity, fogging and dehumidification systems
  The greenhouse's humidity is limited by upper and lower boundaries, which is comparable to meeting the following restrictions.

$$H_{m,n}^{in,\min} \leq H_{m,n}^{in}(t) \leq H_{m,n}^{in,\min} \qquad \forall\, m, n, t. \tag{4.36}$$

$$L_{m,n}^{in,\min} \leq L_{m,n}^{in}(t) \leq L_{m,n}^{in,\max} \qquad \forall\, m, n, t. \tag{4.37}$$

$$u_{m,n}^{deh\,\min} \leq u_{m,n}^{deh}(t) \leq u_{m,n}^{deh,\max} \qquad \forall\, m, n, t. \tag{4.38}$$

$$u_{m,n}^{fog\,\min} \leq u_{m,n}^{fog}(t) \leq u_{m,n}^{fog,\max} \qquad \forall\, m, n, t. \tag{4.39}$$

- CO_2 concentration
  Every time slot's CO_2 concentration inside the greenhouse is controlled by upper and lower limitations.

$$Z_{m,n,\min}^{Co2,int} \leq Z_{m,n}^{Co2,int}(t) \leq Z_{m,n,\min}^{Co2,int} \qquad \forall\, m, n, t. \tag{4.40}$$

$$u_{m,n}^{CO_2\,\min} \leq u_{m,n}^{CO_2}(t) \leq u_{m,n}^{CO_2,\max} \qquad \forall\, m, n, t. \tag{4.41}$$

- Air circulation
  The proposed approach uses the window opening angle, which is restricted between upper and lower bounds, to regulate the ventilation operation.

$$\alpha_{m,n_{\min}} \leq \alpha_{m,n}(t) \leq \alpha_{m,n_{\max}} \qquad \forall\, m, n, t. \tag{4.42}$$

$$o_{m,n}^{vent,\min} \leq o_{m,n}^{vent}(t) \leq o_{m,n}^{vent,\max} \qquad \forall\, m, n, t. \tag{4.43}$$

- Artificial lighting
  The greenhouse's artificial lighting is managed by upper and lower restrictions for each time slot.

$$\alpha_l {l^{\text{int}}}_{\min} \leq l_{m,n}^{\text{int}}(t) \leq \alpha_l {l^{\text{int}}}_{\max} \tag{4.44}$$

$$\alpha_l = \begin{Bmatrix} 1 & if \;\; l_{m,n}^{int}(t) \leq l_{\min}^{int} \\ 0 & otherwise \end{Bmatrix} \tag{4.45}$$

$$u_{m,n}^{l,\min} \leq u_{m,n}^{l}(t) \leq u_{m,n}^{l,\max} \qquad \forall\, m, n, t. \tag{4.46}$$

in which l_{min}^{int} is the minimum light intensity.

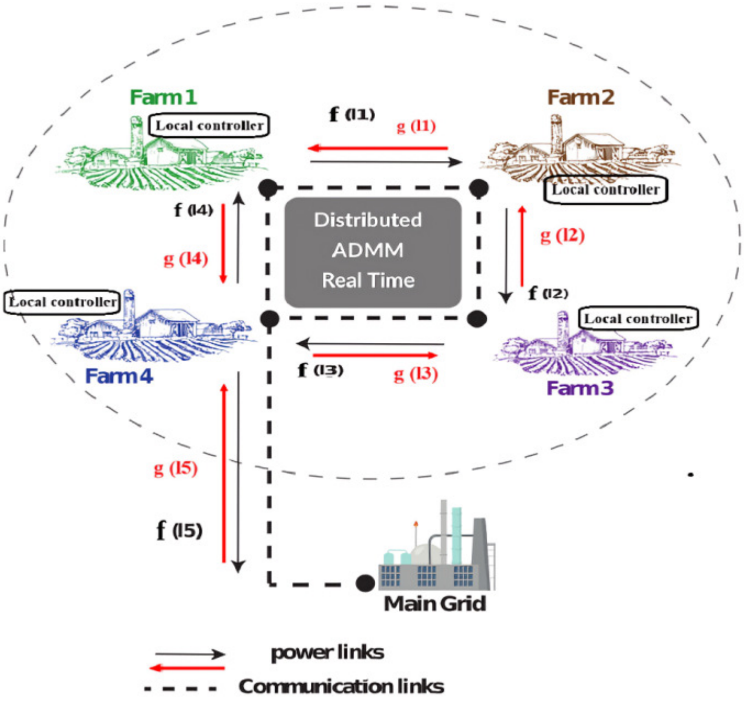

Figure 4.3: System Design Using (ADMM)

4.2.2 Distributed Approach

We initially used a centralized optimization approach, but it was computationally demanding and slow, requiring significant processing power to solve the entire system as a single problem. Moreover, centralized control is highly at risk in terms of robustness to failures; if a sensor fails, it can disrupt the entire system. In contrast, the distributed approach with ADMM enhances scalability and resilience. By dividing the problem into smaller, farm-specific subproblems, it reduces computational complexity and ensures that if one farm encounters an issue, the others continue operating adequately. While ADMM may not always fully converge due to model nonlinearity, it still provides results comparable to the centralized approach with significantly improved speed and real-time performance.

ADMM Formulation

The general formulation of the algorithm is the following[84] :

$$\begin{aligned} \min f(x) + g(z) \\ s.t. \quad Ax + Bz = c \end{aligned} \tag{4.47}$$

where x, z are variables and $f(x)$, $g(z)$ are completely separated functions, sharing a common equality constraint. As in the method of multipliers, the augmented Lagrangian is created in this way:

$$L_\rho(x, z, y) = f(x) + g(z) + y(Ax + Bz - c) + \frac{\rho}{2}||Ax + Bz - c||_2^2 \tag{4.48}$$

ADMM consists of the iterations. The solutions can be reached according to the following procedure.

$$x^{k+1} = \arg\min_x (L_\rho(x, z^k, y^k)) \tag{4.49}$$

$$z^{k+1} = \arg\min_z ((L_\rho(x^{k+1}, z, y^k)) \tag{4.50}$$

$$y^{k+1} = y^k + \rho(Ax^{k+1} + Bz^{k+1} - C) \tag{4.51}$$

In the case of the farm problem, the different F_m functions are coupled by the power flow variable $f_l(t)$. To separate these functions, as a convention, these variables are renamed as $g_l(t)$ when they enter a farm and left as $f_l(t)$ when they are going out from a farm according to Fig.4.3. So, it is possible to rewrite the objective as a sum of completely separated functions:

$$\min \sum_{m=1}^{M} F_m(f_l(t), g_l(t)) \tag{4.52}$$

Where $F_m = 1...4$ are the subproblems representing the individual objective functions of each farm resulting from the distributed optimization, they are explained as follows:

$$\begin{aligned} F_{m1..4} = &\sum_{t=0}^{T-1}\sum_{l=1}^{L} Z_{l,l}\left[f_l(t) + g_l(t)\right] + \sum_{t=0}^{T-1} \xi_1 (T_m^{in,rb}(t) - \bar{T}_m^{in,rb}(t))^2 \\ &+ \xi_2 (Q_m^{an}(t) - \bar{Q}_m^{an,in}(t))^2 + \xi_3 (T_m^{in,ab}(t) - \bar{T}_m^{in,ab}(t))^2 + \\ &\sum_{t=0}^{T-1}\sum_{n=1}^{N} \xi_4 (Q_{m,n}^{gh}(t) - \bar{Q}_{m,n}^{gh}(t))^2 + \xi_5 (T_{m,n}^{in,gh}(t) - \bar{T}_{m,n}^{in,gh}(t))^2 \\ &+ \xi_6 (H_{m,n}^{in}(t) - \bar{H}_{m,n}^{in}(t))^2 + \xi_7 (u_{m,n}^{l}(t) - \bar{u}_{m,n}^{l}(t))^2 \\ &+ \xi_8 (Z_{m,n}^{CO2}(t) - \bar{Z}_{m,n}^{CO2}(t))^2 \end{aligned} \tag{4.53}$$

In this distributed approach, each farm model must still adhere to the original constraints (4.24...4.46) to ensure their plans are viable. Consequently, we also need to add the following local constraints: subject to

$$\sum_{t=0}^{T-1}\sum_{l=1}^{L} f_l(t) = \sum_{t=0}^{T-1}\sum_{l=1}^{L} g_l(t) \tag{4.54}$$

So, the following Lagrangian can be defined for this ADMM system:

$$\begin{aligned} L_\rho(f_l(t), g_l(t), y) = &\sum_{t=0}^{T-1}\sum_{l=1}^{L} F_m(f_l(t), g_l(t), y) + y_m. \\ \sum_{t=0}^{T-1}\sum_{l=1}^{L}(f_l(t) - g_l(t)) + \rho/2 &\sum_{t=0}^{T-1}\sum_{l=1}^{L}(f_l(t) - g_l(t))^2 \quad \forall m \end{aligned} \tag{4.55}$$

The resulting ADMM algorithm is the following:

$$\begin{aligned} (f_l^{k+1}(t)) = \arg\min_{f_l(t)} &\sum_{t=0}^{T-1}\sum_{l=1}^{L} F_m(f_l(t), g_l^k(t)) + y_m^k. \\ \sum_{t=0}^{T-1}\sum_{l=1}^{L}(f_l(t) - g_l^k(t)) + \rho/2 &\sum_{t=0}^{T-1}\sum_{l=1}^{L}(f_l(t) - g_l^k(t))^2 \quad \forall m \end{aligned} \tag{4.56}$$

$$\begin{aligned} (g_l^{k+1}(t)) = \arg\min_{g_l(t)} &\sum_{t=0}^{T-1}\sum_{l=1}^{L} F_m(f_l^k(t), g_l(t)) + y_m^k. \\ \sum_{t=0}^{T-1}\sum_{l=1}^{L}\left(f_l^k(t) - g_l(t)\right) + \rho/2 &\sum_{t=0}^{T-1}\sum_{l=1}^{L}\left(f_l^k(t) - g_l(t)\right)^2 \quad \forall m \end{aligned} \tag{4.57}$$

$$y_m^{k+1} = y_m^k + \rho(\,(f_l^{k+1}(t)) - (g_l^{k+1}(t))) \quad \forall m \tag{4.58}$$

The ADMM-based distributed optimization algorithm is executed sequentially for each time step. The algorithm uses a fixed penalty parameter ρ. At the start of a time step, it initializes the primal variables (f_l^0, g_l^0) and the dual variables (y_m^0) for each farm. In each iteration, farms update f_l and g_l by solving their local sub-problems to minimize the augmented Lagrangian. The Lagrange multiplier y_m^k is updated to ensure consistency. This repeats until the difference between f_l^{k+1} and g_l^{k+1} meets a threshold or maximum iterations are reached, then proceeds to the next time step according to Algorithm 3[85].

Algorithm 3: ADMM-based Distributed Optimization

```
for time step t = 1, 2, ..., T − 1. do
    ρ = 10;
    Initialize y_m^0 for each farm m ∈ M;
    Initialize f_l^0, g_l^0 for each power link l ∈ L;
    Set k = 0 ;
    repeat
        k ← k + 1 ;
        for each farm m (in parallel) do
            for each l of farm m do
                update by solving: f_l^{k+1} = arg min_{f_l} L_ρ(f_l, g_l^k, y_m^k) ;
                g_l^{k+1} = arg min_{g_l} L_ρ(f_l^k, g_l, y_m^k) ;
            update Lagrange multiplier: y_m^{k+1} = y_m^k + ρ (f_l^{k+1} − g_l^{k+1}) ;
    until ||f_l^{k+1} − g_l^{k+1}||^2 ≤ ϵ Convergence or (k = k_max);
    t ← t + 1 ;
```

4.3 Case Study and Numerical Results

4.3.1 Case Study and Application

In this particular case study, a simulation is conducted for a cooperative network comprising four connected farms over a one-day period. The simulation takes into account real weather data from four different sites, specifically on the 1st of July. Each individual farm is equipped with three smart greenhouses cultivating various crops, an animal building housing different animals, and a residential building; the parameters and settings for the system used in this simulation are all listed in that order in Table 4.1.

Table 4.1: System Components Parameters

Parameter	*Value*		*Unit*
P_m^r	12	$\forall m \in M$	$[kW]$
w_a	1.5		$[m/s]$
w_r	10		$[m/s]$
w_c	35		$[m/s]$
A_{pv}	6		$[m^2]$
η_{pv}	0.20		$[---]$
P_f	0.90		$[---]$
η_{pc}	0.97		$[---]$
ρ_w	1000		$[kg/m^3]$
g	9.81		$[m/s^2]$
h_m^{mp}	21, 12, 24, 8		$[m]$
h_n^{gh}	7	$\forall n \in N$	$[m]$
h_m^{ab}	5, 9, 6, 8		$[m]$
R_n^{gh}	1.64	$\forall n \in N$	[°C/kW]
C_n^{gh}	0.53	$\forall n \in N$	$[kW\Delta t/°C]$
R_m^{rb}	1.33	$\forall m \in M$	[°C/kW]
C_m^{rb}	3.3	$\forall m \in M$	$[kW\Delta t/°C]$
R_m^{ab}	1.33	$\forall m \in M$	[°C/kW]
C_m^{ab}	3.3	$\forall m \in M$	$[kW\Delta t/°C]$
η_n^{gh}	2.5	$\forall n \in N$	$[---]$
η_m^{rb}	2.1	$\forall m \in M$	$[---]$
η_m^{ab}	2.1	$\forall m \in M$	$[---]$
$A_{m,n}^{vo}$	1	$\forall n \in N$	$[m^2]$
$S_{m,n}^{gh}$	80	$\forall n \in N$	$[m^2]$
S_m^{rb}	60	$\forall m \in M$	$[m^2]$
S_m^{ab}	60	$\forall m \in M$	$[m^2]$
P_{atm}	101325		$[Pa]$
ρ^a	1.225		$[kg/m^3]$
$V_{m,n}^{gh}$	280	$\forall n \in N$	$[m^3]$
C_r^{ev}	0.12		$[kg/m^2h]$
$L_{max,n}^{fog}$	0.0096	$\forall n \in N$	$[kg/m^2h]$
$L_{max,n}^{deh}$	0.145	$\forall n \in N$	$[kg/(m^2h)]$
$P_{m,n}^{fog}$	3	$\forall n \in N$	$[kW]$
$P_{m,n}^{deh}$	2.2	$\forall n \in N$	$[kW]$
C_1	100		$[--]$
C_2	1.7001		$[Pa]$
C_3	7.7835		$[Pa]$
C_4	0.058		$[K^{-1}]$
C_5	0.6228		$[(kgw/kga)]$
$C_{\max}^{inj}$	0.8×10^{-3}		$[kg/m^2]$
C_{res}	1.22×10^{-6}		$[kg/(m^2hK)]$
C^{phot}	165.7×10^{-3}		$[kg/Wh]$
$P_{m,n}^{CO2}$	2	$\forall n \in N$	$[kW]$
C_6	-0.27		$[--]$
C_7	0.05		$[W/mK]$
$L_{m,n}^{int}$	5000	$\forall n \in N$	$[Lux]$
$I_{\min}^l$	50		$[W/m^2]$
η_l	200		$[lm/W]$
a_m	0.9	$\forall m \in M$	$[---]$

An overview of the architectural layout of these farms is provided in Fig.4.1 and Fig.4.3 although each farm comprises renewable energy production in the form of a PV system of 1 (kW) (Dimplex PV 4*250 (W)), a wind turbine of 12 (kW), an energy storage inventory with a maximum capacity of 100 (kWh), and a water reservoir of 50 (m^3), the efficiency of the master pumps is 0.9, and the local pumps are thought to be the same, with an efficiency of 0.85. In each farm, the power produced by REG and the ambient temperature, outdoor relative humidity, and CO_2 outdoor are represented, respectively, in Figure 4.4. The generation of REG is the sum of powers in the deterministic component (using measurements of solar (PV) and wind power model). Each farm has an outside temperature range of 34 (°C) to 50 (°C) and a renewable energy production of zero to 13 $[kW]$. While the outdoor CO_2 remains constant at 407.85 (ppm), the relative humidity varies from 35% to 80%.

The architecture of the cluster outlining the power links between the m-farm's network topology is described by the matrix b(m,l)[86]. As a convention, there is no restriction on the direction of power exchange; the link is designed to distinguish between the two possible ways. The incidence matrix, whose elements are $b_{m,l}$ = -1 if the l-th connection is leaving the m-th farm, represents the topology of the network. 1 If the l-th link is entering the m-th farm, then $0 \leq b_{m,l} \leq 1$. When the l-th link is not incident to the m-th farm, $b_{m,l} = 0$, otherwise.

$$\mathbf{b}(m,l) = \begin{array}{c c} & \begin{array}{ccccc} l1 & l2 & l3 & l4 & l5 \end{array} \\ \begin{array}{c} m_1 \\ m_2 \\ m_3 \\ m_4 \end{array} & \begin{pmatrix} -1 & 0 & 0 & 1 & 0 \\ 1 & -1 & 0 & 0 & 0 \\ 0 & 1 & -1 & 0 & 0 \\ 0 & 0 & 1 & -1 & -1 \end{pmatrix} \end{array}$$

Optimal greenhouses reference signals

In the first farm, the greenhouses GH(1,n), n ∈ [1,2], are set to have internal temperatures of 24 and 22 (°C) throughout the remainder of the day, but between 00:00 and 5:00, they are considered to be respectively equal to 26 and 27 (°C). Although GH (1,3) has been designed to provide a constant interior temperature of 25 (°C) all day, the temperature signal references for other GH (2,n) and GH (3,n) are depicted in Fig.4.5. It is assumed that the desired water volume is 0.8, 1.8, and 1.2 (m^3) for GH (2,n), GH (3,n) signals are presented in Fig. 4.8. The required illumination power reference in GH(1,n) and n ∈ [1,3] is 4, 2.75, and 3 (kW) between 19:00 and 5:00, and equivalent to 0 (kW) outside of that time in relation to GH(2,n), GH(3,n), the signal references can be seen in Fig.4.11.

In the fourth farm, the greenhouses GH(4,1) and GH(4,3) are set to have internal temperatures of 30 and 26 (°C), respectively, from 00:00 to 5:00, and 25 and 23 (°C) for the rest of the day. Although GH (4,2) has been designed to provide a constant interior temperature of 28 (°C) all day, it is assumed that the desired water volume is 1.5, 0.5, and 1.4 (m^3). For illumination, the required power in GH(4,n) and n ∈ [1,3] is 2.5, 3, and 3.75 (kW) between 19:00 and 5:00, and equivalent to 0 (kW) outside of that time. The relative humidity and CO_2 levels desired for every greenhouse are intended to maintain an internal humidity of 0.65 (%) and 800 ppm of CO_2 at all times.

Residential and animal buildings reference signals

All residential buildings existing on every farm are set to have internal temperatures of 25 (°C) between 05:00 and 18:00 and 22 (°C) throughout the remainder of the day. for Animal building Each farm has different temperatures in its animal buildings. The first animal building has a target temperature of 20 (°C) all day long. It is expected that throughout the day, the intended temperatures for the second animal building (2), third animal building (3), and fourth animal building (4) will be 25 (°C), 22 (°C), and 24 (°C), respectively. The projected amount of water needed for animal buildings 1, 2, 3, and 4 existing on each farm is two times a day, with a value of 2, 2.5, 2.75, and 3 (m^3), respectively, in the hours of 09:45 to 10:00 and 15:45 to 16:00.

4.3.2 Numerical Results and Analysis

In order to validate and prove the energy management algorithm performance and efficacy through detailed numerical findings, the optimization problem outlined in the preceding sections is performed and applied to a case study. The constrained distributed optimization formulation is applied to connected farms with smart greenhouses, residential buildings, and animal buildings. The ADMM-based distributed optimization approach has been implemented using Python Pyomo and IPOPT

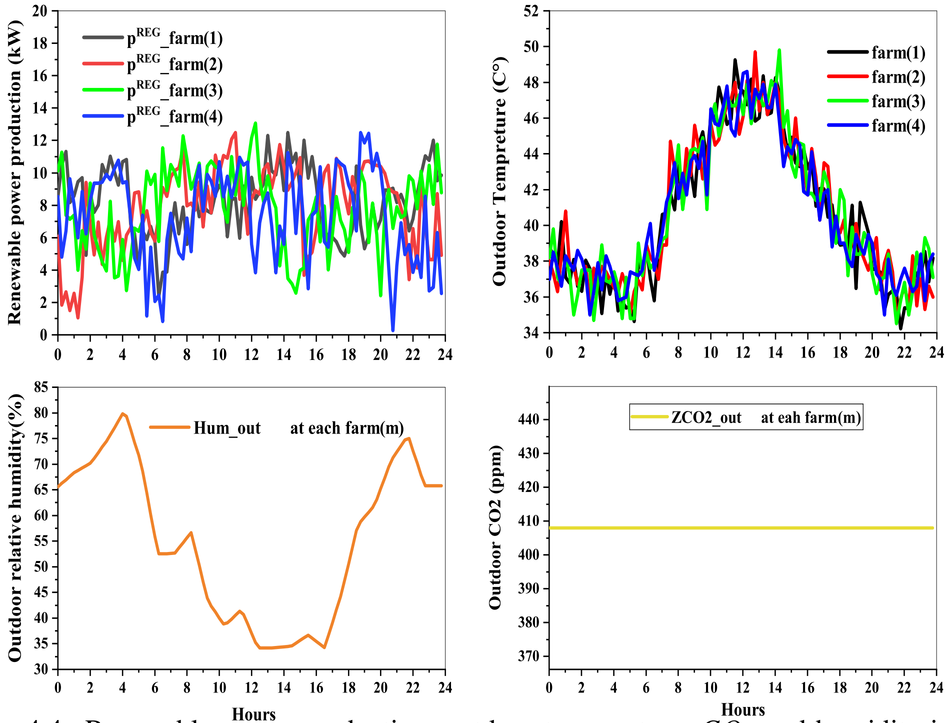

Figure 4.4: Renewable power production, outdoor temperature, CO_2 and humidity in each farm.

as a solver for the best optimization of the system operation, which is determined and examined by comprehensive simulations for a few situations in order to satisfy the needed factors necessary for plant growth, which are in this study temperature, water, lighting, humidity, and CO_2 for each greenhouse, add to temperature and water for the animal building and temperature for the residential building, and minimize the power exchange between farms. The optimal interior temperatures for

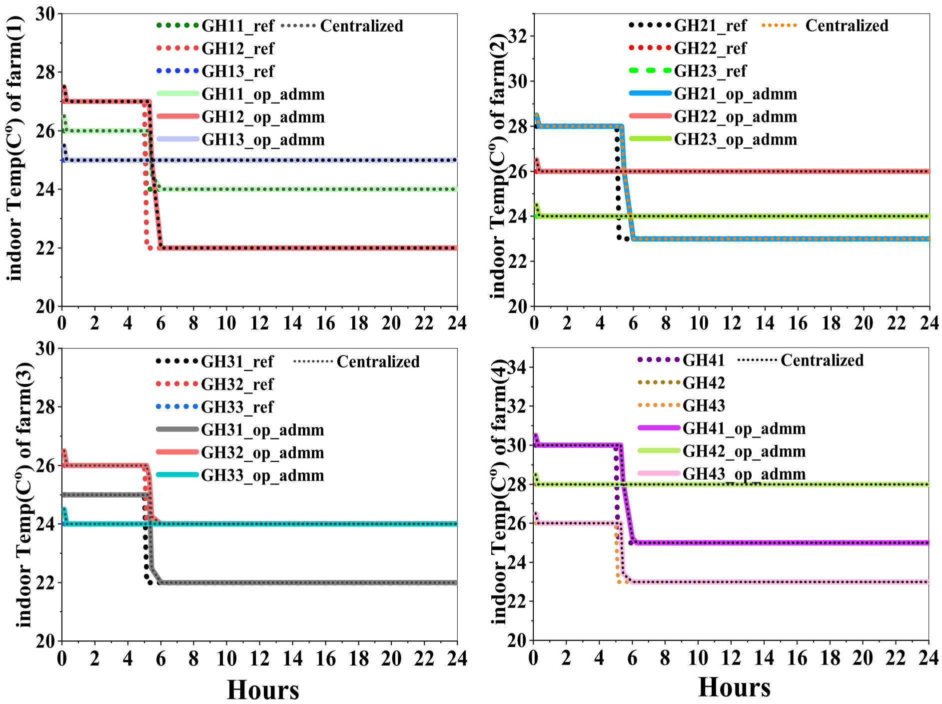

Figure 4.5: Optimal indoor temperature in each greenhouse.

greenhouses on each farm are depicted in Fig. 4.5. It's evident that the required temperature reference has been accurately tracked well (particularly for GH(1,3), GH(2,2), GH(2,3), GH(3,3), and GH(4,2)), thanks to the consistent temperature maintained throughout the day. Conversely, for the remaining greenhouses, the indoor temperature closely matched the reference temperature, except for a minor deviation observed between 5:15 and 6:00 a.m. A slight variance, akin to that seen in GH (1,2), was noted. The ideal temperature reference range experiences a delay, shifting from 27(°C) to 22(°C). This delay is typical, as it takes time for the HVAC system to cool down and reach the ideal temperature, aligning it with the reference temperature. GH(1,1), GH(2,1), GH(3,1), GH(3,2), GH(4,1), and GH(4,3) are all subject to this characteristic.

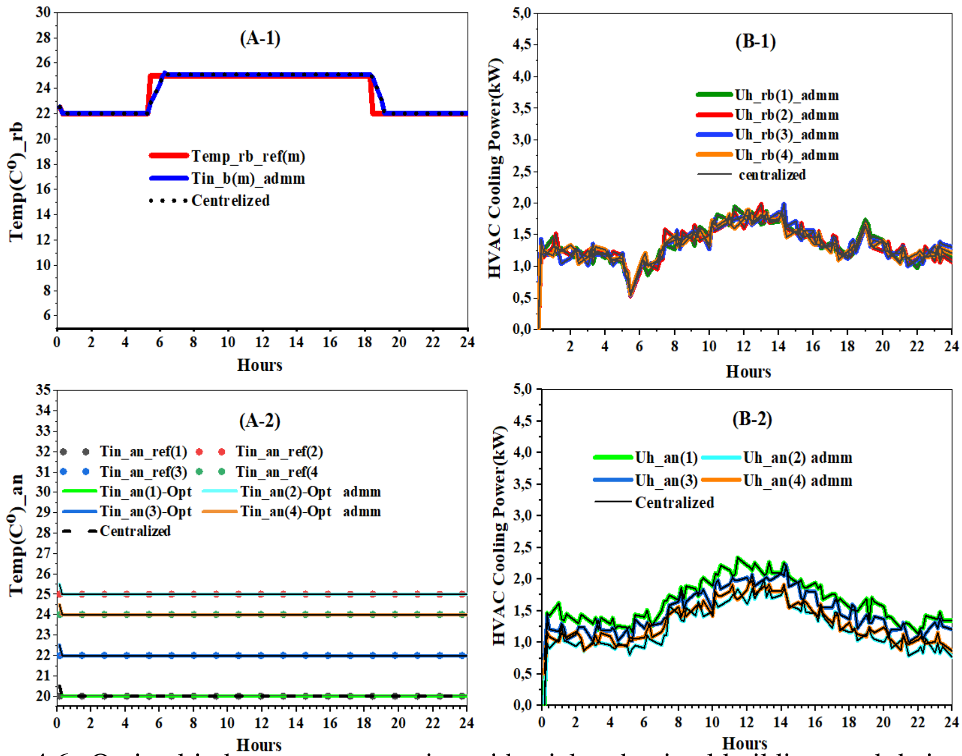

Figure 4.6: Optimal indoor temperature in residential and animal buildings and their power consumption (kW) by HVAC's.

In each farm's residential zone, as shown in Fig(4.6-A-1), the internal temperatures closely follow the desired references, with some delays. Specifically, there is a shift from 22(°C) to 25(°C) between 05:45 and 06:15 due to the influence of external temperatures. Similarly, another delay occurs when the temperature decreases from 25(°C) to 22(°C) between 18:15 and 18:45. These delays are expected, as the HVAC system requires time to adjust and reach the target temperature. It is evident that optimal comfort is attained at the specific temperatures required for various animals housed within each animal building, as depicted in Fig(4.6-A-2), despite the diverse temperature needs of the animals. The optimal operations of HVAC systems in greenhouses are presented in Fig.4.7. It can be seen that the HVAC systems initially operate at a lower cooling power level to fulfill the temperature requirements. Notably, between 05:15 and 06:00, for GH(1,1), GH(1,2), GH(2,1), GH(3,1), GH(3,2), GH(4,1), and GH(4,3), the HVAC systems consume more power for cooling, responding actively to fluctuations in the temperature reference and dynamically adapting to the maximum outside temperatures during the day period from 07:30 to 19:00.

Fig.(4.6-B-1) illustrates the optimal operation of HVAC systems in residential buildings. A noticeable drop in HVAC activity occurs due to fluctuations in the temperature reference during this period. During the daytime, the systems consume more power in response to peak outdoor temperatures. Additionally, between 18:45 and 19:15, the HVAC adjusts its operation to track the temperature shift from 25(°C) to 22(°C), ensuring optimal tracking of reference values. Regarding the animal buildings, as shown in Fig.(4.6-B-2), the HVAC system consumes more power during the daytime due to high outdoor temperatures. The performance of water demand tracking in GH(1,n), where n ranges from 1 to 3, is presented in Fig.4.8. It can be seen that the water loads are fully satisfied. The local pumps are effectively controlled and operate optimally in alignment with the water loads as

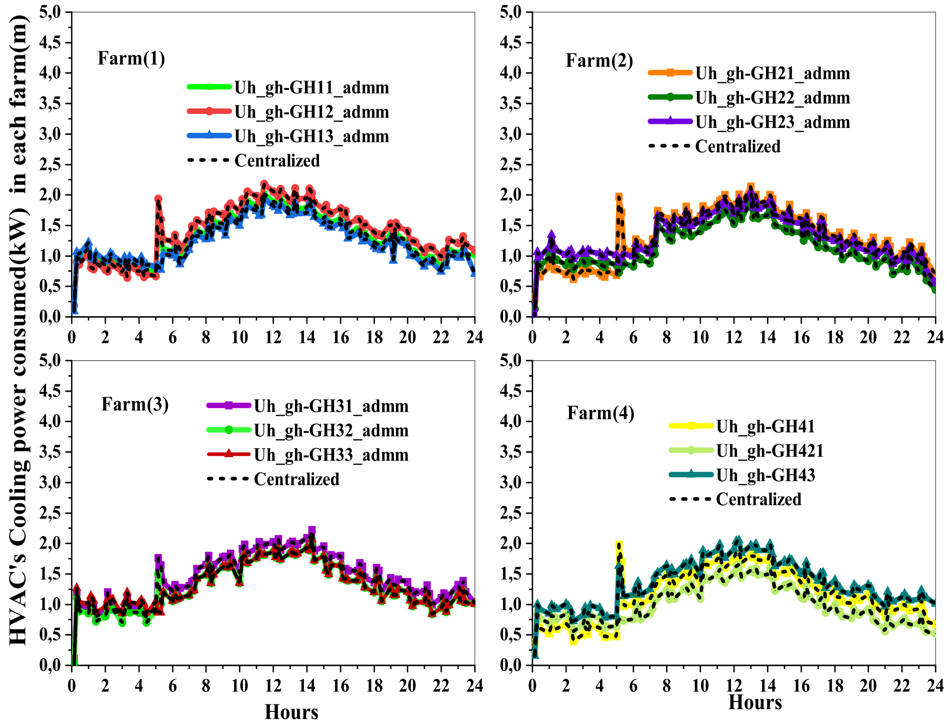

Figure 4.7: power consumed by HVAC's in each greenhouse (kW).

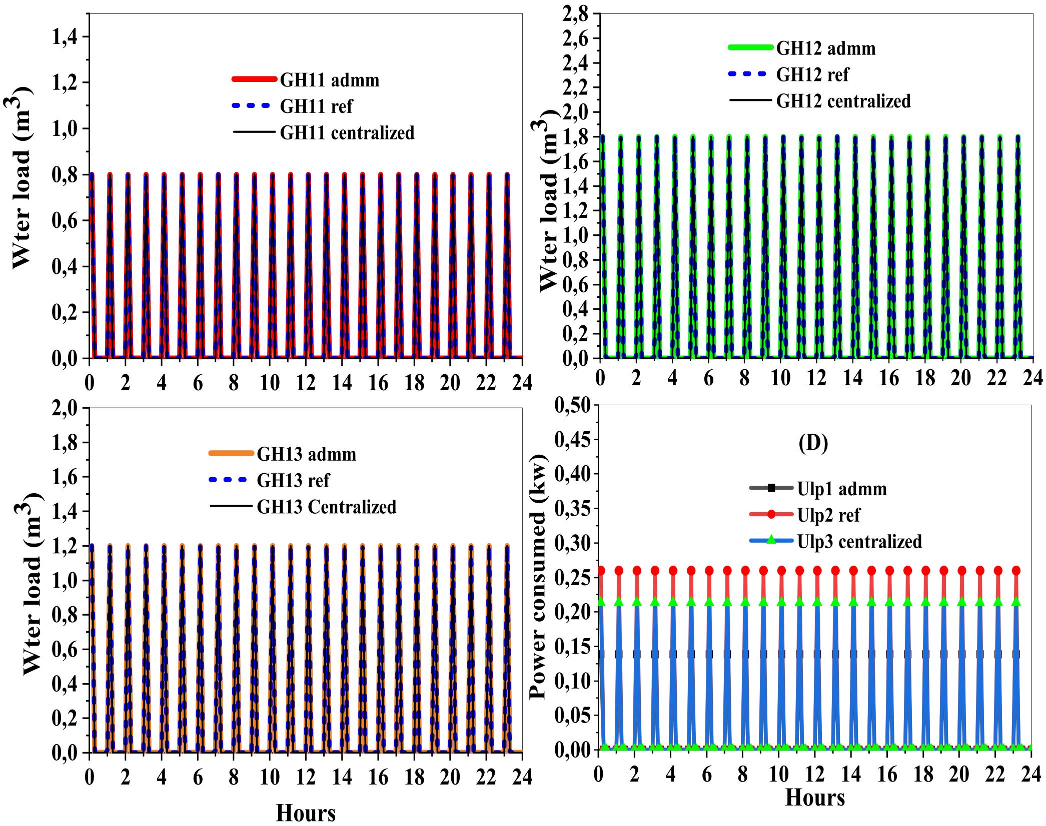

Figure 4.8: Optimal tracking of the water references in GH(1,n) with their power consumption.

it is described in Fig.(4.8-D)This efficient control extends to other greenhouses, GH(m,n), where m ranges from 2 to 4 and n ranges from 1 to 3, as well as to animal buildings. It is evident from Fig.4.9 that the water requirements are completely fulfilled.

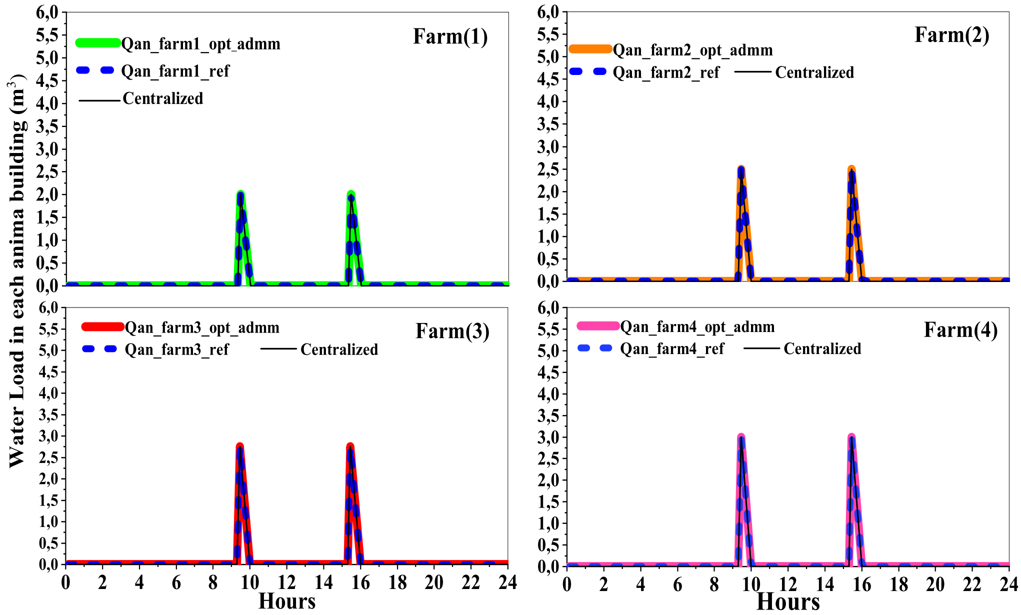

Figure 4.9: Optimal tracking of the water references in animal buildings.

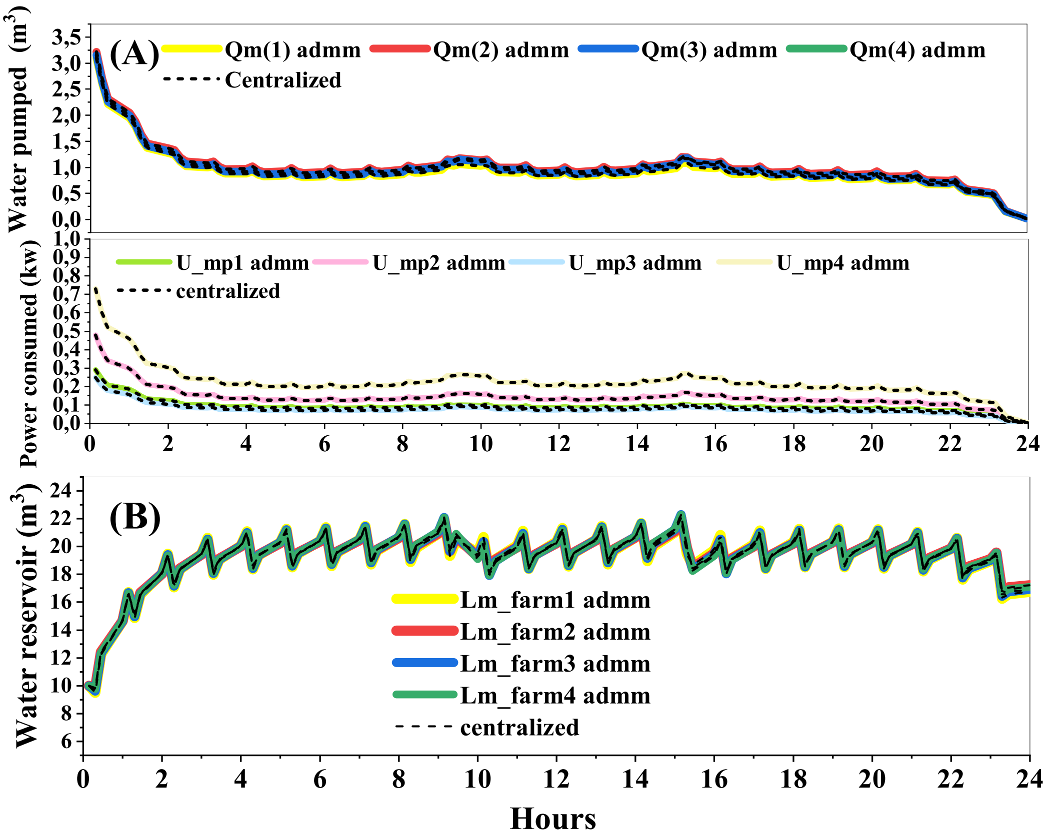

Figure 4.10: Optimal water is pumped into reservoirs with tier power consumption and level water reservoirs at each farm.

Figure (4.10-A) presents the optimal water flows pumped by the master pumps from the water source to each farm's reservoir, along with their corresponding power consumption. A variation in water flow between farms can be observed, which is attributed to differences in greenhouse water demand and the varying water requirements of the animal buildings.

The optimal performance of the water storage reservoirs available on the farm is depicted in Fig.(4.10-B). Assuming identical starting levels of 10 (m^3), we consider the water reservoirs to be comparable, each with a storage capacity of 50 (m^3). Additionally, it is observed that the activation of local pumps serving the greenhouses coincides with the activation of main pumps feeding the water reservoirs, even when artificial lighting is turned on. The water reservoirs on each farm exhibit similar patterns, characterized by periodic charging and discharging phases following the activation of local pumps. The graph illustrates how the trend and behavior of water storage are influenced by the operation of local pumps, particularly by their cyclical activations, as well as by pumps in animal buildings. Figure 4.11 illustrates the tracking of artificial lighting loads across all greenhouses in each

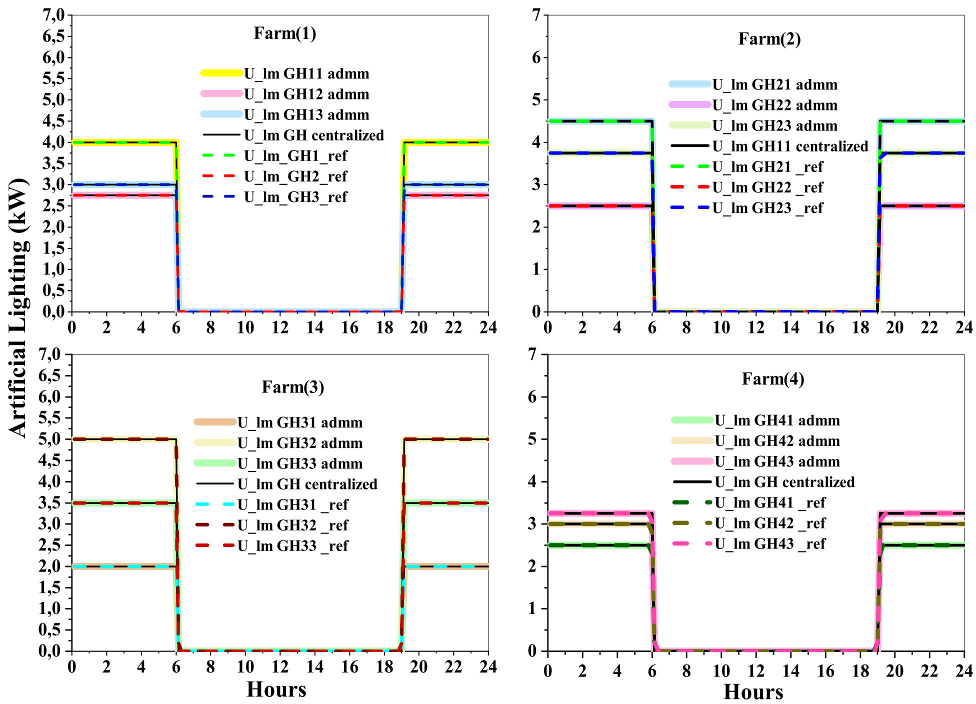

Figure 4.11: Optimal tracking of the artificial lighting loads in each GH(m,n)

farm. Notably, all lighting requirements are met with the support of power purchased from the grid via power link (5), as shown in Fig. (4.14-A). This reliance on grid power is particularly evident during two periods, from 00:00 to 03:00 and 19:00 to 00:00, due to the lack of energy production, especially the absence of photovoltaic (PV) sources during these hours. Fig.4.12 presents the tracking performance of environmental variables at their optimal levels, including interior relative humidity and CO_2 concentration. The injected CO_2 concentration in the greenhouses closely follows the required setpoint, showing minimal variation. The relative humidity remains stable at approximately 64.8 (%), aligning well with the reference for most greenhouses. However, humidity fluctuates between 65 (%) and 70 (%) in GH(1,2), GH(2,1), GH(3,1), and GH(4,3). This variation is primarily affected by temperature drops, specifically from 27(°C) to 22(°C) in GH(1,2), 28(°C) to 23(°C) in GH(2,1), 25(°C) to 22(°C) in GH(3,1), and 26(°C) to 23(°C) in GH(4,3). These fluctuations occur only when the temperature change exceeds 3(°C) , which is expected, as a decrease in temperature leads to an increase in humidity. The results of the optimization depicted in Fig.4.13 generate the optimal powers consumed by equipment for dehumidification, CO_2 injection, and fogging. It's evident that all equipment operates efficiently to regulate the greenhouse microclimate. The CO_2 injection powers continue to operate until they reach their optimal capacity to meet the greenhouse's CO_2 demand, after which they remain constant to maintain the reference concentration throughout the day. Additionally, as shown in Fig.(4.13-B), the dehumidifier initially operates at a lower power with minor fluctuations until 06:00. After 06:30, its power consumption increases until 19:00 due to higher humidity levels in greenhouses, which result from temperature drops inside the greenhouses during the day.

In Fig.(4.13-C), it is evident that the fogging system operates during the day in all greenhouses to help cool the environment, acting as a supplementary system to the HVAC. As the water droplets evaporate, they absorb heat from the surrounding air, creating a cooling effect. This process is especially important during periods of high outdoor temperatures, which can impact the internal

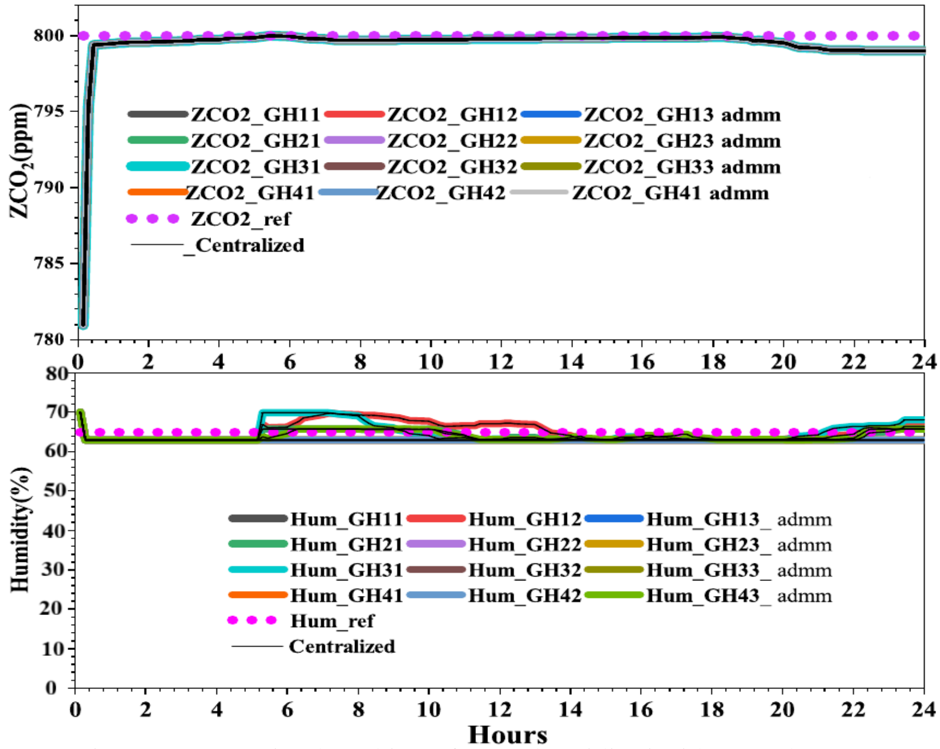

Figure 4.12: Optimal tracking of CO_2, humidity inside greenhouses

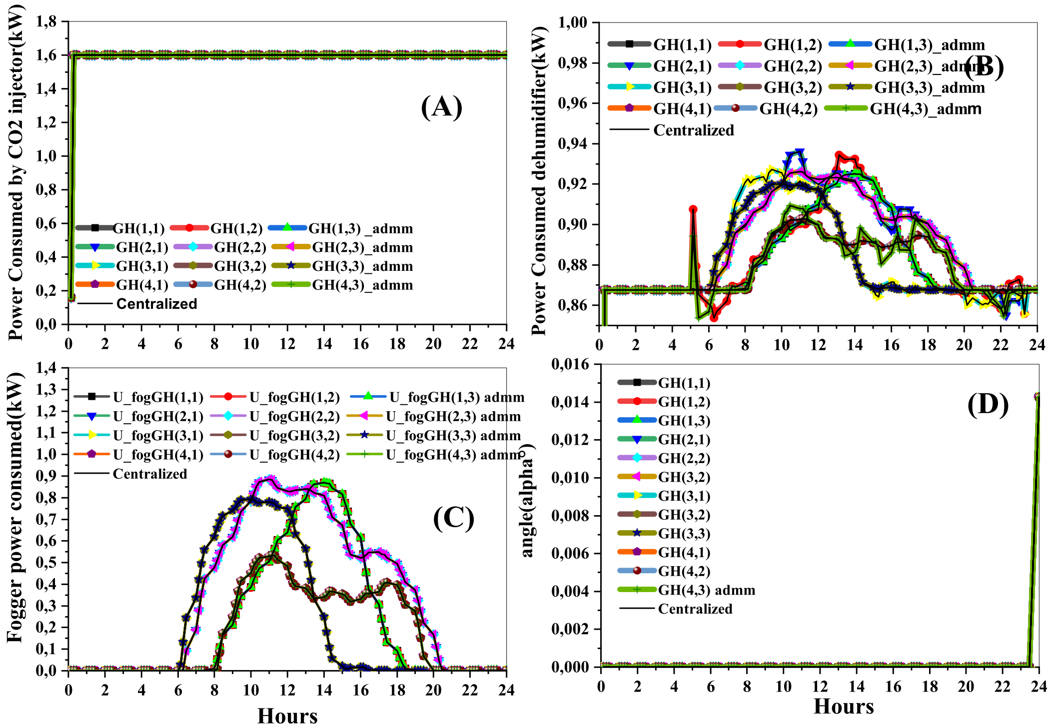

Figure 4.13: Optimal powers are consumed by CO_2 injection, dehumidifiers, and fogging systems with an opening angle in each greenhouse.

microclimate. By preventing excessive heat buildup, the fogging system helps protect plants from heat stress and ensures optimal growing conditions. When considering natural ventilation in greenhouses, it's common to observe a minimal opening angle, as depicted in Fig.(4.13-D). This signifies the deliberate closure of ventilation to minimize heat and CO_2 losses, along with the associated energy waste needed to compensate for such an air exchange reduction.

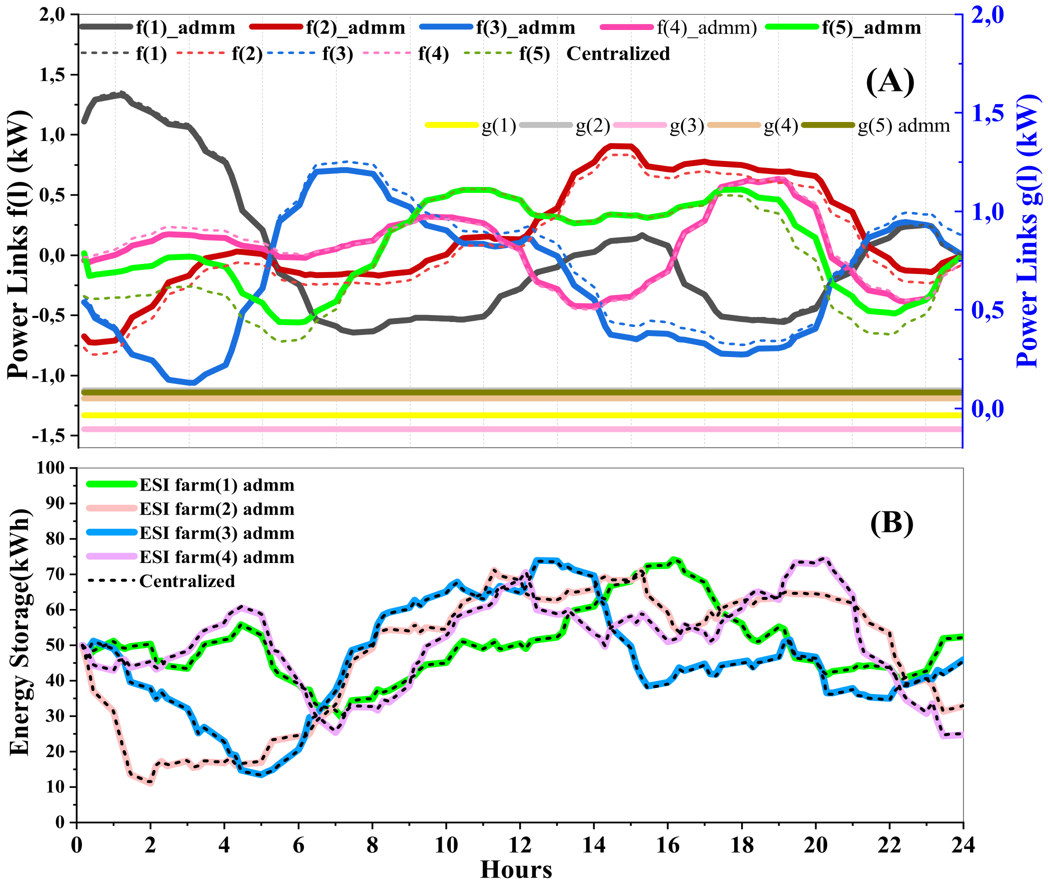

Figure 4.14: The optimal Energy Storage Inventory (ESI) present on each farm and the optimal power exchanges between farms and with the main grid.

In Fig.(4.14-A), optimal power transfers between farms and the main grid are highlighted, allowing energy buying and selling with collaborative efforts among farms. Throughout the day, farms actively respond to power loads, exchanging power via links aligned with farm power balances and influenced by renewable energy source variations. Farm power balances intricately dictate power exchange trends, maintaining a balance between peak demands and renewable generation. Clusters ensure power supply with main grid support from 01:00 to 08:00 and exhibit a similar pattern from 20:00 to midnight. Power is sold to units from 8:00 to 19:00 due to low renewable energy and peak artificial lighting loads, with excess power (power link 5) sold to the main grid during periods of low artificial lighting loads. For $g_l(t)$, the power links remain close to zero due to the constraint in Equation (58), which ensures that the total power exchanged in both directions stays balanced. Since the incidence matrix $b(m,l)$ defines the primary flow of power, the optimization prioritizes $f_l(t)$ as the main exchange variable, while $g_l(t)$ stays minimal to maintain consistency. This confirms that power transfers follow the expected directions, with $g_l(t)$ serving mainly to uphold the balance rather than actively contributing to the exchange.

The optimal dynamic states of the Energy Storage Inventory (ESI), determined by solving the optimization problem, are depicted in Fig.(4.14-B). By accommodating stochastic changes in renewable production, actively responding to power needs, and optimizing supply reliability, the ESI balances energy generation and electric loads while adhering to operational restrictions. It is evident that all ESIs, particularly those located on farms 2 and 3, gradually discharge from their initial value of 50 $[kWh]$ until they reach the minimum allowable amount. This is primarily due to the high peak loads of artificial lighting, as it is presented in Fig.4.11 from 00:00 to 06:00, comparing with other farms. A similar trend is observed between 20:00 and midnight, compounded by the low production of renewable energy, especially solar energy, during this period. From 06:30 to 19:00, the Energy Storage Inventory (ESI) shifts between charging and discharging, driven by renewable energy availability. While HVAC systems consume a significant amount of energy, their impact is lower than that of artificial lighting. Since lighting is not required during the day, overall demand decreases, allowing the ESI to store excess renewable energy and release it when needed to balance the power supply.

The results highlight the effectiveness of the ADMM-based distributed approach in optimizing the microclimate inside greenhouses with optimal operation of equipment. Its performance closely matches that of the centralized approach while offering improved management of power exchanges between interconnected farms and the grid. As shown in Fig.(4.14-A), this is particularly evident in power link (5), which represents power exchanged with the grid. The distributed approach reduces grid dependence between 00:00–08:00 and 20:30–00:00, promoting better use of local energy production. Moreover, the distributed method offers key advantages in terms of scalability and fault tolerance. In a centralized system, computational complexity increases significantly, as illustrated in Fig.**??**. Additionally, centralized control is more vulnerable to failures; if a sensor malfunctions and disrupts the main optimizer or controller, the entire system may fail and crash. In contrast, a distributed approach ensures that if one farm encounters an issue or gets disconnected, the remaining farms can continue operating independently, maintaining system stability. These benefits make ADMM-based distributed optimization a more practical and resilient choice for managing interconnected farms efficiently.

Next, we explore a scenario where power exchanges with the grid are penalized. As depicted in the updated matrix $Z(l,l)$ illustrating the control cost of power in each link, the optimization problem imposes penalties on transactions with the main grid. Specifically, it prevents clustered farms from buying or selling electricity through power link (5) due to the high associated cost. In Figure 4.15-A, power flows through links (1) and (4) follow a similar pattern to the previous scenario, with a slight reduction. Meanwhile, power links (2) and (3) exhibit minor fluctuations, decreasing at certain times and increasing at others, due to cooperative power sharing among farms to meet demand, particularly as farms 2 and 3 generate less energy production. As expected, power link (5) remains at zero, confirming that grid exchanges have been effectively restricted. In Figure 4.15-B, a similar pattern in ESI behavior is evident, although there's a small reduction in stored energy due to the absence of support from the main grid. This emphasizes the importance of meeting cluster power demands. The goal is to confirm the distributed cooperative framework's ability to balance productions and loads, emphasizing the benefits of this cooperative control strategy, which considers variability in renewable energy and fluctuations in loads.

$$\mathbf{Z}(l,l) = \begin{array}{c c} & \begin{array}{ccccc} l1 & l2 & l3 & l4 & l5 \end{array} \\ \begin{array}{c} l_1 \\ l_2 \\ l_3 \\ l_4 \\ l_5 \end{array} & \begin{pmatrix} 0.001 & 0 & 0 & 0 & 0 \\ 0 & 0.001 & 0 & 0 & 0 \\ 0 & 0 & 0.001 & 0 & 0 \\ 0 & 0 & 0 & 0.001 & 0 \\ 0 & 0 & 0 & 0 & 1 \end{pmatrix} \end{array}$$

Additionally, in this scenario, only the operation of the master pumps is affected, which in turn impacts the water levels in each farm's reservoir, as shown in Fig. 4.16-A-B. The decrease in power consumption by the master pumps leads to a reduction in the amount of water transferred from the source to the reservoirs, compared to Fig. 3.11-A-B. This adjustment helps conserve energy, allowing it to be allocated to periods of higher demand, ultimately improving overall energy efficiency. However, this does not compromise the water supply for greenhouses or animal buildings, as the local pumps continue to function effectively, ensuring that water demands are fully met.

Table 4.2: Comparison of Optimization Methods

Criterion	Centralized	Distributed ADMM (ϵ=0.5)	Distributed ADMM (ϵ=0.01)
Objective function (Value)	$2.38782 \cdot 10^2$	$2.35017 \cdot 10^2$	$2.35016 \cdot 10^2$
Grid exchange (kW/24 h)	19.213	17.854	17.853
Computation time (sec)	3780.055	415.236	676.116
No grid exchange (kW/24 h)	−−	< 1	< 1
Computation time (sec)	−−	477.189	477.188

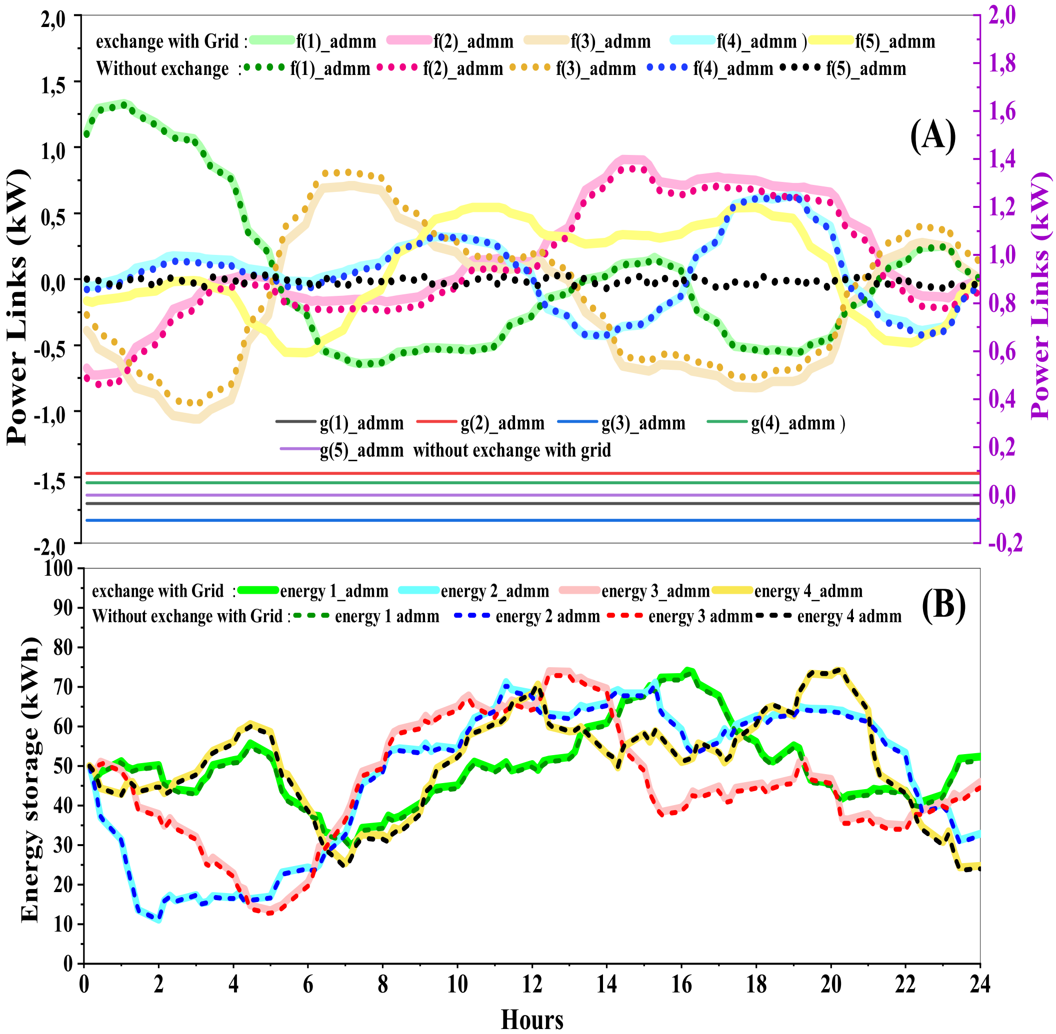

Figure 4.15: The optimal Energy Storage Inventory (ESI) is present on each farm, and the optimal power exchanges between farms without exchange with the main grid.

The optimization problem was solved using both centralized and distributed approaches to evaluate their practical applicability. The system was implemented on an Intel Core i7-1255U laptop using Python-Pyomo with the IPOPT solver. To harness the full potential of the distributed algorithm, parallel programming was employed, assigning each farm's sub-problem to a dedicated CPU core. Algorithm.3 was executed in parallel for each farm, with its scalability illustrated in Fig. 4.17. To validate that adopting an ADMM convergence tolerance of $\epsilon = 0.5$ does not compromise solution optimality, we conducted a sensitivity analysis with more stringent thresholds ($\epsilon = 0.1$ and $\epsilon = 0.01$). The findings (Table 4.2) revealed that the objective function values varied only marginally across all cases, while the computational time for $\epsilon = 0.5$ was substantially reduced. These results confirm that $\epsilon = 0.5$ provides a near-optimal solution with significantly lower runtime, making it a practical choice for real-time farm-level control applications. It yielded a lower objective value ($2.35017 \cdot 10^2$) than the centralized method ($2.38782 \cdot 10^2$) and reduced grid exchange by approximately 7.1% (17.854 [kW/24h] vs. 19.213 [kW/24h]). The algorithm demonstrated remarkable practical efficiency by finding this high-quality solution in just 415.236 seconds, a reduction of nearly 90% in computation time compared to the centralized approach (3780.055 seconds). Even with a stricter $\epsilon = 0.01$ criterion, the computation time (676.116 seconds) remained significantly lower. In a second scenario with penalties for grid exchange to support net-zero energy objectives, the computation time remained low at 477.189 seconds, the same for the second scenario where there was no exchange with the grid. These findings confirm the scalability of the ADMM-based approach, which not only alleviates the computational burden but also

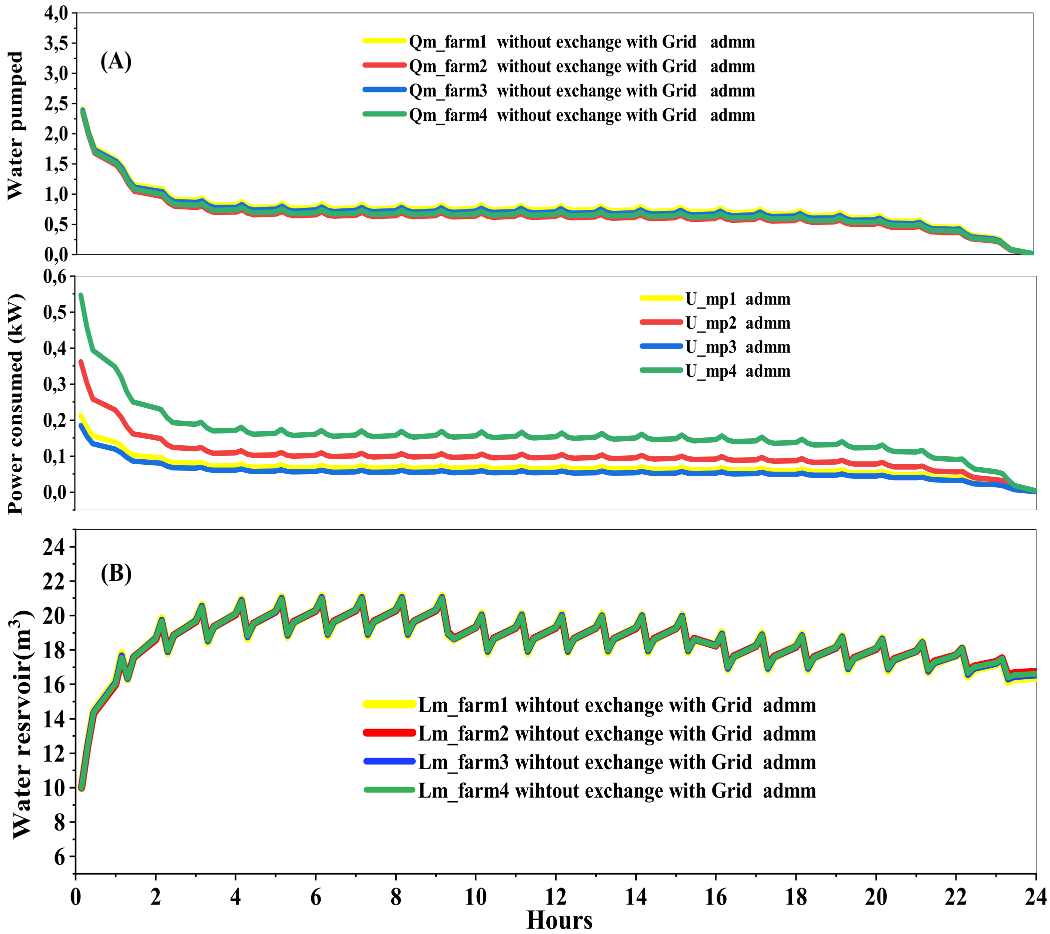

Figure 4.16: Optimal water is pumped into reservoirs with tier power consumption and level water reservoirs at each farm without exchange with the main grid.

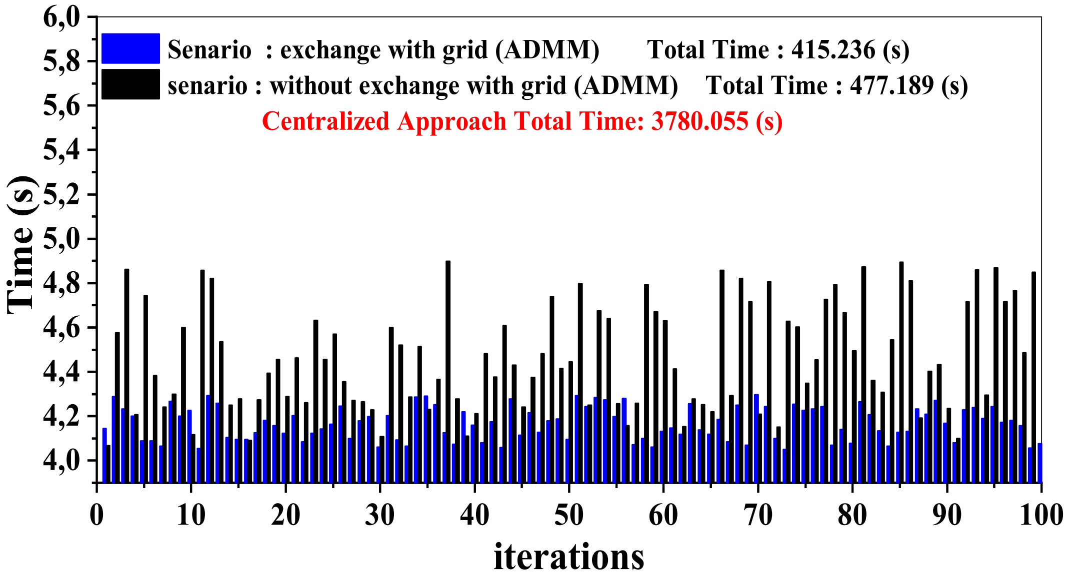

Figure 4.17: The ADMM time is spent for each iteration until max iterations to solve algorithm 1 in both scenarios (with exchange and penalized) compared to the centralized approach.

proves highly suitable for real-time energy optimization in networked farm systems.

4.4 Conclusion

This study introduces a distributed control framework for interconnected net zero-energy farms with integrated microgrids, encompassing smart greenhouses, residential buildings, and animal buildings. This model establishes a smart local power grid within the broader framework of smart grids, serving as an effective tool for regulating indoor climatic environmental parameters in both greenhouses and buildings. Real-time optimization is employed to control the operation of interconnected farms, ensuring optimal tracking of various environmental factors, including temperature, water availability, lighting, humidity, and CO_2 concentration, while managing power flow exchanges and providing superior service quality. The connectivity of farms via power lines enables power exchanges, balancing loads, and leveraging renewable energy sources. The bidirectional communication architecture fosters cooperation, with a distributed controller utilizing an ADMM-based algorithm for enhanced performance. The primary objective is to maximize the transmission and utilization of local renewable generation by capitalizing on the intermittent nature of demands and renewable sources, exploring potential power exchange opportunities across farms to achieve net-zero energy greenhouses. The proposed control approach effectively demonstrates its capacity to meet power load requirements, address various environmental factors, and optimize equipment operation. Through the adept management of four local power linkages, the farms achieve a harmonious balance between renewable energy and power loads, ensuring a stable power supply and advancing the aspiration of achieving net-zero energy greenhouses, independent of the main grid. Overall, the study underscores the importance of collaborative approaches in achieving sustainability goals, emphasizing the significance of smart grid technologies in enabling efficient energy management and environmental control in agricultural settings.

Chapter 5

Optimal Operation Scheduling of a Combined Wind-Hydro System for Peak Load Shaving

5.1 Background and Rationale

Energy demand rises as a result of development, and modern countries rely on energy-intensive industries [87]. Developing clean, renewable energy to replace traditional fossil fuels in the energy system [88] has recently become a goal for all countries [89]. Wind energy is one of the main forms of energy generation because of its promising, sustainable, and clean attributes [90]. Installed wind capacity has been rising from 17 (GW) in 2000 to 732 (GW) in 2020 [91]. By the end of 2020, offshore wind energy deployments will have reached 30 (GW) globally. It still only accounts for a relatively small proportion of the renewable energy produced globally [92]. But due to the uncertainty and intermittency combined with the instability of wind energy, its direct connection to the grid is very limited [93]. There are effective techniques for reducing wind energy's intermittency and power fluctuation, including using a multi-energy hybrid system (MEHS) and relying on energy storage technologies. A bi-level optimal control scheme for grids characterized by renewable and traditional power production, dynamic storage systems, and stochastic modeling issues has been proposed [94]. However, from another perspective, a hybrid system combining different energy sources, such as a hydro-solar-wind system [95], renewable energy, and a wind photovoltaic hybrid system, is a desirable option Each energy source is efficiently exploited in the hybrid multi-energy system, and all of these sources are merged with the goal of attaining full utilization to improve the grid's capacity and reinforce the energy supply to cope with severe environments [96]-[97]. Renewable energies, on the other hand, are difficult to forecast because they are largely dependent on weather and climate conditions. Energy storage is one of the most promising and crucial strategies to increase the efficiency of renewable energy sources while also enhancing environmental sustainability through carbon sequestration [98]-[99]. On a worldwide scale, energy storage is inextricably linked to energy production, with storage requirements continually increasing as intermittent energy demand rises to control generation and load variations [100]. Energy storage often requires transformations by inertia flight [101], energy storage by battery [102], energy storage by thermal energy [103], or energy storage by hydroelectric power [104]. Because of their flexibility and stability, pumped hydroelectric energy storages (PHES) are one of the most commonly used large-scale energy storage systems [105]-[106], allowing for greater penetration of variable renewable energies [107]. Xu and Zhang [108] worked on quantifying the global benefits of hydroelectricity in order to reduce wind energy fluctuation in a hybrid carbon/hydro/wind system. In [109], the authors proposed a mathematical model for estimating the best dimensioning and evaluating the performance of an autonomous electric hybrid system entirely based on variable renewable energy sources and coupled to a hybrid energy storage system. In [110], authors proposed a method for evaluating the complementarity of hydroelectricity in a hybrid energy system while taking into account the volatility in network charge demand. In [111], the authors proposed an optimized energy management for a residential application to reduce grid usage for electricity consumption in the load while increasing the sale of renewable energy. In addition, during high tariff periods, battery storage is allowed to sell excess energy [112]. In the literature, numerous investigations on hybrid wind and hydroelectric systems have been conducted [113]-[114]-[115]. According to their analysis of the operational efficiency of a hybrid wind-hydro power plant on El Hierro, a 11.48 (MW) wind farm and a pumping station are combined in this 11.32 (MW) power facility, which was developed with the aim of harnessing renewable energy to meet the needs of the island rather than the existing diesel generators [116]. In [117], the best daily operating methods for a wind-hydro hybrid system were created. An optimization model for maximizing daily revenue is combined with a long-term and short-term memory network for anticipating power prices on the spot market for electricity the day before. Another study looks at the joint contribution of variable-speed wind turbines (VSWT) and a pumped storage hydropower (PSHP) plant to frequency regulation. The inertial, proportional, and their combinations of control techniques are investigated using the kinetic energy stored in the (VSWT). In general, the (VSWT) controller gains proposed in the literature for interconnected systems are insufficient for isolated systems. As a result, for each of the control techniques, a methodology for tuning the controllers is presented based on an extensive study [118]. In [119], coupling (PHS) equipment to wind power emerged as a solution to overcome the wind power problem. To achieve a balance of power differences, they studied two different operating strategies to maximize market profits and generate a constant target power output. Das et al.[120] investigated the importance of pumped storage systems for grid-connected and stand-alone hybrid systems based on renewable energy. Based on technical and economic data, they found that pumped storage is a superior and more cost-effective storage method than other storage systems. According to Zhang and Xiang [121], they found a case method that verifies the PSH's feasibility and effectiveness to mitigate the rapid fluctuations of PV systems in real time. The configuration between the regulation capacity of PV and PSH is achieved with the requirements of real-time applications. Despite this, according to A. Blakers and M. Stocks [122], PHES research is confined to the investigation of the location of suitable sites for PHES. To oversee the functioning of the integrated smart greenhouse network, Ouammi [123] has developed a thorough finite-horizon scheduling optimization model. The functioning of the integrated smart greenhouse network, which includes forecasts and recently updated information acquired from accessible data, is controlled by a thorough finite-horizon scheduling optimization model. In fact, due to the coupled agriculture need for water, agriculture is probably the main application that can benefit from WF-PHES. Sustainable agriculture cultivation in greenhouses is constantly evolving thanks to new technologies and methodologies able to improve crop yield and solve the common concerns that occur in protected environments [124].

In [125]-[126], a model of the combined transport system was created to account for the additional imbalance costs produced by deviations from the given daily plan while maximizing the total operational benefit of system wind-hydro. To estimate how well a wind farm can work with a pumped storage system to maximize income, shorten the combination's payback period, and fix cascading faults in an electrical grid, a new methodology has been created [127]-[128]. Given its numerous advantages, we investigated hydropower storage rather than battery storage in this study. Hydropower storage has a higher energy density since it can store vast volumes of water in reservoirs, which makes it possible to store a lot of energy. In contrast, the size and capacity of the individual battery cells determine the battery's energy density. In addition, hydropower storage systems provide higher power density and power ratings, particularly in large-scale installations with large turbines and high water flow rates. This allows the generation of substantial power outputs and the ability to quickly ramp up power production when required. Battery power density and power ratings are generally lower and may have limitations due to internal resistance and temperature constraints. Furthermore, hydropower storage systems possess greater capacitance as they can store large quantities of water in reservoirs, enabling long-duration energy storage. Batteries, on the other hand, have limited capacitance due to the size and capacity of individual cells, although they can be scaled by connecting multiple battery modules or banks. Hydropower storage also exhibits high energy efficiency as it converts potential energy in water into electricity, often exceeding 80–90%. In comparison, battery systems have varying energy efficiencies depending on the specific chemistry and operating conditions, typically around 80–90% for lithium-ion batteries. Besides, hydropower storage systems have long lifetimes, often exceeding several decades, and the ability to undergo numerous charging and discharging cycles without significant degradation. Battery lifetimes, while improving, still have finite cycles before capacity degradation, typically lasting several years depending on the chemistry and operating conditions. Finally, the cost of constructing and maintaining hydroelectric power storage systems can be significant, especially for large-scale installations. However, with advancements in technology and economies of scale, battery storage costs have been decreasing. Nonetheless, the overall cost of battery storage depends on factors such as size, chemistry, installation, and system integration. In view of these factors, hydropower storage holds advantages in terms of energy density, power density, power ratings, capacitance, energy efficiency, discharge duration, lifetime, and cycling times, making it a favorable choice for large-scale energy storage applications. As a comparison, reference [129] presented an accurate voltage management and current sharing technique based on distributed adaptive dynamic programming for wind and solar hybrid systems. Comparative simulation results demonstrated the effectiveness of the suggested adaptive dynamic programming approach. Authors in reference [130] proposed a reduced-order aggregate model based on the balanced truncation technique in order to provide a preprocessing method for the real-time simulation of large converters with inhomogeneous beginning conditions in DC microgrids.

From the study of the state of the art, it can be seen that not all the works have studied in depth the aspect of wind energy valorization through the use of the clean energy produced by the wind farms for water pumping in order to reduce the peak powers. To the best of our knowledge, this is the first attempt to control system performance and lessen network load using finite-horizon scheduling optimization. The originality of this paper can be summarized as follows:

- The objective is to propose a new system' design and a practical and complete operational control scheme formulated as a constrained optimization problem embedded in a decision model. The main aim is to optimally control the operation of the WF-PHES system to reduce/shave the peak load in case of occurrence. A finite horizon planning optimization problem is developed to control the real-time operation of the WF-PHES that incorporates both predictions of new states of the power load and winds.
- The proposed framework offers a robust control method that has a comprehensive approach. The primary objective of this method is to reduce or shave peak loads while utilizing the operational flexibility of the Wind WF-PHES system. The framework takes into account uncertainties in factors such as wind power production, power load, rain, water evaporation, and pipeline friction losses. This approach is designed to address these uncertainties effectively within a closed-loop system.
- The developed model is implemented and applied to a case study. The proposed framework has been compared to two distinct non-linear optimization methods: Pyomo with IPOPT solver and Genetic Algorithm (GA) to prove its performance and effectiveness over extensive numerical simulations. The proposed approach may be considered a practical solution to mitigate and address the development challenges of wind energy. The main advantage of the proposed model lies in its capability to cope with the dynamics and uncertainties of wind power production and provide a stable power supply.

The rest of this document is structured as follows: After an introduction in Section I, Section II presents the methodology of the study and the modeling of wind and hydropower plants. The optimization problem is described in Section III. The results and discussions are given in Section IV. The conclusion is presented in Section V.

5.1.1 Methodology

In this study, the combination of two WFs as a clean energy source and a PHES as a pumped storage system are presented. The PHES technology uses the electrical energy provided by the two wind farms to store water in the upper reservoir during off-peak hours when electricity prices are low. Under the effect of gravity, the water stored in the upper reservoir is discharged, saving energy during periods of high demand (peak) or high prices. This means a net benefit despite a small energy loss.

The flowchart in Figure 5.1 shows the relationships between the models used in this paper and the organization of the functions of the proposed methodology. The task of the proposed mathematical model for the system (WF-PHES) is to determine the production of the two wind farms, the pumping station, and the storage capacity of the reservoirs, taking into account the frictional losses in the PHES transfer facilities to cope with the problems caused by the high power demand of the electricity grids, which has been increasing over the years. In order to have a clear understanding of the many possibilities for the best weekly operation of the optimization model, the expected wind speeds and power load for the following week have been shown in Fig. 5.2 and 5.3.

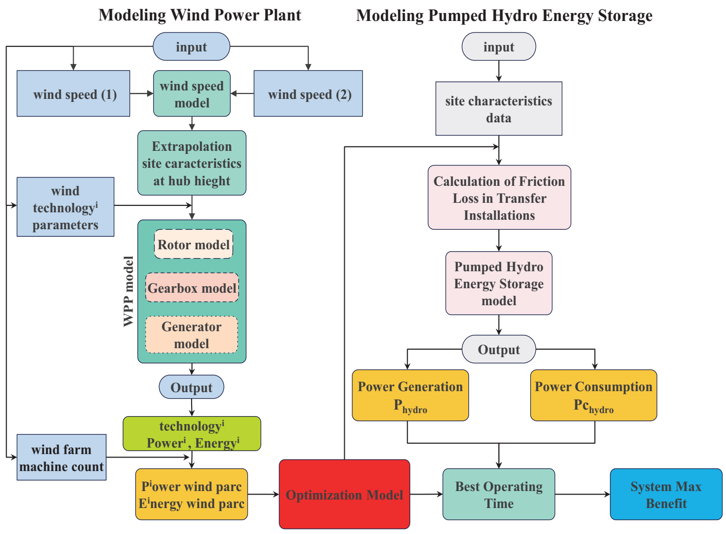

Figure 5.1: Methodology flow chart for model components.

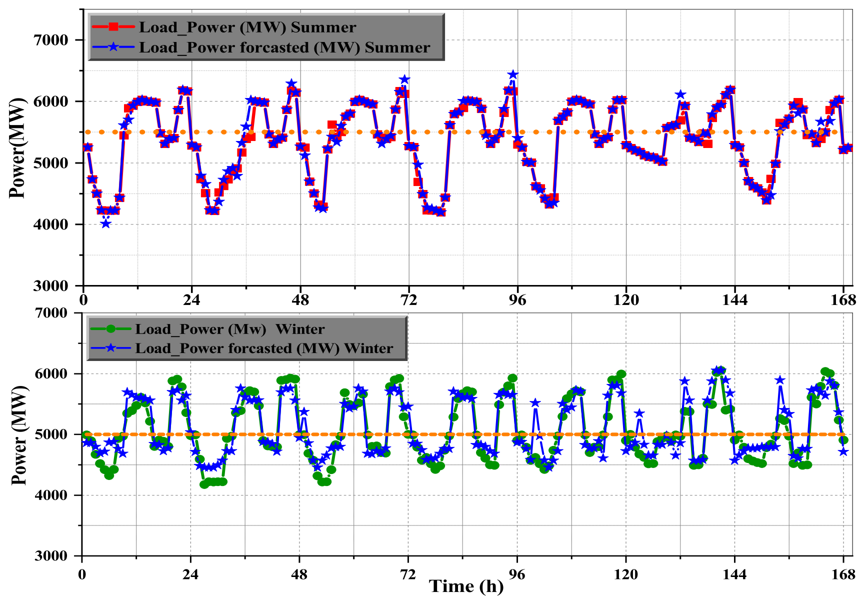

Figure 5.2: Actual and forecasted load power for one week and the next week during the winter and summer seasons.

5.2 Model of Wind power plant production

The power output of the device as a function of wind speed is referred to as the power curve of wind turbines. The rotor (R), gearbox (GB), and generator are the three primary WPP components that determine how much energy and power the machine produces (GE). Consequently, the model used Fig. 5.4 does not consider the system's inertia.

5.2.1 Wind power

The wind power is the time derivative of the kinetic energy of an air mass flowing at a velocity in the direction shown below.

$$P^t_{wind,j} = \frac{dU_c}{dt} = \frac{1}{2} \cdot \frac{d\bar{m}}{dt} \cdot (w^t_{s,j})^2 = \frac{1}{2}\rho_a \cdot A_r \cdot (w^t_{s,j})^2 \cdot \frac{dy}{dt} \tag{5.1}$$

$$\bar{m} = \rho_a \cdot A_r \cdot y \tag{5.2}$$

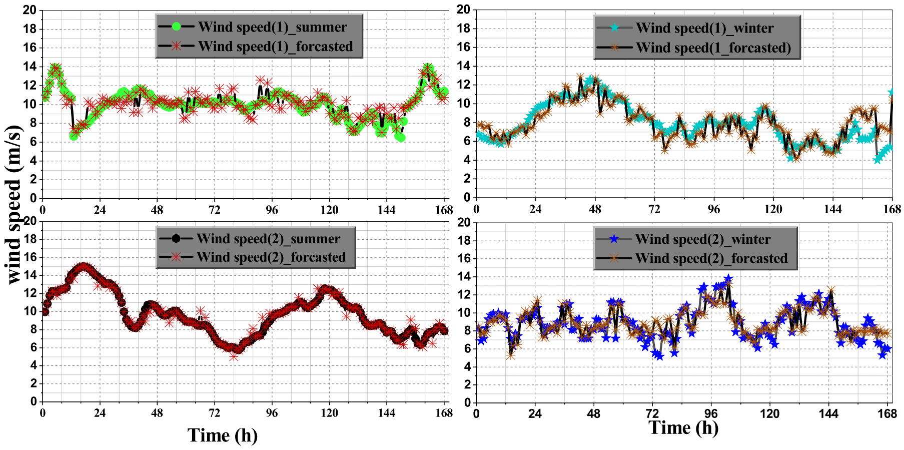

Figure 5.3: Actual and forecasted wind speed for the coming week and the following week during the winter and summer.

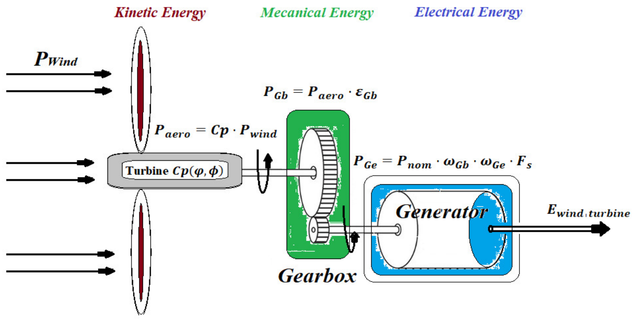

Figure 5.4: wind turbine simple schematization

where $\bar{m}$ is the mass flow of air (kg/s), ρ_a is the air density (kg/m^3), A_r is the rotor's swept surface, j is the wind speed class index, and $w^t_{s,j}$ is the wind speed of the j-th class. As

$$\frac{dy}{dt} = w^t_{s,j} \tag{5.3}$$

It follows that

$$P^t_{wind,j} = \frac{1}{2}\rho_a \cdot A_r \cdot (w^t_{s,j})^3 \tag{5.4}$$

5.2.2 Wind speed extrapolation at various hub heights

Wind speed measurements are taken at a reference height for economic reasons, which is insufficient for the establishment of a wind farm at a location. The vertical wind profile is calculated using the power law. It is written as proposed by [131]:

$$w^t_{hub,j} \;=\; w^t_{s,j}\left(\frac{H_{hub}}{H_{ref}}\right)^{\beta} \tag{5.5}$$

$$\beta = \frac{0.37 - 0.088\ln(w_{s,j})}{1 - 0.088\ln\left(\frac{H_{ref}}{10}\right)} \tag{5.6}$$

where $w_{s,j}$ is the observed wind speed at reference height H_{ref}, $w_{hub,j}$ is the speed that must be computed at height H_{hub}, and β is the power law exponent determined by Equation (5.6).

5.2.3 Modelling a WPP's rotor

The power produced by each technology (i) represents the wind power captured by the rotor in order to transform it into mechanical energy and is written as follows:

$$P^{t,i}_{aero,j} = C^t_P(\phi^i, \varphi^i) \cdot \frac{1}{2}\rho_a \cdot A^i_r \cdot (w^t_{hub,j})^3 \qquad \forall i, j. \tag{5.7}$$

$$A^i_r = \frac{\pi \cdot (D^i_b)^2}{4} \tag{5.8}$$

where D^i_b is the rotor diameter of the $i-th$ technology (m), $C^t_P(\phi^i_t, \varphi^i)$ The power coefficient of the rotor varies over time depending on several parameters, such as wind speed, the operating range parameter φ of wind speed, and by w_{op}, which is the optimal wind speed of the technology used and presented according to the following equation:

$$C^t_P(\phi^i, \varphi^i)_j = C^i_{p\,\max}(\phi^i) e^{\left[-\frac{(\ln w^t_{hub,j} - \ln w_{op})^2}{4 \cdot \ln(\varphi^i)^2}\right]} \forall i, j. \tag{5.9}$$

$$w^i_{op} = \frac{w^i_{nom}}{e^{\left(4.45 \cdot (\ln \varphi^i)^2\right)}} \qquad \forall i. \tag{5.10}$$

where w_{nom} is the nominal wind speed of wind technology, $C_{p\,\max}$ (ϕ_t), is the maximum power coefficient of the rotor. According to the limit of Betz, this coefficient cannot exceed 0.593, which shows that a wind turbine cannot extract more than 59.3% of the kinetic energy of wind. This is expressed by the following equation:

$$C^i_{p\,\max}(\phi^i) = \frac{0.593 \cdot \phi^i \cdot (B^i_l)^{2/3}}{2.5 \cdot 10^{-3} \cdot (\phi^i)^2 + \phi^i((B^i_l)^{2/3} - 0.04) + 1.48} - \frac{0.593 \cdot 2.5 \cdot (\phi^i)^2 \cdot B^i_l}{1 + 2\phi^i \cdot B^i_l} \cdot C_{d/l}. \tag{5.11}$$

$$\phi^i_{op} = \frac{D^i_{bl}}{2 \cdot w^i_{op}} \cdot \varpi^i \qquad \forall i. \tag{5.12}$$

where B_l is the number of blades, ϕ is the rotor speed rate,ϖ angular rotation speed of the ith technology, and $C_{d/l}$ is defined as the ratio of drag and lift coefficients.

5.2.4 Modelling a WPP's gearbox

The gearbox, located at the heart of the wind turbine, transfers the lower speed of the rotor shaft to high speed on the generator side. The overall efficiency of a gearbox $\varepsilon^{t,i}_{GB,j}$ is determined by the rotor's power $P^{t,i}_{aero,j}$, the nominal power P^i_{nom} of the technology utilized, and the efficiency factor of the gearbox ω^i_{GB}, as shown below[132]:

$$\varepsilon^{t,i}_{GB,j} = 1 - \left(1 - \omega^i_{GB}\right)\left(\frac{0.25 \cdot P^i_{nom}}{P^{t,i}_{aero,j}} + 0.75\right) \forall i, j. \tag{5.13}$$

$$\omega^i_{GB} = 0.89 \cdot (P^i_{nom})^{0.012} \qquad \forall i. \tag{5.14}$$

The total produced power, $P^{t,i}_{GB,j}$, taking into account the impact of the gearbox, is thus given by:

$$P^{t,i}_{GB,j} = P^{t,i}_{aero,j} \cdot \varepsilon^{t,i}_{GB,j} \qquad \forall i, j. \tag{5.15}$$

5.2.5 Modelling a WPP's generator

The generator is the component of a wind turbine that turns mechanical energy into electrical energy. The total efficiency of the wind turbine generator may be represented using the following formula:

$$\omega^i_{GEN} = 0.87 \cdot (P^i_{nom})^{14\times10^{-3}} \qquad \forall i. \tag{5.16}$$

$$P^{i}_{GEN} \;=\; F^{i}_{s}(P^{i}_{nom} \cdot \omega^{i}_{GB} \cdot \omega^{i}_{GEN}) \quad \forall i. \tag{5.17}$$

where ω^{i}_{GEN} is the generator efficiency factor, P^{i}_{GEN},is the power of the generator, $P^{t,i}_{GB,j}$, is the amount of power produced by the gearbox, and F^{i}_{s} is the gearbox's factor of service, which can be chosen among various feasible possibilities for each technology: stall-constant-speed (SCS); pitch-constant-speed (PCS); or pitch-variable-speed (PVS) according to the following values:

$$F_s = \begin{cases} 2 \; if \; (SCS) \\ 1.75 \; if \; (PCS) \\ 1.25 \; if \; (PVS) \end{cases} \quad \forall i. \tag{5.18}$$

The efficiency factor of the generator is modelled by the following equation:

$$\varepsilon^{t,i}_{GEN,j} = 1 - (1 - \omega^{i}_{GEN})\left(\frac{5(P^{i}_{GEN})^2}{(P^{t,i}_{GB,j})^2} + 1\right)\left(\frac{P^{t,i}_{GB,j}}{10P^{i}_{GEN}}\right), \forall i, j. \tag{5.19}$$

5.2.6 Modeling a WPP's energy production

To determine the energy produced by a wind farm, three major components of WPPs are considered: the rotor, the gearbox, and the generator. As a result, the model used does not account for power plant features such as the ability to respond to wind changes due to system inertia. The power produced by each wind turbine with a rotor area may be computed as follows:

$$P^{t,i}_{wind\_turbine,j} \;=\; 0.5 \cdot \rho_A \cdot A^{i}_{r} \cdot Cp^{t,i}_{tot,j} \cdot (w^{t}_{hub,j})^3 \quad \forall i,\, j. \tag{5.20}$$

where $Cp^{t,i}_{tot,j}$ denotes the total efficiency of a wind turbine. It may be calculated as follows:

$$Cp^{t,i}_{tot,j} = C^{t}_{P}(\phi^{i}, \varphi^{i})_j \cdot \varepsilon^{i}_{GB,j} \cdot \varepsilon^{i}_{GEN,j} \quad \forall i,\, j. \tag{5.21}$$

The power of the wind farm $P^{t,i}_{wind\_parc,j}$ can be readily calculated by summing the output of each wind turbine in the farm[133].

$$P^{t,i}_{wind\_parc,j} \;=\; \sum_{k=1}^{N_{machine}} P^{t,i}_{wind\_turbine,j} \quad \forall i,\, j. \tag{5.22}$$

The energy produced by each wind turbine $E^{i,t}_{wind\_turbine,j}$ is written as follows:

$$E^{i,t}_{wind\_turbine,j} \;=\; \frac{\Delta t}{2}\rho_a A^{i}_{r} \sum_{j=c_{ut-off}}^{j=c_{ut-in}} Cp^{t,i}_{tot,j}(w^{t}_{hub,j})^3 \, \forall i,\, j. \tag{5.23}$$

In this case, we suppose that c_{ut-in} and c_{ut-off}, which are the wind turbine's cut-in and cut-out wind speeds and Δt denotes the length of the $t - th$ time period in (h). The real energy produced by wind farm may be simply calculated by adding together the wind farm's individual turbines as:

$$E^{t,i}_{wind\_parc,j} = \sum\nolimits_{k=1}^{k=N_{machine}} E^{t,i}_{wind\_turbine,j} \cdot \psi^{i} \quad \forall i,\, j. \tag{5.24}$$

5.3 Model of a pumped hydroelectric energy storage system

The system that needs to be modeled includes a hybrid electrical energy production process that uses two wind farms, one hydroelectric plant, and one booster pumping station to generate electricity. As illustrated in Fig.5.5 the pumping station is connected to a reversible pump-turbine unit along with two reservoirs, and the booster pumping station is connected to the lower reservoir via a hydraulic pump.

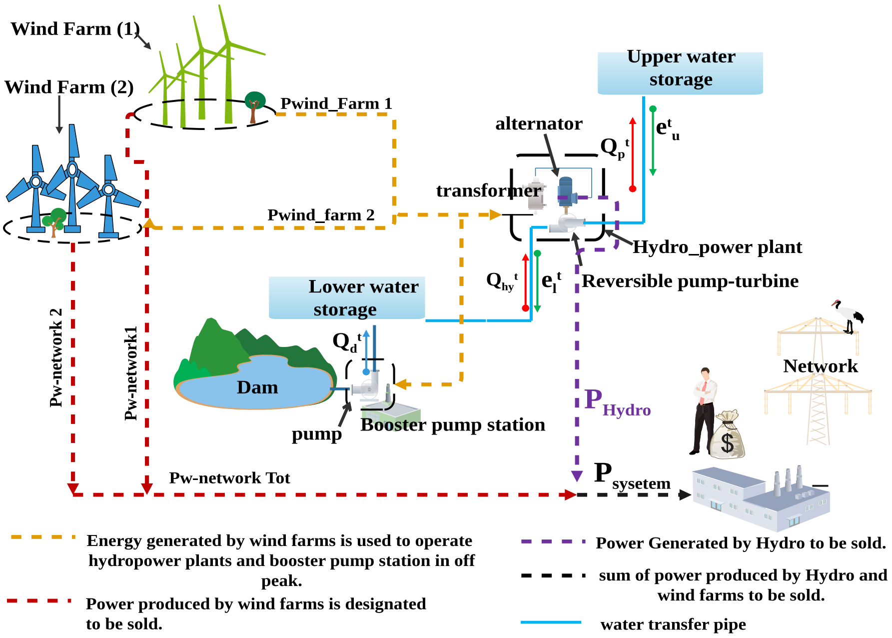

Figure 5.5: The hybrid system of renewable energy.

5.3.1 Power generation in hydroelectric power plants

The water entering the lower water reservoir after leaving the hydroelectric facility is provided by:

$$Q^t_{hy} = e^t_u \cdot \mu_{hy} = \frac{P^t_{hydro}}{\rho \cdot g \cdot (h_{ut} - F^t_{losses})} \tag{5.25}$$

where P^t_{hydro} is the power generated in a power plant in time interval $[t, t+1)$ (MW), ρ is the water density $(kg \cdot m^{-3})$, g is the gravity acceleration constant $(m \cdot s^{-2})$, h_{ut} represents the difference between the altitude of the upper water reservoir and the hydroelectric turbine (m), e^t_u is the outflow from the upper reservoir at time interval $[t, t+1)$ (m^3/s), μ_{hy} is the water loss coefficient in the hydroelectric turbine and F_{losses} is the frictional losses in transfer installations in time interval $[t, t+1)$ (m).

5.3.2 Friction loss in transfer installations

The friction losses in transfer facilities are the sum of major friction losses according to the Darcy-Weisbach equation [134], and minor-local friction losses, as shown in the following equation:

$$F^t_{losses} = \frac{8 f_D}{g\pi^2}\left[\sum_{i=1}^{N^s_p} \frac{L^s_i}{(D^s_i)^5}\left(\frac{Q^t_{hy}}{N^s_{br}}\right)^2 + \sum_{j=1}^{N^d_p} \frac{L^d_j}{(D^d_j)^5}\left(\frac{e^t_u}{N^d_{br}}\right)^2\right] \tag{5.26}$$

where L^s_i, L^d_j are the lengths of the pipes used for suction and discharge (m), D^s_i, D^d_j are pipe diameters for suction and discharge (m), N^s_p, N^d_p are total number of pipe lengths used for suction and discharge, N^s_{br}, N^d_{br} number of pipes used to transport water flows from the upper reservoir through the hydroelectric plant to the lower reservoir and f_D is the Darcy factor which depends on ε the relative roughness of the pipe used. The Colebrook-White equation is the one widely adopted for the calculation of the Darcy factor in the turbulent part of the Moody diagram . It is expressed as:

$$\frac{1}{\sqrt{f_D}} = -2\log_{10}\left(\frac{\left(\frac{\varepsilon}{d}\right)}{3.7} + \frac{2.51}{\mathrm{Re}\cdot\sqrt{f_D}}\right) \tag{5.27}$$

where $\left(\frac{\varepsilon}{d}\right)$ is the ratio of relative roughness to pipe diameter and Re is the Reynolds number. In this study, the implicit formula (27) was solved using the Newton-Raphson mathematical method (numerical method).

5.3.3 Energy production in hydroelectric power plants

The energy generated by the hydroelectric plant is given by:

$$Energy^t_{hydro} = \rho \cdot g \cdot (h_{ut} - F^t_{losses}) \cdot e^t_u \cdot \eta_{hy} \cdot t_{T_r} \tag{5.28}$$

Where η_{hy} is the efficiency of the hydroelectric turbine and t_{T_r} is the operating time of the hydroelectric plant at the time of turbining (h).

5.3.4 Modelling reservoir's

The following two state equations linked to water reservoirs must be modelled:

$$L^{t+1}_u = L^t_u + (Q^t_p - e^t_u) \cdot \Delta t - L^t_{oss,u} - L^t_{Sy,u} \tag{5.29}$$

$$L^{t+1}_l = L^t_l + (Q^t_{hy} - e^t_l + Q_d) \cdot \Delta t - L^t_{oss,l} - L^t_{Sy,l} \tag{5.30}$$

where L^{t+1}_u , L^t_u are volumes of water stored at the upper reservoir at time t and $t+1$ (m^3),L^{t+1}_l,L^t_l are volumes of water stored at the lower reservoir per time step $[t, t+1)$ (m^3),Q^t_p is the water flow entering the upper water reservoir per time step $[t, t+1)$ (m^3/s),Q_d is water flow that supplies the lower basin with water at the first filling and continuously to compensate for the effects of evaporation at time t and $t+1$ (m^3/s) and $L^t_{osses,(u,l)}$ is the water loss due to the difference between evaporation and precipitation related to the reservoir per time interval $[t, t+1)$ (m^3) [135]. It is expressed as:

$$L^t_{osses,(u,l)} = S^t_{r(u,l)} \cdot Eev^t_{(u,l)} \tag{5.31}$$

where $S^t_{r(u,l)}$ is the area of reservoirs structure (upper and lower) (m^2) and $Eev^t_{(u,l)}$ is the difference between the evaporation and precipitation rates of the reservoirs per time interval $[t, t+1)$ (m), and $L^t_{Sy,u}$, $L^t_{Sy,l}$ are volumes of sediment yield in upper and lower reservoirs per time interval [t, t+1)(m3) [136]. The reservoir spillway equation is written according to the following equation [**?**]:

$$\left(1 - \frac{L^t_{(u,l)}}{C_{ap(u,l)}}\right) \cdot L^t_{sp(u,l)} = 0 \tag{5.32}$$

In which $L^t_{sp(u,l)}$ is the volume of water discharged from the reservoirs (upper and lower) at the time step (m^3), It is expressed as:

$$L^t_{sp(u)} = e^t_u \cdot \Delta t \qquad and \qquad L^t_{sp(l)} = Q^t_p \cdot \Delta t \tag{5.33}$$

$C_{ap,(u,l)}$ is the reservoir's storage capacity either (upper) or (lower) (m^3). This equation (5.32) demonstrates that overflow can occur when the volume of water stored in a reservoir exceeds the reservoir's storage capacity.

5.3.5 Power Consumption in Hydroelectric Power Plants

According to the following equation, the flow rate of water entering the top reservoir is proportional to the power used:

$$e^t_l = \frac{P^t_{C,hydro}}{\rho \cdot g \cdot (H_{ul} + F^t_{losses})} \tag{5.34}$$

$$Q^t_P = e^t_l \cdot \eta_P \tag{5.35}$$

in which $P^t_{C,hydro}$ is the power consumed in a power plant in time step t (MW), H_{ul} is the difference between the altitude of the upper and lower water reservoir (m) and Q^t_P is the water flow entering the upper water reservoir per time step t (m^3).

5.3.6 Energy Consumption in Hydroelectric Power Plants

The energy consumed by the hydroelectric plant at the time of pumping is given by:

$$Energy^{t}_{C,hydro} = \frac{\rho \cdot g \cdot (H_{ul} + F^{t}_{losses}) \cdot Q^{t}_{P}}{\eta_{P}} \cdot t_{p} \tag{5.36}$$

where η_p is the efficiency of the pump and t_p is the hydroelectric plant's pumping time (h).

5.3.7 Modelling of booster pump station

The purpose of the booster pumping station is to supply water to the lower reservoir at the first fill and continuously thereafter to compensate for the effects of evaporation. In order to guarantee the water supply regardless of the water levels in the reservoir and to prevent sediment problems during floods, a booster pumping station will be installed near the dam.

Energy of consumption of the booster pump station

The Booster Pump Station's energy consumption while pumping is given by:

$$Energy^{t}_{C,(BPS)} = P^{t}_{C,(BPS)} \cdot t_{lp} = \frac{\rho \cdot g \cdot H_{dl} \cdot Q^{t}_{d}}{\eta_{lp}} \cdot t_{lp} \tag{5.37}$$

In which $P^{t}_{C,(BPS)}$ is the power consumed by the booster pump station in time step t (MW), H_{dl} is the difference between the altitude of lower water reservoir (m) and the dam, Q^{t}_{d} is the water flow entering the lower water reservoir per time step t (m^3) η_{lp} is the efficiency of the pump and t_{lp} is the operating time of the Booster pumping station (h).

5.4 Planning optimization for WF-PHES

The objective function and restrictions of the WF-PHES scheduling optimization problem are described below. The goal of the proposed optimization model in this study is to determine the best weekly operating strategy to maximize system revenue. In times of high demand, this means a likely smaller disparity between the power produced by the system and the power of the load.

5.4.1 Objective Function

The objective function is defined as the minimization of the peak load powers on 7 days sampled each hour.

$$J^{*} = min \sum_{t=1}^{168} (P^{t}_{Global} - P^{t}_{load})^{2} \tag{5.38}$$

5.4.2 State equations

The volumes of water stored in hourly steps in the reservoirs during the week are given by equations (5.29)-(5.30).

Equations of the model

$$P^{t}_{Global} = P^{t}_{system} + P^{t}_{Grid} \tag{5.39}$$

$$P^{t}_{system} = P^{t}_{w.Network\_tot} + P^{t}_{hydro} \tag{5.40}$$

$$P^{t}_{wind,parc\_tot} - P^{t}_{C,hydro} - P^{t}_{C,(BPS)} = P^{t}_{w.Network\_tot} \tag{5.41}$$

$$P^{t}_{wind,parc\_tot} = P^{t}_{wind,parc(1)} + P^{t}_{wind,parc(2)} \tag{5.42}$$

$$P^{t}_{w.Network\_tot} = P^{t}_{w.Network(1)} + P^{t}_{w.Network(2)} \tag{5.43}$$

$$P^{t}_{hydro} \cdot P^{t}_{C,hydro} = 0 \tag{5.44}$$

Benefits of the system

The benefits of the system will be calculated according to the following equation:

$$C^t_{benifit} = C_{(wind)} \cdot P^t_{w.Network\_tot} \cdot \Delta t + C^t_{(hydro)} \cdot P^t_{hydro} \cdot \Delta t \tag{5.45}$$

The optimization variables are all described in Table.(5.1).

5.4.3 System operation (WF-PHES) in summer and winter seasons

During the summer and winter seasons, researchers investigated how much power is consumed in a typical week and how much is predicted for the following week. Because of the weather, demand is higher in the summer than in the winter, as indicated in Fig. 5.2. There are two operational scenarios for the system, one for each season.

Off-peak periods (Pumping - Mode)

: These periods are defined in summer with $P^t_{load} \leq 5500$ and in winter with $P^t_{load} \leq 5000$. In these periods, it holds that:

$$\begin{cases} P^t_{hydro} = 0 \\ P^t_{wind,parc(1)} + P^t_{wind,parc(2)} = P^t_{C,hydro} - P^t_{C,(BPS)} \\ P^t_{w,Network\_tot} = 0 \end{cases} \tag{5.46}$$

Peaks periods (Turbining - Mode)

: These periods are defined in summer with $P^t_{load} > 5500$ and in winter with $P^t_{load} > 5000$. In these periods, it holds that:

$$\begin{cases} P^t_{wind,parc(1)} = P^t_{w,Network(1)} \\ P^t_{wind,parc(2)} = P^t_{w,Network(2)} \\ P^t_{Grid\_(summer)} = 5500 \quad \& \quad P^t_{Grid\_(winter)} = 5000 \end{cases} \tag{5.47}$$

5.4.4 Constraints governing the problem

The WF-PHES system planning optimization issue is constrained by the following factors:

Power constraints

The installed pumping capacity of the power plant must be met or exceeded by the power generated by wind farms.

$$P^{t,i}_{wind\_parcs,j} \leq P^t_{C,hydro} \qquad \forall i, t. \tag{5.48}$$

Storage constraints (volume stored)

$$L^t_{u,(\min)} \leq L^t_u \leq L^t_{u,(\max)} \qquad \forall t. \tag{5.49}$$

$$L^t_{l,(\min)} \leq L^t_l \leq L^t_{l,(\max)} \qquad \forall t. \tag{5.50}$$

Spillway constraints

$$L^t_{sp(u,l)\min} \leq L^t_{sp(u,l)} \leq L^t_{sp(u,l)\max} \quad \forall t. \tag{5.51}$$

$$L^t_{(u,l)\max} \leq C_{ap,(u,l)} \qquad \forall t. \tag{5.52}$$

This requires solving a constrained non-linear programming problem, which can be done using any currently used optimization solver, such as NLP's LINGO.18.

Table 5.1: Optimization Variables

$Variables$	$Definition$	$Unit$
P_{load}	Power load over time.	[MW]
P_{Global}	is the total of the grid's existing power plus system-generated power.	[MW]
P_{system}	the sum of powers generated by hydroelectric and wind farms.	[MW]
P_{hydro}	power generated by a hydropower plant.	[MW]
$P_{w.Network_tot}$	Power total to sell generated by some wind farms(1) and (2).	[MW]
P_{Grid}	existing power in the grid over time.	[MW]
$P_{C,hydro}$	power consumed by a hydropower plant.	[MW]
$P_{C,(BPS)}$	power consumed by a booster-pumped station.	[MW]
$P_{wind,parc_tot}$	the sum of powers produced by wind farms (1) and (2).	[MW]
$C^t_{Benefit}$	is the system profit over time	[/MWh]
$C_{(wind)}$	price of kilowatt hour produced by wind farms.	[–]
C_{hydro}	price of kilowatt hour produced by hydroelectric plant.	[–]

5.5 Application to case studies and numerical results

5.5.1 WPP model accuracy

The WPP model proposed in Section (5.2) has been widely applied, and its reliability is confirmed by the calculation of the technical power curves of the following commercial wind power plants: Gamesa G52-850 and SWT 2.3-101. Table (5.2) specifically considers facilities with the following geometric and technical characteristics:

Table 5.2: WPP parameters

$Parameters$	$Gamesa$ $ga52/850$	$Simiens$ $SWT/2300$	$Unit$
$Hhub$	65	100	$[m]$
Ar	2124	8000	$[Kg.m^2]$
N	30	16	$[rpm]$
B_l	3	3	$[---]$
$C_{d/l}$	0.0083	0.0083	$[---]$
Fs	1.25	1.25	$[---]$
Wop	14	12.5	$[m/s]$
φ	1.45	1.45	$[---]$
Db	52	101	$[m]$
$Pnom$	850	2300	$[KW]$

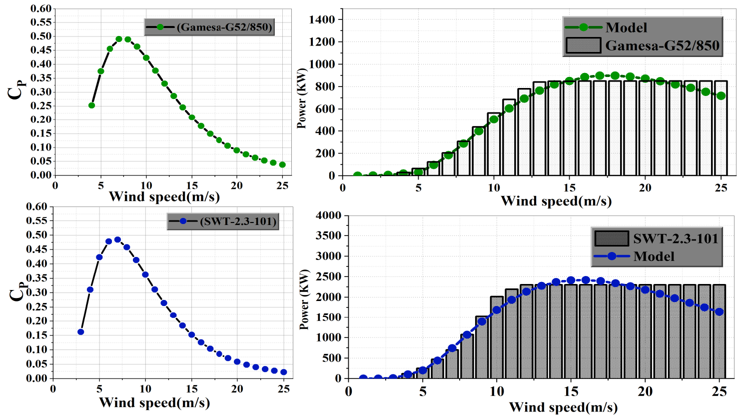

Figure 5.6: power coefficient Cp of each technology as derived by equation (5.9), and a comparison between the manufacturer's power curve and the model's computed power curve.

The technical power curves for the technologies used in the two wind farms are shown in Fig. 5.6 together with the power curves derived from equation (5.20).

The wind turbine model presented in this section has been validated in the previously conducted works of the authors. The first verification of the model has been performed using a comparison with the technical power curve for a commercial WPP (S52- 600 kW-50 Hz). The second verification has been performed on an existing WPP farm. The reader may also find more detailed discussions on the model reliability in[137]-[87]

5.5.2 Hybrid model WF-PHES

The optimal control of the WF-PHES system is formulated based on the system modeling described in Sections (5.2, 5.3) and (5.4) and is simulated and tested through two different seasons and by applying the deterministic case based on real data and the probabilistic case based on outputs obtained by a forecast, which is not an objective of this work. According to the system architecture proposed in Fig. 5.5, this study has been applied and solved based on the information available for WF1 and the other WF2, in addition to a hydrological system that is being completed. In particular, there are two pumping stations, lower and upper water reservoirs, and a dam, and all these features are present in the study area. The main pumping station, which forms a closed system with the two reservoirs, is intended to store water during off-peak periods and generate energy during peak periods. The second pumping station, known as the booster pumping station, is designed to pump water from the dam to the lower reservoir to compensate for water losses such as those caused by evaporation during periods of rising temperatures.

5.5.3 Simulation setup

Two wind farms make up the suggested system. The total installed power in WF1 is 60.3 (MW), with the first one having 71 turbines of the Gamesa type, each with a capacity of 850 (kW).The second WF2 is made up of 131 Siemens-type turbines with a combined power of 2.3 (MW), with a total installed power of 301 (MW). In this paper, historical wind speeds have been inferred using an Artificial Neural Network (ANN) algorithm to establish a forward or reverse correspondence between the calendar data and the wind speed. A three-layered, back-propagation standard ANN classifier has been used, consisting of three layers: input, hidden, and output. 80% of the data has been used for training the ANN, and the rest is used in the testing phase. Finally, a comprehensive wind power plant is used to estimate the wind power generation. A storage system based on the PHES technology, which entails a reversible pump-turbine grouping with a power greater than or equal to the combined power of the two wind farms to pump the water to the upper reservoir and turbinate it to the lower reservoir through the transfer facilities, and finally, the presence of a booster pumping station to account for the effects of evaporation for both reservoirs. the water circuit of about 3 (km), including a penstock connecting the two basins and feeding the plant. The reservoirs have a storage capacity of $4 * 10^6$ (m^3), and the parameters and settings are all listed in that order in Table (5.3).

Table 5.3: PHES parameters

Parameters	*Value*	*Unit*
g	9.81	$[m.s^{-2}]$
ρ	999.93	$[Kg.m^{-3}]$
$C_{ap(u,l)}$	4.10^6	$[m^3]$
h_{ut}	550	[m]
H_{ul}	580	[m]
Δt	1	[hour]
$S_{r(u,l)}$	2.10^5	$[m^2]$
η_p	0.9	[—-]
μ_{hy}	0.75	[—-]
H_{dl}	70	[m]
η_{lp}	0.9	[—-]
$D_{s(min-max)}$	(3.6 - 5)	[m]
$D_{d(min-max)}$	(3.5 - 5)	[m]
L_s	736	[m]
L_d	2300	[m]
$N_{br}^{s,d}$	1	[—-]

The power produced by WF1 and WF2 during a week in July and a week in January are presented in Figure.5.8 and Figure.5.7. By storing water in the upper reservoir outside the hours when the load power is less than 5500 (MW) in summer and 5000 (MW) in winter, as shown in Fig 5.7, these powers are often used for PHES. The additional power should be mainly covered by the WF-PHES system if the load power exceeds 5000 (MW) in winter and 5500 (MW) in summer. Based on accurate and forecasted data on load capacities and wind speed, the duration of the real-time simulation was set to 168 hours with a time step of one hour. For each time step, the optimization has been solved to identify the optimal control strategy that reduces the power peaks, which leads to significant system benefits. Lingo optimization software has been used to solve the proposed problem.

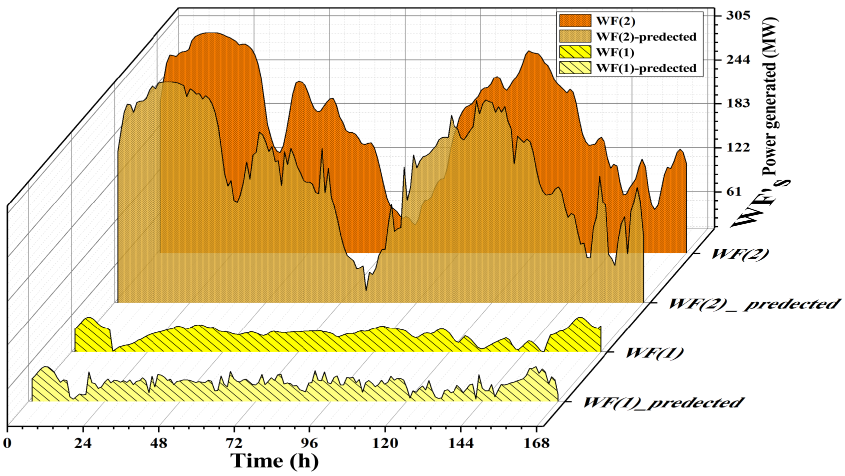

Figure 5.7: The variation of the power produced and predicted by each wind farm over the course of a week during the summer season is determined by Eq (5.22).

5.5.4 Price structure

A procedure known as a power purchase agreement (PPA) is used to determine the cost of wind energy over a specific length of time, such as a week or a month. In a PPA, a wind power producer and a customer, like a utility company, agree to sell a specific amount of electricity at a specific cost. Water

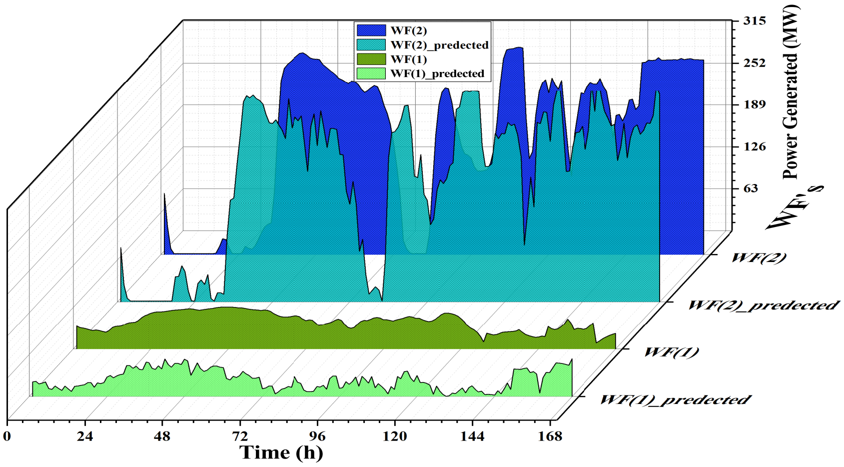

Figure 5.8: The variation of the power produced and predicted by each wind farm over the course of a week during the winter season is determined by Eq (5.22).

availability, electricity demand, and the cost of producing electricity from other sources are some of the variables that can affect how much hydro costs. In this study, 1 (kWh) will be sold at a price that is generally considered to be fixed compared to the price of electricity generation from other energy sources. for 1 (kWh) to be sold at 0.200 (), although the cost of the (kWh) produced by hydroelectricity is fluctuating. Unlike fossil fuels, the price per (KWh) can vary according to market demand and other factors, although it is about 0.300 () per (kWh) during average peaks and about 0.450 () per (kWh) during peak hours.

5.5.5 Results and analysis

The optimization problem aims at minimizing the power peaks through the system operation strategies provided by the optimization, taking into account the actual and anticipated wind data and power loads in order to provide future state trajectories for ensuring optimal system operation during various seasons. The water reservoirs' initial states as $L_u^t(0) = 1000(m^3)$ and $L_l^t(0) = 3.7 \cdot 10^6(m^3)$, respectively. In both deterministic and probabilistic scenarios, Fig. 5.7 and 5.8 display the power generated by the two wind farms during the summer and winter seasons that is used by the hydroelectric plants during off-peak times and that is offered for sale to the grids $P^t_{w,Network_tot}$ during peak times. Fig. 5.9 and 5.10 show how the overall weekly peak loads have changed dynamically. In the deterministic and probabilistic instances for the system throughout the summer, the peak loads are decreased by 99%. With a contribution of 49 % and a rate of up to 14119.91 (MW), or over half of the system. The system shows good performance;in addition, a contribution of 50% has been made at a rate of up to 14522.08 (MW) by the $P_{wnetwork-tot}$, which reflects the entire amount of power produced by wind farms for sale to the network. There is only one noticeable difference, a small difference, which is the low energy of hydropower at a value of 13996.71 (MW) equivalent to 48.86% while at the same time, there is a notable increase in $P_{wnetwork-tot}$ at a value of 14645.28 (MW), which is 90% of the capacity produced by WF2 and 10% for WF1. In Fig. 5.10, during the winter season, the system manages to reduce peak power by 88.5% for the deterministic case and 75.34% for the probabilistic case, respectively. With a contribution of 50.69% and a rate of up to 18020.81 (MW), i.e., more than half of the system. In addition, a contribution of 49.31% was made at a rate of up to 17527.29817 (MW) by the $P_{w,Network-tot}$, which reflects all the energy produced by the wind farms for sale to the grid, i.e., 15.2% of the capacity produced by the wind farm (1) and 84.88% for the wind farm (2) for the probabilistic, a contribution of 53.15% and a rate of up to 17750.84 (MW), i.e., more than half of the system, by the $P_{w,Network-tot}$, which reflects all the energy produced by the wind farms and is destined to be sold to the grid. This is 10.12% of the capacity produced by the wind farm (1) and 90.98% for the wind farm (2). Hydroelectricity has contributed 46.84% at a rate of up to 15644.9817 (MW).The discrepancy between wind speed and load power forecasts and actual data is what causes this divergence between probabilistic and deterministic scenarios. The best results of the PHES technology during the pumping periods and their flow rates during the summer and winter seasons are shown in Figure 5.11. $P_{C,hydro}$ pumping became active in the summer during the off-peak

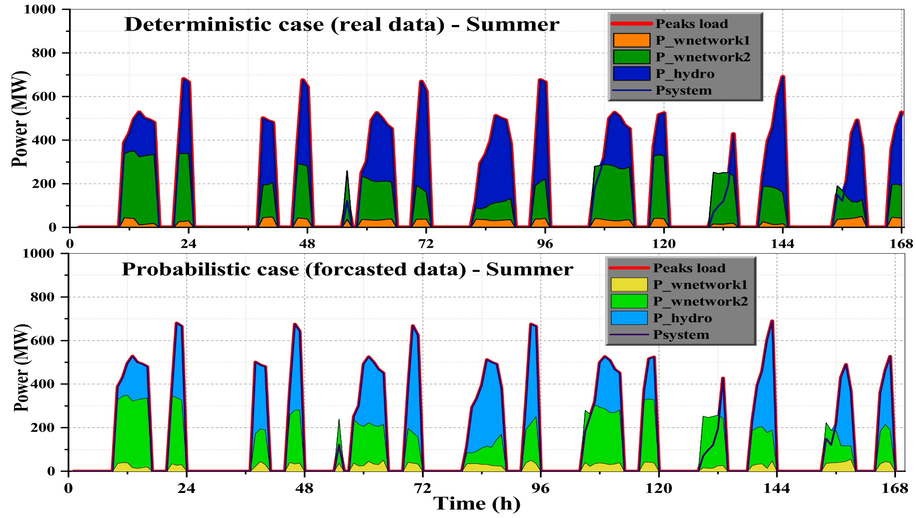

Figure 5.9: Reduction of the peak load by the system during the winter season in the deterministic and probabilistic cases.

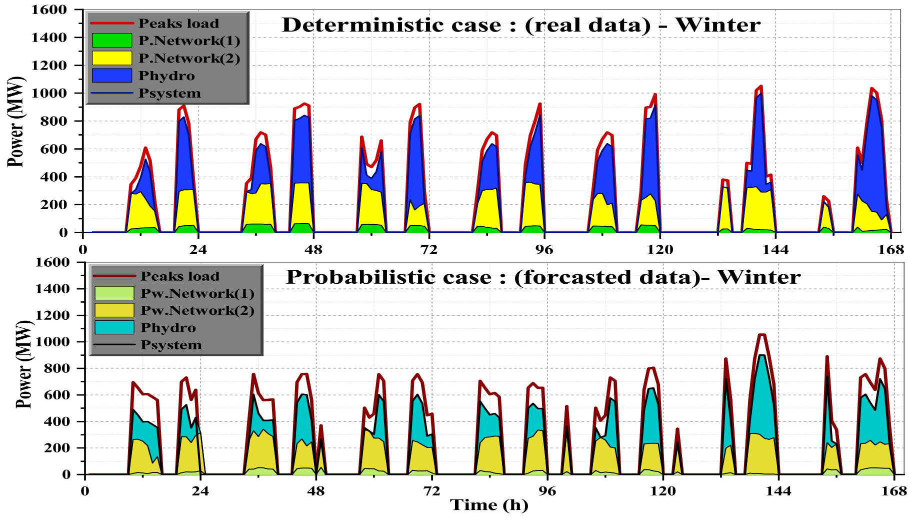

Figure 5.10: Reduction of the peak load by the system during the winter season in the deterministic and probabilistic cases.

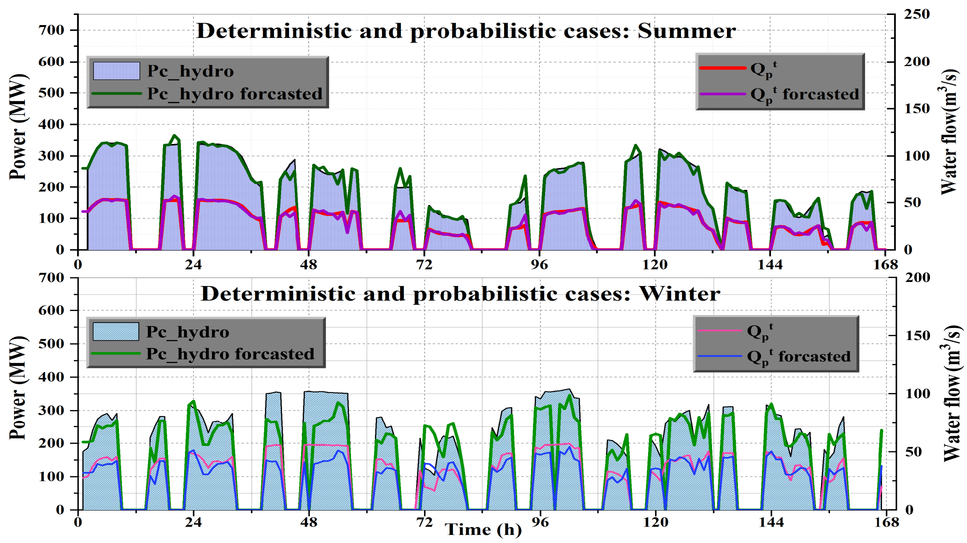

Figure 5.11: Optimal operation of the PHES technology proposed by the optimization model during a summer week.

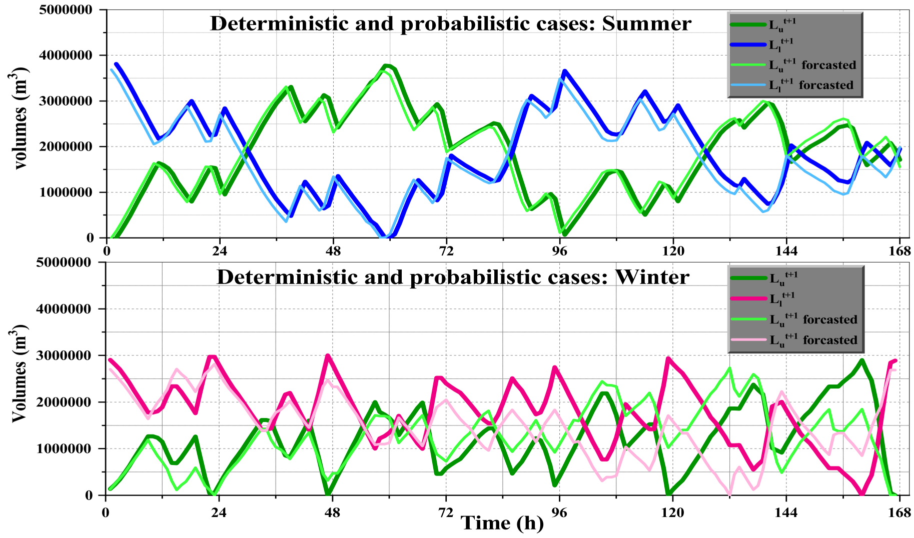

Figure 5.12: The variation of the volumes of water stored in the reservoirs during the function of the PHES technology during a week.

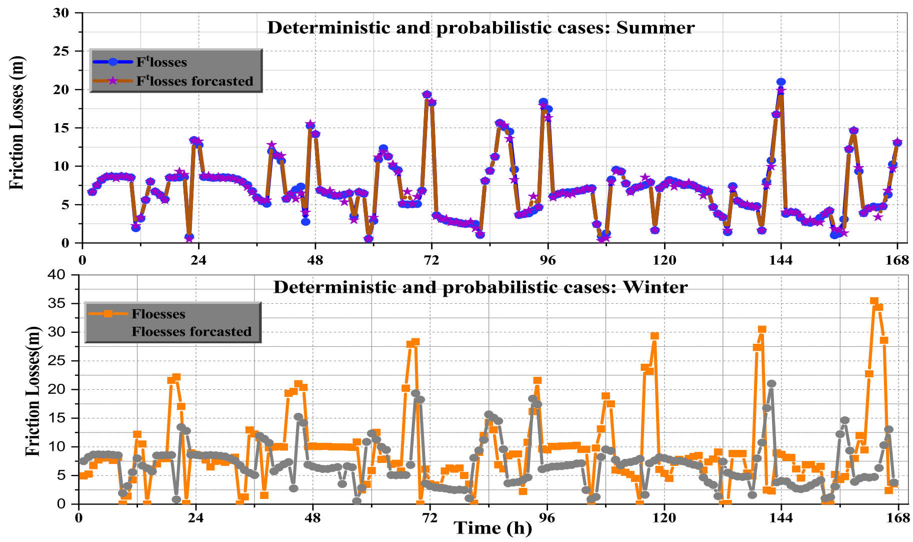

Figure 5.13: The variation of the friction losses in transfer installation during the function of the PHES technology .

period using the energy supplied by the wind farms and reached a maximum value of 342 (MW) on the first day of the week in the deterministic case and a maximum value of 366 (MW) in the probabilistic case In winter, the pumping $P_{C,hydro}$ reaches a maximum value of 351 (MW) on the fifth day of the week in the deterministic case and a maximum value of 348 (MW) in the probabilistic case. The operating conditions given to the optimization model were well respected. Fig. 5.12 shows the ideal results of measuring the summer and winter water storage volumes in the proposed upper and lower reservoirs. It can be seen that it is assumed that the maximum reference volume should not exceed the storage capacity of the reservoirs, which according to equation (5.32) has a value of $4 * 10^6(m^3)$ over the whole time horizon. This test demonstrates the fact that the stored water quantities, reach a maximum value of $3.7 * 10^6(m^3)$ in summer and $2.8 * 10^6(m^3)$ in winter in both reservoirs for the real and probable scenarios. The reason for the decrease in water volumes in winter is due to the increase in peak power and the decrease in wind speed throughout the wind farm (2) compared to the summer season. During one week of study, it is usual that extremely low reservoir siltation values have no impact on the water quality or reservoir levels. due to the fact that the effects of reservoir siltation and water level decreases on system operation begin to manifest after a year and beyond. The results of the frictional loss in the transfer facilities, as shown in equation (5.26), are presented in Fig. 5.13. High losses occur at different seasons of the year and in deterministic and probabilistic situations,

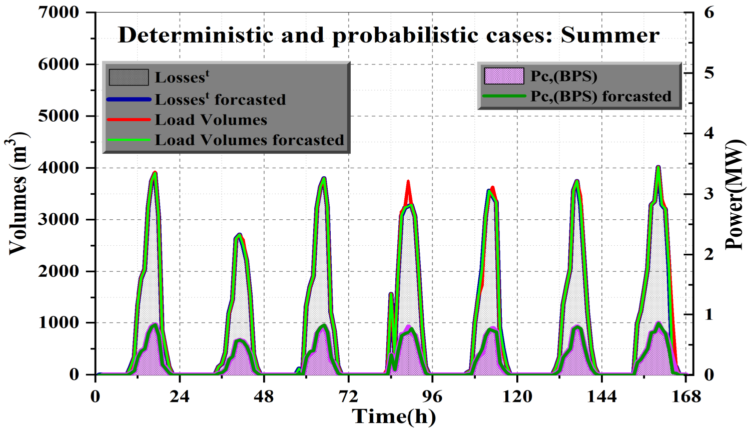

Figure 5.14: Depicts the change in the amount of water evaporated by the two reservoirs over the course of a summer week.

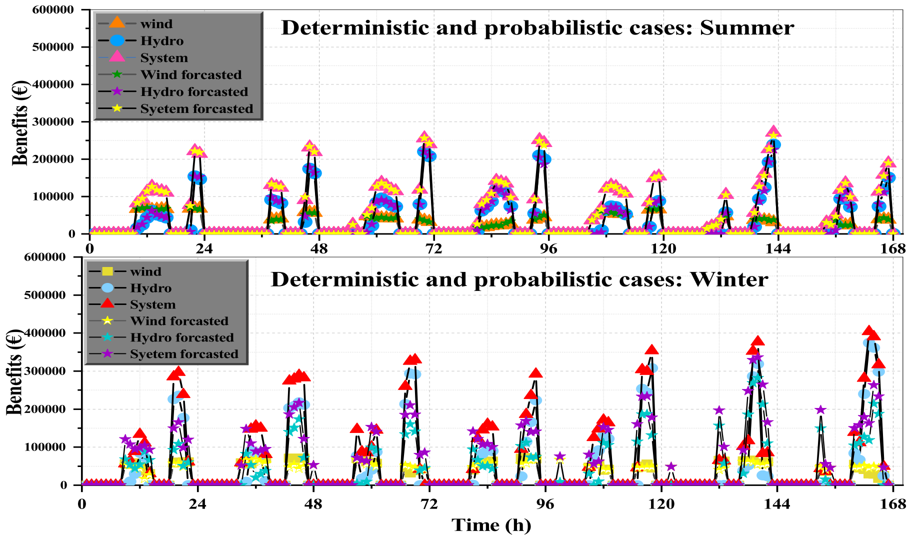

Figure 5.15: The benefits of the system for the summer and winter seasons for one week in the probabilistic and deterministic cases.

especially during peak periods, or "turbining periods," due to the extremely high values of turbined water flows that result in higher impacts on the pipe walls as the system is turbulent, unlike pumping periods where pumped water flows are typical. The evolution of the amount of water evaporated by the two reservoirs during a foreseeable and probabilistic summer week is presented in Fig. 5.14. The peaks can be observed almost every day, from 10 a.m. to 5 p.m., which is natural because of the high temperatures during these periods of the day during the summer. The booster pumping station managed to reduce the total peak evaporation volumes of both reservoirs during the week by a maximum value of 0.85 (MW) of power consumption. In this study, the amount of water evaporated by both reservoirs in the winter season for both scenarios is null due to the low temperatures. Fig. 5.15 shows the advantages of the system for deterministic and probabilistic instances during the summer and winter seasons. These advantages include the energy provided by the two WFs and the PHES technology. It is evident that hydroelectricity demonstrated excellent and significant benefits because it accounted for 66.39% of the system's benefits over the summer, or 6.14 (M) in the deterministic case and 6.07 (M) in the probabilistic case. Profits from wind energy reached 33,61 %, which is equivalent to 3,10 (M) in the deterministic case and 2,98 (M) in the probabilistic case, or 18,41(M) overall for the system this season. While in the winter, hydroelectricity accounts for 67.49% of an amount that totals 7.27 (M) for the deterministic case and 6.04 (M) for the probabilistic case, representing 62.99%, while wind energy comes in at 32.50% and 37.001% for both the deterministic and probabilistic cases, respectively. corresponding to 9.59 (M) and 10.78 (M). The total cost of the system is 20.37 (M).

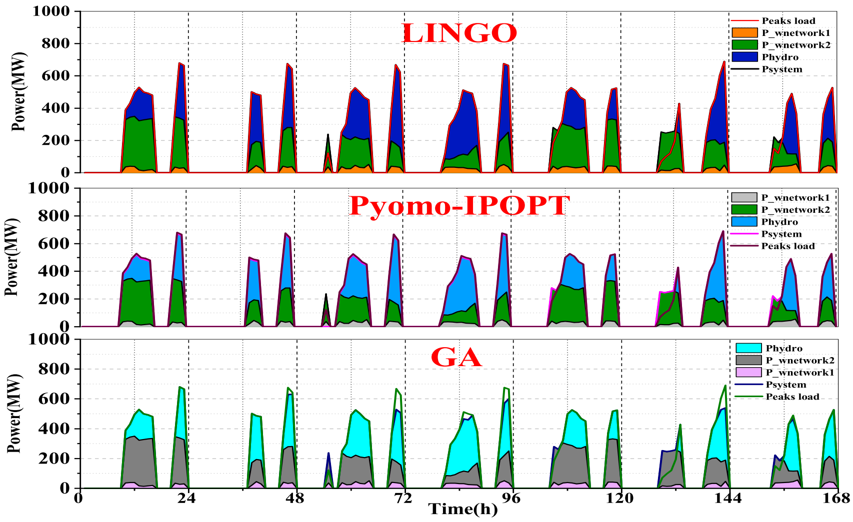

Figure 5.16: Comparison of optimization methods for lowering the system's summertime peak load.

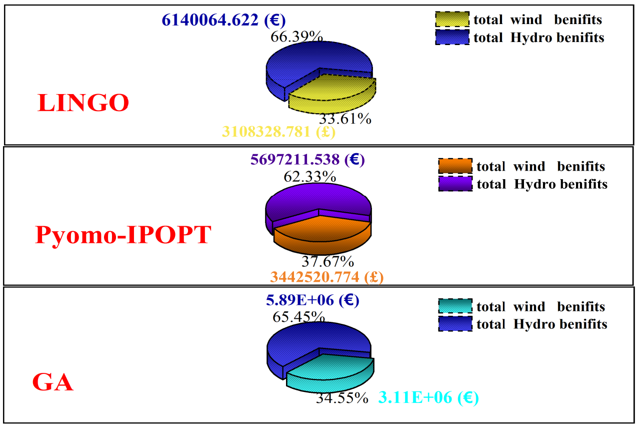

Figure 5.17: Percentages of wind and hydropower as well as their earnings for various optimization methods.

5.5.6 Comparison analysis

A comparison study has been conducted to show the effectiveness and performance of the proposed model compared to other methods available in the literature. The objective is to identify the most effective solution in a deterministic scenario. After conducting extensive simulations and analyzing the results, it became evident that the proposed model emerged as the optimal choice, flawlessly satisfying and achieving a remarkable 99.6% of the peak load requirements. Pyomo with the IPOPT solver demonstrated commendable performance, achieving a remarkable 98.8% satisfaction rate. Meanwhile, the genetic algorithm, although effective, exhibited a slightly lower yet respectable 95.87% success rate. This empirical evidence underscores the significance of tailored optimization techniques, with LINGO leading the way in ensuring optimal peak shaving and system performance, providing valuable insights for future implementations and system enhancements. As shown in figure 16. The percentages and earnings of each energy source (wind, hydro), as well as the overall benefits for each approach, are compared in Figs. 5.17 and 5.18. As can be observed, the proposed model implemented in LINGO and GA optimization methods with Pyomo-IPOPT, there is convergence in the percentage of energy produced by hydro. The real measure for the effectiveness of optimization techniques, however, continues to be the system's overall revenues (WF-PHES). It can be seen that the proposed control approach leads to the highest income, as depicted in figure 18. We conclude that the proposed approach achieves a total of 9.248 (M€), which is higher than Pyomo-IPOPT and GA, which have values of 9.139 (M€) and 9.003 (M€), respectively.

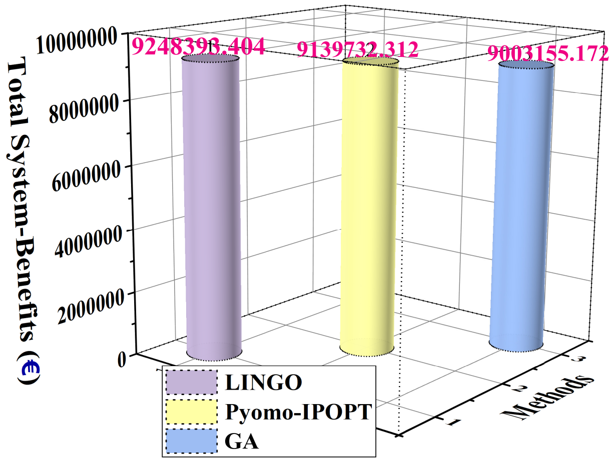

Figure 5.18: Total system incomes for different optimization methods.

5.6 Conclusion

In this work, we investigated and evaluated the effectiveness of using the energy generated by the contributions of two wind farms and a large-scale pumped hydro energy storage system to reduce peak loads in the power system. To track the grid power in real time (deterministic) and predict it (probabilistic), including the peak load, we propose a complete mathematical model of WF-PHES and a related optimization problem. These tools allow for the identification of the best operational approach that reduces the peak load and maximizes the benefits of the system. By taking advantage of the behavior and performance of PHES during the charging and discharging of water tanks, production and storage operations are monitored. The proposed model already takes into account, at an important level of detail, several technical and economic constraints. However, many other constraints may be present, depending on the practical application. For example, limitations in terms of cost of equipment, energy loss, storage capacity, and reliability may need to be taken into account in order to more accurately assess the effectiveness of the algorithm in the specific case study. The results demonstrate significant benefits and advantages due to the contribution of wind power, which generates free energy, and reliable and affordable PHES storage technology due to its ability to store a significant amount of energy for long periods of time with minimal energy losses. The amount of water that evaporates and the rate at which it rises and falls to meet changes in energy demand are used as indicators. The peak loads were reduced by 99% in summer, with inflows reaching a value of 18.46(M) for both the deterministic and probabilistic scenarios, but in winter, the peak loads were reduced by 88.5% for the deterministic case and 78.35% for the probabilistic case, with inflows evaluated at 20.37 (M) for both scenarios. We have convincingly demonstrated that the adoption of hybrid WF-PHES systems can be beneficial both to the main grid and to those making decisions about energy systems.

In the context of real-world applications, an intriguing perspective and future development involve the integration of this approach with Model Predictive Control (MPC). MPC, grounded in a sliding-horizon framework, entails computing optimal control sequences for a defined time horizon, with only the initial control action being executed. To incorporate the latest information for potential scenarios, the model operates on a rolling horizon principle, enabling access to new measurements at subsequent time steps. This facilitates the recalculation of the optimal control routine for the upcoming periods. It is important to note that the accuracy, reliability, and disparities between predicted and actual data significantly impact the effectiveness of the proposed approach. In order to address these challenges within a dynamic operational environment, the use of MPC allows for leveraging updated predictions derived from the most accurate short-term forecasts available.

Bibliography

[1] C. Béné and et al., "Feeding 9 billion by 2050–putting fish back on the menu," *Food Security*, vol. 7, pp. 261–274, 2015.

[2] Y. Chen and G. Shi, "How cooperation and competition arise in regional climate policies: Rice as a dynamic game," *IEEE Transactions on Control Systems Technology*, vol. 32, no. 2, pp. 595–610, 2024.

[3] C. Bai and J. Sarkis, "The water, energy, food, and sustainability nexus decision environment: A multistakeholder transdisciplinary approach," *IEEE Transactions on Engineering Management*, vol. 69, no. 3, pp. 656–670, 2022.

[4] C. Béné and et al., "Feeding 9 billion by 2050–putting fish back on the menu," *Food Security*, vol. 7, pp. 261–274, 2015.

[5] J. Espinosa-Tasón, J. Berbel, and C. Gutiérrez-Martín, "Energized water: Evolution of water-energy nexus in the spanish irrigated agriculture, 1950–2017," *Agricultural Water Management*, vol. 233, p. 106073, 2020.

[6] A. Soussi and et al., "Smart greenhouse farming: a review towards near zero energy consumption," *Discover Cities*, vol. 2, no. 1, pp. 1–29, 2025.

[7] W. Lu, X. Xu, G. Huang, B. Li, Y. Wu, and N. Zhao, "Energy efficiency optimization in swipt enabled wsns for smart agriculture," *IEEE Transactions on Industrial Informatics*, vol. 17, no. 6, pp. 4335–4344, 2021.

[8] J. Su, D. Yi, and B. Su, "Aerial visual perception in smart farming: Field study of wheat yellow rust monitoring," *IEEE Transactions on Industrial Informatics*, vol. 17, no. 3, pp. 2242–2249, 2021.

[9] M. Gunasekaran, H. Ching-Hsien, and R. B. S., "Isof: Information scheduling and optimization framework for improving the performance of agriculture systems aided by industry 4.0," *IEEE Internet of Things Journal*, vol. 8, no. 5, pp. 3120–3129, 2021.

[10] S. Adebola and et al., "Automated pruning and irrigation of polyculture plants," *IEEE Transactions on Automation Science and Engineering*, vol. 21, no. 3, pp. 2199–2210, 2024.

[11] S. Goddek and et al., "How greenhouse horticulture in arid regions can contribute to climate-resilient and sustainable food security," *Global Food Security*, vol. 38, p. 100701, 2023.

[12] Y. Achour, A. Ouammi, and D. Zejli, "Technological progresses in modern sustainable greenhouses cultivation as the path towards precision agriculture," *Renewable and Sustainable Energy Reviews*, vol. 147, p. 111251, 2021.

[13] F. Rodríguez, M. Berenguel, J. L. Guzmán, and A. Ramírez-Arias, "Modeling and control of greenhouse crop growth," *Springer, Basel, Switzerland*, 2015.

[14] R. Rayhana, G. Xiao, and Z. Liu, "Internet of things empowered smart greenhouse farming," *IEEE Journal of Radio Frequency Identification*, vol. 4, no. 3, pp. 195–211, 2020.

[15] S. Adebola and et al., "Automated pruning and irrigation of polyculture plants," *IEEE Transactions on Automation Science and Engineering*, vol. 21, no. 3, pp. 2199–2210, 2024.

[16] Y. Su, L. Xu, and D. Li, "Adaptive fuzzy control of a class of mimo nonlinear system with actuator saturation for greenhouse climate control problem," *IEEE Transactions on Automation Science and Engineering*, vol. 13, no. 2, pp. 772–788, 2016.

[17] J. Jiang, A. Mohagheghi, and M. Moallem, "Energy-efficient supplemental led lighting control for a proof-of-concept greenhouse system," *IEEE Transactions on Industrial Electronics*, vol. 67, no. 4, pp. 3033–3042, 2020.

[18] Y. Su, Q. Yu, and L. Zeng, "Parameter self-tuning pid control for greenhouse climate control problem," *IEEE Access*, vol. 8, pp. 186157–186171, 2020.

[19] A. Soussi and et al., "Integrating digital twins and mpc for sustainable greenhouse management in smart agriculture," *IEEE Transactions on AgriFood Electronics*, 2025.

[20] A. Pérez-González, O. Begovich-Mendoza, and J. Ruiz-León, "Modeling of a greenhouse prototype using pso and differential evolution algorithms based on a real-time labview™ application," *Applied Soft Computing*, vol. 62, pp. 86–100, 2018.

[21] K. Zhukovskii and et al., "Energy consumption optimisation for horticultural facilities," 2024.

[22] M. Zhang and et al., "Energy-saving design and control strategy towards modern sustainable greenhouse: A review," *Renewable and Sustainable Energy Reviews*, vol. 164, p. 112602, 2022.

[23] E. Rezaei and H. Dagdougui, "Optimal real-time energy management in apartment building integrating microgrid with multizone hvac control," *IEEE Transactions on Industrial Informatics*, vol. 16, no. 11, pp. 6848–6856, 2020.

[24] R. Carli and M. Dotoli, "Cooperative distributed control for the energy scheduling of smart homes with shared energy storage and renewable energy source," *IFAC-PapersOnLine*, vol. 50, no. 1, pp. 8867–8872, 2017.

[25] R. Minciardi and M. Robba, "A bilevel approach for the stochastic optimal operation of interconnected microgrids," *IEEE Transactions on Automation Science and Engineering*, vol. 14, no. 2, pp. 482–493, 2017.

[26] A. Ouammi, H. Dagdougui, and R. Sacile, "Optimal control of power flows and energy local storages in a network of microgrids modeled as a system of systems," *IEEE Transactions on Control Systems Technology*, vol. 23, no. 1, pp. 128–138, 2015.

[27] R. Carli and M. Dotoli, "Cooperative distributed control for the energy scheduling of smart homes with shared energy storage and renewable energy source," *IFAC-PapersOnLine*, vol. 50, no. 1, pp. 8867–8872, 2017.

[28] X. Fu and Y. Zhou, "Collaborative optimization of pv greenhouses and clean energy systems in rural areas," *IEEE Transactions on Sustainable Energy*, vol. 14, no. 1, pp. 642–656, 2023.

[29] A. Soussi and et al., "Smart sensors and smart data for precision agriculture: a review," *Sensors*, vol. 24, no. 8, p. 2647, 2024.

[30] A. Ouammi and et al., "Optimal operation scheduling for a smart greenhouse integrated microgrid," *Energy for Sustainable Development*, vol. 58, pp. 129–137, 2020.

[31] X. Fu and Y. Zhou, "Collaborative optimization of pv greenhouses and clean energy systems in rural areas," *IEEE Transactions on Sustainable Energy*, vol. 14, no. 1, pp. 642–656, 2023.

[32] A. Hussain, I.-S. Choi, Y. H. Im, and H.-M. Kim, "Optimal operation of greenhouses in microgrids perspective," *IEEE Transactions on Smart Grid*, vol. 10, no. 3, pp. 3474–3485, 2019.

[33] N. Choab and et al., "Effect of greenhouse design parameters on the heating and cooling requirement of greenhouses in moroccan climatic conditions," *IEEE Access*, vol. 9, pp. 2986–3003, 2021.

[34] S. Xia and et al., "Regulation flexibility assessment and optimal aggregation strategy of greenhouse loads in modern agricultural parks," *Protection and Control of Modern Power Systems*, vol. 9, no. 3, pp. 98–111, 2024.

[35] Y. Jin and et al., "Comprehensive optimization of shading and electrical performance of roof-mounted photovoltaic system of venlo-type greenhouse in the severe cold region," *Energy*, vol. 296, p. 131125, 2024.

[36] D. Lin, L. Zhang, and X. Xia, "Model predictive control of a venlo-type greenhouse system considering electrical energy, water and carbon dioxide consumption," *Applied Energy*, vol. 298, p. 117163, 2021.

[37] J. Ge and et al., "Variation and simulation of tomato transpiration in a greenhouse under different ventilation modes," *Agricultural Water Management*, vol. 308, p. 109281, 2025.

[38] M. Di Martino and et al., "Food-energy-water nexus considerations in optimal greenhouse farming systems design and operation," *Applied Energy*, vol. 379, p. 124900, 2025.

[39] Y. Su, L. Xu, and D. Li, "Adaptive fuzzy control of a class of mimo nonlinear system with actuator saturation for greenhouse climate control problem," *IEEE Transactions on Automation Science and Engineering*, vol. 13, pp. 772–788, Apr. 2016.

[40] A. Soussi *et al.*, "Integrating digital twins and mpc for sustainable greenhouse management in smart agriculture," *IEEE Transactions on AgriFood Electronics*, 2025.

[41] X. Fu and Y. Zhou, "Collaborative optimization of pv greenhouses and clean energy systems in rural areas," *IEEE Transactions on Sustainable Energy*, vol. 14, pp. 642–656, Jan. 2023.

[42] A. Ouammi *et al.*, "Optimal operation scheduling for a smart greenhouse integrated microgrid," *Energy for Sustainable Development*, vol. 58, pp. 129–137, 2020.

[43] D. Lin *et al.*, "Hierarchical optimization for the energy management of a greenhouse integrated with grid-tied photovoltaic–battery systems," *Applied Energy*, vol. 374, p. 124006, 2024.

[44] A. Boccalatte, M. Fossa, and R. Sacile, "Modeling, design and construction of a zero-energy pv greenhouse for applications in mediterranean climates," *Thermal Science and Engineering Progress*, vol. 25, p. 101046, 2021.

[45] B. M. Karambasti *et al.*, "Optimal solar greenhouses design using multiobjective genetic algorithm," *IEEE Access*, vol. 10, pp. 73728–73742, 2022.

[46] A. Boccalatte, M. Fossa, and R. Sacile, "Modeling, design and construction of a zero-energy pv greenhouse for applications in mediterranean climates," *Thermal Science and Engineering Progress*, vol. 25, p. 101046, 2021.

[47] D. Lin and et al., "Hierarchical optimization for the energy management of a greenhouse integrated with grid-tied photovoltaic–battery systems," *Applied Energy*, vol. 374, p. 124006, 2024.

[48] D. Zhao and et al., "Differential privacy energy management for islanded microgrids with distributed consensus-based admm algorithm," *IEEE Transactions on Control Systems Technology*, vol. 31, no. 3, pp. 1018–1031, 2023.

[49] C. Bersani, H. Dagdougui, A. Ouammi, and R. Sacile, "Distributed robust control of the power flows in a team of cooperating microgrids," *IEEE Transactions on Control Systems Technology*, vol. 25, no. 4, pp. 1473–1479, 2017.

[50] M. Jawad, M. Fayaz, M. Aman, and D. Kim, "Energy optimization and plant comfort management in smart greenhouses using the artificial bee colony algorithm," *Scientific Reports*, vol. 15, no. 1, p. 1752, 2025.

[51] B. M. Karambasti and et al., "Optimal solar greenhouses design using multiobjective genetic algorithm," *IEEE Access*, vol. 10, pp. 73728–73742, 2022.

[52] Jinko Solar, *Tiger Neo N-type 72H: JKM570-590N-72HL4-V Datasheet*, 2023. Available: https://www.pvo-int.com/wp-content/uploads/2023/04/JKM570-590N-72HL4-V-F5-EN-1.pdf.

[53] H. Dagdougui, L. Dessaint, G. Gagnon, and K. Al-Haddad, "Modeling and optimal operation of a university campus microgrid," in *Proc. IEEE Power Energy Soc. Gen. Meeting (PESGM)*, (Boston, MA, USA), pp. 1–5, 2016.

[54] Aeolos Wind Energy, *H-30kW Wind Turbine Brochure*, 2020. Available: https://www.neicjapan.com/wp/wp-content/uploads/2020/11/Aeolos-H-30kW-Brochure.pdf.

[55] S. Zahmoun, A. Ouammi, R. Sacile, R. Benchrifa, and E. Zero, "Optimal operation scheduling of a combined wind-hydro system for peak load shaving," *IEEE Trans. Autom. Sci. Eng.*, vol. 21, pp. 7117–7130, oct 2024.

[56] T. Zhang *et al.*, "Comparison of different irrigation methods to synergistically improve maize's yield, water productivity and economic benefits in an arid irrigation area," *Agric. Water Manag.*, vol. 243, p. 106497, jan 2021.

[57] G. van Straten, G. van Willigenburg, E. van Henten, and R. van Ooteghem, *Optimal Control of Greenhouse Cultivation*. Boca Raton, FL, USA: CRC Press, 2010.

[58] M. Olle and A. Viršile, "The effects of light-emitting diode lighting on greenhouse plant growth and quality," *Agric. Food Sci.*, vol. 22, no. 2, pp. 223–234, 2013.

[59] A. Ouammi, Y. Achour, H. Dagdougui, and D. Zejli, "Optimal operation scheduling for a smart greenhouse integrated microgrid," *Energy Sustain. Dev.*, vol. 58, pp. 129–137, oct 2020.

[60] Fluence Bioengineering, *SPYDR 2p Product Specification Sheet*, 2022. Available: https://fluence-led.com/wp-content/uploads/2025/02/FLU-SpecSheet_SPYDR2p47_EU_A4_052022-D-1.pdf.

[61] A. Soussi *et al.*, "Integrating digital twins and mpc for sustainable greenhouse management in smart agriculture," *IEEE Transactions on AgriFood Electronics*, 2025. To be published.

[62] M. C. Bozchalui, C. A. Cañizares, and K. Bhattacharya, "Optimal energy management of greenhouses in smart grids," *IEEE Trans. Smart Grid*, vol. 6, pp. 827–835, mar 2015.

[63] J. Sun, C.-H. Lai, and X.-J. Wu, "Quantum-behaved particle swarm optimization: Analysis of individual particle behavior and parameter selection," *Evol. Comput.*, vol. 20, pp. 349–393, sep 2012.

[64] A. Flori, H. Oulhadj, and P. Siarry, "Quantum particle swarm optimization: An auto-adaptive pso for local and global optimization," *Comput. Optim. Appl.*, vol. 82, pp. 525–559, jul 2022.

[65] Vertify, "Vertify greenhouse climate solutions," 2023.

[66] Y. Achour, A. Ouammi, D. Zejli, and S. Sayadi, "Supervisory model predictive control for optimal operation of a greenhouse indoor environment coping with food-energy-water nexus," *IEEE Access*, vol. 8, pp. 211562–211575, 2020.

[67] S. Zahmoun, A. Ouammi, R. Sacile, R. Benchrifa, and E. Zero, "Optimal operation scheduling of a combined wind-hydro system for peak load shaving," *IEEE Trans. Autom. Sci. Eng.*, vol. 21, pp. 7117–7130, oct 2024.

[68] K. Ojand and H. Dagdougui, "Q-learning-based model predictive control for energy management in residential aggregator," *IEEE Trans. Autom. Sci. Eng.*, vol. 19, pp. 70–81, jan 2022.

[69] F. Rodríguez, M. Berenguel, J. L. Guzmán, and A. Ramírez-Arias, *Modeling and control of greenhouse crop growth*. Cham: Springer International Publishing, 2015.

[70] G. van Straten, G. van Willigenburg, E. van Henten, and R. van Ooteghem, *Optimal Control of Greenhouse Cultivation*. Boca Raton, FL, USA: CRC Press, 2010.

[71] A. Ouammi, Y. Achour, H. Dagdougui, and D. Zejli, "Optimal operation scheduling for a smart greenhouse integrated microgrid," *Energy Sustain. Dev.*, vol. 58, pp. 129–137, 2020.

[72] M. C. Bozchalui, C. A. Cañizares, and K. Bhattacharya, "Optimal energy management of greenhouses in smart grids," *IEEE Trans. Smart Grid*, vol. 6, pp. 827–835, mar 2015.

[73] S. Zahmoun, A. Soussi, and F. Sacile, "Optimal operation of a smart greenhouse-integrated microgrid for strawberry growth in atlantic climate," in *2025 20th Annual System of Systems Engineering Conference (SoSE)*, (Tirana, Albania), pp. 1–6, 2025.

[74] F. F. N. Marcussi, R. L. Villas Bôas, L. J. G. de Godoy, and R. Goto, "Macronutrient accumulation and partioning in fertigated sweet pepper plants," *Scientia Agricola*, vol. 61, pp. 62–68, 2004.

[75] J. A. Sánchez-Molina, N. Perez, F. Rodríguez, J. L. Guzmán, and J. C. López, "Support system for decision making in the management of the greenhouse environmental based on growth model for sweet pepper," *Agricultural Systems*, vol. 139, pp. 144–152, 2015.

[76] H. Dagdougui, A. Ouammi, and L. A. Dessaint, "Peak load reduction in a smart building integrating microgrid and v2b-based demand response scheme," *IEEE Systems Journal*, vol. 13, pp. 3274–3282, sep 2019.

[77] S. Zahmoun, A. Ouammi, R. Sacile, R. Benchrifa, and E. Zero, "Optimal operation scheduling of a combined wind-hydro system for peak load shaving," *IEEE Transactions on Automation Science and Engineering*, vol. 21, pp. 7117–7130, oct 2024.

[78] S. Cui, Y.-W. Wang, and J.-W. Xiao, "Peer-to-peer energy sharing among smart energy buildings by distributed transaction," *IEEE Transactions on Smart Grid*, vol. 10, pp. 6491–6501, nov 2019.

[79] T. Boulard, P. Feuilloley, and C. Kittas, "Natural ventilation performance of six greenhouse and tunnel types," *Journal of Agricultural Engineering Research*, vol. 67, pp. 249–266, aug 1997.

[80] T. M. Tran, A. Ouammi, and L. A. Dessaint, "A near-zero energy smart greenhouse integrated into a microgrid for sustainable energy and microclimate management," *IEEE Access*, vol. 13, pp. 22243–22258, 2025.

[81] M. C. Bozchalui, C. A. Cañizares, and K. Bhattacharya, "Optimal energy management of greenhouses in smart grids," *IEEE Transactions on Smart Grid*, vol. 6, pp. 827–835, mar 2015.

[82] A. Hussain, I.-S. Choi, Y. H. Im, and H.-M. Kim, "Optimal operation of greenhouses in microgrids perspective," *IEEE Transactions on Smart Grid*, vol. 10, pp. 3474–3485, may 2019.

[83] A. Ouammi, H. Dagdougui, L. Dessaint, and R. Sacile, "Optimal operation scheduling for a smart greenhouse integrated microgrid," *Energy for Sustainable Development*, vol. 58, pp. 129–137, oct 2020.

[84] S. Boyd, "Alternating direction method of multipliers," tech. rep., Stanford University, Stanford, CA, USA, 2011. Lecture Notes EE364b, pp. 1–70.

[85] Y. Gu and N. Yamashita, "Alternating direction method of multipliers with variable metric indefinite proximal terms for convex optimization," *arXiv preprint arXiv:1906.12112*, jun 2019.

[86] A. Ouammi, "Optimal power scheduling for a cooperative network of smart residential buildings," *IEEE Transactions on Sustainable Energy*, vol. 7, pp. 1317–1326, jul 2016.

[87] A. Ouammi, V. Ghigliotti, M. Robba, A. Mimet, and R. Sacile, "A decision support system for the optimal exploitation of wind energy on regional scale," *Renewable Energy*, vol. 37, no. 1, pp. 299–309, 2012.

[88] A. Qazi, C. Bhowmik, F. Hussain, S. Yang, U. Naseem, A.-A. Adebayo, A. Gumaei, and M. Al-Rakhami, "Analyzing the public opinion as a guide for renewable-energy status in malaysia: A case study," *IEEE Transactions on Engineering Management*, 2021.

[89] S. Barja-Martinez, F. Rücker, M. Aragüés-Peñalba, R. Villafafila-Robles, Í. Munné-Collado, and P. Lloret-Gallego, "A novel hybrid home energy management system considering electricity cost and greenhouse gas emissions minimization," *IEEE Transactions on Industry Applications*, vol. 57, no. 3, pp. 2782–2790, 2021.

[90] G. Aquila, A. R. de Queiroz, P. R. Junior, L. C. S. Rocha, E. de Oliveira Pamplona, and P. P. Balestrassi, "Contribution for bidding of wind-photovoltaic on grid farms based on nbi-efa-snr method," *Sustainable Energy Technologies and Assessments*, vol. 40, p. 100754, 2020.

[91] J. D. Hunt, B. Zakeri, R. Lopes, P. S. F. Barbosa, A. Nascimento, N. J. de Castro, R. Brandão, P. S. Schneider, and Y. Wada, "Existing and new arrangements of pumped-hydro storage plants," *Renewable and Sustainable Energy Reviews*, vol. 129, p. 109914, 2020.

[92] J.-A. Pérez-Rúa, M. Stolpe, K. Das, and N. A. Cutululis, "Global optimization of offshore wind farm collection systems," *IEEE Transactions on Power Systems*, vol. 35, no. 3, pp. 2256–2267, 2019.

[93] S. D. Ahmed, F. S. Al-Ismail, M. Shafiullah, F. A. Al-Sulaiman, and I. M. El-Amin, "Grid integration challenges of wind energy: A review," *IEEE Access*, vol. 8, pp. 10857–10878, 2020.

[94] R. Minciardi and M. Robba, "A bilevel approach for the stochastic optimal operation of interconnected microgrids," *IEEE Transactions on Automation Science and Engineering*, vol. 14, no. 2, pp. 482–493, 2016.

[95] K.-C. Chu, K. Kaifuku, and K. Saitou, "Optimal integration of alternative energy sources in production systems with customer demand forecast," *IEEE Transactions on Automation Science and Engineering*, vol. 13, no. 1, pp. 206–214, 2015.

[96] M. Qian, N. Chen, Y. Chen, C. Chen, W. Qiu, D. Zhao, and Z. Lin, "Optimal coordinated dispatching strategy of multi-sources power system with wind, hydro and thermal power based on cvar in typhoon environment," *Energies*, vol. 14, no. 13, p. 3735, 2021.

[97] R. Xu, X. Ji, C. Liu, J. Hou, Z. Cao, and H. Qian, "Design and control of a wave-driven solar tracker," *IEEE Transactions on Automation Science and Engineering*, vol. 20, no. 2, pp. 1007–1019, 2022.

[98] E. Naderi, K. Bibek, M. Ansari, and A. Asrari, "Experimental validation of a hybrid storage framework to cope with fluctuating power of hybrid renewable energy-based systems," *IEEE Transactions on Energy Conversion*, vol. 36, no. 3, pp. 1991–2001, 2021.

[99] S. S. Rathore, S. Babu, K. Shekhawat, R. Singh, S. Yadav, V. K. Singh, and C. Singh, "Designing energy cum carbon-efficient environmentally clean production system for achieving green economy in agriculture," *Sustainable Energy Technologies and Assessments*, vol. 52, p. 102190, 2022.

[100] M. Alhaider and L. Fan, "Planning energy storage and photovoltaic panels for demand response with heating ventilation and air conditioning systems," *IEEE Transactions on Industrial Informatics*, vol. 14, no. 11, pp. 5029–5037, 2018.

[101] L. Tziovani, L. Hadjidemetriou, C. Charalampous, M. Tziakouri, S. Timotheou, and E. Kyriakides, "Energy management and control of a flywheel storage system for peak shaving applications," *IEEE Transactions on Smart Grid*, vol. 12, no. 5, pp. 4195–4207, 2021.

[102] L. Zhu, G. Lian, and S. Hu, "Research on a real-time control strategy of battery energy storage system based on filtering algorithm and battery state of charge," *Sustainable Energy Technologies and Assessments*, vol. 47, p. 101524, 2021.

[103] F. Verrilli, S. Srinivasan, G. Gambino, M. Canelli, M. Himanka, C. Del Vecchio, M. Sasso, and L. Glielmo, "Model predictive control-based optimal operations of district heating system with thermal energy storage and flexible loads," *IEEE Transactions on Automation Science and Engineering*, vol. 14, no. 2, pp. 547–557, 2016.

[104] Z. Dong, J. Tan, E. Muljadi, R. M. Nelms, A. St-Hilaire, M. Pevarnik, and M. D. Jacobson, "Developing of quaternary pumped storage hydropower for dynamic studies," *IEEE Transactions on Sustainable Energy*, vol. 11, no. 4, pp. 2870–2878, 2020.

[105] K. Kumar and R. Saini, "A review on operation and maintenance of hydropower plants," *Sustainable Energy Technologies and Assessments*, vol. 49, p. 101704, 2022.

[106] I. Ahmed, A. Dagnino, and Y. Ding, "Unsupervised anomaly detection based on minimum spanning tree approximated distance measures and its application to hydropower turbines," *IEEE Transactions on Automation Science and Engineering*, vol. 16, no. 2, pp. 654–667, 2018.

[107] Z. Zhao, J. Yang, W. Yang, J. Hu, and M. Chen, "A coordinated optimization framework for flexible operation of pumped storage hydropower system: Nonlinear modeling, strategy optimization and decision making," *Energy Conversion and Management*, vol. 194, pp. 75–93, 2019.

[108] B. Xu, J. Zhang, S. Yuan, H. Li, D. Chen, and J. Zhang, "Comprehensive regulation benefits of hydropower generation system in reducing wind power fluctuation," *Water*, vol. 13, no. 21, p. 2987, 2021.

[109] P. Roy, J. He, T. Zhao, and Y. V. Singh, "Recent advances of wind-solar hybrid renewable energy systems for power generation: A review," *IEEE Open Journal of the Industrial Electronics Society*, vol. 3, pp. 81–104, 2022.

[110] D. Apostolopoulou and M. McCulloch, "Optimal short-term operation of a cascaded hydro-solar hybrid system: a case study in kenya," *IEEE Transactions on Sustainable Energy*, vol. 10, no. 4, pp. 1878–1889, 2018.

[111] M. Azaroual, M. Ouassaid, and M. Maaroufi, "An optimal energy management of grid-connected residential photovoltaic-wind-battery system under step-rate and time-of-use tariffs," *International Journal of Renewable Energy Research*, vol. 10, no. 4, 2020.

[112] Z. Yang, L. Xia, and X. Guan, "Fluctuation reduction of wind power and sizing of battery energy storage systems in microgrids," *IEEE Transactions on Automation Science and Engineering*, vol. 17, no. 3, pp. 1195–1207, 2020.

[113] S. V. Papaefthymiou, E. G. Karamanou, S. A. Papathanassiou, and M. P. Papadopoulos, "A wind-hydro-pumped storage station leading to high res penetration in the autonomous island system of ikaria," *IEEE Transactions on sustainable energy*, vol. 1, no. 3, pp. 163–172, 2010.

[114] Y. Gong, Q. Jiang, and R. Baldick, "Ramp event forecast based wind power ramp control with energy storage system," *IEEE Transactions on Power Systems*, vol. 31, no. 3, pp. 1831–1844, 2015.

[115] G. Pathak, B. Singh, and B. K. Panigrahi, "Wind–hydro microgrid and its control for rural energy system," *IEEE Transactions on Industry Applications*, vol. 55, no. 3, pp. 3037–3045, 2019.

[116] F. Briongos, C. A. Platero, J. A. Sánchez-Fernández, and C. Nicolet, "Evaluation of the operating efficiency of a hybrid wind–hydro powerplant," *Sustainability*, vol. 12, no. 2, p. 668, 2020.

[117] E. Ercan and E. Kentel, "Optimum daily operation of a wind-hydro hybrid system," *Journal of Energy Storage*, vol. 50, p. 104540, 2022.

[118] G. Martínez-Lucas, J. I. Sarasúa, and J. Á. Sánchez-Fernández, "Frequency regulation of a hybrid wind–hydro power plant in an isolated power system," *Energies*, vol. 11, no. 1, p. 239, 2018.

[119] A. Golshani, W. Sun, Q. Zhou, Q. P. Zheng, J. Wang, and F. Qiu, "Coordination of wind farm and pumped-storage hydro for a self-healing power grid," *IEEE Transactions on Sustainable Energy*, vol. 9, no. 4, pp. 1910–1920, 2018.

[120] P. Das, B. K. Das, N. N. Mustafi, and M. T. Sakir, "A review on pump-hydro storage for renewable and hybrid energy systems applications," *Energy Storage*, vol. 3, no. 4, p. e223, 2021.

[121] S. Zhang, Y. Xiang, J. Liu, J. Liu, J. Yang, X. Zhao, S. Jawad, and J. Wang, "A regulating capacity determination method for pumped storage hydropower to restrain pv generation fluctuations," *CSEE Journal of Power and Energy Systems*, vol. 8, no. 1, pp. 304–316, 2020.

[122] A. Blakers, M. Stocks, B. Lu, and C. Cheng, "A review of pumped hydro energy storage," *Progress in Energy*, vol. 3, no. 2, p. 022003, 2021.

[123] A. Ouammi, Y. Achour, D. Zejli, and H. Dagdougui, "Supervisory model predictive control for optimal energy management of networked smart greenhouses integrated microgrid," *IEEE transactions on automation science and engineering*, vol. 17, no. 1, pp. 117–128, 2019.

[124] C. Bersani, M. Fossa, A. Priarone, R. Sacile, and E. Zero, "Model predictive control versus traditional relay control in a high energy efficiency greenhouse," *Energies*, vol. 14, no. 11, p. 3353, 2021.

[125] T. Xie, C. Zhang, T. Wang, W. Cao, C. Shen, X. Wen, and C. Mao, "Optimization and service lifetime prediction of hydro-wind power complementary system," *Journal of Cleaner Production*, vol. 291, p. 125983, 2021.

[126] C. Su, C. Cheng, P. Wang, J. Shen, and X. Wu, “Optimization model for long-distance integrated transmission of wind farms and pumped-storage hydropower plants,” *Applied Energy*, vol. 242, pp. 285–293, 2019.

[127] M. Ghaisi, M. Rahmani, P. Gharghabi, A. Zoghi, and S. H. Hosseinian, “Scheduling a wind hydro-pumped-storage unit considering the economical optimization,” *American Journal of Electrical and Electronic Engineering*, vol. 5, no. 1, pp. 16–22, 2017.

[128] Y. Yang, Y. Zhou, J. Wu, Z. Xu, S. He, X. Guan, and T. Liu, “An event-triggered hybrid system model for cascading failure in power grid,” *IEEE Transactions on Automation Science and Engineering*, vol. 19, no. 3, pp. 1312–1325, 2022.

[129] R. Wang, D. Ma, M.-J. Li, Q. Sun, H. Zhang, and P. Wang, “Accurate current sharing and voltage regulation in hybrid wind/solar systems: an adaptive dynamic programming approach,” *IEEE Transactions on Consumer Electronics*, vol. 68, no. 3, pp. 261–272, 2022.

[130] e. a. R. Wang, “Approach and reduced-order aggregate model for large-scale converters with inhomogeneous initial conditions in dc microgrids,” *IEEE Transactions on Energy Conversion*, vol. 36, no. 3, pp. 2473–2484, 2021.

[131] H. Dagdougui, R. Minciardi, A. Ouammi, M. Robba, and R. Sacile, “A dynamic decision model for the real-time control of hybrid renewable energy production systems,” *IEEE Systems Journal*, vol. 4, no. 3, pp. 323–333, 2010.

[132] A. Ouammi, H. Dagdougui, and R. Sacile, “Optimal planning with technology selection for wind power plants in power distribution networks,” *IEEE Systems Journal*, vol. 13, no. 3, pp. 3059–3069, 2019.

[133] A. Bellat, K. Mansouri, and A. Raihani, “Optimizing the layout of wind turbines by upgrading a wind farm,” in *E3S Web of Conferences*, vol. 297, p. 01038, EDP Sciences, 2021.

[134] G. S. C. Assunção, D. Marcelin, J. C. Von Hohendorff Filho, D. J. Schiozer, and M. S. De Castro, “Friction factor equations accuracy for single and two-phase flows,” in *International Conference on Offshore Mechanics and Arctic Engineering*, vol. 84430, p. V011T11A043, American Society of Mechanical Engineers, 2020.

[135] O. Bozorg-Haddad, M. Azad, E. Fallah-Mehdipour, M. Delpasand, and X. Chu, “Verification of fpa and pso algorithms for rule curve extraction and optimization of single-and multi-reservoir systems’ operations considering their specific purposes,” *Water Supply*, vol. 21, no. 1, pp. 166–188, 2021.

[136] S. Dutta, “Soil erosion, sediment yield and sedimentation of reservoir: a review,” *Modeling Earth Systems and Environment*, vol. 2, pp. 1–18, 2016.

[137] A. Ouammi, R. Sacile, D. Zejli, A. Mimet, and R. Benchrifa, “Sustainability of a wind power plant: Application to different moroccan sites,” *Energy*, vol. 35, no. 10, pp. 4226–4236, 2010.